The University Of Sheffield.

3D Printing of Activated Carbon/UHMWPE Polymer Composite using Laser Sintering

Yas K Khalil

The University of Sheffield

Faculty of Engineering

Department of Mechanical Engineering

Thesis submitted in partial fulfilment of the requirements for the degree of Doctor of Philosophy

August 2018

Abstract

Portable water purification systems are used to deliver safe and clean drinking water that can be used in remote villages and disaster zones and can purify water from potential pathogens like typhoid, cholera, dysentery and diarrhoea.

One of the main components in these systems is Activated Carbon filter (ACF). The composite materials used in manufacturing ACFs are Activated carbon (AC), as a matrix, and Ultra High Molecular Weight Polyethylene (UHMWPE), as a binder.

The current challenges are to provide filters with enhanced internal structure, coupled with a desire to further reduce costs by reducing the amount of binding material and the energy required for processing. A further consideration is to improve the performance of the Activated Carbon filters. Therefore, it would be desirable to provide an advanced technology for manufacturing Activated Carbon filters that decreases manufacturing time, increases dimensional accuracy, durability and performance. One possible path to accomplish this goal is through the use of state-of-the-art technology, such as Additive Manufacturing.

This work has been motivated to establish that there are many areas where Additive Manufacturing technologies can be used with shorter manufacturing time, lower cost, control of internal structure and improved performance, in comparison with the conventional techniques of manufacturing the Activated Carbon filters.

Processing the materials used in manufacturing Activated Carbon filters by Laser Sintering was investigated, with the aim of developing an understanding of the influence of processing parameters, such as laser power and bed temperature, on the internal structure, morphology and mechanical properties of laser sintered parts. Additionally, if further reduction in binder (UHMWPE) content while maintaining the performance will result in material and cost savings.

The work presented in this thesis studies the novel process, and investigates a new material for Additive Manufacturing. The influence of laser power, part bed temperature and UHMWPE binder content on physical, mechanical and morphological properties of the AC-UHMWPE parts fabricated by laser sintering were investigated. The water flow through laser sintered parts was investigated as a method to evaluate the filtration performance of the produced parts.

The key finding that have been addressed in this work can be summarised as follows:

Trials to laser-sinter the commercial UHMWPE GUR 2122 powder (Celanese, Germany) have been made. Although, processing UHMWPE using laser sintering was challenging, good parts were fabricated successfully at various laser powers using a commercial laser sintering machine (EOS P100, Germany). There are still difficulties of processing UHMWPE due to highly agglomerated structure of smaller particles with the presence of fibrils in the UHMWPE particles.

The mechanical test results show that flexural strength is influenced by laser energy density and a good flexural strength (1.37 ± 0.30 MPa) is still achievable with energy density of 0.016 J/mm2 (LP = 6 watts).

A high level of porosity was achieved in the laser sintered UHMWPE parts with a range of 60-62% and 61-65% measured by micro-CT and helium gas pycnometry, respectively. Porous structures hold distinctive physical properties that are associated with their low density and construction. The mechanical, thermal and electrical attributes provide a vast range of potential applications, including thermal insulation, packaging, filtration, food and beverage, biomedical applications, military, automobile, aerospace and shipping industries.

The present work demonstrated that AC-UHMWPE composite can be processed using Laser Sintering with a range of processing parameters at

different binder content. An average relative density of 20.95 ±0.08%, 17.74 ±0.18% and 16.49 ±0.40% was achieved for laser sintered AC-UHMWPE parts with compositions of 70:30, 80:20 and 85:15 AC-UHMWPE, respectively.

The average total porosity of the 85:15 AC-UHMWPE was approximately 83% (measured by helium gas). A slight reduction in porosity (by 4% approximately) has been observed when the UHMWPE content increased from 15% to 30%. This result suggests that the porosity decreases with the increase in UHMWPE content and the effects on porosity are not significantly driven by the process parameters of the laser sintering within the range of parameters analysed.

The water flow rate is substantially influenced by the weight fraction of UHMWPE in the AC-UHMWPE composite. The average flow rate of the disc-shaped filters decreases with increasing of the fraction weight of UHMWPE. It was also observed that the flow rate increased with the high energy input generated either by the laser power or by the bed temperature.

This project has demonstrated that, for the first time, 3D printed activated carbon filters can be produced using laser sintering process. In comparison with the filters produced by the conventional process, the following outcomes can be drawn:

- Higher water flow rate
- Possibility to reduce cost by using less binder
- Filtration that matches current benchmarks
- Lower process temperature, which should allow for high melt flow index materials to be used as binders. This in turn allows cheaper and degradable polymers
- High repeatability

Acknowledgements

I would like to express my deepest gratitude and appreciation to Professor Neil Hopkinson for his support and guidance during the first 14 months of my study. His attitude, enthusiasm and insight in the research are appreciable and will always be source of inspiration and motivation. His patience and encouragement regarding my study and personal development are greatly appreciated. I would also like to appreciate the guidance, invaluable inputs and advice from my industrial supervisor Professor Adam Kowalski. I would like to express my deepest gratitude and appreciation to Professor Patrick Fairclough for agreeing to continue my PhD journey with me, after the departure of Professor Neil Hopkinson, and also for his continued support and guidance.

I would like to thank all the staff in Additive Manufacturing laboratory (AdAM centre) and I am very grateful for all their support and help. I must also thank my PhD colleagues for their support, advice, and encouragement. Without their collective madness the research office would be a far gloomier place to work. I also wish to convey my appreciation to all people who have given me their support, help and love.

I must thank my wife and my sons Ali and Adam which have suffered the most through my PhD journey. They provided me with endless love, support and put up with my long working hours and to revive me when I feel defeated.

My mother has made many sacrifices to see me through higher education and I hope that I have made her proud. My sincerest gratitude to her for her love, support, and encouragement on every angle of my life. I wish to convey my deepest gratitude to my father, who sadly isn't here with us, and also to my youngest brother Abbas, who was kidnapped during the sectarian violence in 2007 in my original torn-apart country, Iraq and he has not been found since then. I dedicate this work in memory of my dad and my brother.

Publications

The following papers have been published:

1. Khalil, Y., Kowalski, A., and Hopkinson, N., *Influence of energy density on flexural properties of laser-sintered UHMWPE.* Additive Manufacturing, 2016. 10: p. 67-75.

2. Khalil, Y., Kowalski, A., and Hopkinson, N., Influence of laser power on tensile properties and material characteristics of laser-sintered UHMWPE. Manufacturing Rev., 2016. 3.

3. Khalil, Y., Hopkinson, N., Kowalski, A., and Fairclough, P., Influence of laser power on morphology and properties of laser-sintered UHMWPE. In 27th Annual International Solid Freeform Fabrication Symposium. 2016. Austin, Texas.

Table of Contents

List of Figures

List of Tables

Nomenclature

Symbol	Description, unit
γ	Surface tension, N/m
t	Sintering time, s
η, η_0	Zero-shear viscosity, Pa s
T_m	Melting point, °C
T_g	Glass transition temperature, °C
T_c	Solidification/Crystallisation temperatures, °C
LP	Laser power, watt
SS	Scan speed, mm/s
HS	Hatch spacing, mm
ED	Energy density, J/mm^2
M_W	Weight-average molecular weight, g/mol
θ	Angle of reflection, degree
2θ	Scattering angle, degree
d	Space between the planes of atoms, nm
λ	Wavelength of the radiation, nm
X_C	Degree of crystallinity, %
ΔH	Heat of fusion, J/g
I	Scattering intensity, a. u. (arbitrary unit)
UTS	Ultimate Tensile Strength, MPa
ρ	Density, g/cm^3

Chapter 1 Research Scope

1.1 Research Background

The scarcity of safe and clean drinking water is a prime public health issue in developing countries in which 80% of diseases are water borne (Figure 1.1). In 2015, around 800 million people in the world were without a proper access to safe and clean water [1] and around 3.4 million die each year from water associated diseases [2] mainly in developing countries like India. In India, 76 million do not have access to safe and clean drinking water and around 37.7 million are affected by water associated diseases each year [1]. More than 140 thousand children die each year from diarrhoea due to un-safe water and poor sanitation [3].

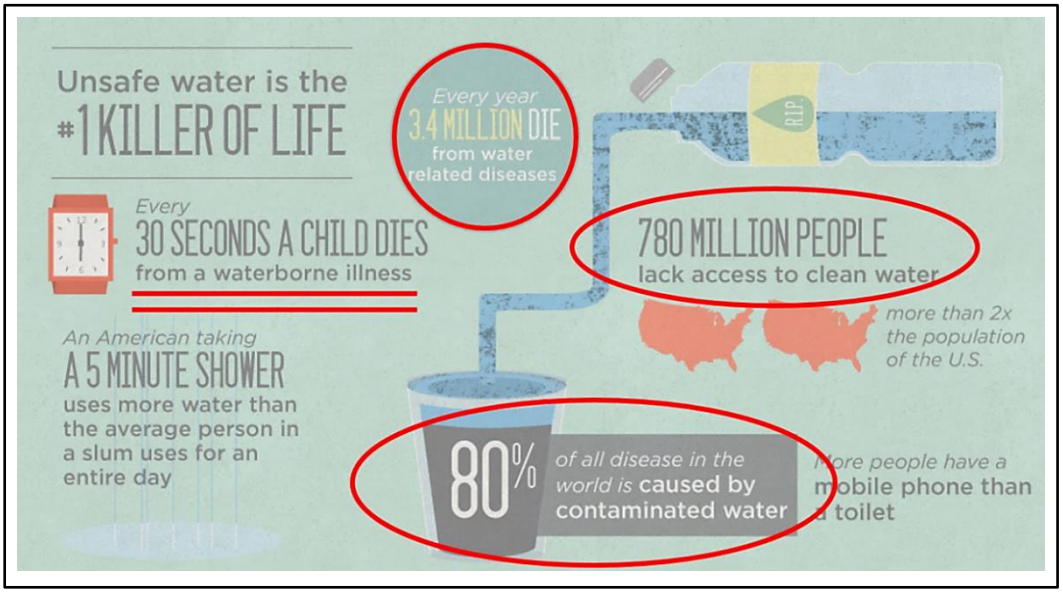

Figure 1.1: Drinking water issue (adapted from National Geographic magazine)

Portable water purification systems are used to deliver safe drinking water as one of the solutions to tackle this problem. These systems can be used in remote villages and disaster zones and can purify water from potential pathogens like typhoid, cholera, dysentery and diarrhoea.

Unilever plc, a fast-moving consumer goods company, spent five years developing a solution for water purification and the result was in-home water purifier, "Pureit" (Figure 1.2). This system provides a drinking water without the need for electricity, gas or a pressurised water supply. One of the main components in this system is Activated Carbon filter. Activated Carbon is one of the most commonly used materials for water filtration. It is effective because of its ability to adsorb higher concentrations of various harmful substances such as pesticides, industrial chemicals, chlorine and various organic chemicals. "Pureit" comes in various models targeted at consumers with different income ranges across markets and the most affordable model in India costs €20 (INR 1,550) [4].

Figure 1.2: Unilever's "Pureit" Classic (adopted from [5])

The system works in four stages and produces a safe drinking water that is odourless, tastes good and natural. The stages of the purification process are shown in Figure 1.3.

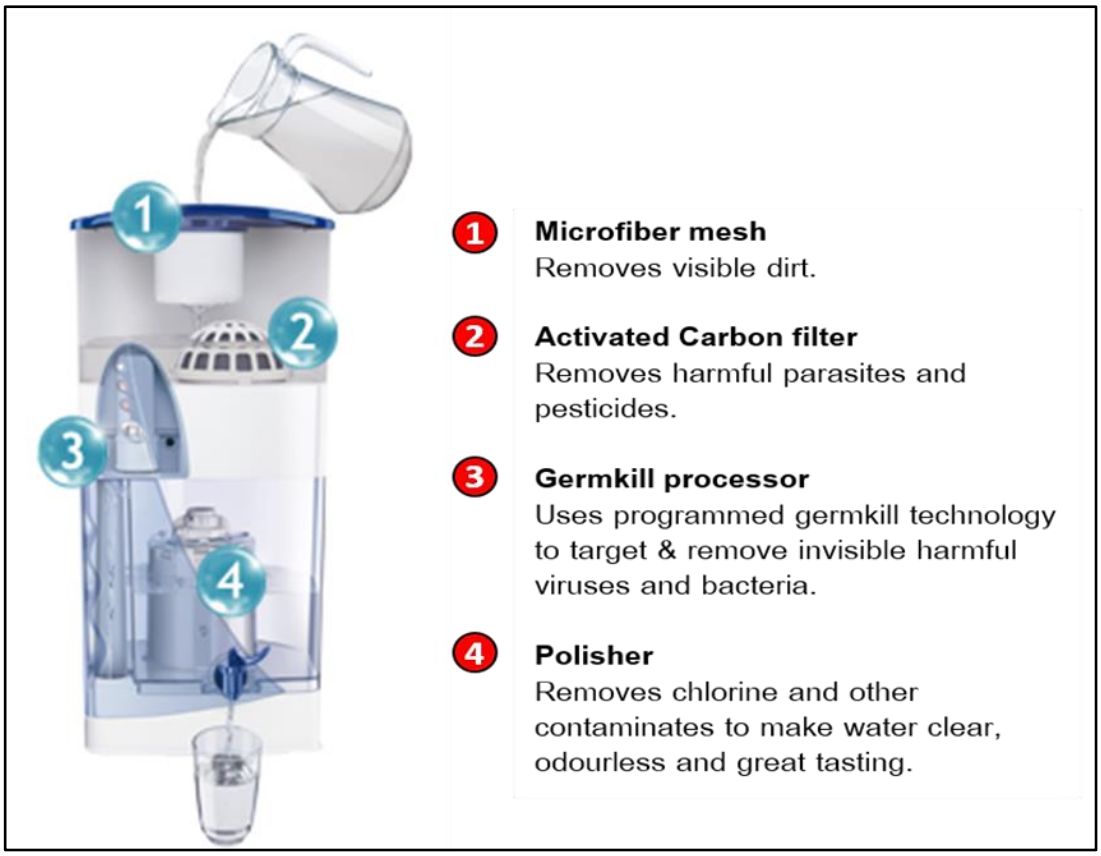

Figure 1.3: Pureit four stages water purification process (adopted from [6])

The research area in this project was focused on the manufacturing of Activated Carbon filter (ACF) which is shown in Figure 1.3, item number 2.

The current process (Figure 1.4) of manufacturing ACFs at Unilever, as described in section [0059], patent EP2635362B1 [7], involves the following steps:

- Mixing Activated Carbon (80% w/w) with Ultra-High Molecular Weight Polyethylene (UHMWPE) binder (20% w/w).
- The dry mixture is then placed in a mould and compacted.
- The mould is placed in an oven at 250°C for two and a half hours.
- The moulded element is left to cool for over an hour.
- Then the ACF is removed from the mould by a mechanical release.

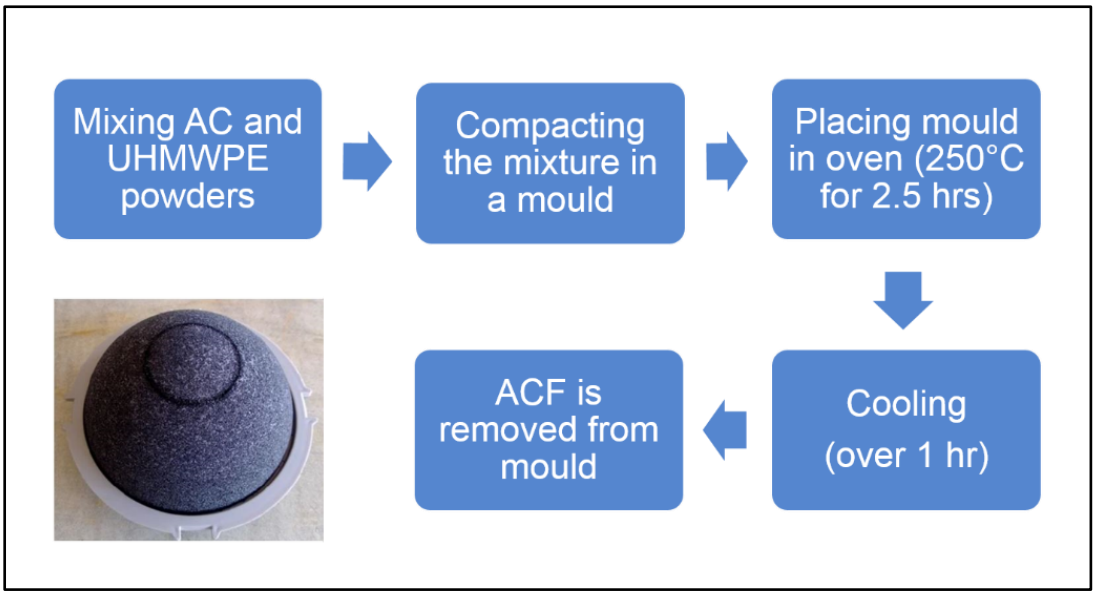

Figure 1.4: Current process of manufacturing Unilever's ACF

The current process has some drawbacks including:

- Low-production efficiency, due to the long heating and cooling times
- High energy consumption
- Limited mould life
- Highly expensive and time intensive tooling moulds
- Does not allow the free-control of microstructures causing inefficient performance

A typical example of a compacted powder structure is illustrated in Figure 1.5. When the powder is compressed during the heating process, this reduces the space among particles which in turn can result in a low porosity and irregular structures. This issue would have a considerable impact on the water flow rate and also the efficiency of filtration.

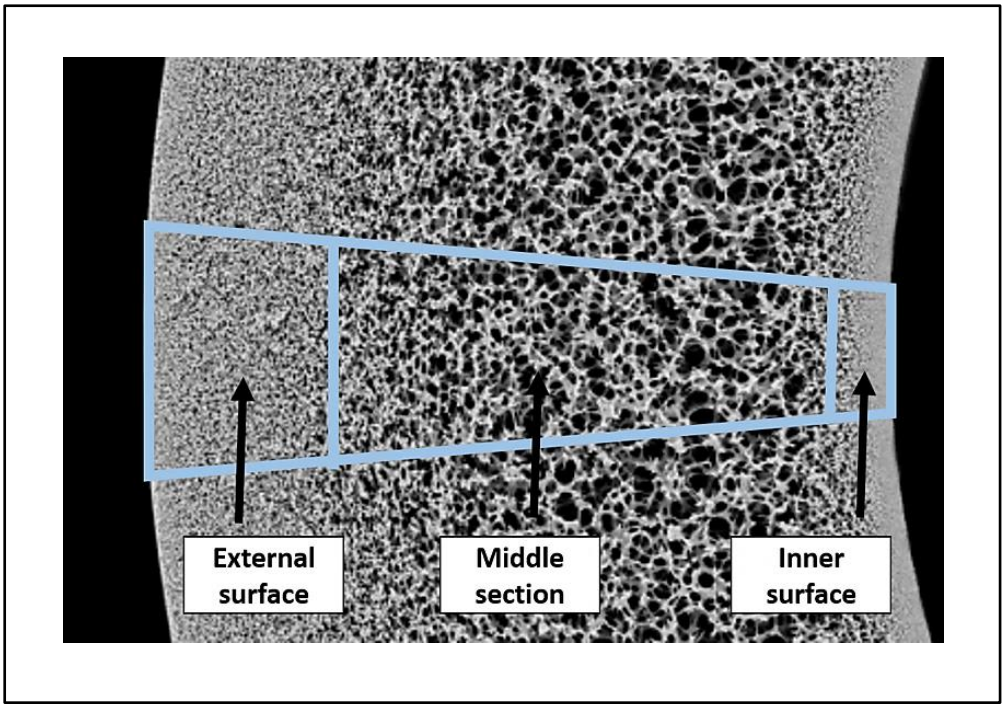

Figure 1.5: Typical example of a compacted powder structure
(Image adopted from Separation Technology & Materials website [8]
for illustration purposes)

1.2 Novelty Statement

Additive Manufacturing techniques, such as Laser Sintering, have a number of advantages over conventional techniques when producing porous structures:

- Good control over pore network design and properties
- Good reproducibility
- Greater pore interconnectivity
- Enhanced mechanical properties

The mechanical and thermal properties of porous structures can be influenced by the microstructure and the composition of the initial material, as well as the morphological and geometrical properties of the basic cell structure [9]. Additionally, the density and mechanical behaviour of laser sintered parts depend on the laser energy density, part bed temperature, and part orientation. However, the achievable laser sintered part density is directly

associated with powder density in the part bed, which is linked to the shape of particles and their free flowing behaviour [10]. Powder flow, which depends on several factors including particle size and shape, as an example, plays a significant role in laser sintering as the lack of homogeneous and even layers contributes to producing porous laser sintered parts [11].

Results from other work indicated that the microstructure, physical, mechanical properties and quality of the laser sintered parts are fundamentally affected by laser power, laser speed and hatch spacing which are directly related to the amount of energy applied on the powder surface in the part bed. These parameters are seen as a function of energy density [12].

Therefore, hypothetically, the density of laser sintered parts would increase as the energy density increases, in this case, the mechanical properties would be enhanced but on the other hand the porosity will be decreased. However, the percentage of the internal porous region would increase with the increase in particle size and decrease with the increase in laser power. The degree of particle fusion and porosity are affected by the particle size of the powder as well as the processing parameters [13, 14].

The present work investigates a new material for Additive Manufacturing processes with the current challenges being to control the internal structure (i.e. porosity profile). To the author's knowledge, no investigation has been reported related to the effect of process parameters on the porosity of laser sintered UHMWPE GUR 2122 parts. The laser power was varied to investigate how this influences the mechanical properties and porosity of the structure. The difference in the porosity levels and the pore morphology between different laser sintered parts was investigated.

This work also shows that the sintering behaviour of polymers is controlled by the morphology of the particles in addition to the viscous flow of UHMWPE. Therefore, polymer sintering model, such as Frenkel-Eshelby model, would underestimate the sintering rate of UHMWPE and leads to a substantial

deviations from the experimental result [15]. The images from the hot stage microscopy suggest that the particles morphology of UHMWPE did not change and the structures preserved their confirmations even after the hot stage reached the melting temperature of UHMWPE (i.e. 141°C). Andjelić *et al.* suggested that the chain location remains un-changed, even after melting. The UHMWPE lamellae contains a high concentration of entangled tie macromolecules in the amorphous region. The formation of these stable entanglements may prevent the conformational changes of the chains from crystalline phase into amorphous phase [16].

This work, for the first time, shows the processing of AC-UHMWPE composite using Laser Sintering with a range of processing parameters at different binder content. The results and subsequent analysis have generated an understanding of the influence of processing parameters, such as laser power and bed temperature, on the internal structure, morphology and mechanical properties of the parts produced.

This project has demonstrated that, for the first time, 3D printed activated carbon filters can be produced using laser sintering process. In comparison with the filters produced by the conventional process, the following outcomes can be drawn:

- Higher water flow rate
- Possibility to reduce cost by using less binder
- Filtration that matches current benchmarks
- Lower process temperature, which should allow for high melt flow index materials to be used as binders. This in turn allows cheaper and degradable polymers
- High repeatability

1.3 Research Aim

The aim of this research is to investigate the feasibility of processing the materials used in manufacturing of Activated Carbon filters (i.e. UHMWPE GUR 2122 and Activated Carbon/UHMWPE GUR 2122 composite powders) using a commercial Laser Sintering machine. The results and subsequent analysis will generated an understanding of the influence of processing parameters, such as laser power and bed temperature, on the internal structure, morphology and mechanical properties of the parts produced.

This work has also been motivated to substantiate that there are many areas where Additive Manufacturing technologies, such as Laser Sintering, can be applied to produce 3D printed activated carbon water filters with a good control of the internal geometry and size of the pores in comparison with the conventional method of manufacturing these filters. The experimental findings and analysis will create a base of fundamental knowledge on the potential of Additive Manufacturing as a new technology for manufacturing Activated Carbon filters.

1.4 Research Objectives

This work can be divided in two phases:

Phase 1: Investigating the feasibility of processing the commercial UHMWPE (GUR 2122) powder by Laser Sintering including the following objectives:

1. Processing UHMWPE by Laser Sintering.
2. Investigate the effect of laser energy density (i.e. laser power) on material characteristics and mechanical properties of laser sintered UHMWPE.
3. Investigate the effect of laser power on morphological properties of laser sintered UHMWPE.

Figure 1.6 shows the flowchart of research tasks that are required for phase 1 of this study.

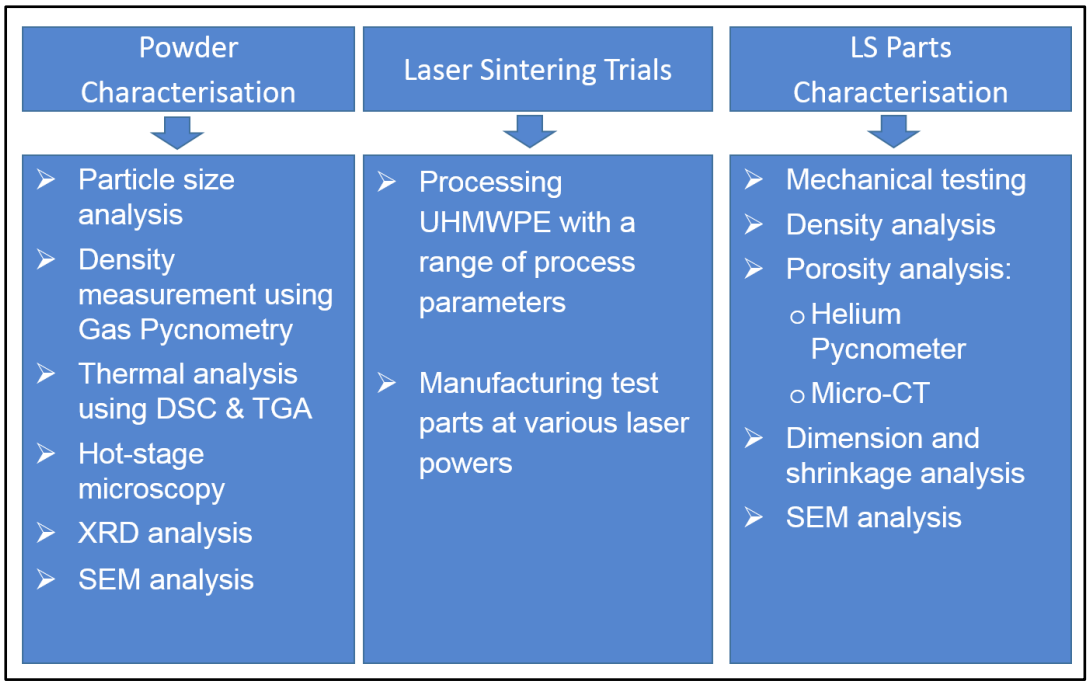

Figure 1.6: Flowchart of research tasks of phase 1

Phase 2: Investigating the feasibility of processing AC-UHMWPE composite by Laser Sintering including the following objectives:

1. Processing AC-UHMWPE composite by Laser Sintering at various laser powers, bed temperatures and binder content.
2. Investigate the effect of laser power, bed temperature and binder content on flexural properties of laser sintered parts.
3. Investigate the influence of laser power, bed temperature and binder content on density, morphology properties and water flow of laser-sintered parts.
4. Create a base of fundamental knowledge on the potential of Additive Manufacturing as a new technology for manufacturing Activated Carbon filters.

Figure 1.7 shows the flowchart of research tasks that are required for phase 2 of this study.

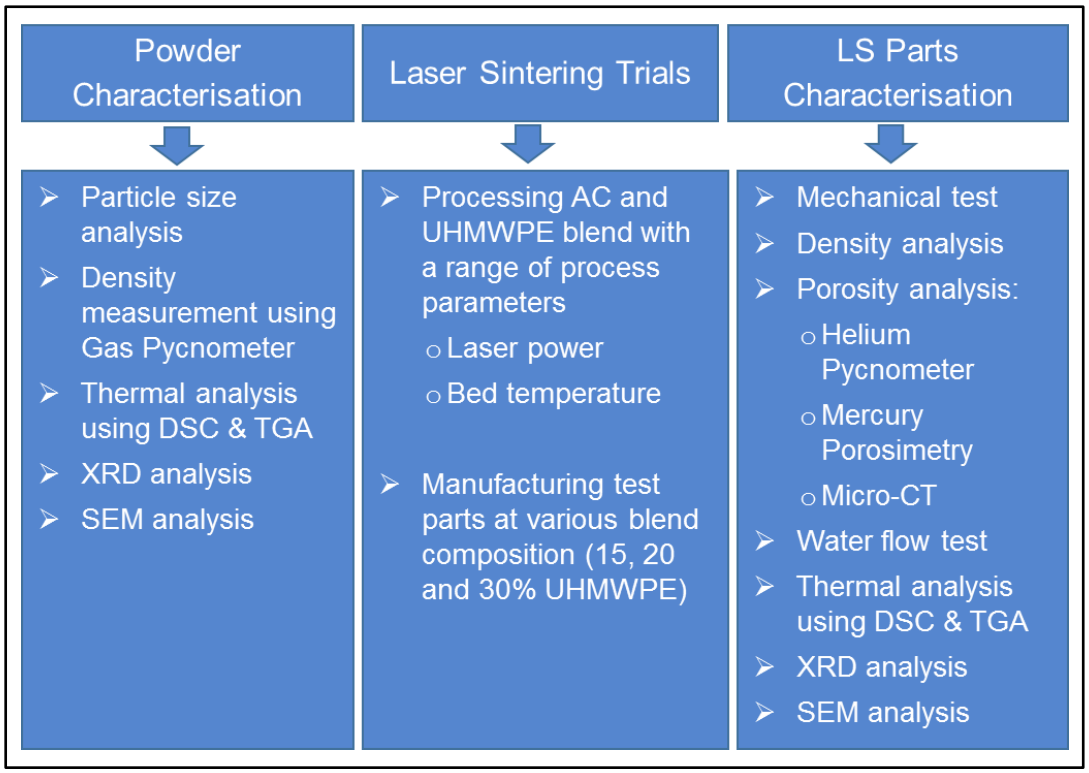

Figure 1.7: Flowchart of research tasks of phase 2

1.5 Experimental Methodology

Powder characterisation is an essential step for processing polymers by laser sintering. Laser sintering is well suited process to manufacture a variety of polymeric materials including non-standard laser sintering materials (i.e. off-the-shelf powders). However, powder characteristics and properties, such as particle size, shape and powder flow, can greatly influence the quality of the parts produced as well as the processing of the powder [190]. However, no single analytical method alone can be used to reliably characterise a powder. Methods such as x-ray powder diffraction, scanning electron microscopy, density, thermal analysis (DSC and TGA), hot stage microscopy, XRD analysis all contribute to define the powder characteristics that best suited for laser sintering.

Previous investigation shows that the degree of control over the microstructure of the laser sintered parts depends on the process parameters, especially the properties of the powder. Particle size distribution

and morphology influence the packing density of the powder, whereas the thermal behaviour and stability define the laser energy density required in laser sintering [17]. Understanding the thermal stability of UHMWPE powder is essential for the simulation of laser sintering process.

1.5.1 Powder Flow

Powder flow, which depends on several factors including particle size and shape, as an example, plays a significant role in laser sintering as the lack of homogeneous and even layers contributes to producing porous laser sintered parts [11]. The shape and surface of the powder particles determines the behaviour of the powder [10]. The irregular shape leads to poor powder flow that in turn leads to poor powder deposition and subsequent laser sintering processing difficulties [18]. Particles with flakes on the surface, or particles with less dense structures can easily produce laser sintered parts with high porosity [19].

The particles of laser sintering powders should be approximately spherical to induce a free flowing behaviour and ensure the powder is distributed on the part bed, by a blade or a roller, will not be compacted further [10]. Therefore, SEM examination of UHMWPE powder can reveal whether the particles are spherical or non-spherical in shape and also if the microstructure of the particles shows any presence of agglomeration and fibrils which are unfavourable for laser sintering powders.

Hausner ratio (HR), which is the ratio between the tapped density and the apparent density, is one of the most commonly used method to quantify flowability in powder-based sintering processes [20]. The determination of bulk and tapped densities is a simple method and correlate well to flow behaviour. HR can be affected by particles shapes (i.e., irregular, spherical and flake) and particle size. If the particle shape deviates more from spherical, then the HR becomes higher. Also, the HR decreases with increasing particle size [21].

1.5.2 Sintering Behaviour

The consolidation process in laser sintering is initiated by heat, generated by a laser, which results in the formation of the part layers. The Frenkel theory, one of the polymer sintering models, states that the sintering process begins with the formation of necks between adjacent particles, which then followed by full coalescence. The sintering behaviour can be predicted by direct visualisation of the coalescence on a hot stage microscope [15, 22, 23]. The simulation of the sintering process is an important stage for the development of new materials in polymer processing [24]. Therefore the Hot Stage Microscopy (HSM) procedure will aid to visually record the event of consolidation of UHMWPE powder and practically verify its consolidation behaviour.

1.5.3 Thermal Analysis

The thermal behaviour and stability define the laser energy density required in laser sintering [17]. Understanding the thermal stability of UHMWPE is essential for the simulation of laser sintering process.

Differential Scanning Calorimetry (DSC) allows the determination of the melting and crystallisation behaviour of a polymer, it is a useful tool for the evaluation of the suitability of the polymers for the sintering process. The phase transformations during melting and cooling (crystallisation) are the key parameters. For materials that show a relatively sharp melting endotherm, their powder can be heated to a temperature just under the melting point throughout the sintering process cycle [24]. Another thermal characteristic required for successful sintering is to have a wide processing window [25], which is defined as the difference between the temperatures at the onset of melting on heating and the onset of re-crystallisation on cooling.

Thermogravimetric Analysis (TGA) is a common method of evaluating degradation in materials and is used to identify the various thermal transformations of the material during sintering. The technique is useful for compositional analysis of multi-component material or blends, thermal

stability, moisture and volatiles content [26]. Materials for laser sintering must withstand a high thermal load during the preheating stage and also the laser application. Therefore, determining the thermal stability of the polymer is highly recommended.

1.5.4 Degree of Crystallinity

It is commonly known that many of the physical and mechanical properties of polymers are affected by the crystallinity degree, such as Young modulus, yield stress, strength, fatigue, and shrinkage [27-30]. The degree of crystallinity in polymers can be determined by a various methods, such as thermal analysis using DSC, volumetric analysis, infrared, Raman spectra and X-ray diffraction. But each of these methods does not produce identical results, mainly because each method measures different physical parameters and morphological structures [31]. In this work, DSC and XRD methods were considered to determine the degree of crystallinity of UHMWPE and AC-UHMWPE.

1.5.5 Density and Porosity

Material properties are highly influenced by density and porosity. In laser sintering, the powder particles are sintered together by heat supplied by a laser and therefore the part density strongly depends on the energy density as provided by the laser [32]. With a high energy density, thermal volatilisation of polymer can be more severe and the mass of parts decreased [33], which decreases the density of the parts indicating an increasing of porosity. Further increase in energy density would cause further reduction in density due to increased polymer degradation and expansion of the voids by trapped gases.

Therefore, laser sintered parts can be characterised through density and porosity measurements. The bulk density can be determined using a volumetric method and the skeletal density can be measured using helium gas pycnometry. Three methods were considered to evaluate the porosity; X-ray micro-computed tomography (micro-CT), helium gas pycnometry and mercury porosimetry. By using micro-CT, the mean internal porosity as well as

the size and spatial distribution of pores inside the structure of the UHMWPE parts can be evaluated. This was undertaken with the aim of developing a better understanding of the three-dimensional internal morphology of the laser sintered UHMWPE and AC-UHMWPE parts. The porosity measured by this method can be then compared with the porosity measured using helium gas pycnometry or mercury porosimetry for verification. Relationships between manufacturing process parameters, density, porosity and mechanical properties can then be established.

1.5.6 Mechanical Properties

The mechanical properties are measured to evaluate the importance of energy density in laser sintering. When sintering at higher laser energy densities, there is greater flow and the bonding necks between the particles are larger, resulting in stronger bonds which in turn leads to a more ductile behaviour with large plastic regions in the stress–strain curves as has been seen with laser sintering of other polymers [34]. However, Gill *et al.* reported that when processing SiC/Polyamide matrix composites by laser sintering, degradation of the polymer occurs with increasing laser energy density from the optimum, which then results in a reduction in strength [35]. Caulfield *et al.* [34] observed similar phenomena with Nylon 12 (DuraForm^{TM} polyamide) and suggested this may be due to degradation of the polymer as a result of excessive exposure of the laser to the powder causing the particles to pyrolyse. The mechanical properties, such as ultimate strength, can provide evidence of how strong the bonding between UHMWPE particles which can be related to whether a complete/ incomplete fusion occurs as a result of the sintering process.

1.6 Thesis Structure

The thesis is comprised of 10 chapters. Following on from this chapter, Chapter 2 provides an overview of Additive Manufacturing and mainly focusing on powder-base sintering. These methods, (current or modified procedures), can be potentially used in processing the materials used in manufacturing

Activated Carbon filters. Chapter 3 describes the materials used in this work including properties and applications. The experimental work, results, discussion, conclusions and recommendations for future work are presented in Chapters 4 - 10. The details of each chapter is described in Table 1.1.

Table 1.1: Thesis structure

Chapter	Title	Description
1	Research Scope	Research background, aim and objectives are presented in this chapter.
2	Introduction	Generic information about Additive Manufacturing, highlighting the commonly methods used in polymer powder-based AM techniques. Principle and mechanism of sintering were highlighted.
3	Materials of Activated Carbon Filters	This chapter provides generic information about the materials used in manufacturing Activated Carbon filters used in Pureit system.
4	Characterisation of UHMWPE Powder for Laser Sintering	Powder characterisation including physical properties, thermal analysis and crystallinity and investigate the feasibility of processing UHMWPE by Laser Sintering.
5	Mechanical Behaviour and Material Characteristics of Laser Sintered UHMWPE	Investigates the effect of laser energy density on mechanical properties and material characteristics of laser sintered UHMWPE.
6	Morphology Behaviour of Laser Sintered UHMWPE	Investigates the effect of laser power on morphological properties of laser-sintered UHMWPE.
7	Characterisation of AC-UHMWPE Composite for Laser Sintering	Powder characterisation including physical properties, thermal analysis and crystallinity and investigate the feasibility of processing AC-UHMWPE composite powder by Laser Sintering.
8	Characterisation of Laser Sintered AC-UHMWPE Composites	Investigates the influence of laser power, bed temperature and binder content on flexural properties, density and morphology properties of laser-sintered parts.

Chapter	Title	Description
9	Manufacture of AC-UHMWPE Filters using Laser Sintering	Investigates the influence of laser power, bed temperature and binder content on physical properties and performance of 3D printed ACFs
10	Conclusions and Recommendations for Future Work	

Chapter 2 Introduction

2.1 Overview of AM Technologies

Additive Manufacturing (AM), or 3D printing as it is more commonly referred to, is defined by the ISO Technical Committee 261 on Additive Manufacturing, in cooperation with ASTM Committee F42 on Additive Manufacturing Technologies, as "a process of joining materials to make parts from 3D model data, usually layer upon layer, as opposed to subtractive manufacturing (e.g. machining) and formative manufacturing (e.g. casting) methodologies" [36]. AM technologies are also referred to as additive layer manufacturing, solid free-form fabrication, additive fabrication, direct digital manufacturing, and rapid prototyping, amongst others. They are all based on the additive principle and Figure 2.1 illustrates the AM process chain.

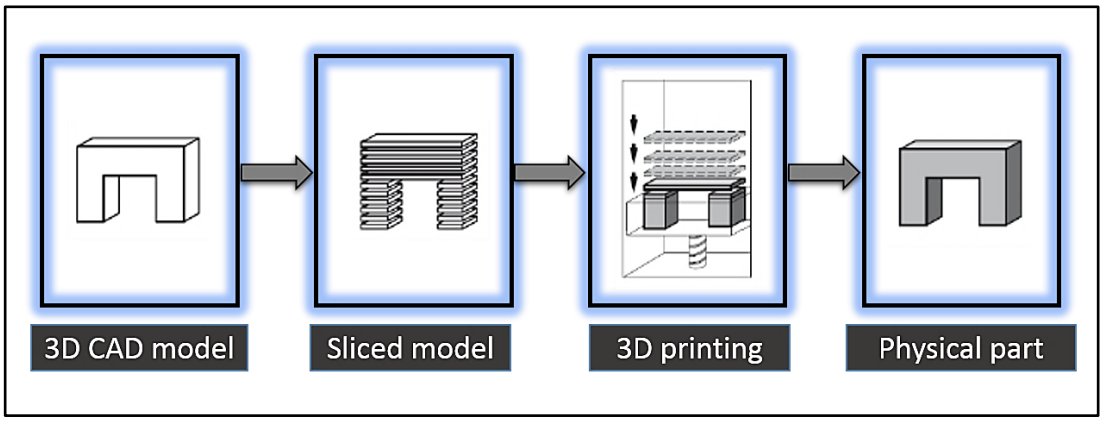

Figure 2.1: Basic principle of AM process (adapted from Gebhardt [37])

There are over twenty different recognised AM technologies based on the additive principle, but the method of layer consolidation differs from one to another [38]. These technologies were classified into seven AM process categories, as adapted by the ISO/TC 261 and ASTM F42 standards [39]:

- ***Vat Photopolymerisation***: A vat of liquid photopolymer resin is used, out of which the model is built layer upon layer using an ultraviolet light to cure or harden the resin where required.

- ***Material Jetting***: The material is jetted and deposited from a nozzle onto the build surface or platform. Then the material is cured or hardened using an ultraviolet light and the model is built layer upon layer.

- ***Binder Jetting***: Two materials are used; a powder based material and a binder. Generally, the binder is in liquid form and works as an adhesive between the layers of the powder. The binder is deposited by a print head on top of the powder where required.

- ***Material Extrusion***: Material is drawn through a nozzle, in which it is heated and is then deposited layer upon layer. A common material extrusion method is Fuse Deposition Modelling (FDM).

- ***Powder Bed Fusion***: The commonly printing techniques used include Laser Sintering (LS), Selective Laser Melting (SLM), Electron Beam Melting (EBM), Direct Metal Laser Sintering (DMLS) and Selective Heat Sintering (SHS). These techniques use either a laser or electron beam to melt and fuse material powder together. The process involves the spreading of the powder over previous layers using a roller or a blade and the powder is sintered layer upon layer. SHS differs from other processes in which the powder material is consolidated by using a heated thermal print head.

- ***Sheet Lamination***: Ultrasonic Additive Manufacturing (UAM) and Laminated Object Manufacturing (LOM) both fall under this category. UAM technique uses sheets or ribbons of metal (such as aluminium, stainless steel, titanium and copper), which are joined together using ultrasonic welding. Different materials can be bond in this method and relatively a little energy is required, as the metal is not melted. LOM, on the other hand, utilises paper, which is coated with an adhesive layer, as a build material that can be joined by heated roller instead of welding. Selective Lamination Composite Object Manufacturing (SLCOM), recently introduced by Envision TEC, additively manufactures woven

fibre composites pre-impregnated with thermoplastics replacing the traditional paper materials [40].

- ***Directed Energy Deposition***: A melted material is deposited onto the specified surface using a nozzle which can move in multiple directions. This process is typically used for metals but it can be suitable for polymers and ceramics too (in either wire or powder form). The material is melted upon deposition by a laser or electron beam.

The above technologies were described in details in "Additive Manufacturing Technologies: 3D Printing, Rapid Prototyping, and Direct Digital Manufacturing" by Gibson *et al.* [39] and also in "Rapid Manufacturing: An Industrial Revolution for the Digital Age" by Hopkinson *et al*. [38].

A range of polymers, metals, and ceramics can be used with AM to produce end use parts with minimal post processing. AM eliminates tooling from the conventional manufacturing process chain and therefore reduces costs and lead time to market [38]. These technologies enable manufacturers to produce parts of high complexity with better design features that could lead to light weight, high strength parts. The possibility to manufacture complex features with high resolution complements is the technology's main advantage and therefore finds wide applications in aerospace, automotive and medical industries. Figure 2.2 shows examples of parts manufactured using some of the most common AM technologies such as Stereolithography, Material Jetting, and Metal/Polymer Powder Bed Fusion.

Processing polymers using AM processes has had a wide interest within the manufacturing sector. Processes such as Laser Sintering (LS) and High Speed Sintering (HSS) have the capability to process various types of polymers and composites.

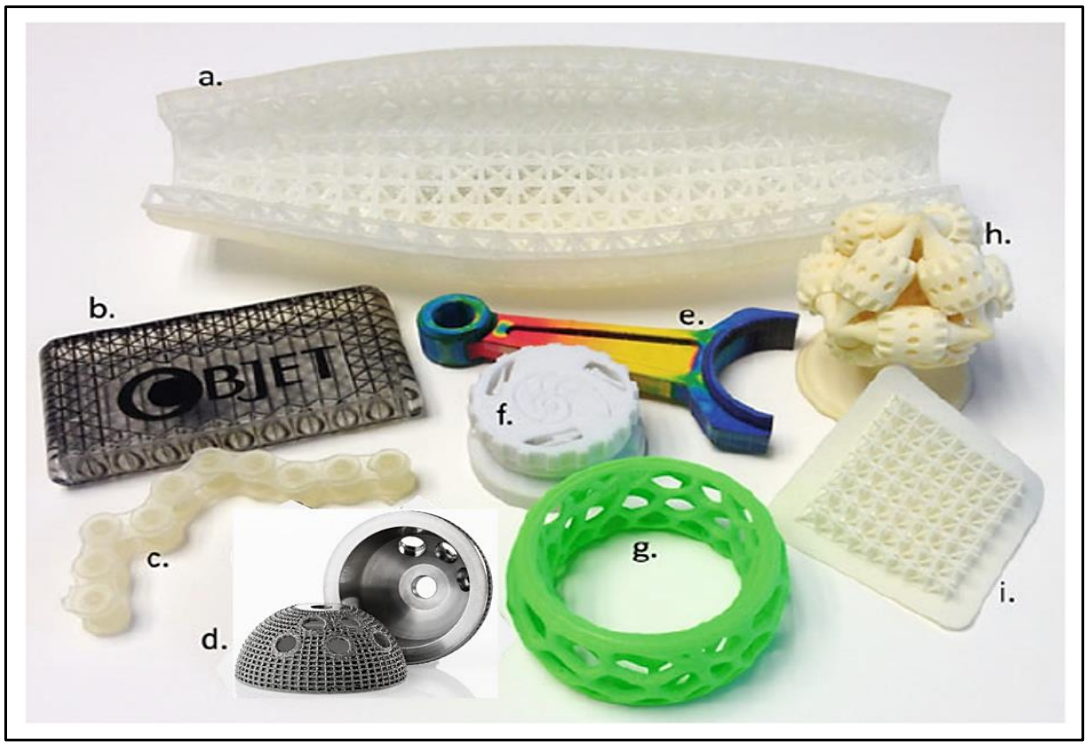

Figure 2.2: Parts produced by AM processes (adopted from [39] and [41])
a) Stereolithography, b) and c) Material Jetting,
d) Metal Powder Bed Fusion (Electron Beam Melting),
e) Selective Deposition Lamination, f) and g) Material Extrusion,
h) and i) Polymer Powder Bed Fusion

AM is changing from being a rapid prototyping technique to a mainstream manufacturing process, which is used in a vast range of applications, including industrial manufacturing, medical manufacturing to 3D home printing with desktop applications. Recently, the market of low-cost personal 3D printer has achieved massive growth, with an estimated average rate of 346% every year from 2008 to 2011. The overall market for AM, in terms of products and services, are expected to increase to around $10.8 billion by 2021, compared to $1.7 billion in 2011 [42].

The history of AM begins in the late 80's and early 1990s with the development of the main current AM processes; Stereolithography, Laser Sintering and Fused Deposition Modelling. Charles W. Hull invented the Stereolithography technique in 1984 [43], which uses a laser to selectively solidify a layer of plastic in a pool of fluid based material. In 1986, Hull established the company 3D

Systems, which is one of the pioneers and global players in the AM market to date. 3D Systems started selling their first machines in 1992 that uses Stereolithography to produce complex prototypes faster than with conventional processes.

In 1986, a patent was filed by Carl R. Deckard describing a method for selectively sintering a layer of powder to produce a multilayer part [44]. This method allowed the use of materials other than reactive resins for AM techniques, such as metals and thermoplastic polymers. Deckard founded the company DTM Corporation (previously Nova Automation). In the same year, the first commercial Selective Laser Sintering (SLS) machines were sold by DTM Corporation. 3D Systems acquired DTM Corporation in 2001 [45].

"Three Dimensional Printing" (3DP) is another AM technique, also known as binder jetting, was patented in 1993 (Patent: US 5204055 A) by a group of researchers (E. Sachs, M. Cima, J. Haggerty and P. Williams) in the Massachusetts Institute of Technology (MIT) [46]. This technique utilises a powder base material that is fused selectively by jetting a binder into the powder bed. This technique is used for application in many different areas, such as manufacturing medical devices and prototyping. MIT licensed "3DP" to a number of companies such as ZCorporation (ZCorp) which developed the first full-colour 3D printer. ZCorp was acquired by 3D Systems in 2012 [47].

2.2 AM Technologies for Polymers (Powder-based sintering)

Since there are over twenty, commercially recognised, processes developed [38], the following sections will briefly focus on techniques which employ thermal fusing of polymers powders.

Powder-based sintering processes are a group of AM techniques by which a solid object is fabricated by fusing powder particles together by a focused beam of laser or an infrared light source. After spreading a thin layer of powder on the build bed, thermal energy (i.e. laser or infrared) selectively melts the

powder layer that correspond to the shape of the desired part. The build bed then is lowered down by one layer thickness and a new layer of powder is spread and the process is repeated again.

2.2.1 High Speed Sintering

High Speed Sintering (HSS) technique (UK patent No. 0317387.9 and US 7879282 B2) is a novel powder-based AM process [48]. This process involves the sintering of 2D layers of powder without the need for a laser. Eliminating the laser reduces build time and machine cost, combining these factors makes the HSS technique suitable for high volume manufacture [49].

In HSS process, a layer of powder is deposited, typically a 100 μm thick, and the required area is printed using a Radiation Absorbing Material (RAM), such as carbon black. The powder layer is then sintered using a wide infrared radiation lamp (Figure 2.3). The desired area which have been deposited with RAM, that contains carbon black, absorbs the infrared radiation at a higher rate than the unprinted areas causing the powder particles to sinter [50].

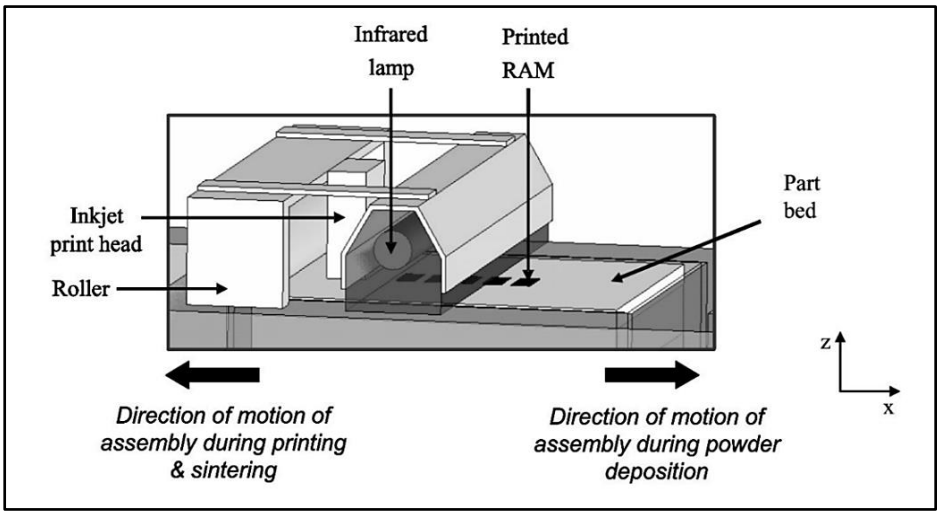

Figure 2.3: Schematic of high speed sintering process [51]

2.2.2 Selective Mask Sintering

Selective Mask Sintering (SMS) process involves printing a mask of the negative form of each layer, with a reflective material to infrared radiation, on

to a glass plate and then placing the plate over the powder bed (Figure 2.4). Infrared radiation is applied to the glass plate and allowed to pass through the mask selectively to sinter the powder directly below the mask. After sintering a layer, the building chamber is lowered and then a new layer of powder is applied. At the same time, the glass plate is moved aside and the previous image is removed and the next mask is printed. For the next layer, the glass plate is moved back into the building chamber and the process is repeated until the required component is completed [52].

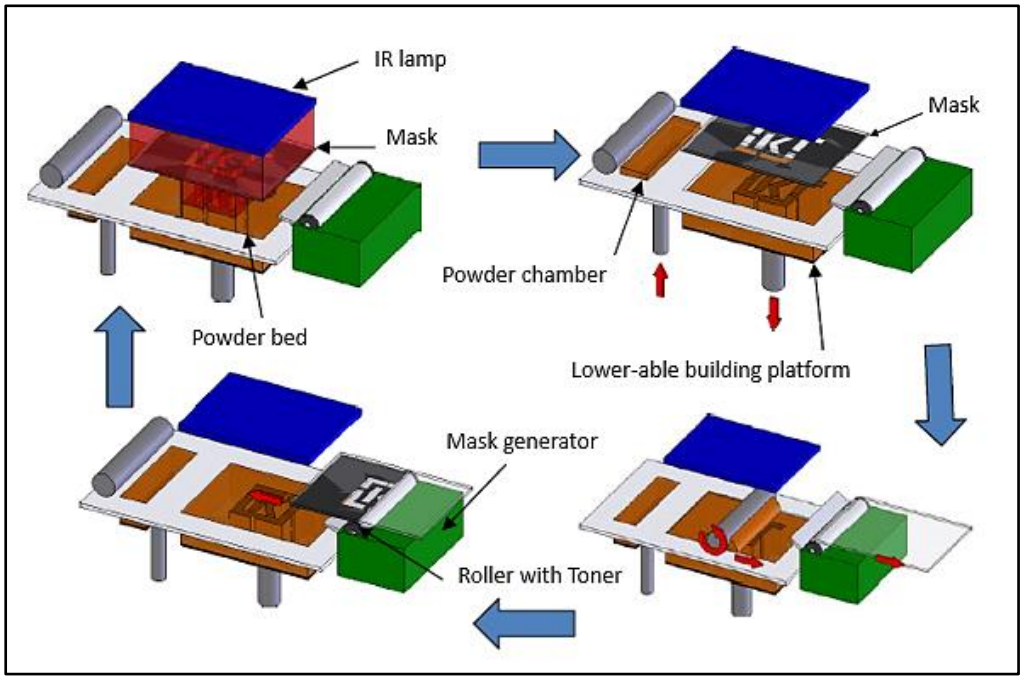

Figure 2.4: Selective Mask Sintering [53]

2.2.3 Selective Inhibition Sintering

Selective Inhibition Sintering (SIS) is an AM process that generates parts layer by layer [54] patented by B. Khoshnevis (University of Southern California) [55]. In this process (Figure 2.5), a thin layer of powder is spread over the build bed and then a liquid inhibitor is deposited along the layer profile with an inkjet print head. Then a frame is positioned to minimise radiation and prevent the sintering of the areas of the powder which lie outside the part envelope. Then the entire layer is sintered by thermal radiation from an infrared heater [56]. The steps are repeated until the entire part has been completed layer by layer.

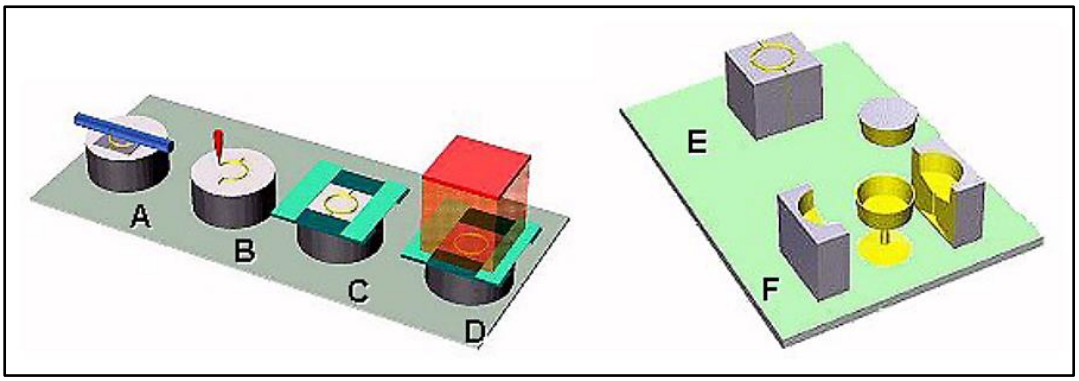

Figure 2.5: SIS process: building stage (left), fabricated part extraction (right) [57]

Materials such as polycarbonate, polyester and polystyrene can be used as powders in the SIS process with a number of liquids including water, commercial cleaning agents, isopropyl alcohol, light lubricating oils, organic solvents [58], and soluble salt (Potassium Iodide) [59] were used as sintering inhibitors.

2.2.4 Laser Sintering

Laser Sintering (LS) is an AM-process, in which parts are built layer upon layer using a laser to fuse powdered material from 3D computer aided design models. A schematic of laser sintering process is shown in Figure 2.6.

The principle of polymer laser sintering can be summarised as follows:

- Laser sintering machine lays down a thin layer of polymer powder, typically 100μm thick, in the part-build bed
- The powder is heated up by a laser to fuse the powder layer with the previous layers
- After the laser has finished tracing one cross section of the model, the part bed is lowered down by a distance equivalent to a layer thickness and then a new load of powder is deposited on top by roller or blade mechanism
- The next cross section is then laser sintered and the process is repeated until the whole geometry is completed.

In this process, the un-sintered powder acts as a supporting material, which eliminates the need for the removal of the supports during post processing.

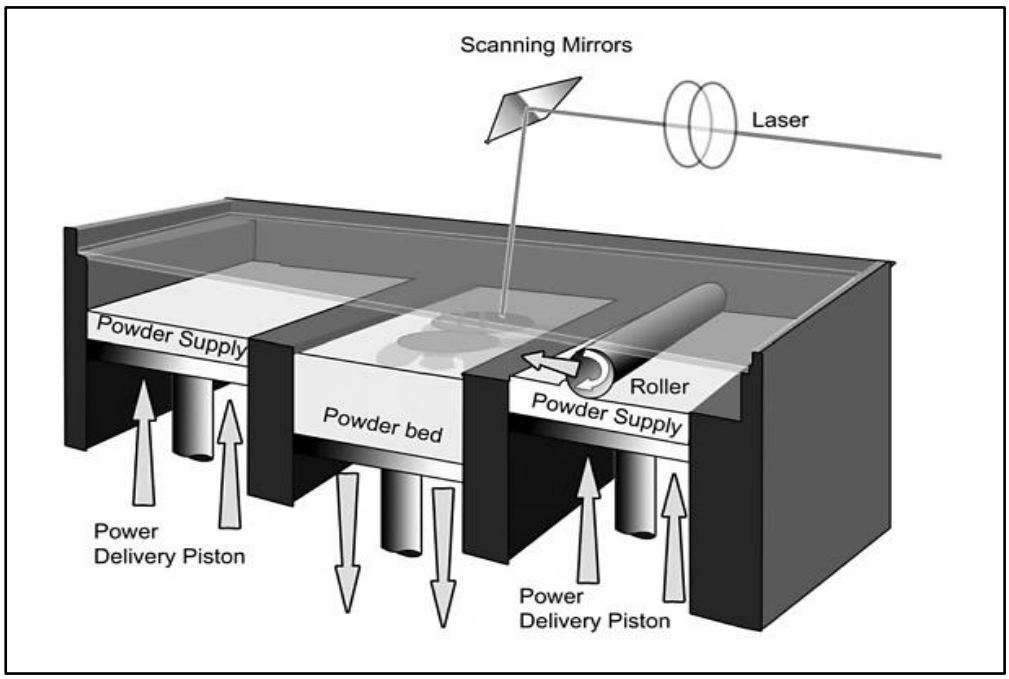

Figure 2.6: Schematic of laser sintering [38]

The build parameters of laser sintering include laser power and speed, hatch spacing, number of scans, layer thickness, part bed temperature, feed bed temperature, roller speed, build size, time between layers, and heating-cooling rates [27]. Results from literature indicate that the physical and mechanical properties and the microstructure of the laser sintered parts are influenced by laser power, scan speed and hatch spacing which are associated directly to the amount of energy subjected on the surface of the powder in the part bed [12, 60].

Laser sintering process has the capability to produce parts with highly complex geometries, accurate dimensions, and good mechanical strength [27]. Controlled complex geometries can be obtained internally and externally. These internal structures are interconnected porous network that are highly regular and reproducible which could offer excellent applications, such as bone implants [61].

2.3 Example AM Applications

There are a number of products currently being produced using polymeric AM that are used in many applications including automotive, aerospace, consumer, medical, industrial as well as education and research (Figure 2.7). AM is especially suitable for low volume parts manufacturing, particularly with complex geometries. AM offers a great potential for customisation of products, such as producing personalised implants for knee and hip joint replacements, hearing aids and dental devices [41].

Aerospace parts often have complex geometries and low volumes. AM technologies have been used in this industry to build plastic parts such as complex venting and ducting components. Polymers, such as PEEK (a flame retardant material), have been tailored to meet the aerospace requirements [41].

AM techniques have been successfully applied to develop and produce different parts for the motor sports industry. The cooling duct, used in the Renault F1 car, was designed to enhance the cooling of the electrical system. The duct was made from nylon-12 using laser sintering. Jordan F1 team is another example where 12 connection boxes were manufactured using laser sintering. Traditionally, these boxes were fabricated by hand laying carbon fibre into tooling, taking a number of days. On the other hand, the laser sintered 12 connection boxes were manufactured within the same time required to make one box [38].

Lighting and 3D textiles are examples for consumer applications. Laser sintering was used to manufacture a series of nested lampshades that are currently being sold from many retail outlets worldwide [38]. AM was also used in manufacturing fabric-type flexible products such as clothes or hand bags using laser sintered polyamide [62].

AM techniques have been applied in medical applications such as orthopaedic and dental implants, tissue scaffold, artificial organs and medical devises [41]. These medical products are produced from 3D data of the part obtained from the patient using medical imaging technologies such as CT scan [62].

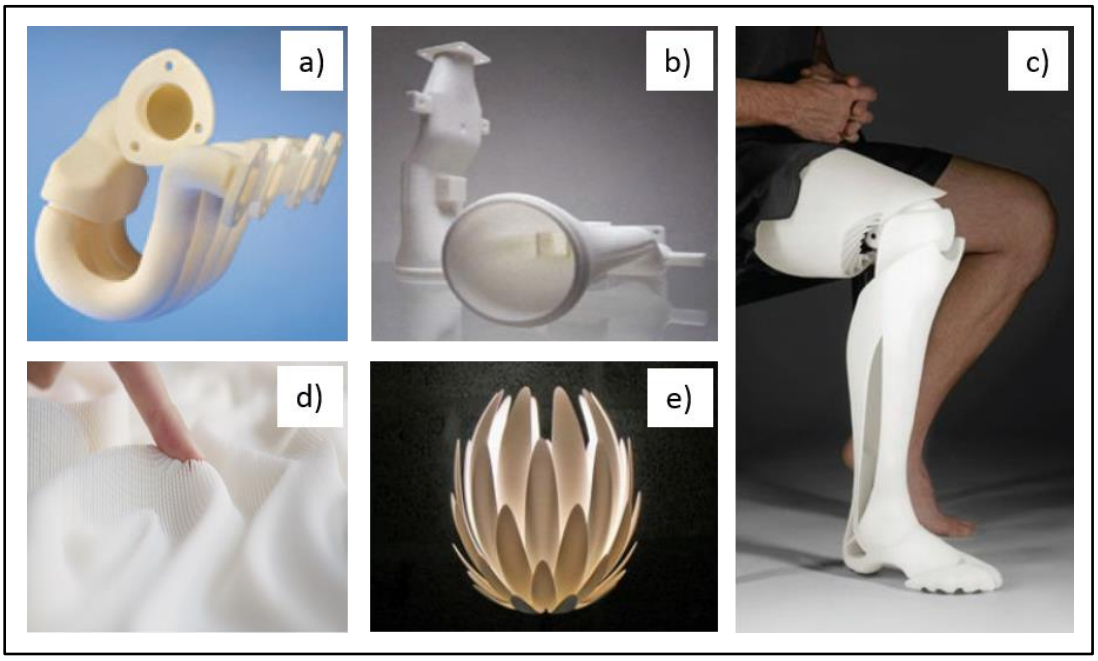

Figure 2.7: Example applications of AM
a) Exhaust gas device [62], b) Air ducting for the aerospace industry [63], c) Artificial leg [64], d) Fur tiles – Textile industry [65], e) Lotus lampshade [38].

2.4 Principle of Sintering

Traditional sintering process is a method of consolidating compacted powder by thermal energy. This method is used in manufacturing processes for ceramics, metals and polymers [66].

Sintering involves the fusion of two or more particles by heating them either to a temperature just under the melting point or to the melting point of any phase within the sintered material. For most cases, the sintering process starts with initial bonds ranging from point contacts to highly deformed interfaces depending on the preparation method of the compacted particles (Figure 2.8 a). The contacts grow with sintering and the formation of necking develops

(Figure 2.8 b). Following this stage, the pore structure becomes rounded and the discrete particles are less evident. For porous structures sintering is usually terminated in this stage but for fully dense structures, pores shrink with eventual formation of closed and spherical pores (Figure 2.8 c) [67].

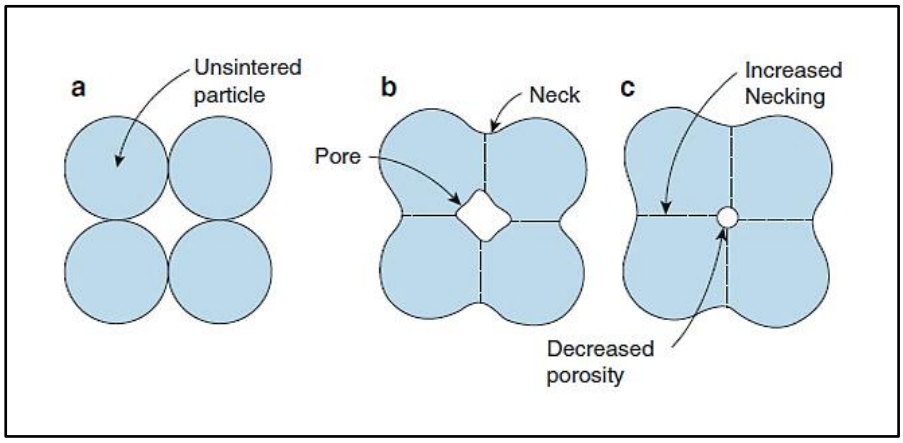

Figure 2.8: Stages of sintering [39]

Most industrial sintering processes are carried out without an external pressure including solid state sintering and liquid phase sintering. On the other hand, processes such as hot pressing, spark sintering and hot isostatic pressing are performed with pressures range from 0.1 MPa up to 6 GPa [68].

2.4.1 Powder Sintering Mechanisms

There are four different sintering mechanisms that are existing in powder bed fusion processes, including solid state sintering, chemically induced binding, liquid phase sintering and full melting (Figure 2.9).

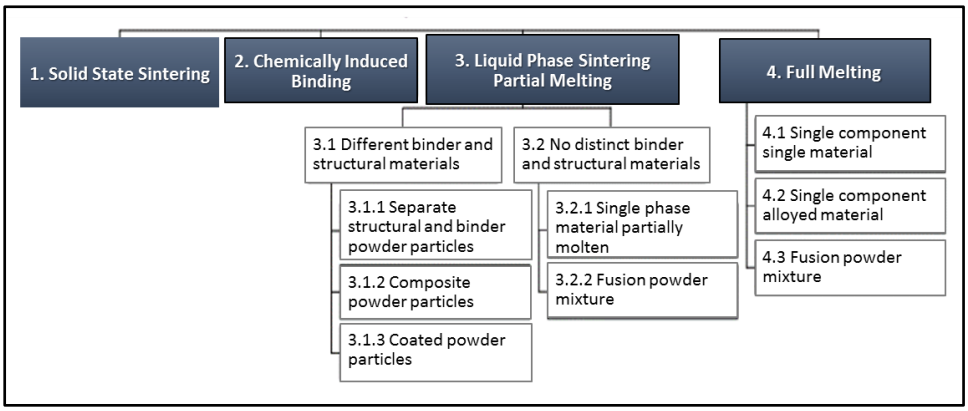

Figure 2.9: Sintering mechanisms [69]

2.4.1.1 Solid State Sintering

In this type of sintering, the consolidation occurs below the material's melting point [69]. The sintering mechanism is primarily diffusion, which involves the formation of necks between neighbouring powder particles (Figure 2.10). A wide range of materials are processed via solid state sintering. However, this process is slow and preheating of the powder is needed so that high diffusion rate can be achieved [70].

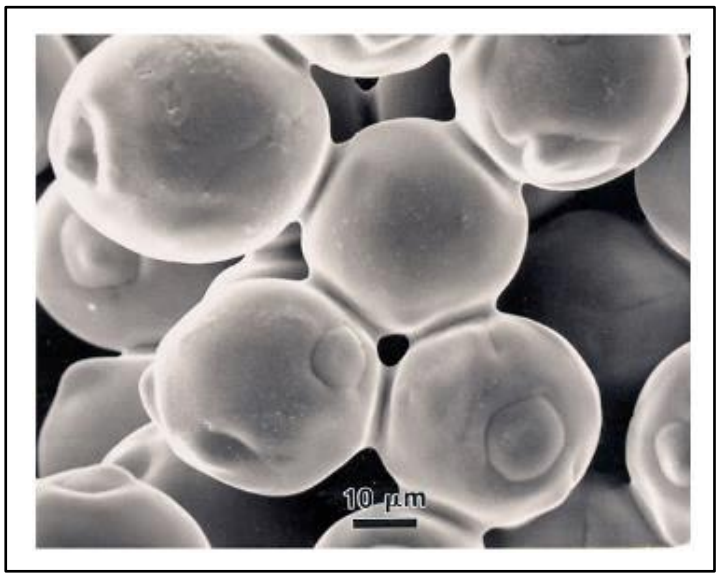

Figure 2.10: Particles neck formation [68]

2.4.1.2 Chemically Induced Sintering

In this process, chemical reactions are thermally activated between two types of powders or between powders and atmospheric gases that form a by-product, which binds the powder particles together. This process is mainly used for ceramics. Laser processing of SiC in the presence of O_2 is an example of a reaction between powders and atmospheric gases. SiO_2 is formed and then binds SiC and SiO_2 composite together [39].

2.4.1.3 Liquid Phase Sintering - Partial Melting

Many different types of processes fall under this category, but in most of them the powder particles fusion occurs when a part of constituents within the

group of particles become molten, while other parts remain solid. However, in some cases the solid and the liquid phases come from the same material [39].

Kruth *et al.* [70] suggested that in this type of sintering, binders and structural materials can be distinct or indistinct. In the case of distinct materials, different structural materials and binder can be used in this process whereby the structural and binding materials can be combined in three different systems:

- Separate particles: Binder and matrix powder particles are well mixed
- Composite particles: Are consist of binder and matrix materials agglomerate together. They can be made up of mixtures of polymer binder materials with higher melting polymer, ceramic or metal matrix materials.
- Coated particles: The composite is formed by coating the particles of the matrix with a binder material.

On the other hand, with the indistinct binder and matrix materials, the smaller particles of the polymer and the outer parts of larger particles melt, but without melting the whole structure [39]. This phenomenon, known as "partial melting", illustrated in Figure 2.11, which shows a typical microstructure of laser sintered nylon 12.

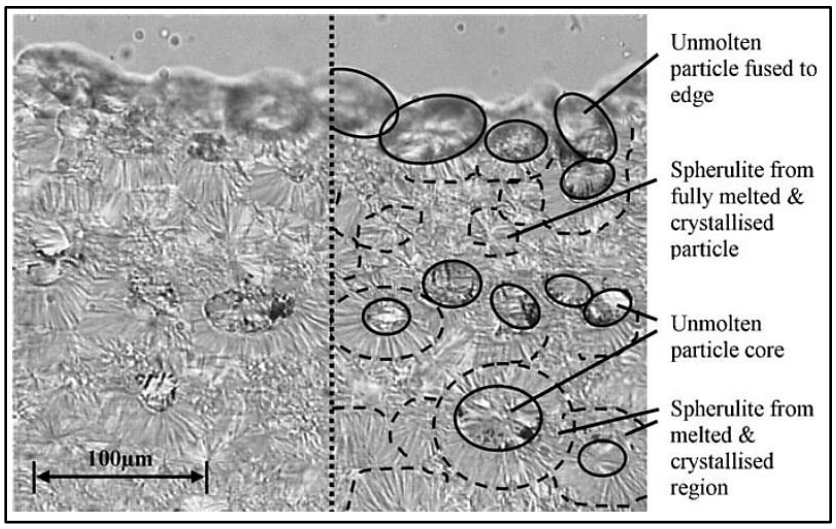

Figure 2.11: Partial melting in laser sintered Nylon 12 part [71]

2.4.1.4 *Full Melting*

Full melting is generally related to Powder Bed Fusion processing of semi-crystalline polymers and engineering metal alloys. In order to obtain components with the highest strength, polymers such as nylon 12 has a distinct melting point and should be fully melted during the process [39]. Figure 2.12 shows an example of neck formation of semi-crystalline polypropylene, then followed by full coalescence.

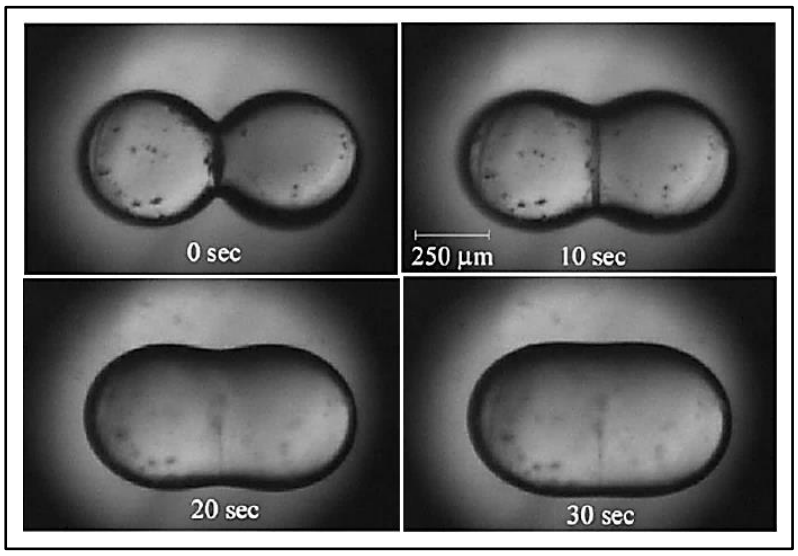

Figure 2.12: Particles neck formation and coalescence [72]

2.4.2 Polymer Sintering Model

Sintering models have been used as a means to investigate the suitability of materials for sintering. These models are based on two symmetric spherical or cylindrical particles in contact with each other and are concerned with the neck growth occurs during sintering.

Frenkel's model is one of the early theories used to describe the principle of sintering [73]. However, it has since undergone many modifications to remove some of the approximations associated with this theory and also to allow application to individual situations. The Frenkel's analytical model describes the rate of coalescence of two identical spherical particles (Figure 2.13) via the

viscosity of the material and the surface tension over a given time period at elevated temperatures. The model suggests that the rate of sintering is inversely proportional to the melt viscosity of the polymer at low shear rate [74].

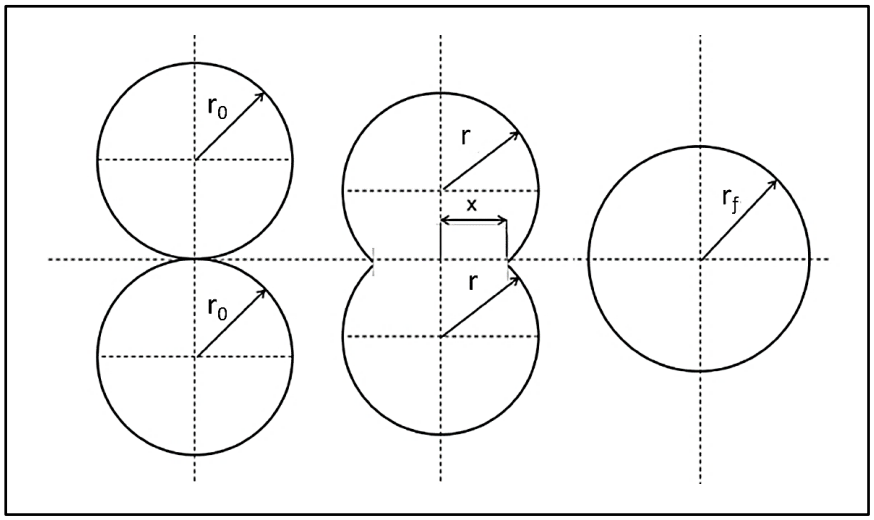

Figure 2.13: Schematic of sintering of two spherical particles [74]

Frenkel's model is described by the following Equation:

$$\frac{x}{r} = \left(\frac{3\gamma.t}{2\eta.r_0}\right)^{\frac{1}{2}} \quad (1)$$

Where x, r_0, r, γ, t and η are sintering neck radius, initial particle radius, particle radius, surface tension, sintering time and zero-shear viscosity of the polymer respectively. Frenkel's model is restricted to Newtonian flow, where viscosity remains constant, and only valid for the initial stages of sintering, when the diameter of the particle remains relatively fixed. It was noticed that the viscosity used in Frenkel's model is three folds higher than the shear viscosity and therefore this model was modified and subsequently became known as Frenkel/Eshelby model [75]:

$$\frac{x}{r} = \left(\frac{\gamma.t}{\eta.r_0}\right)^{\frac{1}{2}} \quad (2)$$

These models are not applicable for irregularly shaped particles due to un-well defined dimensions and necking of these particles [22]. The sintering behaviour of polymers is controlled by the morphology of the particles in addition to the factors included in the Frenkel-Eshelby model [15]. However, the model provides insight on the influence of material properties and particle size on the coalescence rate and it has been used by many authors as part of a materials characterisation process to investigate sintering behaviour [15, 24, 74, 76-79].

2.4.3 Laser Sintering of Polymers

Laser Sintering of polymers is one of the most promising AM technologies because of its capability to create parts with complex and dimensionally accurate geometries, and good mechanical strength [27]. The basic material developed for laser sintering is a polymeric powder. A limited number of polymers are available for laser sintering and this leads to restrictions for many applications such as industrial or medical. The complicated thermal phenomena during LS process and also the lack of knowledge of how various materials respond to these phenomena play a main role in limiting the availability of materials for laser sintering, compared with the traditional manufacturing methods, such as screw extrusion and injection moulding [80].

In laser sintering, when polymer materials are heated up to high temperatures, their state changes from a solid material at ambient temperature to a soft material and then to a flowing viscus melt. The transition temperature is polymer dependent and has great influence on processing the material by laser sintering successfully [81].

Generally, there are differences between amorphous and semi-crystalline polymers in relation to laser sintering. The melting point (T_m) of amorphous polymers are not well-defined, but these polymers are gradually soften and consolidated by heating them up to a temperature above the glass transition temperature (T_g), which is the critical sintering temperature for these

materials. Parts with good dimensional accuracy and feature resolution can be produced from amorphous polymers, due to lower shrinkage (as density does not change on cooling). However, these parts exhibit less strength and higher porosity as particles do not consolidate fully as a result of low flow (i.e. higher viscosity and only a small difference in viscosity around the T_g) and sintering rate. Semi-crystalline polymers used in AM, on the other hand, have a T_g around room temperature or below (-100°C to 50°C) with a clear melting point, which is above 100°C (100°C to 400°C). These polymers change quickly from a solid state to a viscous liquid when adequate heat is absorbed. Semi-crystalline polymers used in AM have low viscosity above their melting temperature than non-crystalline polymers at a given temperature, therefore the laser sintered parts produced are near-fully dense with mechanical properties similar to moulded parts [69]. However, shrinkage is more evident in semi-crystalline polymers due to the volume change on crystallisation, as the crystal phase is generally more dense than the amorphous phase [81]. Figure 2.14 gives examples of the glass transition and melting temperatures ranges of some semi-crystalline polymers (such as PP, PA6 and PE) and the glass transition and flow temperatures ranges of some amorphous polymers (PS, PC and PMMA) [82].

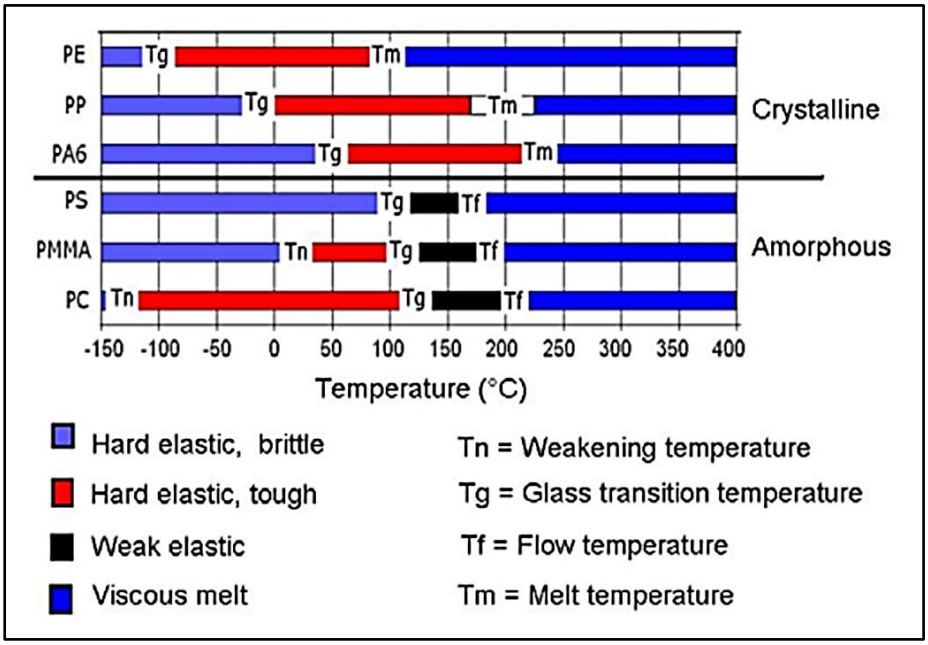

Figure 2.14: Transition temperatures and phases of some polymers [82]

The most widely used polymers in LS are Polyamide 12 (PA-12) based [18], as a one material, blended or reinforce with nanoparticles or other materials [81]. Additionally, Thermoplastic Elastomers (TPE) [24], Polystyrene (PS) and Polycarbonate (PC) [82] are regularly used (Figure 2.15). However, new polymers such Polyetherketone (PEEK) [11, 83], Polypropylene (PP) [30, 83], Polyoxymethylene (POM) [83], Thermoplastic Polyurethane (TPU) [84], High Density Polyethylene (HDPE) [83, 85], High Molecular Weight Polyethylene (UHMWPE), Polylactic acid (PLA) [81], Poly-ε-caprolactone (PCL) and Poly(L-lactide) (PLLA) [86] are currently showing increasing potential as LS materials.

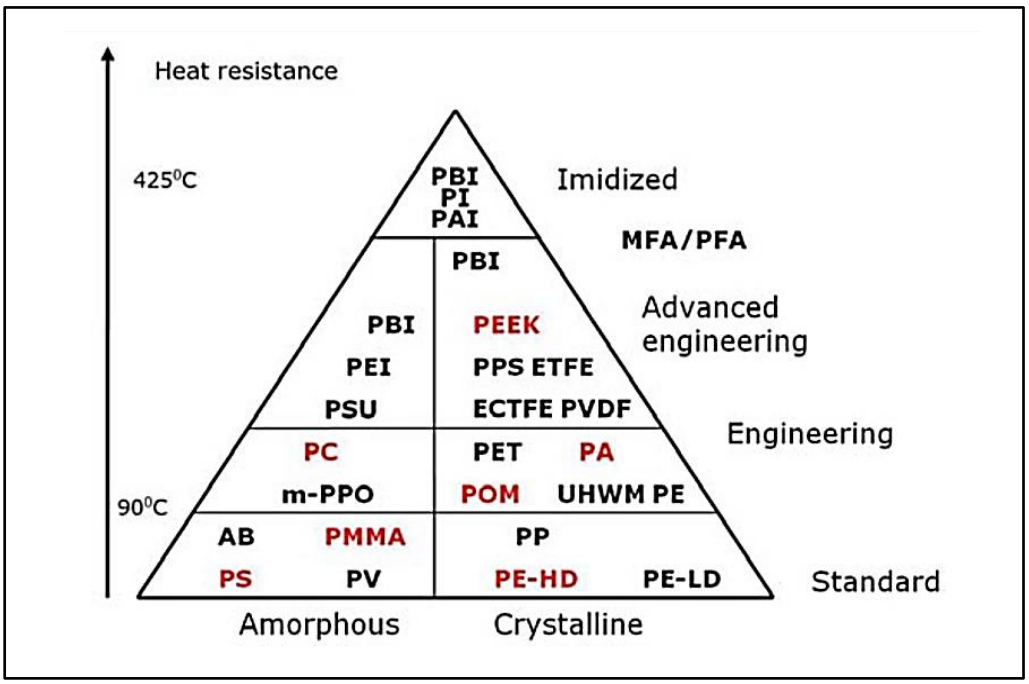

Figure 2.15: Thermoplastic polymers. LS materials are highlighted in red. [82]

Full melting consolidation is a preferred approach for semi-crystalline polymers and partial melting mechanism is more common for amorphous polymers [69]. However, full and partial melting both exist in laser sintering of semi-crystalline polymers [71].

2.4.4 Process Optimisation using Laser Sintering

2.4.4.1 Process Parameters of Laser Sintering

The physical and mechanical properties, microstructure and quality of the parts produced by laser sintering are mainly influenced by LS process parameters. The main parameters include laser power, laser speed (scan speed), hatch spacing (scan spacing) and scan count, which are directly associated with the amount of energy applied on the surface of the powder in the part bed [12, 81]. These parameters are described in Table 2.1.

Table 2.1: Process parameters of laser sintering [81]

Parameter	Unit	Description
Laser power	watts	Heat source applied as it scans the area of each layer
Scan speed	mm/s	Speed at which the laser travels
Hatch spacing	mm	Distance between two parallel laser scan
Scan count	-	Number of times the laser beam travel over a layer

At fine hatch spacing and low laser speed, the energy density generated on the powder bed can be high, leading to degradation of the polymer material which then leads to parts with high porosity. When the laser speed and hatching space are set at high levels, the energy density generated will be inadequate to fully sinter the parts, resulting in an increase in porosity [35].

There are other important parameters affect the properties of the parts produce by laser sintering, which include part bed temperature and layer thickness that make up the part. Sufficient energy is needed for the powder to be consolidated and to bond to the previous layer. Nevertheless, undesirable growth of the part in the z-axis may occur if the laser beam penetrates beyond the desired thickness of the layer and bond undesirable powder particles. This phenomenon is commonly referred to as "Bonus-Z" or "Z-growth" [81, 87].

2.4.4.2 Parameters influencing the quality of laser sintered parts

Research in polymer processing using LS has mostly focused on optimising the process parameters and evaluating their effects on the mechanical properties of the produced parts [88]. The density and mechanical behaviour of laser-sintered parts depend on the laser energy density, part bed temperature (PBT), and part orientation. The most studied LS parameter in the literature is laser power, or laser energy density. The suitable laser energy density depends on the PBT, where a higher part bed temperature requires less laser energy density to melt the polymer powder. However, too low PBT can lead to warping and insufficient melting, whereas too high PBT can lead to un-wanted bonding and a hardening of the cake that forms around the part. Part bed temperature is generally fixed 3 - 4°C below the peak melting temperature for semi-crystalline polymers [27].

Caulfield *et al.* [34] investigated the effects of laser energy density on the density and mechanical properties of polyamide components. The study showed that mechanical properties (i.e. Young's modulus, tensile strength and elongation at break), increased with increasing energy densities but began to decrease after a critical value. Caulfield *et al.* suggested that increasing energy densities resulted in greater powder consolidation and stronger inter-layer bonding which resulted in stronger parts. However, energy densities greater than a critical value damaged the polymer and thereby decreased the mechanical properties.

The effect of process parameters on morphological properties was also investigated, such as pore size and porosity distribution of laser sintered parts using micro-CT. Dupin *et al.* [32] used micro-CT in their work and reported that the laser power has a significant impact on the porosity of polyamide 12 sintered parts. Their results show that the open and closed porosities decrease when laser energy density increases. Rouholamin and Hopkinson [89] showed that micro-CT analysis can be used as a non-destructive technique to

assess the morphology of nylon 12 and measure the porosity and pore size of the laser sintered parts.

The molecular weight is one of the important parameters for describing the polymer characteristics and it affects the quality of laser sintered parts through the melt viscosity. The melting viscosity is directly affected by the weight-average molecular weight (M_W) of a linear polymer and this relationship is described in Equation (3). The melt viscosity varies greatly with the change of the molecular weight. The higher molecular weight causes higher melt viscosity [90, 91], which can decrease the consolidation of the powder and makes it more difficult to process.

$$\eta_0 = k(M_w)^n \qquad (3)$$

η_0 = zero shear melt viscosity
k = constant depends on the material and is sensitive to the density
n = 3.4 (if $M_W \geq$ entanglement molecular weight)
$2.5 \geq n \geq 1.0$ (if $M_W \leq$ entanglement molecular weight)

2.4.5 Laser Sintering of UHMWPE

Previous research has demonstrated that laser sintering is capable of processing polyethylene. Salmoria et al. [66] successfully processed high-density polyethylene (HDPE) by laser sintering. They were able to show that the structure and the properties of the laser sintered parts can be controlled by using different particle sizes. Their results showed that a lower sintering degree can be achieved with larger particle size with lower values for the mechanical properties. While smaller particles form a larger contact area contributing to a higher rate of necking between particles and resulting in improved mechanical properties [139].

Little attempts have been made to process UHMWPE by Additive Manufacturing, particularly laser sintering. Rimell and Marquis attempted to produce parts for clinical application from UHMWPE (GUR 4120 and GUR 4170)

by using a non-commercial LS machine. However, the attempts to produce multilayer parts were unsuccessful, due to high degree of shrinkage and curling developed during the laser sintering. The UHMWPE powder used in their work was highly porous, so as the powder bed. Therefore, when the material is fused, a high reduction in volume occurs causing the sintered material to shrink from the surrounding powder bed. Hence, forming continuous sheets was difficult due to the discontinuity of material between adjacent laser paths. Additionally, degradation is a major concern in laser sintering. Rimell and Marquis observed an increase in the degradation of the UHMWPE with increasing the density of the laser power. This degradation can be in the form of cross-linking, chain scission and oxidation, which can be determined by FTIR examination [140].

Rimell and Marquis used a non-commercial laser sintering apparatus in their work and sintered the UHMWPE from room temperature. This method would generate high thermal gradients which makes the shrinkage and curling problems worse. They suggested that using a commercial laser sintering system, where the temperature of the powder can be controlled, would minimise the effect of the thermal gradients. Additionally, highly porous UHMWPE powder with agglomerated and non-spherical microstructure contributed to the poor powder packing and bed density, which makes it difficult to produce dense parts [140].

Goodridge *et al*. produced multilayer parts from UHMWPE (GUR 4170) with a high sintering between particles and layers using the commercial Vanguard Laser Sintering machine (3D Systems) [36]. This LS system has two feed chambers where the powder is heated to a temperature just below the powder bed temperature before spreading across the build area. Goodridge *et al*. used UHMWPE GUR 4170 with an average particle size of 120μm with irregular shaped and agglomerated particles. This powder is highly porous which can contribute more to the shrinkage when processing the powder by laser sinter.

Goodridge *et al*. performed a number of trials to establish suitable parameters for processing UHMWPE by using different laser powers, bed and feed temperatures and scan counts. They indicated that the processing window to obtain UHMWPE components was narrow and therefore very precise process parameters (i.e. laser power combined with correct bed and feed temperatures) were required. Goodridge *et al*. reported that the UHMWPE multilayer parts were produced only by using a laser power of 13 watts, double scan count with bed and feed temperatures of 135°C and 125°C, respectively.

Goodridge *et al*. investigated the mechanical properties of the sintered UHMWPE parts by using tensile and three point bend tests. The results show that the ultimate tensile strength and Young's modulus of these parts were just above 0.2 MPa and 1.5 GPa, respectively and the flexural strength and modulus were 0.52 ±0.2 MPa and 18.67 ±4.3 MPa, respectively. The produced parts have sufficient strength for light handling but with very low mechanical properties.

Goodridge *et al*. concluded that using commercial laser sintering machine with powder pre-heating system can minimise thermal gradients resulting in producing well defined laser sintered UHMWPE parts. However, this can only be achievable when using a certain processing parameters. Additionally, the small window of processing UHMWPE is problematic and could limit the possibility of processing UHMWPE commercially.

2.4.6 Laser Sintering of Composites

Many attempts have been made to enhance the mechanical or thermal properties of polymeric parts produced by LS using fillers as reinforcement materials or polymer blends.

Inorganic micron-sized fillers (e.g. silicon carbide, hydroxyapatite, glass beads and aluminium powder) or nano-sized fillers (e.g. nanosilica, carbon nanofibres, clay, and nano-Al_2O_3 particles) were used to enhance the physical and mechanical properties of laser sintered parts [81].

Hao *et al.* [92] attempted to laser sinter a composite of hydroxyapatite (HA) and high density polyethylene (HDPE) and reported that the parts sintered with small particles showed improved particle fusion compared to those sintered with large particles. Hao *et al.* suggested that higher sintering rate and densification occur with finer powder particles. Additionally, Hao *et al.* reported that the laser sintered parts exhibited highly interconnected porous structures. The percentage of the internal porous region increased with the increase in particle size and decreased with the increase in laser power. The degree of particle fusion and porosity are affected by the particle size of the powder and the processing parameters [13, 14].

Salmoria *et al.* [93], used mixtures of PA-12 and HDPE in ratios of 80:20, 50:50 and 20:80 (weight/weight), respectively to achieve dedicated properties. The elastic modulus of the parts produced from PA-12-HDPE 80:20 blend was higher than those of the 50:50 and 20:80 parts. However, Salmoria *et al.* indicated that higher ultimate strength was achieved for parts produced from PA-12/HDPE 20:80 and suggested that the HDPE phase provides higher toughness.

Carbon-based materials and polymer matrix composites are emerging materials as fillers for LS to enhance the properties of the produced parts. Successful attempts have been made to laser sinter a complex carbon/carbon composite components using a mixture of carbon fibre (CF) and phenolic resin [94] or PA-12/CF composites [28]. PA-12/carbon nanofibre, PA-12/carbon nanotube, graphite powder/phenolic binder and PA-12/carbon black composites were also successfully processed by laser sintering [95-98].

2.4.7 Laser Sintering of Porous Structure

Porous structures hold distinctive physical properties that are associated with their low density and construction. The mechanical, thermal and electrical attributes provide a vast range of potential applications, including thermal insulation, packaging, filtration, food and beverage, biomedical applications,

military, automobile, aerospace and shipping industries [99]. The mechanical and thermal properties of porous structures can be influenced by the microstructure and the composition of the initial material, as well as the morphological and geometrical properties of the basic cell structure [9].

Additive Manufacturing techniques have a number of advantages over conventional techniques when producing porous structures:

- Good control over pore network design and properties
- Good reproducibility
- Greater pore interconnectivity
- Enhanced mechanical properties

Porous structures in LS can occur as a result of inadequate energy densities and time scales. These structures can also form as a result of high energy intensities, which produce extremely high temperatures. This can cause polymer pyrolysis and subsequently forming a porous structure. This phenomenon can be further exacerbated by the addition of carbon-based substance such as carbon black. This addition increases the localised heating because of their high absorption of CO_2 infra-red laser radiation [98].

Porosity can be controlled through a suitable selection of process parameters, including laser power, scanning speed, powder temperature and particle size [100]. It has been found that laser sintered part density increases with the decreasing of particle size. Particles smaller than 45 μm can make powder spreading more difficult as a result of the electrostatic forces [81]. Powder flow, which depends on several factors including particle size and shape, as an example, plays a significant role in laser sintering as the lack of homogeneous and even layers contributes to producing porous laser sintered parts [11]. Particles with flakes on the surface, or particles with less dense structures can easily produce laser sintered parts with high porosity [19].

The energy density influences the microstructure of the produced parts. A lower porosity, a higher shrinkage and improved mechanical properties may

be achieved with a higher energy density. However, too high energy may degrade the material decreasing its mechanical properties [101]. This case was also observed by Gill *et al.* as their study shows that with increasing laser energy density from the optimum, degradation of the polymer may occur, resulting in an increase in porosity and a decrease in tensile strength [35].

At fine hatch spacing and low laser speed, the energy density generated on the powder bed can be high, leading to degradation of the polymer material which then leads to parts with high porosity. When the laser speed and hatching space are set at high levels, the energy density generated will be inadequate to fully sinter the parts, resulting in an increase in porosity [35].

Minor changes in powder bed temperature may result in a notable effect on porosity and mechanical properties of the part produced. When the temperature of the powder bed is too low, inadequate energy can lead to a high porosity in the sintered parts as a result of incomplete melting and coalescence of the powder particles [27].

2.4.8 Thermal Properties of Polymers

Differential Scanning Calorimetry (DSC) is a method used to measure the thermal properties of polymeric materials, based on changes of the difference in the flow of the heat into the specimen compared to a reference material under a controlled temperature ramp [102]. The technique monitors thermal influences related to chemical reactions and phase transitions as a function of temperature and this allows a number of properties of the polymer to be determined such as melting point, glass transition temperature, enthalpy of melting (fusion), and crystallisation and degradation temperatures.

Since DSC allows the determination of the melting and crystallisation behaviour of a polymer, it is a useful tool for the evaluation of the suitability of the polymers for the sintering process. The phase transformations during melting and cooling (crystallisation) are the key parameters. For materials that show a relatively sharp melting endotherm, their powder can be heated to a

temperature just under the melting point throughout the sintering process cycle [24].

Another thermal characteristic required for successful sintering is to have a wide processing window [25], which is defined as the difference between the temperatures at the onset of melting on heating and the onset of re-crystallisation on cooling (Figure 2.16).

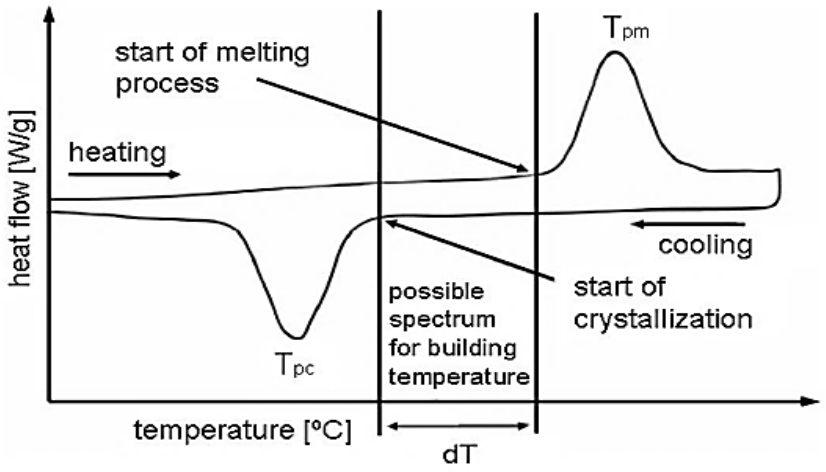

Figure 2.16: Typical DSC-curve for melting and crystallisation of Nylon 12 [82]

In semi-crystalline polymers, two sharp peaks can be observed in the DSC curve representing the melting and re-crystallisation phases of the polymer and the area between them is considered to be the super-cooling window. The part bed temperature is ideally set to a point within this window for most materials used in LS (and HSS). This allows good control of sintering when the powder absorbs energy from the laser or infrared radiation and then leads to effective part consolidation by avoiding early crystallisation on cooling.

Unlike semi-crystalline polymers, amorphous polymers do not show obvious transitions and the changes in thermal and flow behaviour are more gradual. This behaviour can make the sintering process very challenging as a small amount of the polymer may start to flow at lower temperatures, which then could prevent powder from flowing over the part bed [24]. Generally, the

powder bed is preheated to a temperature below the T_g of the amorphous polymers and the additional heat generated by the laser allows sintering to take place at this temperature [103].

Reducing shrinkage and eliminating distortion are important in laser sintering. If the powder bed temperature is too low, the sintered layers may shrink significantly from the surrounding area and then curl. When the part is complete, the finished part will be distorted and warped. However, if the temperature of the powder bed is too high, the surrounding powder around the part becomes consolidated, making removal of the parts more difficult [81]. In the DSC curve, if the melting and crystallisation peaks are very close or overlapped, the processed material will quickly crystallise as soon as it cools, resulting in shrinkage and distortion. Therefore, polymers that can be processed at a wide range of temperatures are the more desirable in LS. These materials allow a better processing freedom and space, especially when optimising processing parameters [61]. Additionally, the literature indicates that the values of the glass transition and melting temperatures largely depend on the polymer molecular weight, especially at lower molecular weights. The glass transition temperature increases with molecular weight and approaches a maximum value asymptotically. This effect is not pronounced for high molecular weight polymers. This explains why there is a considerable difference in laser sintering processability between high and low molecular weight polymers [82].

Chapter 3 Materials of Activated Carbon Filters

3.1 Introduction

Activated Carbon filter materials are composites of activated carbon and a binder that are compressed and fused into a generally coherent porous structure. Traditionally, these filters have been produced using Ultra High Molecular Weight Polyethylene (UHMWPE), High Density Polyethylene (HDPE), Low Density Polyethylene (LDPE) or Polyethylene Vinyl Acetate (PEVA), binders.

The Activated Carbon filter used in Unilever's "Pureit" system is produced from a mixture of Activated Carbon and powdered UHMWPE binder which is compressed, heated, and then cooled to cause the binder particles to fuse the mixture into a porous carbon solid structure. The binder does not completely fill the pores of the filter, and thus open pores remain.

This chapter provides basic information about UHMWPE and Activated Carbon and describes their structures, properties, production and application.

3.2 Ultra High Molecular Weight Polyethylene (UHMWPE)

UHMWPE is a thermoplastic semi-crystalline polymer with outstanding properties of good mechanical strength, a low friction coefficient [104], excellent wear resistance [105], and is highly resistant to corrosive chemicals [106]. UHMWPE is odourless, tasteless, and nontoxic [107] and it is used in many applications including artificial medical joints, sporting goods, bullet proof jackets and armour, fishing lines and ropes [108].

UHMWPE polymer has very long chains with a molecular mass distribution between 3.5 to 7.5 million g/mol [109]. The longer chains strengthens intermolecular interactions and enables transfer of load effectively to the backbone of the polymer and produces a tough material with excellent impact strength [110]. However, UHMWPE cannot be processed easily by traditional

techniques such as injection moulding and extrusion and because of its very high melt viscosity owing to the extremely long chains [111].

3.2.1 Structure and Properties

UHMWPE is a linear homopolymer produced by the polymerisation of ethylene (CH_2=CH_2). UHMWPE is made up of very long and tangled chains of polyethylene. These molecular chains become mobile at elevated temperature and when cooled below the melting point, they tend to rotate about the C-C bonds and fold back and forth upon themselves creating chain folds. This chain folding forms local ordered regions known as crystalline lamellae [112]. The thickness of this crystal lamella is associated with the average number of folds per chain [113]. A combination of one crystalline lamella and one non-crystalline region between lamellae forms a lamellar stack. A collection of these lamellar stacks form spherulites, which are important structural features found in polymers crystallised from the melt [114]. Figure 3.1 shows a representation of the structure of crystalline polymers.

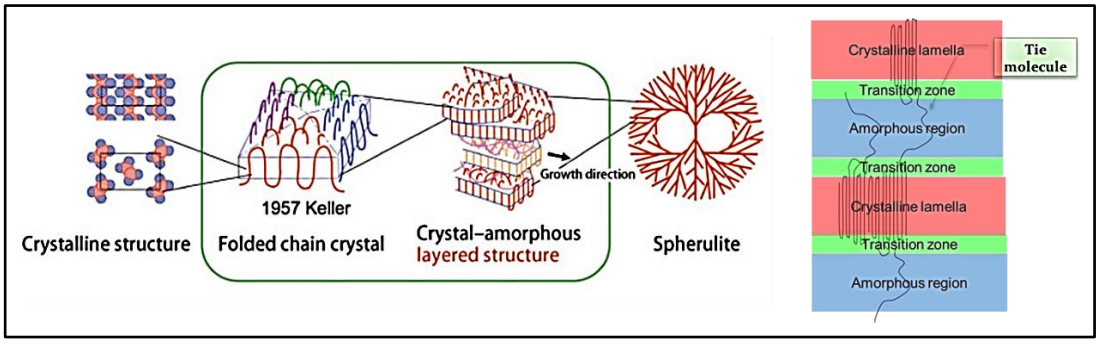

Figure 3.1: Schematic of morphological structure of crystalline polymers forming folded chain lamellae and spherulites. Left) Folded structures of polymer crystals and spherulite [115]. Right) Crystal lamella [116]

Spherulites are formed around crystal nuclei and they grow radially outwards from the nuclei by adding lamellae between the gaps formed between preceding lamellae. Spherulites growth is limited by the meeting of spherulites boundaries and their size depends on the time of crystallisation and the separation of the nuclei from which they grow. Under polarised light

microscopy, spherulites exhibit a unique pattern that consists of radiating bands and a Maltese crosses pattern [114].

The degree of super-cooling is determined to some degree by the cooling rate. It increases at higher cooling rates resulting in a high nucleation density and consequently, the average spherulite size decreases with increased cooling rate [117].

Results from literature indicated that the lamellae size increases with slow cooling and decreases by quenching. Therefore, the slowly cooled UHMWPE polymer has more or larger lamellae resulting in a higher degree of crystalline volume [118]. The degree of chain folding determines the thickness of the lamellar, which consequently, affects the melting temperature of the crystals. The melting temperature of these chain-folded crystals increases with increasing lamellar thickness [113].

The microstructure of UHMWPE includes two regions, amorphous and crystalline as illustrated in Figure 3.2. The crystalline phase of UHMWPE is made up of folded rows of carbon atoms packed into lamellae, which are typically 10 to 50 nm in thickness with a length of approximately 10 to 50 μm. On the other hand, the amorphous phase made up of randomly oriented and entangled chains. The amorphous regions are crossed over by tie molecules from one crystalline region to another [119].

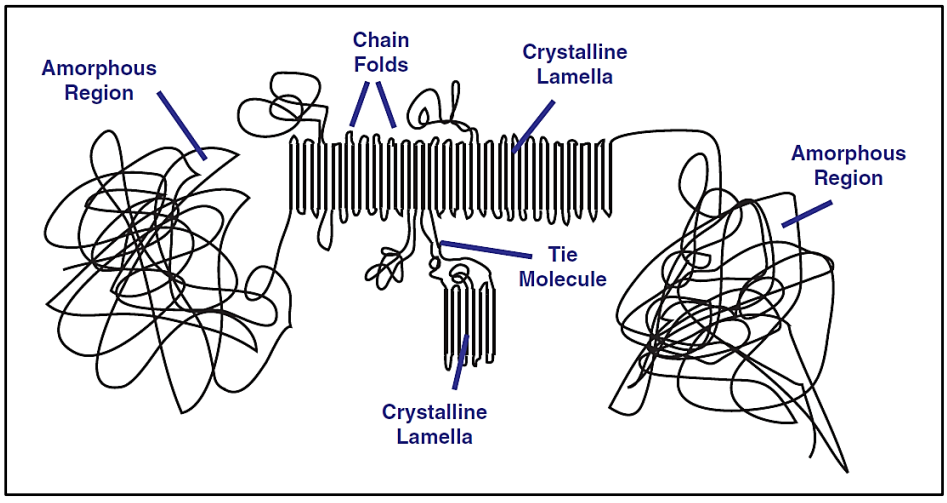

Figure 3.2: Morphological structure of UHMWPE [112]

The existing and additional topological restriction of molecular motion by other chains referred to as entanglements, which can be thought of as knots or crossings between the surrounding chains within the amorphous phase. The high molecular weight and high degree of entanglements, limit the mobility of the polymer chains (i.e. higher viscosity) and prevents it from flowing, resulting in difficulties in processing the polymer [91]. Therefore, the extremely high melt viscosity of UHMWPE, results from the entanglements of the polymer chains, prevents UHMWPE from being processed by conventional processing techniques [120].

It is widely accepted that the entanglements in the amorphous phase and the high density of tie molecules, contribute to the high mechanical properties (such as excellent toughness, highest impact strength and high elongation) of UHMWPE in comparison with other commercial polymers [61].

UHMWPE is formed from coarse particles which are in turn made up of smaller ones as shown in Figure 3.3. These small particles are also formed from even smaller particles (sub-micron particles). Between these sub-micron particles, some fibrils exist in the structure of UHMWPE. The slow movement of the molecular chain and the gaps between the particles delay the transmission of heat within the material during processing [121].

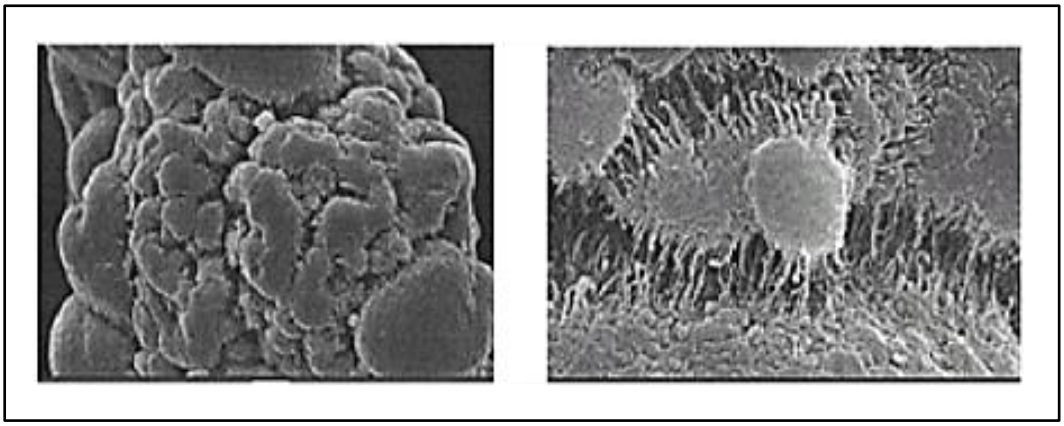

Figure 3.3: SEM images of commercial UHMWPE [121]

UHMWPE is produced in a powder or flake form. Table 3.1 shows the typical physical and mechanical properties of UHMWPE. UHMWPE does not absorb

water or wet easily, which makes it difficult to bond with other polymers. UHMWPE has 0.01% water absorption and it is often used in the food industry and in biomaterials applications due to it being chemically inert and having low water absorption [122]. The mechanical properties of UHMWPE can be enhanced by using a wide range of fillers [123]. Some commonly used fillers and their influence on the mechanical properties of UHMWPE are shown in Table 3.2 [124].

Table 3.1: Typical Physical Properties of UHMWPE [109]

Properties	Typical values
Density (g/cm^3)	0.925-0.945
Melting Temperature (°C)	132-138
Elastic Modulus (GPa)	0.5-0.8
Tensile Yield Stress (MPa)	21-28
Ultimate Tensile Strength (MPa)	39-48
Elongation at Break (%)	350-525
Degree of crystallinity (%)	39-75

Table 3.2: Commonly used fillers with UHMWPE [124]

Fillers	Amount (%)	Improved properties
Carbon nanofibres	0.5-5	Tensile strength
Carbon nanotubes	0.1-5	Young's modulus Tensile strength Toughness
Graphene	0.1-1	Yield strength Tensile strength Reducing friction coefficient Lubrication
Hard particles	10-20	Bearing loading capacity

The addition of graphene to UHMWPE as reinforcement can improve the tensile properties and also reduce creep [123]. The modulus and tensile strength of the UHMWPE increase with the addition of Carbon Nanofibres (CNF), while a decrease appears at 3% content (wt) of CNF [124]. The addition of Carbon Nanotubes (CNT) into UHMWPE matrix introduces changes in shear strength, toughness and surface hardness [76]. Studies show that when UHMWPE is formed into fibres and reinforced with a small amount of carbon nanotubes, the mechanical properties are substantially improved and the fibres are strengthened and toughened [125].

3.2.2 Production and Application

UHMWPE powders have been produced by Celanese (previously known as Ticona) using the Ziegler process, since the 1950s. UHMWPE is produced by polymerisation using three main ingredients; ethylene gas, hydrogen, and titanium tetra chloride as a catalyst. The polymerisation process takes place in a solvent used for mass and heat transfer and is conducted in a specialised production plant suited for handling these volatile and dangerous materials. The catalyst is the most important ingredient to producing white UHMWPE powder with deceased impurities [112].

The consolidation of UHMWPE powder takes place under elevated pressure and temperature due to the high melt viscosity of UHMWPE. This material does not flow freely above its melting temperature (i.e. does not become liquid) and shows pronounced viscoelastic characteristics in the melt and behaves much like a rubbery solid [121]. Therefore UHMWPE cannot be processed by conventional processing techniques such as blow moulding, injection moulding and screw extrusion [112].

Processing UHMWPE requires either extremely high pressures or dissolution. Ram extrusion and compression moulding are typical processing methods for UHMWPE at high pressure. Gel spinning is another way to process UHMWPE by dissolving the polymer in an appropriate solvent to reduce the viscosity and

then drawing it at elevated temperature. UHMWPE powder can also be compacted and sintered [31].

UHMWPE is used in a variety of specialty applications owing to its good wear resistance, chemical inertness, high toughness and low coefficient of friction. The upper use temperature of UHMWPE is limited to around 100°C as at this temperature undesirable softening occurs. It is used as an unlubricated bearing material in applications where routine maintenance is not possible due to inaccessibility, such as hip joint replacements, bushings in office business machines and aeronautical cable guides. Since lubrication is not required, UHMWPE is also suitable for pharmaceutical processing equipment and bushings in food processing, where lubricant materials could be a source of contamination. Chutes and hoppers, in mining and quarrying operations, may be lined with UHMWPE sheeting to decrease friction and prevent wear on underlying metal surfaces. UHMWPE seals and bushings are used in hydraulic rock hammers and drills, which are subject to abrasive dust and grit. UHMWPE parts are also used widely in the textile industry [31].

Sintered UHMWPE can be produced with densities ranging from approximately 0.88 to 0.93 g/cm^3. The UHMWPE product is porous at the lower end of the density range, and has been used for filtration and in storage batteries [31].

UHMWPE fibres, produced by gel spinning, are used in a few niche applications in which a high modulus to weight ratio is important such as military and personal protection equipment [31]. UHMWPE composites and fibres are also used in consumer and industrial applications. The glass fibre blended UHMWPE is used as insulation barriers in lead automotive batteries and the porous UHMWPE finds applications as water filters [109].

3.2.3 Crystallinity

Polyethylene is typically a semi-crystalline polymer and the physical properties are governed by the relative proportions of the crystalline and non-crystalline

phases, as well as their shape, size, orientation, connectivity, etc. It has been observed that the crystallisation of polyethylene does not stop when the material is cooled to room temperature but it may continue slowly at this temperature. Therefore, the physical properties may change with the gradual increase in the crystallinity degree over time [31].

UHMWPE products undergo slow increases in density and significant changes in tensile characteristics at room temperature over a period of time. This increase can be due to the increase in the crystalline fraction or the improvement in the packing within the non-crystalline regions. High melt viscosity restricts the motion of molten chains during the crystallisation process and this decreases the crystallisation rate. The crystallisation rate of polyethylene contributes to its suitability to a given processing technique or end use [31].

3.2.4 Thermal Transition

The glass transition, melt, and flow temperatures are the major thermal transitions that many polymers go through. The glass transition of UHMWPE occurs around -160°C. The polymer behaves like a brittle glass at temperatures below the glass transition temperature. The polymer chains do not have adequate thermal energy to slide past each other and therefore when the polymers respond to mechanical stresses they stretched then break [112].

The smaller lamellae in UHMWPE begin to melt when temperature rises above 60–90°C [112]. The peak melting temperature and crystallinity are the main features in the Differential scanning calorimetry (DSC) (Figure 3.4). The melt temperature may occur between 112 and 150°C and crystallisation during cooling between 85 and 112°C [61].

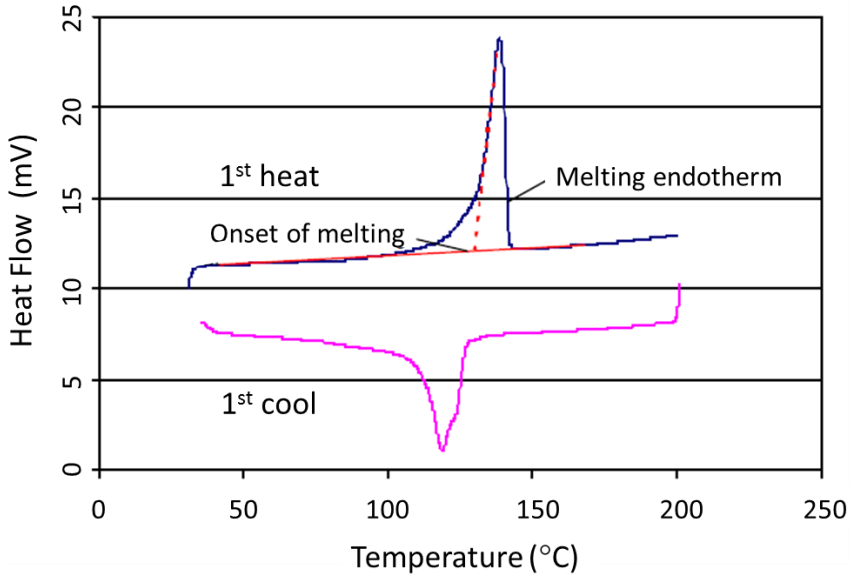

Figure 3.4: A typical DSC trace of UHMWPE [126]

Semi-crystalline polymers usually go through a flow transition and become liquid when the temperature is increased above the melting temperature. Such a transition can be observed in polyethylene with a molecular weight of less than 5 x 10^5 g/mol. Polyethylene with a molecular weight above 5 x 10^5 g/mol cannot flow easily as the entanglement of the large polymer chains stops it from flowing. For this reason, UHMWPE does not show a flow transition [112].

3.3 Activated Carbon

Activated carbon (AC) is a microporous carbonaceous adsorbent with high porosity and internal surface, generally, more than 500 m^2/g. The history of AC was traced back to about 1500 B.C., when wood chars were used as a medicine and also as a purifying agent by the Egyptians [127]. However, the use of AC in industrial applications became common practice in decolourising liquids and also in gas masks, during the WWI, for the protection of soldiers from poisonous gases [128].

AC is produced from carbonaceous materials, such as coconut shells, coal, lignite, hard and soft woods, fruit stones and petroleum [129]. The manufacturing process is varied for each medium but essentially the carbon is

exposed to oxygen to create tiny pores in the carbon at a molecular level. It is these pores that absorb contaminants by physical and chemical attraction. The elements of a typical AC can be 88% C, 1.0% S, 0.5% N, 0.5% H, and 6-7% O, with a balanced representation of inorganic ash contents. The content of the oxygen differs, depending on the raw material source and the activation methods [127].

AC is widely used, as it is reliable and effective material in removing contaminants. It has an enormous adsorptive capacity and a wide variety of dissolved organics and chlorine can be attracted to it. AC has also a capability to be custom tailored to suit certain applications. AC is used in water and gas purification, air filters in respirators and gas masks, medicine, filters in compressed air, gold purification, metal extraction, decaffeination, sewage treatment and many other applications [130].

The majority of carbonaceous materials have a certain extent of porosity with an internal surface area of 10 m^2/g approximately [131]. The activation of the char is performed in an atmosphere of CO_2, air, or steam at a temperature ranges between 800°C and 900°C. This leads to the oxidation of part of the areas within the char and the internal surface may expand to 2500 m^2/g [127].

3.3.1 Application of Activated Carbon

AC is an excellent and versatile adsorbents, that are widely used in both gas-phase and liquid-phase separation processes in many industries such as [127, 132, 133]:

- Domestic and industrial wastewater (e.g. removal of undesirable taste, colour, odour, and other inorganic and organic impurities)
- Chemical industries (e.g. air purification in inhabited places and solvent recovery)
- Pharmaceutical (e.g. colour removal from various products)
- Control of air pollution in industrial and automobile exhausts
- Energy storage, batteries, fuel cells, nuclear power stations

- Food industries (e.g. deodorisation, decolourisation and taste removal)
- Medicine (e.g. toxic drug and chemical adsorption)

3.3.1.1 Liquid-phase application

The AC used in liquid phase applications have larger pore size than that of the gas phase AC. This allows for more rapid diffusion into the meso-pores and micro-pores and also allows large impurities or products to be retained [134]. Liquid-phase activated carbons are used in powder or granular forms. The granular form is used mainly in continuous systems where the liquid being treated is flowed through a fixed bed. There is a large number of liquid phase applications assigned to AC and the followings are examples of relevant areas of application [135]:

- Drinking water, removal of chlorinated and other Volatile organic compounds and improve taste, smell and colour
- Improvements to the purity of ground water, removal of contaminants coming from heavy industries disused sites
- Treatments of municipal and industrial wastewater
- Mining operations, including treatment of feed water, adsorption of excess flotation reagents, Natural Organic Matter and adsorption of metallic ion (e.g. gold mining)
- Pharmaceutical processes, including water and many other products purification
- Oil, food and beverage industries; removal of smell, colour and undesirable tastes
- Dry-cleaning, such as purification of solvents
- Electro-plating industries; wastewater purification (containing Cr, Pb, etc.)
- Household water purification and cleaning of aquariums
- Sugar and sweetener industries such as decolourisation agents for white sugar production

3.3.1.2 Gas-phase application

Gas-phase applications of AC include gas storage, separation and catalysis. Granular or shaped AC (i.e. fibres, pellets, cloths and monoliths) is mostly used in gas-phase applications so that any excessive pressure drop can be avoided when the gas passes through the AC bed. They have a number of important properties such as [134]:

- High adsorptive capacity due to well-formed micro-porosity
- Low resistance to gas flow
- High capacity of retention
- High preferential adsorption of gases in moisture presence
- Full release of adsorbates at high temperature and low pressure

There are many gas-phase applications of AC and below are just some examples of these applications [135]:

- Personal protection
- Cigarette filters
- Chemical warfare agent protection and industrial gas masks
- Purification of effluent gas
- Purification of industrial off-gas (e.g. removal of SO_2, H_2S, CS_2, etc.)
- Petroleum refineries
- Sewage and geothermal plants
- Solvent recovery
- Gas mixtures separation using carbon molecular sieve membranes
- Inorganic and organic process catalysis
- Adsorption of radionuclides
- Storage and purification of natural gas
- Automobile; gasoline recovery
- Odour control

3.3.1.3 Water purification

Activated carbons have been used in water purification primarily in the removal of organic contaminants (natural and synthetic organic matters and by products of chemical water treatment) that produce bad odours and tastes, and also may form a source of infection [136]. Activated carbons are mostly effective at removing organic compounds such as pesticides, volatile organic compounds and benzene and therefore it is used extensively in the purification of drinking water in small household systems [137]. The use of water can be divided into three main categories:

- drinking water
- industrial and municipal wastewater
- groundwater

The application of AC in the treatment of drinking water was originally focused on the removal of the taste and odour of the water. Purification by AC is now considered to be inexpensive and an attractive option for organic and inorganic contaminants removal from both surface and ground waters [138].

The most common sources of drinking water are surface waters (from lakes and rivers) and ground waters (from wells). These waters are usually contaminated with algal toxins, microorganisms (bacteria, viruses), halogenated compounds, volatile organic compounds and the products of natural vegetation decay. In some areas, ground waters also contain radon, a radioactive decay product of natural uranium, causing lung cancer. Furthermore, lead from pipes and fittings may appear in tap water in some older water distribution systems. AC can greatly decrease the concentration of these undesired contaminants [139].

3.3.2 Structure of Activated Carbon

AC has a microporous structure with a very large internal surface area which can adsorb undesirable species from liquids or gases [140]. Figure 3.5 shows a

schematic illustration of an activated carbon particle. AC has both amorphous and microcrystalline regions with a relatively low density just under 2 g/cm^3 and has a low degree of graphitisation [133]. During the carbonisation stage, the porous structure is formed and developed further during the activation process. The volume is enhanced and the diameters of the pores are enlarged when the carbon is activated [127].

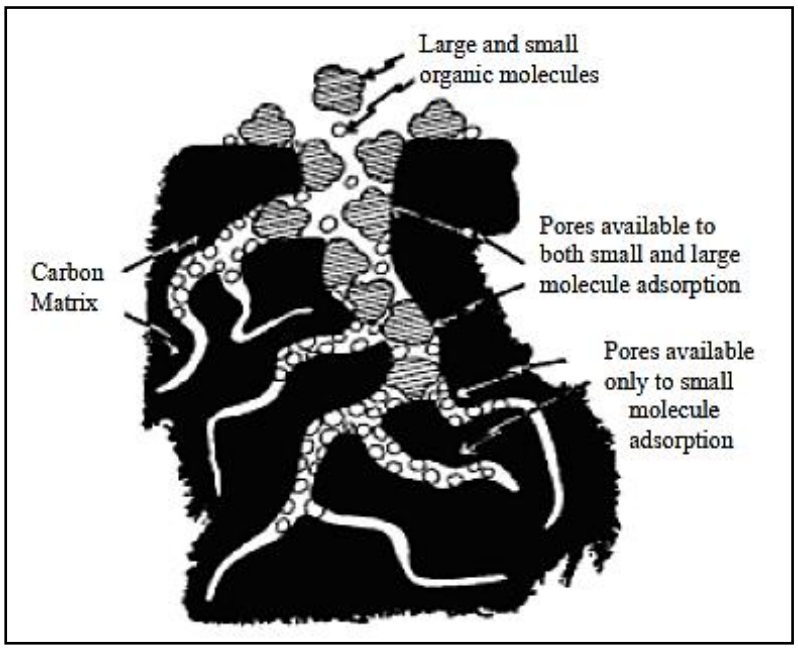

Figure 3.5: Activated carbon particle [141]

Activated carbon particles have randomly arranged pores over a wide range of shape and size. While the pore size is a continuous distribution, this distribution is spilt into different regimes; micro-pores, macro-pores and meso-pores. Micro-pores have a diameter less than 2 nm and the macro-pores are generally larger than 50 nm. While meso-pores are in range between 2 to 50 nm [128]. These can be further divided into super-micro-pores with diameter of 0.7-2.0 nm and ultra-micro-pores of diameter less than 0.7 nm.

The pores structure and the pore size distribution are mainly dependent on the nature of the source material and the conditions of the carbonisation process [127]. As an example, Figure 3.6 shows that the pore structure in wood-based carbons differs based on the type of plant or wood. The pores can be of

similar size and shape and are evenly distributed in some woods like pine. However, these can be of very different sizes and shapes and can be organised in circular fashion as in Bagasse, Babool, and Castor Oil Wood etc.

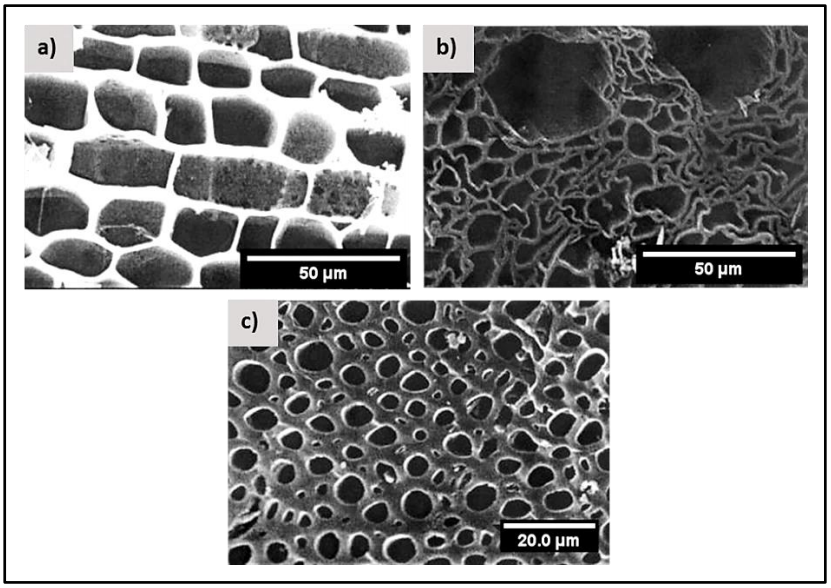

Figure 3.6: SEM images of porous carbon materials [140]:
a) Castor oil plant, b) Bagasse, c) Babool (acacia) wood

3.3.3 Production of Activated Carbon

AC is produced from a wide range of carbon-containing organic materials, mainly coconut shells, wood, coal, fruit stones, sawdust, lignite, peat, petroleum coke, etc. Figure 3.7 shows the flow diagram of the manufacturing process of activated carbon [136].

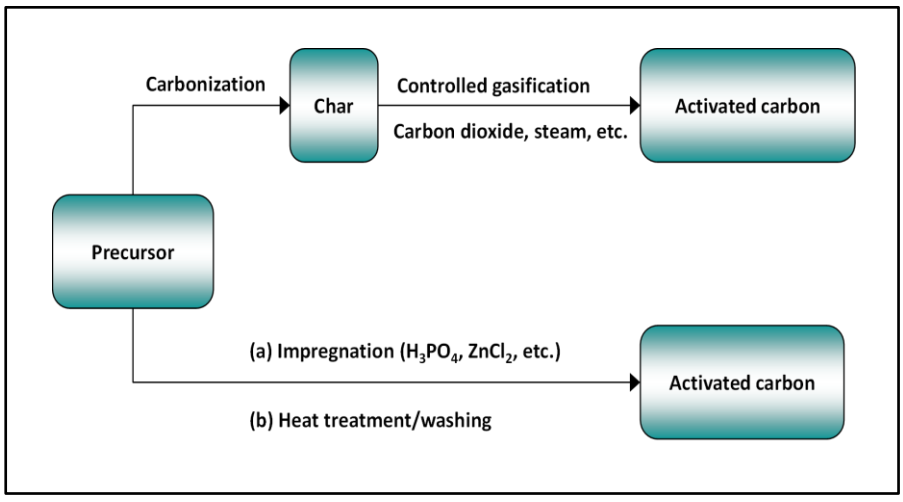

Figure 3.7: Flow diagram of the production of AC

The selection of the raw material for the production of the AC is based mainly on the following criteria:

- Availability and cost
- Low in inorganic matter
- Ease of activation
- Low degradation upon storage

Some of typical raw materials used in the production of AC are listed in Table 3.3. This table shows the properties and the type of AC expected of each raw material. Nutshells, sawdust, wood and fruit stones (Cellulose-type materials) are used for chemical activation. However, some of these raw materials, such as fruit stones and nutshells, are also used for thermal activation, however, the general trend is to utilise lignite, peat and several types of coal depending on availability and cost [136].

Coconut shells are popular raw materials for many types of AC and they are ideal for the manufacturing of hard granular AC, due to their relatively high density, hardness and volatile content. They are used commercially for the production of microporous AC [136].

Table 3.3: Properties of materials used in the manufacture of AC [140]

Raw material	Carbon (wt %)	Volatile (wt %)	Density (cm^3/g)	Ash (wt %)	Texture of AC
Soft wood	40-45	55-60	0.4-0.5	0.3-1.1	Soft, large pore volume
Hard wood	40-42	55-60	0.55-0.8	0.3-1.2	Soft, large pore volume
Lignin	35-40	58-60	0.3-0.4	-	Soft, large pore volume
Nutshells	40-45	55-60	1.4	0.5-0.6	Hard, large micro-pore volume
Lignite	55-70	25-40	1.0-1.35	5-6	Hard, small pore volume
Soft coal	65-80	25-30	1.25-1.50	2.12	Medium hard, Medium pore volume

Petroleum coke	70-85	15-20	1.35	0.5-0.7	Medium hard, Medium pore volume
Semi-hard coal	70-75	1-15	1.45	5-15	Hard, large pore volume
Hard coal	85-95	5-10	1.5-2.0	2.15	Hard, large pore volume

Commercial AC can be manufactured by a two stag process; carbonisation of the raw materials and activation [142, 143]:

3.3.3.1 Carbonisation

The carbonisation is the process in which the organic materials are converted to char under a pyrolysis condition at a temperature under 800°C, in an inert atmosphere. In the first stage of this process most of the water and volatile organics are released and as a result the relative content of carbon is increased and the basic microstructure of the char is formed with micro-porosity at a temperature of approximately 500°C [140]. When the temperature rises the organic compounds break down and form tar coated on the surface of the materials. Since the tar has a low porosity and surface area it is necessary to remove it to form high porous materials by further activation stage.

3.3.3.2 Activation

The purpose of the activation stage is to remove the tar coated on the char surface and achieve a large surface area and form a well-developed and easily accessible pore structure. This stage can be carried out by either physical or chemical activation [143, 144].

In the physical activation, the carbonised materials are exposed to oxidizing atmosphere, such as steam, oxygen or carbon monoxide, at temperature ranges between 800 and 1100 °C [143]. On the other hand, in the chemical activation, the raw materials are impregnated with different chemical agents,

such as acids (phosphoric acid), or strong bases (potassium hydroxide, sodium hydroxide) or a salt (zinc chloride), before the carbonisation process. Following the impregnation process, the precursor is heat treated at a moderate temperatures between 400-600°C in the absence of air and then the material is washed after cooling to remove the activating agents [140].

3.3.4 Activated Carbon Forms

The three main forms of commercially available AC are [140, 145, 146]:

3.3.4.1 Powdered activated carbon (PAC)

Particle sizes with an 80-mesh sieve (mostly less than 0.18 mm) and smaller is classifies as PAC by the ASTM. PAC is generally used directly in applications such as clarifiers, raw water intakes, gravity filters and rapid mix basins.

3.3.4.2 Granular activated carbon (GAC)

These particles are irregular shaped particles and have a relatively larger particle size with a smaller external surface, compared with PACs. Particle sizes range from 0.2 to 5 mm. This carbon is suitable for gas and vapour adsorption and is mainly used in air and wastewater treatment. The advantage of GAC water filters is that large amounts of carbon can be used in the filtering system through fitting a number of filtering units in series. The length of the contact time in filtration process can vary widely from minutes to over an hour and is influenced by the quality and quantity of contaminants to be removed.

3.3.4.3 Pelleted activated carbon

This type is a combination of PAC with a binder that are fused together and extruded into a cylindrical shaped with diameters range from 0.8 to 5 mm. Due to their low pressure drop, low dust content and high mechanical strength they are mainly used for gas phase applications.

3.3.4.4 Other types of AC

AC is available in other forms, such as Impregnated Activated Carbon (IAC). This type of AC is a porous carbon which contains several types of inorganic impregnate (e.g. iodine and silver) and cations (e.g. Zn, Mn, Al, Ca, Fe, Li etc.). These carbons are used for air pollution control and purification of domestic water.

Polymer coated AC is another example of a porous material that is coated with a bio-compatible polymer that forms a permeable coat without closing the pores in the carbon structure. These carbons are used in a medical treatment technique called hemoperfusion to remove toxic substances from the blood of a patient [147].

3.3.5 Properties of Activated Carbon

When the water flows through an AC filter, chemicals and organic particles are removed through a process known as adsorption. This process is influenced by the following parameters [146]:

- Physical properties, such as surface area and pore size distribution
- Chemical properties, such as the chemical nature of the adsorbing surface (amount of hydrogen and oxygen associated with it)
- Contaminant properties, such as chemical composition and contaminants concentration
- Flow rate or exposure time of water to the AC
- Water temperature and pH

3.3.5.1 Physical properties

The pore size and distribution have a great influence on the effectiveness of AC filtration. Better filtration can be achieved when the pores are large enough to allow for the adsorption of contaminants. The type of contaminants that can be filtered by AC will depend on the pore size of the AC, which varies based on

the type of raw material used and the activation method. AC tends to work best for removing larger organic molecules [146].

The adsorption capacity and physical properties of the ACs are required in industrial applications to determine the quality of the ACs [136]. Some examples of the physical tests are highlighted as follows:

Particle size: the effectiveness of the filter, adsorption and flow characteristics are influenced by the size of particles. Particles size has an inverse effect on the adsorption rate where small particles have rapid adsorption compared with larger particles.

Mechanical strength: this is an important property for most application of granular AC where high attrition resistance and mechanical strength are required to withstand the pressure drop and prevent carbon losses under practical conditions.

Bulk density: the mass per unit volume of the AC, including the volume of the pores and the voids within the AC particles. This property is useful to estimate the volume of the packed AC and also to determine the AC grade.

Apparent density: the mass per unit volume of the AC, excluding the pores. The apparent density is used in the measurement of the porosity of the AC, which is an important property with regard to the flow characteristics of AC.

3.3.5.2 Chemical properties

It is desirable that chemical interactions between the AC surface and the organic molecules may occur. Additionally, electrical forces between the contaminants and the surface of AC may also lead to ion exchange or adsorption. The chemical properties of AC are determined by the activation process as different processes may produce an AC with different chemical properties which make the AC material more or less attractive to different

contaminants. For instant, AC with less oxygen in the surface of the pore absorbs chloroform very effectively [146].

3.3.5.3 Contaminant properties

Activated Carbon is an effective adsorbent for large organic molecules. AC and organic molecules are basically non-polar materials which means they tend to associate with each other. Therefore, organic molecules tend to strongly associate with the AC rather than remaining dissolved in water. Normally, if the organic molecules are less soluble then they are more likely to be adsorbed. Additionally, the smallest pores tightly hold smaller organic molecules. Contaminant concentration can also affect the adsorption. AC may perform effectively at low concentrations [146].

3.3.5.4 Water temperature and pH

The rate of adsorption is usually increased at lower temperatures and pH levels. The temperature and pH are closely associated with the surface chemical reactions and therefore the organic chemicals are more readily adsorbed at low temperatures and pH levels [146].

3.3.5.5 Length of exposure

The time of the contact between the contaminant and the AC influences the adsorption process. A greater number of contaminants are removed with a longer length of contact. A greater amount of AC with a slow flow rate enhances the effectiveness of the filtration process. The flow rate and bed depth are critical design parameters in filtration [146].

3.3.6 Adsorption Process

Adsorption is a phase transfer process that is widely used to remove substances from gas and liquid phases [148]. This surface phenomenon can be defined as “the accumulation or concentration of liquid or gas molecules

(adsorbate) at a surface or interface of a solid or a liquid (adsorbent)" [128]. The basic terms of adsorption is shown in Figure 3.8.

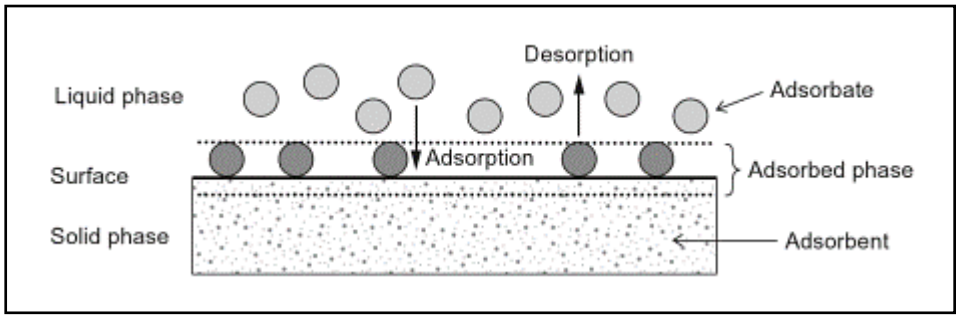

Figure 3.8: Basic terms of adsorption [148]

Adsorption can be categorised as physical adsorption or chemical adsorption. The physical adsorption occurs as a result of the molecular attraction of the Van der Waals type, while the chemical adsorption is based on the chemical reaction between the adsorbate and the adsorbent [148].

In the physical adsorption, which is a dynamic process, some of the adsorbate molecules are transferred from the liquid phase onto the solid phase surface, while some of these molecules are released again to the liquid phase. Figure 3.9 represents the adsorption process, which shows the transfer of the adsorbate molecules in bulk gas phase to the carbon solid surface and diffusing onto the internal surfaces of the adsorbent pores [140].

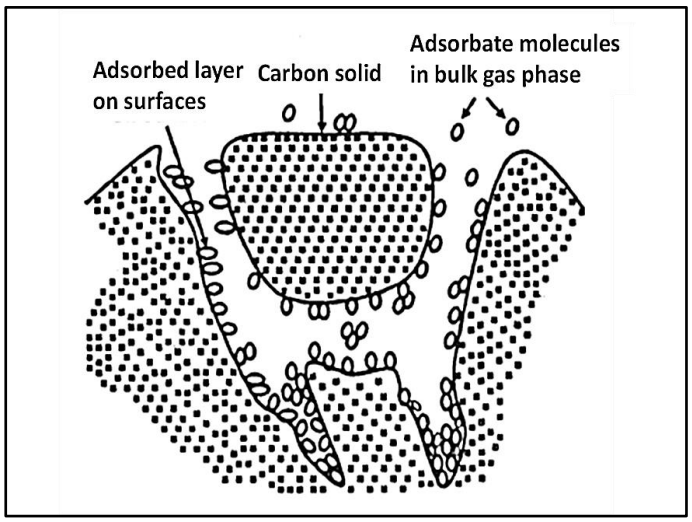

Figure 3.9: Adsorption process in AC [140]

In the physical adsorption, the intermolecular interactions take place between favourable energy sites. Since the adsorbed molecules are attached to the surface by weak Van der Waals forces, these molecules are free to move within the interface. Unlike the physical adsorption, the chemical adsorption involves the transfer of electrons between the adsorbate and the adsorbent forming strong localised bonds. In this process, the adsorbed molecules are not free to move within the interface or on the surface [149].

Many factors affecting the adsorption process, such as porosity and surface area of the adsorbent, temperature and also the chemical and physical characteristics of the adsorbed substances. Generally, higher adsorption occurs with larger internal surface of the adsorbent and also with larger molecule size of the adsorbates, while low adsorption occurs at higher temperature [148].

Chapter 4 Characterisation of UHMWPE Powder for Laser Sintering

4.1 Introduction

Previous research has demonstrated that laser sintering is capable of processing polyethylene. Salmoria *et al.* [85] successfully processed high-density polyethylene (HDPE) by laser sintering. They were able to show that the structure and the properties of the laser sintered parts can be controlled by using different particle sizes. Their results showed that a lower sintering degree can be achieved with larger particle size with lower values for the mechanical properties. While smaller particles form a larger contact area contributing to a higher rate of necking between particles and resulting in improved mechanical properties [150].

Little attempts have been made to process UHMWPE by Additive Manufacturing, particularly laser sintering. Rimell and Marquis attempted to produce parts for clinical application from UHMWPE (GUR 4120 and GUR 4170) by using a non-commercial LS machine. However, the attempts to produce multilayer parts were unsuccessful, due to high degree of shrinkage and curling developed during the laser sintering [151]. Goodridge *et al.* also had limited success and produced multilayer parts from UHMWPE (GUR 4170) with a high sintering between particles and layers using the commercial Vanguard Laser Sintering machine (3D Systems) [61]. Goodridge *et al.* performed a number of trials to establish suitable parameters for processing UHMWPE by using different laser powers, bed and feed temperatures and scan counts. They indicated that the processing window to obtain UHMWPE components was considerably narrow and therefore very precise process parameters (i.e. laser power combined with correct bed and feed temperatures) were required. Goodridge *et al.* reported that the UHMWPE multilayer parts were produced only by using a laser power of 13 watts, double scan count with bed and feed temperatures of 135 °C and 125 °C respectively.

They investigated the mechanical properties of the sintered parts by using tensile and three point bend tests. The results show that the ultimate tensile strength and Young's modulus of these parts were just above 0.2 MPa and 1.5 GPa, respectively and the flexural strength and modulus were 0.52 ±0.2 MPa and 18.67 ±4.3 MPa, respectively.

4.2 Characterisation Methods of UHMWPE Powder

The powder used in manufacturing laser-sintered parts, in this study, was UHMWPE GUR 2122 (Celanese, Germany). UHMWPE GUR 2122 is a linear polyolefin with a molecular weight of around 4.5×10^6 g/mol. It has a unique morphology that produces a low powder bulk density of 0.20 – 0.25 g/cm^3 (Celanese GUR® 2122 PE-UHMW datasheet).

4.2.1 Particle Size and Morphology

A Mastersizer 3000 (Malvern Instruments, UK) was used to determine particle size, by laser diffraction method. In this method the intensity of light scattered is measured as a laser beam passes through a dispersed particulate sample. The sample was characterised by dry powder dispersion method using air as a media. The distribution of the particle size was determined at a feed pressure of 3bar and the run was selected to perform 10 measurements from the available sample. The size distributions were reported by the cumulative volume diameter at 10%, 50% and 90%.

Microstructure of the UHMWPE powder was examined using a scanning electron microscope (Philips XL-20, Holland) at an accelerating voltage of 10 kV. In order to prepare a sample for examination, a sample holder with an adhesive tape mounted on, was dipped in the powder and then was shaken up to remove the excess leaving a small number of particles. The sample was sputtered with gold before the examination.

4.2.2 Density of UHMWPE Powder

The true, bulk and tapped densities of UHMWPE powder were measured and the powder flow was investigated.

4.2.2.1 *True Density*

The true density is the density of the solid material without the volume of any open and closed pores. The true density can match the theoretical density of the material, depending on the material molecular arrangement. Therefore it can be indicative of the degree of crystallinity or the ratios of a binary mixture.

The density of a material (ρ) is defined by the mass of the material (m) per unit volume (v) and it is commonly specified in g/cm^3 [152]. The mass of a material can be easily measured using an appropriate balance, but there is a need for a reliable measurement of the volume of the material. For the purposes of determining the true volume of the powder, a gas displacement method was used in this study.

Gas Pycnometry technique uses a gas displacement method to measure volume of materials precisely. Inert gas (e.g. helium) is used as the displacement medium [32, 153, 154]. Helium has the smallest molecules that are capable to fill inner porosity. The specimen is sealed in the compartment of the pycnometer (with known volume), the helium gas is allowed in, and then expanded into a second internal volume. The pressure before and after expansion is measured and used to determine the spacemen absolute volume [155] and hence the density (i.e. true density of the powder).

4.2.2.2 *Bulk and Tapped Densities and Powder Flow*

The determination of bulk and tapped density is a simple method to assess the flow of powders. The achievable laser sintered part density is directly associated with powder density in the part bed, which is linked to the shape of particles and their free flowing behaviour [10].

The powder bulk density is the mass of the powder per unit volume. The volume includes the gaps between particles and the envelope volume of these particles. The powder bulk density can change enormously, depending on the manner the particles are packed together, and it will also change after compaction and consolidation. Therefore, there is not a unique value for the density of a particular powder. Two basic methods are widely used for determining the bulk density of a powder; bulk density and tapped density. These densities can provide a guide to the flow characteristics of powders [21].

The bulk density is obtained by pouring a powder into a container and allows it to settle under the effect of gravity. A low density powder generally has a good structural strength and does not collapse easily when poured in a container. On the other hand, a high bulk density powder is structurally weak and collapses easily. This behaviour depends on the friction between the particles. The bulk density is low when the friction between particles is high, and vice versa [21].

The tapped bulk density is determined by tapping the container holding the powder. A cohesive powder collapses considerably by tapping, while a weak or free flowing powder exhibits insignificant change. The powder particles lose contact with each other during tapping, resulting in less friction between these particles and allow them to rearrange. Therefore, tapping can improve the packing conditions of the powder [21].

The ratio between the tapped density and bulk density is known as 'Hausner Ratio (HR)' and it classifies the flow of powders. The powder classification regarding HR is [156]:

- HR < 1.25 high powder flow
- 1.25 < HR < 1.4 reduced powder flow
- HR > 1.4 cohesive powder

Laser sintering powders need to be under a limit of 1.25 (i.e. high flow) to be considered as a suitable powder with an adequate density [156]. Powder flow

and packing influence the layer density of the powder in powder bed. When the powder flows easily and better, a little interaction between the particles occurs, resulting in less voids and thus a high density. The layer density is directly related to the laser sintering process. A high layer density decreases porosity and improves the part quality and accuracy [157].

HR can be affected by particles shapes (i.e. irregular, spherical and flake) and particle size. If the particle shape deviates more from spherical, then the HR becomes higher. Also, the HR decreases with increasing particle size [21].

4.2.2.3 *Methodology*

The powder bulk density is determined by pouring powder through a sieve in to a pre-weighed 100 cm^3 steel cup. The excess powder is removed carefully from the top of the cup by a metal ruler, without affecting or compressing the settled powder. To simulate the powder feeding process in laser sintering, the powder was allowed to flow through a funnel before reaching the cup. The height of the funnel is 60 mm with an orifice of 9 mm diameter (Figure 4.1).

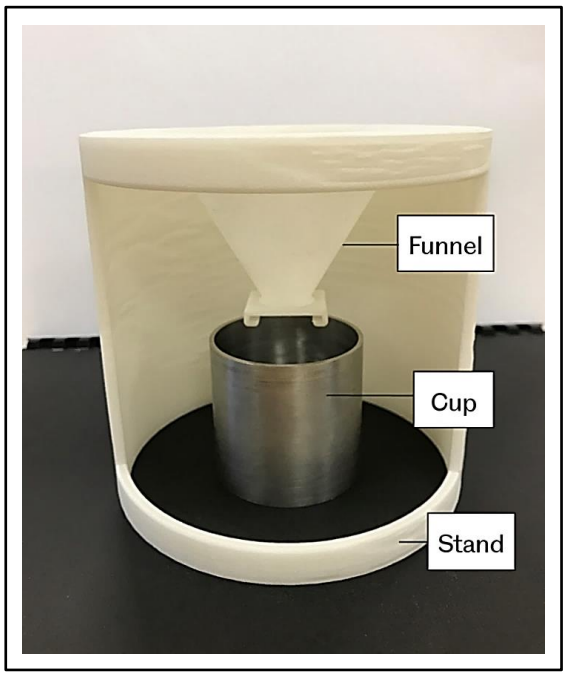

Figure 4.1: Bulk density measurement set-up

For the tapped density, a cup extension is placed on the cup holding the initial powder. An extra powder is added into the extension cup. Then the whole arrangement is subjected to tapping by using a tapping mechanism as shown in Figure 4.2. The tapping action is delivered by a rotating cam which is driven by gears operating manually. The cam lifts the cylinder platform and hence the cylinder itself by a 13 mm distance and then drops again. A recommended number of 500 taps over a period of 4 min, was used. During the tapping process, care was needed to make sure that the level of powder does not fall below the top edge of the bottom cup. After completing the tapping process, the extension cup was removed and the extra powder was then scraped. The content of the cup was weighed and the tapped density was calculated. These experiments were performed at room temperature.

The experiment was repeated three times on each sample for bulk and tapped densities. Three estimates of Hausner ratio were calculated and the average values were taken.

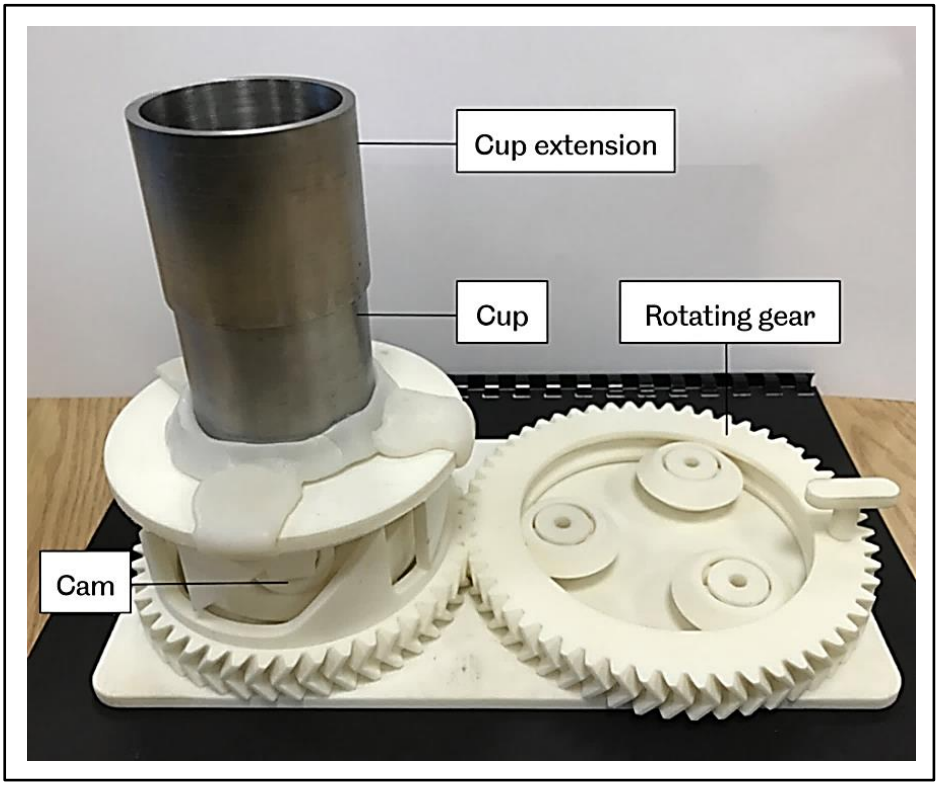

Figure 4.2: Tapped density measurement set-up

4.2.3 Differential Scanning Calorimetry (DSC)

DSC scans were performed using a Perkin Elmer DSC 8500 to determine the melting and crystallisation parameters. Heating and cooling rates of 10°C per minute in a nitrogen atmosphere, with start and end temperatures of 25°C and 220°C, respectively, were used. The samples weight was 6.3 mg on average. The samples were held for 1 minute at 220°C before the cooling cycle started. The results were then analysed using the Pyris™ software. The peaks were identified and the temperatures of these peaks were then labelled as melting or crystallisation temperatures.

4.2.4 Thermogravimetric Analysis (TGA)

TGA is a common method of evaluating degradation in materials and is used to identify the various thermal transformations of the material during sintering. TGA is a thermal analysis that determines mass changes as a function of time and temperature in a controlled atmosphere using a highly sensitive microbalance. The technique is useful for compositional analysis of multi-component material or blends, thermal stability, moisture and volatiles content [26].

Materials for laser sintering must withstand a high thermal load during the preheating stage and also the laser application. Therefore, determining the thermal stability of the polymer is highly recommended.

TGA was performed using TGA analyzer (Pyris 1 TGA, PerkinElmer, USA) to investigate the thermal stability of UHMWPE. Approximately, ten milligrams of the material was placed in a ceramic crucible and was heated from 25°C to 600°C under nitrogen atmosphere at a heating rate of 10°C per minute.

4.2.5 X-Ray Diffraction Analysis (XRD)

XRD analysis of the polymer provides details regarding crystallinity, size and orientation of crystallite and phase composition in semi-crystalline polymers [158].

When x-rays of a specific wavelength pass through a material, they interact with the atoms. This interaction, known as diffraction, is uniform in crystalline solids, because the atoms are regularly spaced in three dimensions. The diffraction allows the x-rays to pass through at specific angles only. The angle of reflection (θ) and the space between the planes of atoms (d) is associated with the wavelength (λ) as described by Bragg equation [114]:

$$\lambda = 2\,\mathrm{d}\,\sin(\theta) \qquad (4)$$

X-rays with a specified wavelength are emitted from an x-ray source and pass through an unknown crystal (crystals) structure. The detector and the crystal are both rotating in the x-ray beam. The x-rays deviate at certain angles as predicted by the Bragg equation. Figure 4.3 illustrates how crystalline structure can be determined through x-ray diffraction.

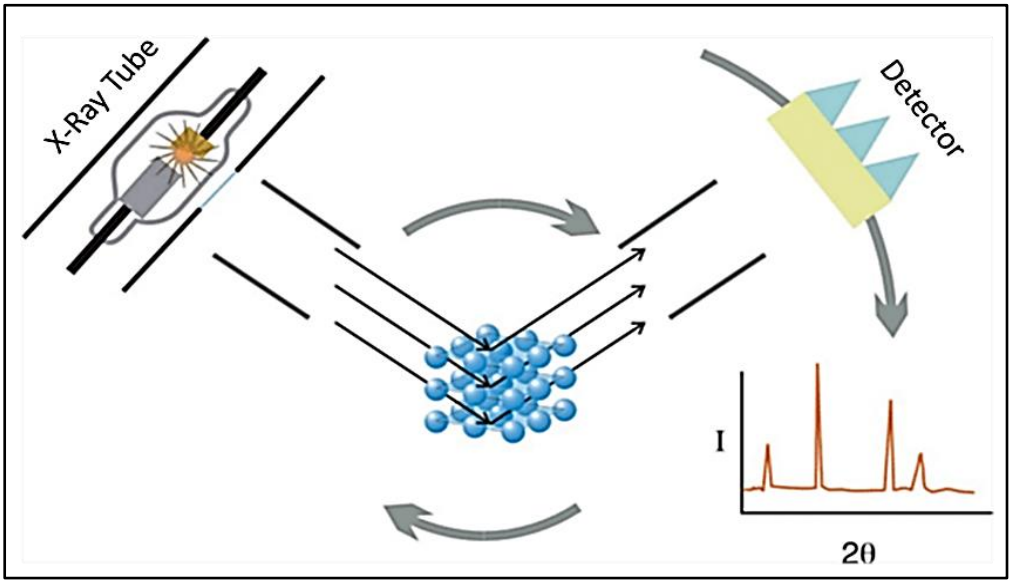

Figure 4.3: The principle of XRD [159]

As the detector and crystal rotate, the x-rays deviate at certain angles. The detector gives the intensity (I) of x-ray photons as it moves. The angles of diffraction are marked by peaks. The height of these peaks is a function of the diffraction of the x-rays with the crystal and the intensity of the source.

The XRD pattern of a completely crystalline polymer is a set of sharp peaks, each representing a reflection from one of the various crystallographic planes. A completely amorphous polymer shows an XRD pattern with a broad halo that represent the average separation of the atoms along and between the polymer chains. Therefore an XRD pattern of a semi-crystalline polymer is a superposition of the reflections of the crystalline on an amorphous halo. An index of crystallinity can be obtained from the ratio of the crystalline peaks integrated intensity to the total area under the XRD curve [158].

An example of XRD profiles of a crystalline and amorphous samples is shown in Figure 4.4.

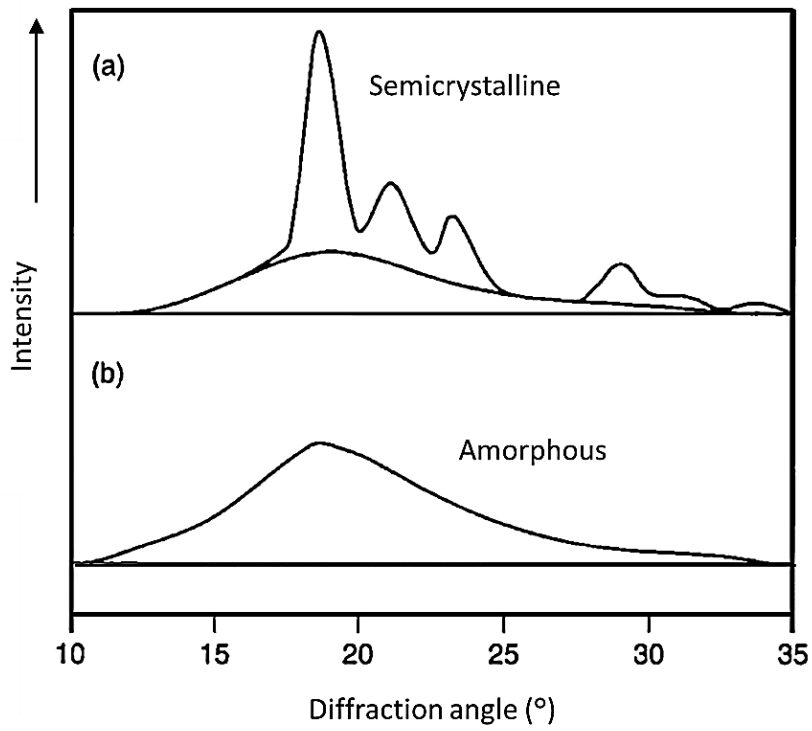

Figure 4.4: Example of an X-ray diffraction profile of (a) crystalline and (b) amorphous samples [160]

XRD analysis was carried out using a Bruker D8 Advance X-ray diffraction system, equipped with a Cu Kα radiation source with a wavelength of λ = 1.5418 nm generated at 40 kV and 40 mA. UHMWPE powder samples were mounted

on the stage and scanned from 10° to 70° using a step size of 0.05° and time per step of 10 seconds.

4.2.6 Degree of Crystallinity

It is commonly known that many of the physical and mechanical properties of polymers are affected by the crystallinity degree, such as Young modulus, yield stress, strength, fatigue, and shrinkage [27-30]. The degree of crystallinity in polymers can be determined by a various methods, such as thermal analysis using DSC, volumetric analysis, infrared, Raman spectra and X-ray diffraction. But each of these methods does not produce identical results, mainly because each method measures different physical parameters and morphological structures [31]. In this work, DSC and XRD methods were used to determine the degree of crystallinity of UHMWPE powder.

Differential Scanning Calorimetry: was used to determine the overall degree of crystallinity of UHMWPE. The degree of crystallinity (X_C) was calculated as follows:

$$X_C(\%) = \left(\frac{\Delta H}{\Delta H_{100}}\right) \times 100 \qquad (5)$$

Where ΔH is the heat of fusion and ΔH_{100} = 293 J/g is the melting enthalpy of polyethylene at 100% crystallinity [161].

The average of three DSC measurements was used to determine the overall crystallinity of the sample.

X-ray diffraction: is a widely used technique to determine the degree of crystallinity in polymers. The diffraction profile is divided in two parts (Figure 4.4); sharp peaks represent the diffraction of crystallites, and the broad peaks represent the scattering of amorphous phase.

The intensity of the scattering can be measured and used to calculate the degree of crystallinity using the following equation [162]:

$$X_C(\%) = \frac{I_C}{I_C + I_A} \times 100 \qquad (6)$$

Where I_C and I_A are the scattered intensities for the crystalline and the amorphous phases, respectively.

Since the assumption is that the areas under the peaks are proportional to the scattering intensities of both crystalline and amorphous phases, therefore the degree of crystallinity was calculated using the following equation [158, 162, 163]:

$$X_C(\%) = \frac{A_C}{A_C + A_A} \times 100 \qquad (7)$$

Where A_C represents the area of crystalline phase (i.e. $A_{110} + A_{200}$) and A_A is the area of amorphous phase.

4.2.7 Hot Stage Microscopy

The consolidation process in laser sintering is initiated by heat, generated by a laser, which results in the formation of the part layers. The Frenkel theory states that the sintering process begins with the formation of necks between adjacent particles, which then followed by full coalescence. The sintering behaviour can be predicted by direct visualisation of the coalescence on a hot stage microscope [15, 22, 23].

The simulation of the sintering process is an important stage for the development of new materials in polymer processing [24]. Therefore the Hot Stage Microscopy (HSM) procedure will aid to visually record the event of consolidation of UHMWPE powder and practically verify its consolidation behaviour.

The optical hot stage experiments were performed using an Olympus BX50 optical microscope equipped with a Linkam heating stage. The temperature was controlled by a Linkam PR600 thermal controller. Images were captured by a VisiCam 10.0 video camera (Linkam Scientific Instruments Ltd., UK) and were analysed using VisiCam® analysis software. The microscope was fitted with crossed polarising filter which was used to assess whether spherulites were present within the UHMWPE.

The powder samples were spread sparsely onto glass cover slide and the slide was then placed in the hot stage sample holder. The maximum temperature limit was set to 230°C, with a heating rate of 10°C per minute. The camera starts capturing the images when the stage reached 50°C and once the stage reached the maximum temperature the heating was stopped and the stage was left to cool back to room temperature. Then the images of the fully melted powder and the development of crystallisation, followed on subsequent cooling to the crystallisation temperature and room temperature, were analysed.

4.3 Results and Discussion

4.3.1 Particle Size and Morphology

Figure 4.5 shows that the average particle size of UHMWPE used in this work was 125µm. 10% of the UHMWPE particles were larger than 293µm and almost 10% of the particles were less than 46.2µm.

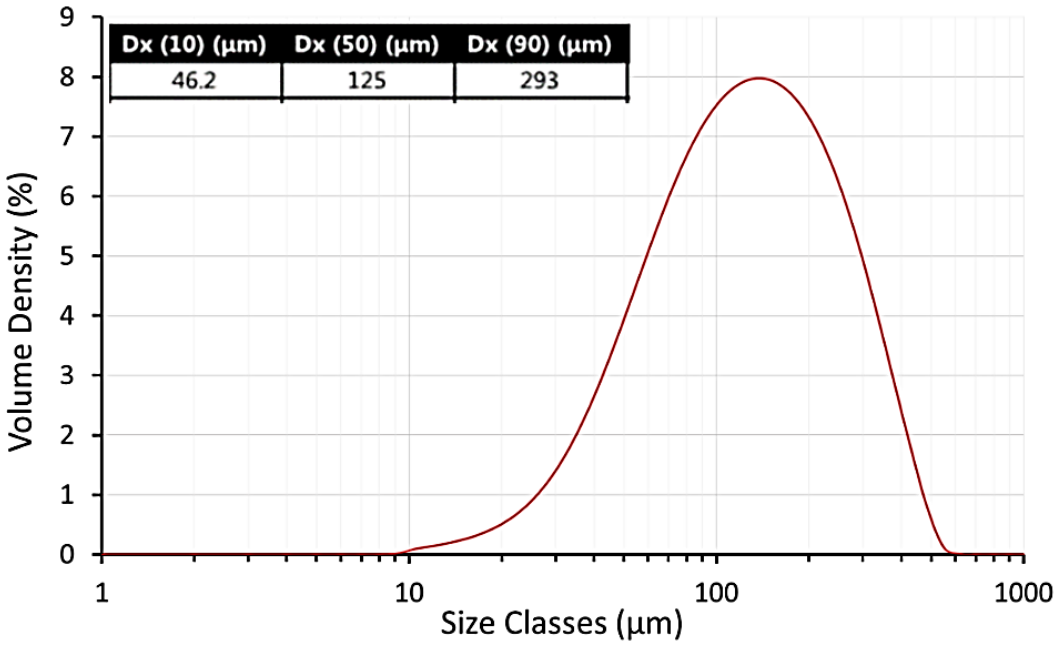

Figure 4.5: Particle size distribution of UHMWPE GUR 2122 powder

SEM examination of UHMWPE powder reveals that the particles are non-spherical in shape with highly agglomerated structure of smaller particles, as shown in Figure 4.6. Fibrils are also exist in the microstructure of the UHMWPE powders.

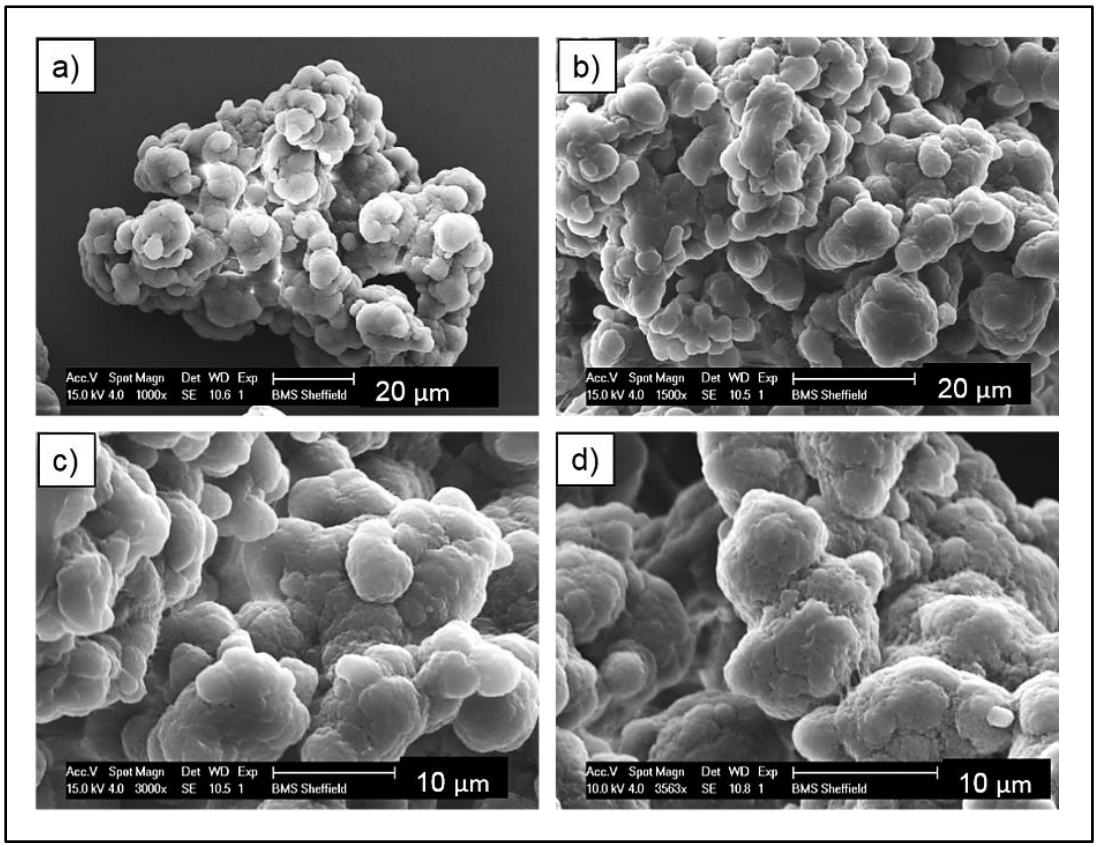

Figure 4.6: SEM images of virgin UHMWPE powder
Magnifications: a) 1000x, b) 1500x, c) 3000x and d) 3500x

UHMWPE particle microstructure is highly complex and from the SEM seems porous. Therefore, the surface structure reduces the ability of the material to pack into regular structures [151].

4.3.2 Density of UHMWPE Powder

The true density of UHMWPE powder was measured by helium gas pycnometer (Micromeritics AccuPyc II 1340, USA) and was found to be 0.954 g/cm^3. The bulk density, tapped density and Hausner ratio, for UHMWPE used in this work, are shown in Table 4.1.

Table 4.1: Densities and Hausner ratio of UHMWPE powder

Bulk density (g/cm^3)	Tapped density (g/cm^3)	Hausner ratio
0.2321 ±0.002	0.3236 ±0.002	1.39 ±0.019

Based on the criteria of distinguishing between cohesive and non-cohesive powder, which was explained in section 4.2.2.2, the Hausner ratio of UHMWPE (GUR 2122) powder was found to be just below 1.4. This result indicates that the powder has decreased flow and is cohesive. This behaviour became evident during spreading and distribution of the powder in the laser sintering machine.

The shape and surface of the powder particles determines the behaviour of the powder [10]. The irregular shape leads to poor powder flow that in turn leads to poor powder deposition and subsequent LS processing difficulties [18]. As discussed in section 4.3.1, SEM examination of UHMWPE powder reveals that the particles are non-spherical in shape with highly agglomerated structure of smaller particles with fibrils also exist in the microstructure of the UHMWPE powders. Angular and point shaped particles show irregular particle formulations within a bulk structure. The irregular rough surface morphology of the particles result in interparticle bridges and internal friction forces [84]. The particles of laser sintering powders should be approximately spherical to induce a free flowing behaviour and ensure the powder is distributed on the part bed, by a blade or a roller, will not be compacted further [10].

4.3.3 Differential Scanning Calorimetry

Figure 4.7 shows very clear distinction between the thermal transitions with a sharp melting point, which is due to the highly ordered crystalline regions in the polymer chains.

The melting (T_m) and the peak of solidification (T_c) temperatures of the UHMWPE were around 141°C and 117°C, respectively. These temperatures were used to help for the determination of the required build temperature for the powder bed (i.e. processing window).

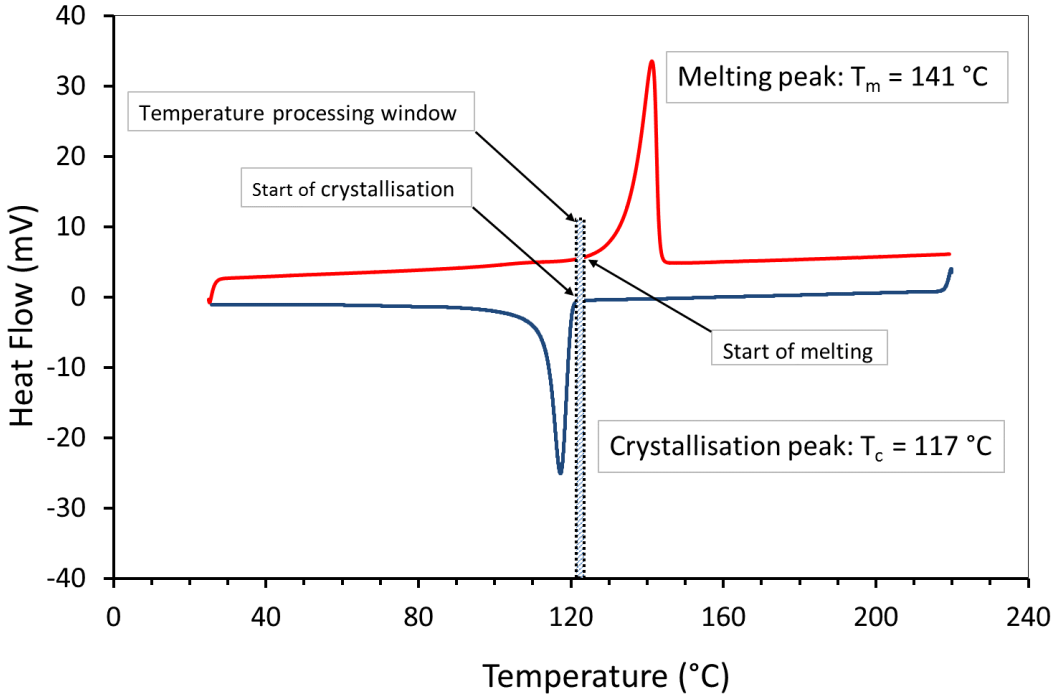

Figure 4.7: DSC curve of first heating cycle of UHMWPE powder (GUR 2122). Heated from 25°C to 220°C at 10°C/min

UHMWPE processing window, which is the deference between the onset melting temperature and the onset crystallisation temperature [164], appears to be narrow (ΔT < 5°C) and this could cause a substantial problem if there are small fluctuations in bed temperature or laser power. However, approximate part bed temperature was defined by observing the powder flow across the powder bed as it was spread by the blade. Previous experiments with UHMWPE, observed similar behaviour where the processing window to achieve laser sintered parts was narrow. The parts curl and the build fail if precise process parameters, laser power combined with correct bed and feed temperatures, were not implemented [61].

4.3.4 Influence of Cooling Rate on Super-cooling Window

Laser sintering is a slow process, in which the temperature of the powder bed is held close to the melting point for a long time, and new pre-heated layers are spread on top of the previously sintered layers [83]. In this work, an attempt was made to investigate the melting and crystallisation behaviour of

UHMWPE and simulate LS process by DSC measurements. Using different cooling rates could show that crystallisation has a high time dependency. Therefore, several heating and cooling rates (1, 5, 10 and 100°C/min) were used (Table 4.2) and the resulting data were analysed. The previous thermal history of the virgin powder was cleared by the first heating and cooling cycles and therefore these cycles were not considered in this analysis including the 6th cycle, which was identical to 2nd cycle, and the 5th cycle, in which the DSC curve was out of scale to be presented in the same graph.

Table 4.2: DSC experiment protocol to examine the effect of cooling rate on super cooling window

Cycle no.	Start (°C)	Dwell (min)	Heating Rate (°C/min)	End (°C)	Dwell (min)	Cooling Rate (°C)	Final (°C)
1	25		10	220	1	10	25
2	25	1	10	220	1	10	25
3	25	1	10	220	1	5	25
4	25	1	10	220	1	1	25
5	25	1	10	220	1	100	25
6	25	1	10	220	1	10	25

Figure 4.8 shows that the crystallisation starts at a higher temperature with lower super-cooling of the molten UHMWPE material as the cooling rate is reduced. A considerable change in the temperature of the crystallisation was observed with a difference of 5°C between a cooling rate of 1°C/min and 10°C/min. The sintering of UHMWPE can be influenced significantly, as the difference between melting and crystallisation peaks is narrow at lower cooling rates. In addition, a significant change in the width of the peaks during the control cooling steps was observed. The peak width increases with the

increase in cooling rate, suggesting an increase in the distribution of crystal lamella size [16].

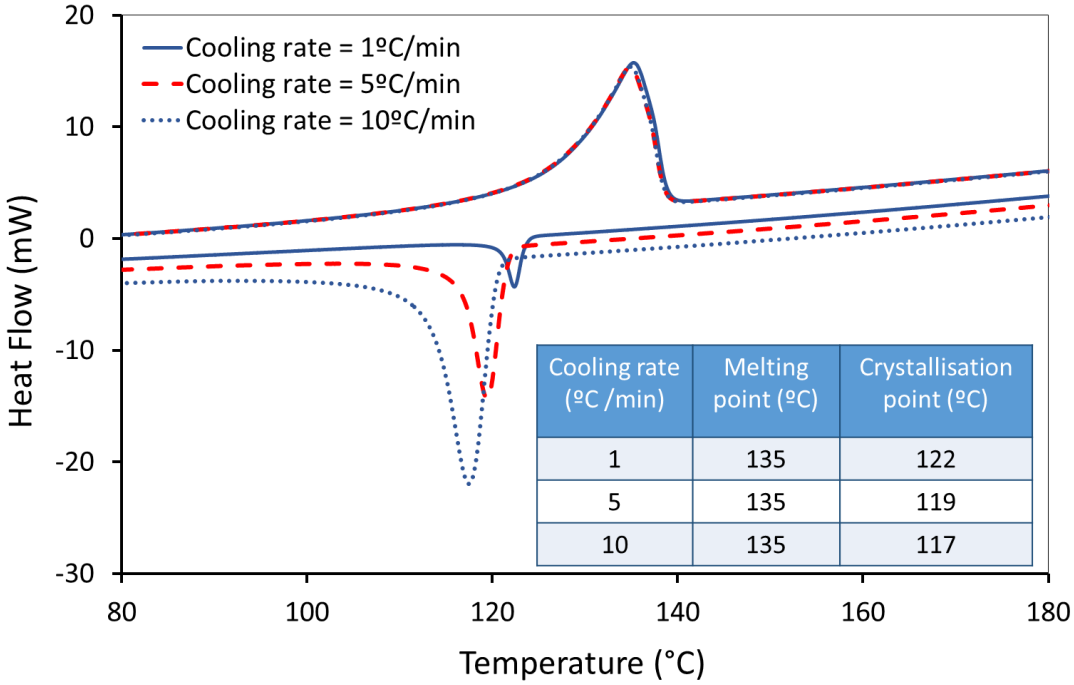

Cooling rate (ºC /min)	Melting point (ºC)	Crystallisation point (ºC)
1	135	122
5	135	119
10	135	117

Figure 4.8: DSC curves of UHMWPE at different cooling rate
The same sample was heated from 25°C to 220°C at 10 /min.

4.3.5 Thermogravimetric Analysis

The TGA analysis shows a stable weight up to about 400°C, as shown in Figure 4.9. At higher temperatures, thermal degradation of the UHMWPE begins with the onset appearing at approximately 478°C. Therefore, UHMWPE should be sufficiently stable and degradation should not occur during the sintering process. The result indicates that no trace or a release of any significant volatile solvent residue that can be detected but a limited amount of residue remaining at 513°C (1.0%) was observed.

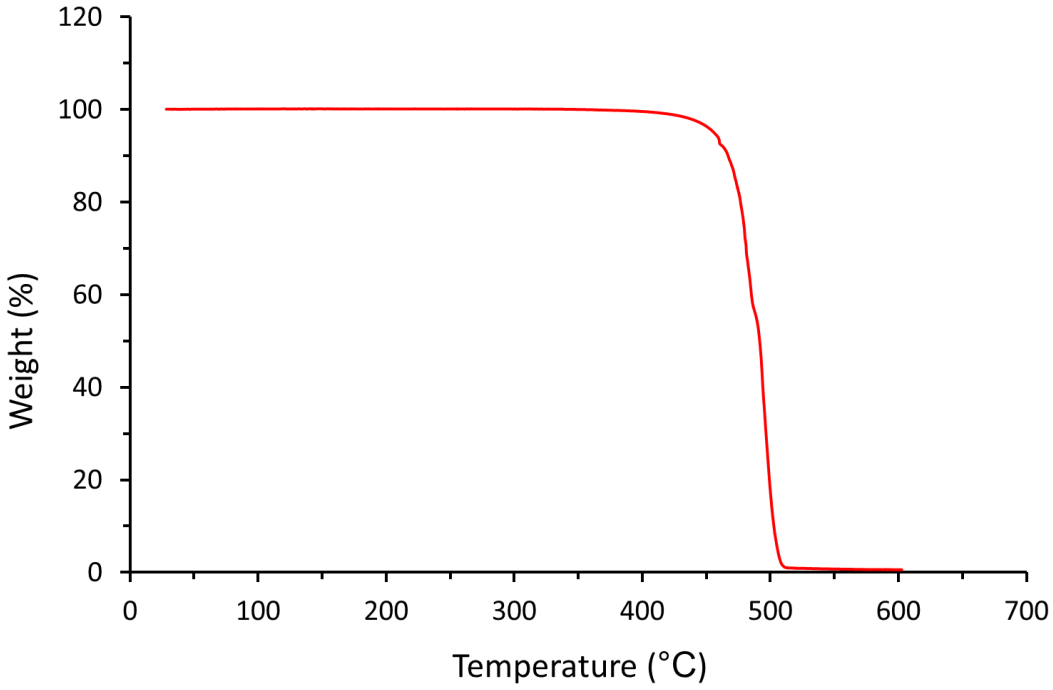

Figure 4.9: TGA analysis of UHMWPE

4.3.6 X-Ray Diffraction Analysis

The XRD spectrum for UHMWPE powder is shown in Figure 4.10.

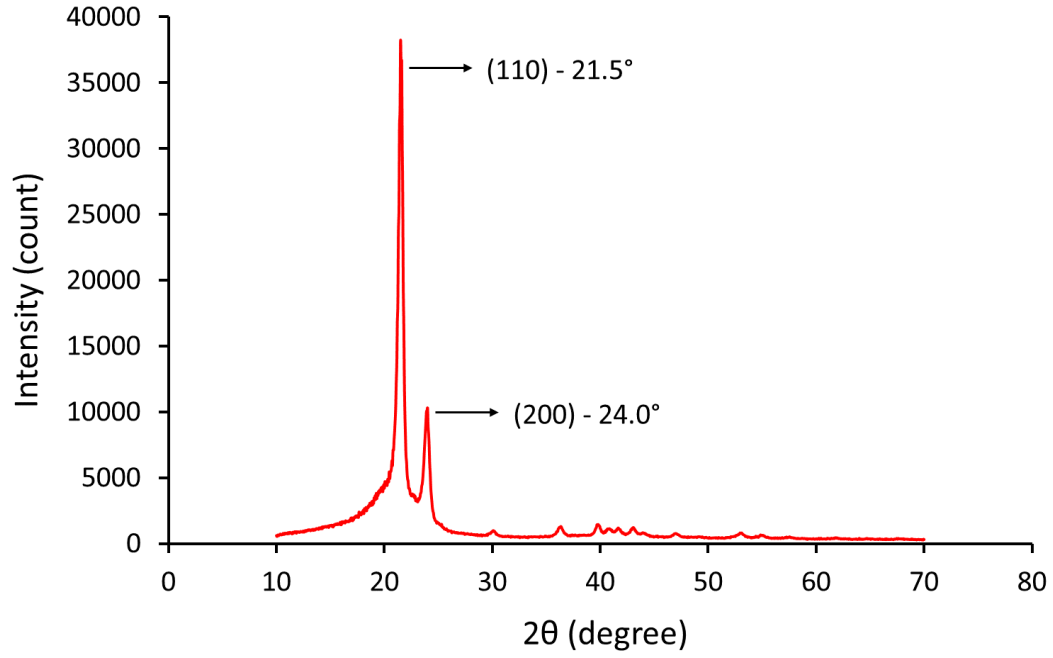

Figure 4.10: XRD pattern of UHMWPE powder

The result shows that UHMWPE is a semi-crystalline polymer which consists of two phases; an amorphous phase and an orthorhombic crystalline phase with two distinctive sharp peaks at 2θ = 21.5° (110) and at 2θ = 24° (200) [165].

4.3.7 Degree of Crystallinity

The degree of crystallinity of UHMWPE powder was determined using DSC and XRD methods and the result is shown in Table 4.3.

Table 4.3: Degree of crystallinity (X_C) of UHMWPE powder

Degree of Crystallinity (%)	
DSC *	XRD
57.45 ±3.70	67.80 ±8.50

** Crystallinity was measured from the first heating cycle.*

The results show that the crystallinity value obtained by XRD is higher compared to DSC measurements. This variation was expected since the crystallinity obtained via DSC analysis is measured under a given thermal profile (i.e. dynamic measurement), where the crystallinity obtained via the XRD analysis is measured under a constant temperature. In addition, the DSC provides data from the bulk of the sample under test where XRD is a surface measurement [166] and in some cases below the surface over a depth of 1 mm.

4.3.8 Effect of Cooling Rate on Crystallisation

Referring to section 4.3.4, the laser sintering process was simulated by DSC to investigate the effect of cooling rate on crystallisation behaviour. Cooling rates of 1, 5, 10 and 100°C/min were used (Table 4.2) and the resulting data were presented in Figure 4.11. The result in Figure 4.11 shows that with the increase in the cooling rate, the crystallisation temperature is decreased. This indicates that the crystallisation was faster for higher cooling rates, implying the nucleation-dominated process [16]. A slower cooling rate causes the crystallisation of the UHMWPE matrix to be neater (i.e. more perfect crystals)

and as a result the final crystallinity of UHMWPE is improved [167]. However, during these measurements different cooling rates did not alter the degree of crystallinity of UHMWPE significantly. This behaviour is related to the extremely long molecular chains in UHMWPE.

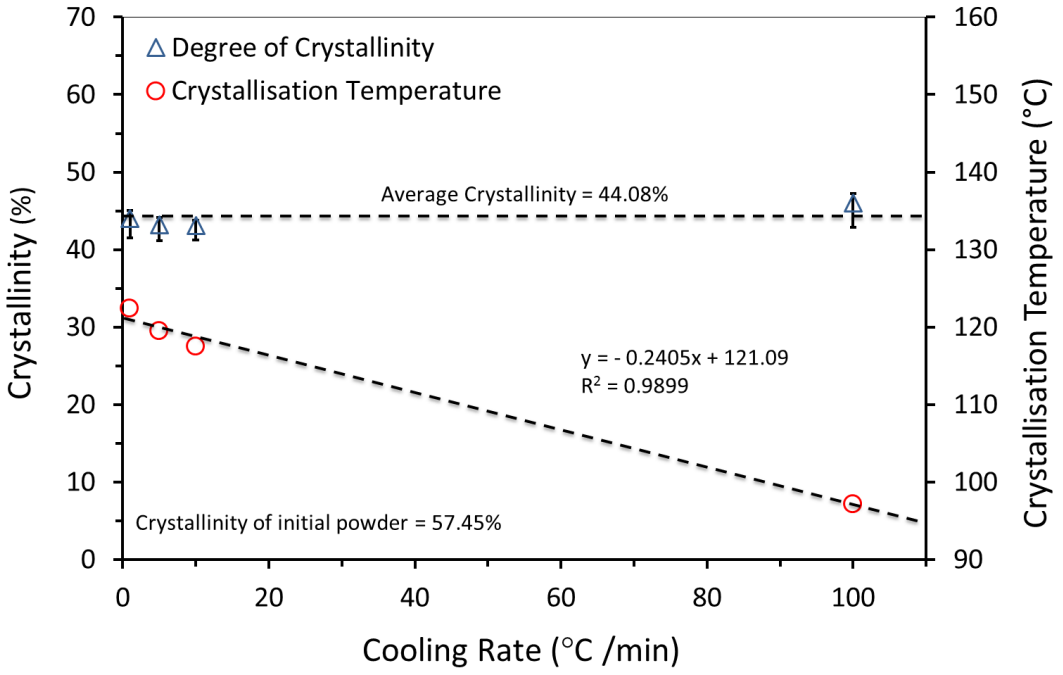

Figure 4.11: Influence of cooling rate on the crystallisation of the UHMWPE

4.3.9 Effect of Heating on Crystallisation

Many factors significantly affect the properties of laser sintered parts, such as laser energy and powder bed temperature, which influence the degree of crystallinity [168]. Crystallinity of polymers depends on the thermal history, which is a widely observed behaviour of semi-crystalline thermoplastics.

Super-cooling occurs when the polymer is cooled below it melting point, here crystallisation is thermodynamically possible but kinetically restricted. A high super-cooling, results in highly folded crystals, low super-cooling less folding occurs. Samples were heated to 117.5°C, at heating rate of 10°C/min and held there for 15 min. The heating then continued to 220°C, and then samples were cooled to 25°C at 10°C/min. The same procedure was repeated for the 2nd and

3rd cycles with the first heating temperature set to 120°C and 125°C respectively. Table 4.4 shows the DSC experiment protocol. First cycle was used to remove any thermal history.

Table 4.4: DSC experiment protocol

Cycle no.	1st Heating (°C)	Hold time (min)	2nd Heating (°C)	Dwell (min)	Cooling (°C)
1	25	1	220	1	25
2	117.5	15	220	1	25
3	120	15	220	1	25
4	125	15	220	1	25

Figure 4.12 shows that the degree of crystallinity of UHMWPE increased with increased super-cooling. In laser sintering, the part bed is preheated and kept at a constant temperature (i.e. part bed temperature) during the process. But this temperature increases when the laser is selectively applied to heat the powder above the melt temperature. Therefore, higher bed temperature results in increased energy input and this impacts on the properties of the parts produced.

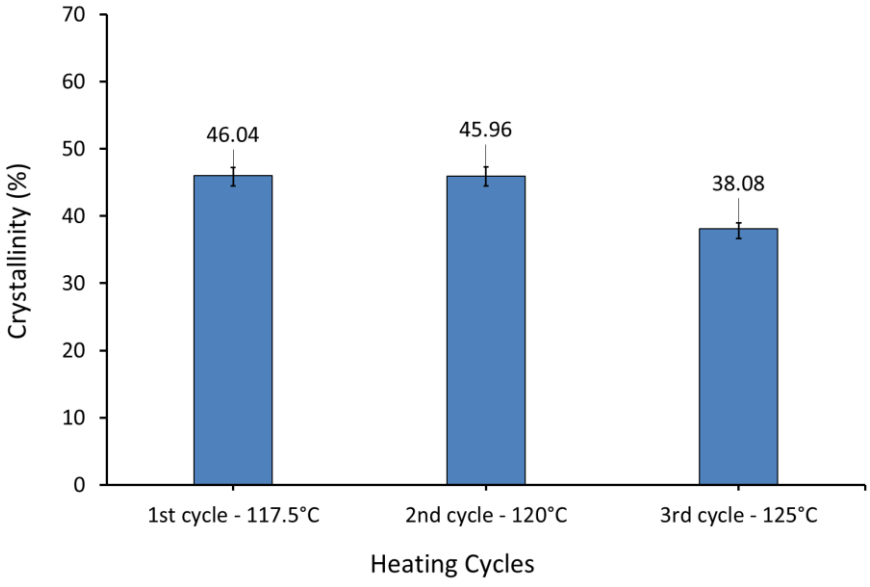

Figure 4.12: Influence of heating on the crystallisation of the UHMWPE

4.3.10 Hot Stage Microscopy

The optical images of the UHMWPE particles during coalescence are presented in Figure 4.13. A series of time lapse images of a number of UHMWPE particles sintering together on a hot stage.

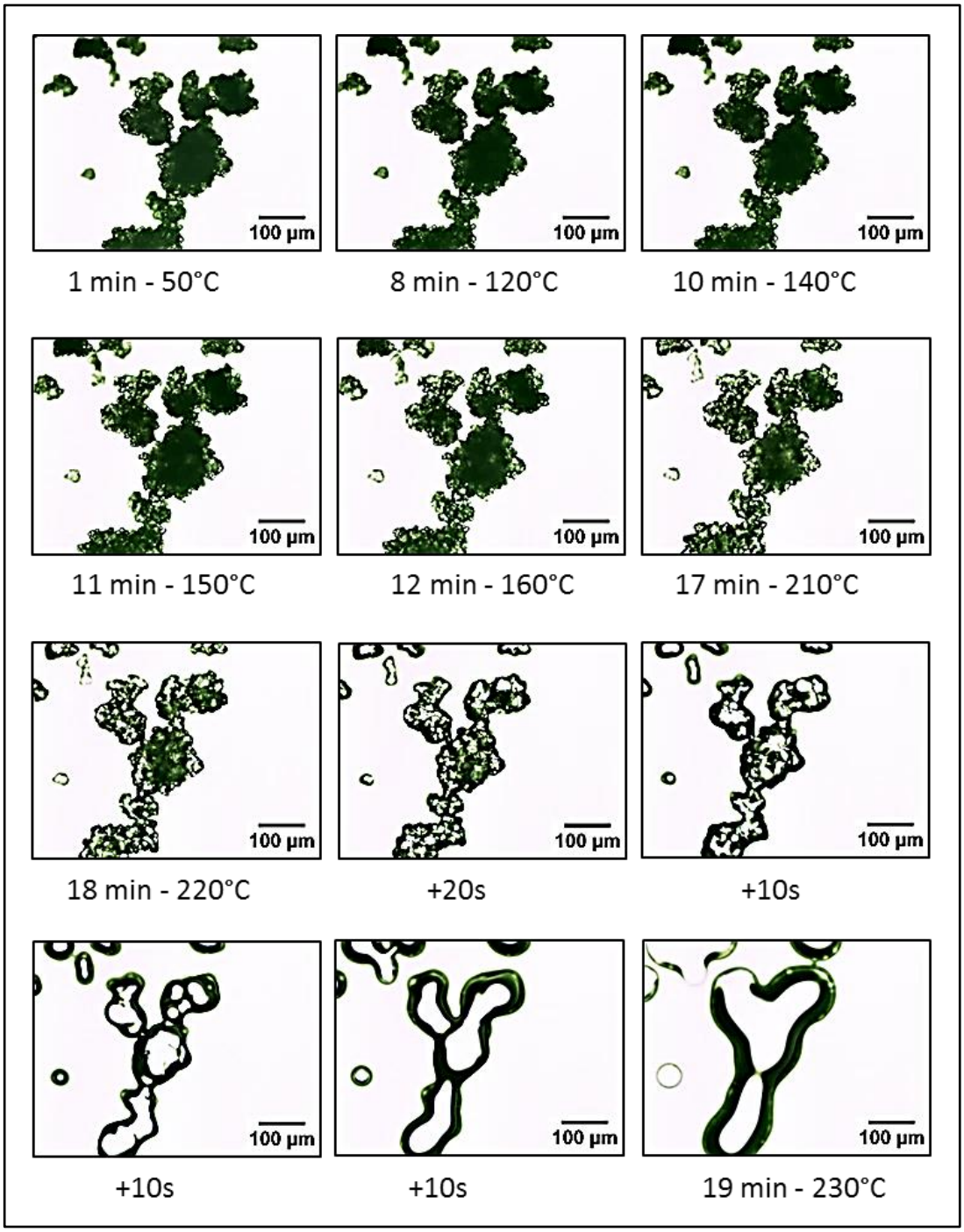

Figure 4.13: Hot stage microscopy images of UHMWPE

The images suggest that the particles morphology of UHMWPE did not change and the structures preserved their confirmations even after the hot stage reached the melting temperature of UHMWPE (i.e. 141°C). Andjelić *et al.* suggested that the chain location remains un-changed, even after melting. They also suggested that the UHMWPE lamellae contains a high concentration of entangled tie macromolecules in the amorphous region. The formation of these stable entanglements may prevent the conformational changes of the chains from crystalline phase into amorphous phase [16].

Noticeable changes were observed at temperatures above 160°C and as the sintering progresses the particles coalesced completely and become translucent as the crystalline phase becomes amorphous.

To confirm the above observation, a DSC test was carried out on a sample of powder with an open pan. The start temperature of 25°C and an end temperature of 150°C were used with a heating and cooling rates of 10°C/min.

The result of the test, shown in Figure 4.14, clearly confirms that the UHMWPE powder was melted when the temperature reached 150°C.

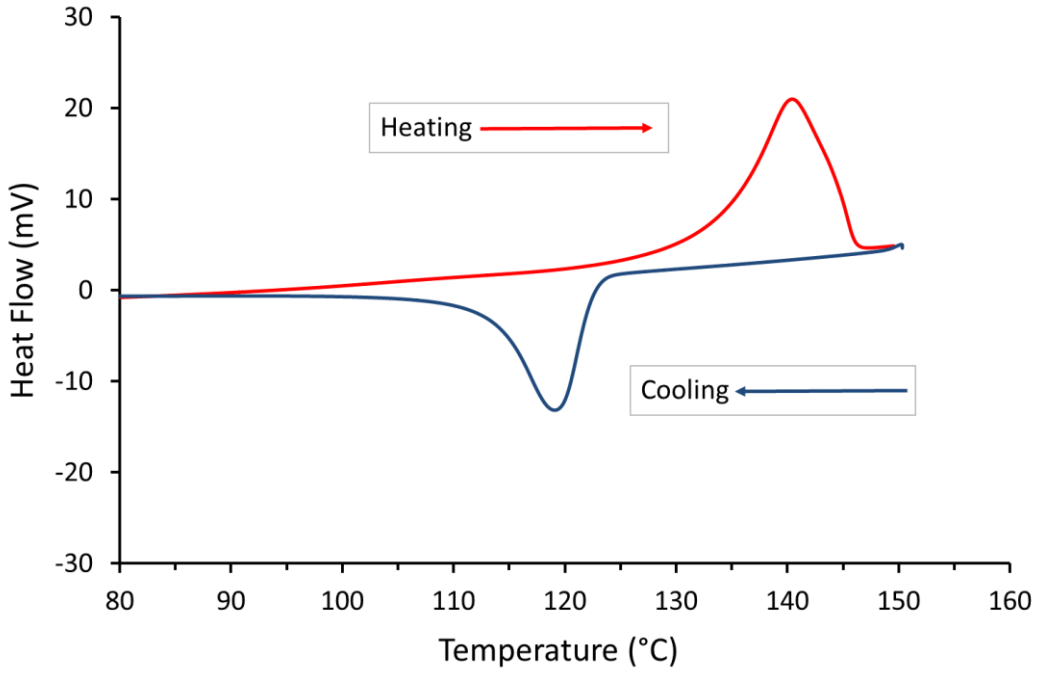

Figure 4.14: DSC curve of UHMWPE powder heated to 150°C

After the DSC test was completed the powder pan was examined visually and it appeared that the powder looked like a frozen powder without any sign of flow and the structures of the powder preserved their confirmations.

The same sample was then examined under the SEM and the result is shown in Figure 4.15. The images clearly show that the particles are coalesced between each other and the fusion was evident at 150°C. This result confirms the findings form the hot stage microscopy test.

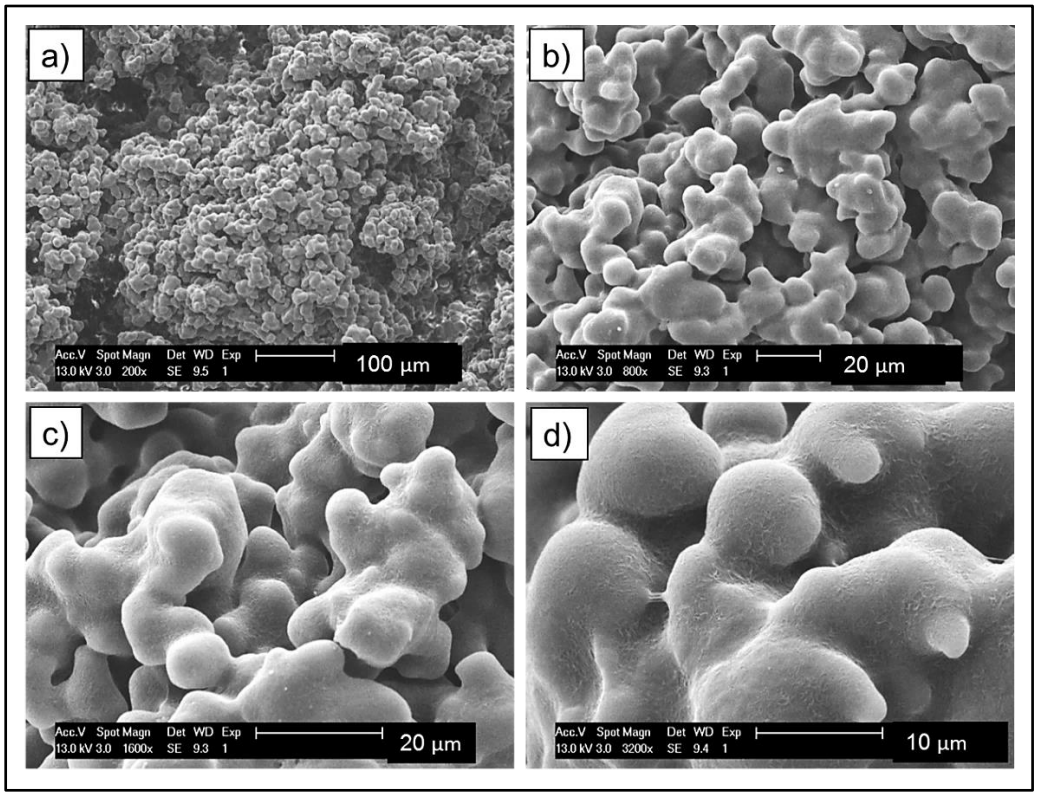

Figure 4.15: SEM micrographs of UHMWPE powder heated to 150°C and cooled down to room temperature.
Magnifications: a) 200x, b) 800x, c) 1600x and d) 3200x

The sintering of UHMWPE is not governed by the viscous flow but it is affected by its unique particle morphology. Therefore, Frenkel-Eshelby model would underestimate the sintering rate of UHMWPE and leads to a substantial deviations from the experimental result [15].

The development of crystallisation within the UHMWPE was followed using a polarising light filter. Hot stage images captured during the crystallisation of

UHMWPE are shown in Figure 4.16. A very characteristic pattern was observed, which consists of a large number and well-defined banded of spherulites. Maltese cross-pattern of crystalline regions, small and large spherulites, are clearly defined in UHMWPE structure.

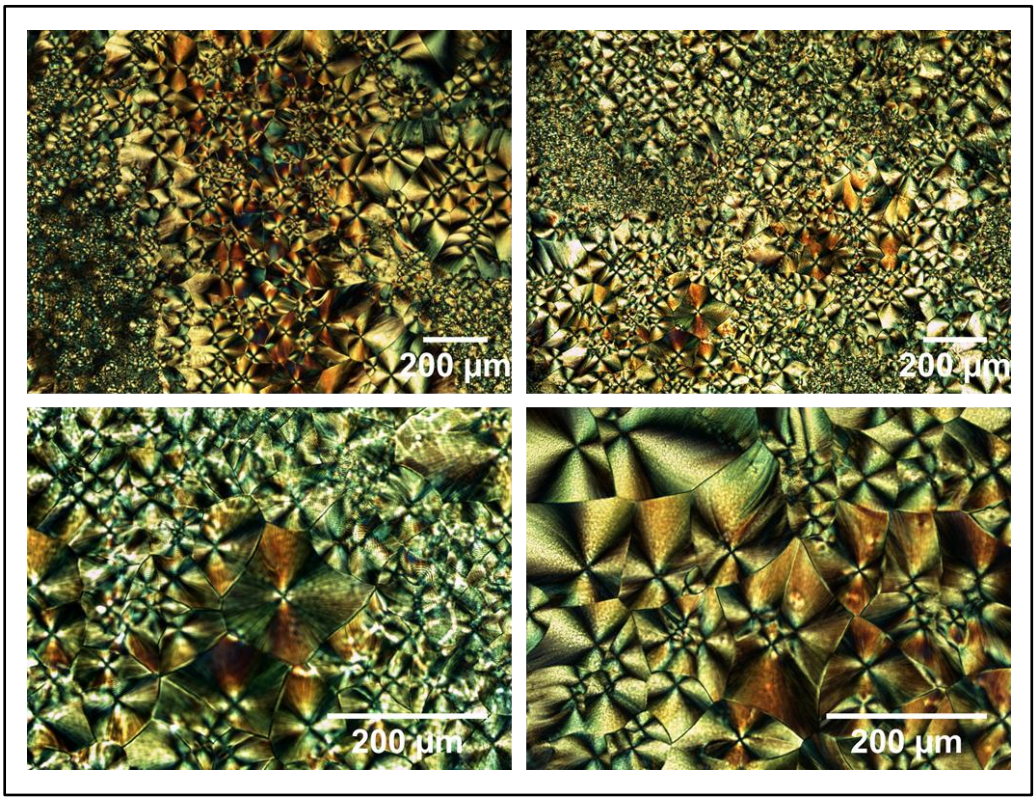

Figure 4.16: Polarised light microscopy images of UHMWPE

Spherulites are formed from distinct nuclei during solidification. When the undercooling is increased below the melting point, the number of these nuclei is increased. Therefore, when semi-crystalline polymers are cooled quickly, a large number of smaller spherulites are formed all over the microstructure. On the other hand, larger spherulites are formed due to slow cooling [27]. The size of spherulites affects the strength and ductility of the polymer. Semi-crystalline polymers containing small spherulites are normally tougher than those consisting coarse spherulites, which have weak boundaries. It was also suggested that an increase in crystallinity or spherulites size reduces the toughness [169].

4.4 Laser Sintering Trials of UHMWPE

A commercial laser sintering machine (EOS FORMIGA P100, Germany), shown in Figure 4.17, was used to manufacture test samples from UHMWPE (GUR 2122) powder. Virgin powder was used for all builds.

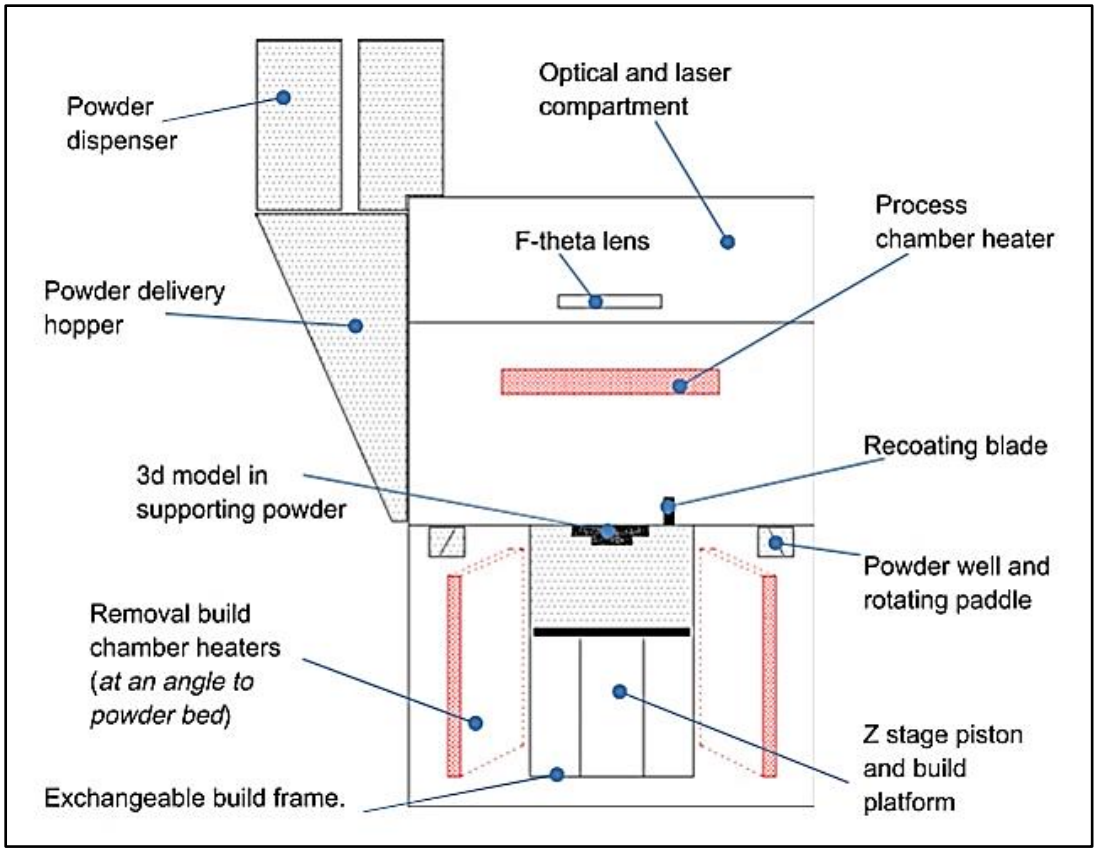

Figure 4.17: Schematic of the EOS P100 system [81]

Before sintering the test samples, a range of processing conditions were trialled so that suitable parameters can be obtained for processing the parts. In the initial trials, combinations of laser powers of 13, 17, 18, 23 and 29 watts and laser scan speed at 1500 and 2500 mm/s with a range of powder bed temperatures from 130 to 145°C at five degree intervals and removal chamber temperature at 125, 130 and 135°C were attempted. Laser count of 1 (single scan) and 2 (double scan) and hatch spacing of 0.15 and 0.25 mm were also trialled. A bed temperature of 142°C and removal chamber temperature of 135°C was found to be suitable in terms of powder spreading and multilayer

sintering. However, powder removal and cleaning of the parts were difficult. Therefore, low levels of laser powers of 6, 8, 10 and 12 watts were attempted and were found to be suitable in terms of ease of powder removal, cleaning, spreading of powder and reducing the effect of curling.

Although processing UHMWPE using laser sintering was challenging (due to a narrow process window), good parts were fabricated successfully at various laser power. Figure 4.18 shows different UHMWPE parts were produced with good definition and good mechanical properties.

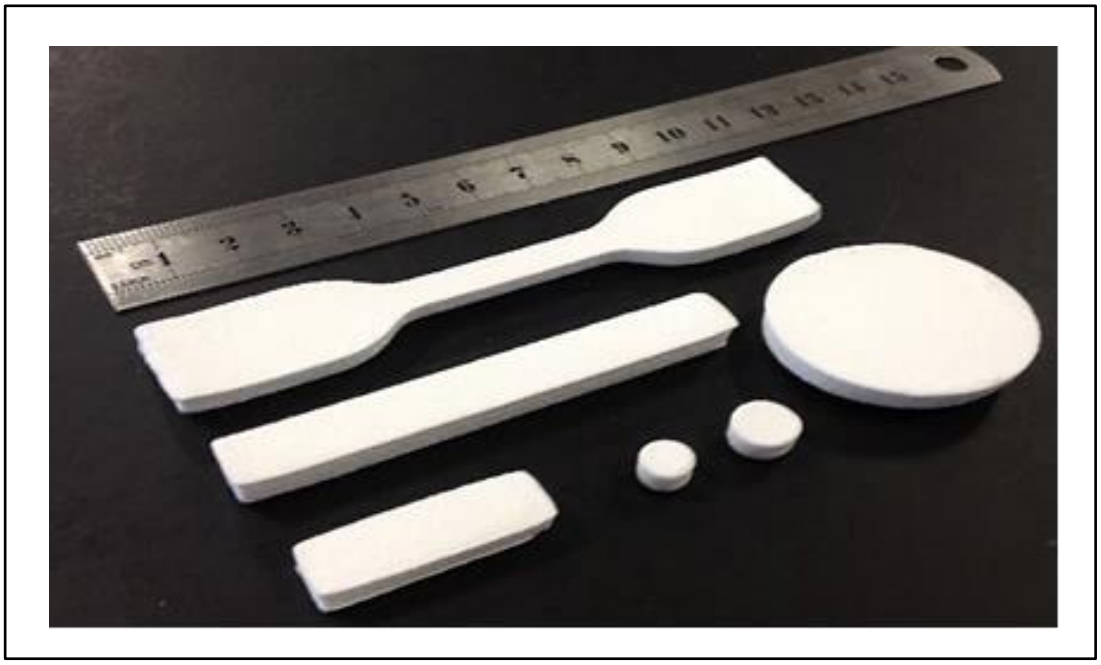

Figure 4.18: UHMWPE parts produced by LS machine EOS P100

The results show a substantial improvements in properties and process parameters used compared with the previous work on UHMWPE using laser sintering carried out by Goodridge *et al.* [61].

4.5 Summary of UHMWPE Powder Characterisation

The aim of the characterisation process is to gain a better understanding of the material requirements and provide a detailed insight on whether UHMWPE can be a suitable material for laser sintering.

UHMWPE particles are non-spherical in shape with highly agglomerated structure of smaller particles with fibrils also exist in the microstructure of the UHMWPE powders. The particles of laser sintering powders should be at approximately spherical in order to induce a free flowing behaviour. The Hausner ratio of UHMWPE powder was found to be just below 1.4 indicating that the powder has decreased flow and is close to being cohesive which is not favourable for laser sintering.

DSC result shows that UHMWPE has sharp thermal transitions indicating areas of crystallinity. Above the melting temperature, UHMWPE has transformed and a neck growth occurred. But, UHMWPE requires a longer exposure before the neck formation and coalescence of the particles. This behaviour was confirmed by the hot stage microscopy. The DSC curve shows that the processing window of UHMWPE is narrow and this could cause a substantial problem during laser sintering process if small fluctuations in bed temperature or laser power occurs.

In laser sintering, the laser provides energy to melt the polymer but applying high energy could damage and degrade the polymer chain. TGA analysis was used to examine the degradation of UHMWPE and assess the window between the melting and degradation of UHMWPE. The result clearly shows that the temperature window is wide enough and favourable for laser sintering in terms of material degradation.

It is commonly known that many of the physical and mechanical properties of polymers are affected by the degree of crystallinity, such as Young modulus, yield stress, fatigue, and shrinkage. X-ray diffraction spectroscopy was used in

this study to verifying measurement of the degree of crystallinity with DSC. The degree of crystallinity found to be 57.45 ±3.70 and 67.80 ±8.50 as measured by DSC and XRD respectively. The result shows that the crystallinity value obtained by XRD is higher compared to DSC measurements.

The effect of cooling rate on the temperature and degree of crystallinity was investigated. The result shows that with the increase in the cooling rate, the crystallisation temperature is decreased. However, different cooling rates did not alter the degree of crystallinity of UHMWPE significantly. This behaviour is very much affected by the extremely long molecular chains in UHMWPE.

UHMWPE parts were fabricated successfully at various laser power with good definition and good mechanical properties.

Chapter 5 Mechanical Behaviour and Material Characteristics of Laser Sintered UHMWPE

5.1 Abstract

The influence of laser energy density on the physical and mechanical properties of UHMWPE parts produced by laser sintering were investigated. The mechanical properties of laser sintered UHMWPE parts were evaluated by performing both flexural and tensile tests. Relative density and dimensional accuracy of the parts were also evaluated in order to examine the effects of laser power on these properties.

The flexural properties of the sintered UHMWPE parts were evaluated by performing flexural three point bending tests and were compared in terms of flexural strength, flexural modulus and ductility (deflection).

Tensile properties, such as Ultimate Tensile Strength (UTS), Young's Modulus and elongation at break were evaluated. The fracture surface of the tensile test specimens was examined by electron microscopy.

The flexural test results show that flexural strength, modulus and ductility are influenced by laser energy density. Part dimensions and bulk density are also influenced by laser energy density.

The tensile test results show that within a laser energy density range of 0.016-0.032 J/mm^2 (Laser power of 6–12 watts) there appears to be an optimum where tensile strength and relative density reach a maximum, and ductility increases with laser energy density. UTS up to 2.42 MPa, modulus up to 72.6 MPa and elongation at break up to 51.4% were observed.

5.2 Manufacture of Flexural Test Parts

Laser sintered parts with a length of 80 mm, width of 10 mm and thickness of 4 mm (according to ISO 178), were built in x-y orientation with the long axis parallel to the x-axis, width parallel to the y-axis and thickness parallel to z-axis (i.e. build direction) as illustrated in Figure 5.1.

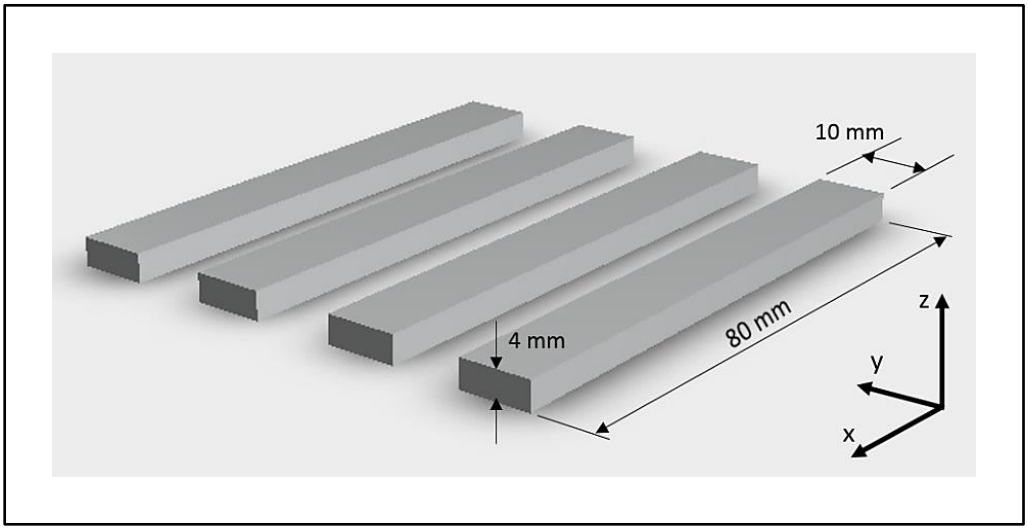

Figure 5.1: Schematic of the orientation of the parts in the build bed

In order to examine the effect of laser power on the flexural properties of the laser sintered UHMWPE parts, laser powers of 6, 8, 10, 12 watts were selected for processing. All other parameters were kept constant as listed in Table 5.1. After building, all the parts were left in the machine for an hour and then were removed and left cooling in the laboratory for 24 hours. The parts were then air blown to remove the un-sintered powder.

Table 5.1: Laser sintering parameters

Scan speed (mm/s)	Hatch spacing (mm)	Powder bed temperature (°C)	Removal chamber temperature (°C)	Layer thickness (mm)	Laser count
2500	0.15	142	135	0.1	2

Results from other work indicated that the microstructure, physical, mechanical properties and quality of the laser sintered parts are fundamentally affected by laser power, laser speed and hatch spacing which are directly related to the amount of energy applied on the powder surface in the part bed. These parameters are seen as a function of energy density and for the purposes of this work, the incident energy density is taken to be [12]:

$$ED = \frac{LP}{SS \times HS} \tag{8}$$

Where ED is the Energy Density (J/mm^2), LP is the Laser Power (watts), SS is the Scan Speed (mm/s) and HS is the Hatch Spacing (mm).

Laser sintered UHMWPE parts were successfully manufactured using various laser powers. Sintered parts were manufactured with significant sintering between particles and layers and good mechanical properties (Figure 5.2).

Figure 5.2: Sintered part of UHMWPE fabricated using 10 watts laser power

5.3 Density of Laser Sintered Parts

5.3.1 Methodology

The bulk density of laser sintered parts was determined using a volumetric method, which is defined by the mass of the laser sintered parts per unit

volume. The mass of the samples was determined by weighing the samples using a digital balance and the volume of the samples was determined using Vernier calliper measurement of dimensions.

The samples for density measurements were prepared by cutting one of the untested flexure test sample from each set, along the width with a razor blade in to approximately 10 mm length. Skeletal density (density excluding pores) of sintered samples was determined using Helium Gas Pycnometer (Micromeritics AccuPyc II 1340, USA).

Density may also be expressed as relative density, which is defined as the ratio of the bulk density of the parts to the density of the material composing the parts (i.e. theoretical density or true density of the powder). A sample which has 80% relative density will have 20% porosity. The relative density was determined by the following equation:

$$\rho_{Relative}(\%) = \frac{\rho_{Bulk}}{\rho_{True}} \times 100 \qquad (9)$$

In this work, the true density of UHMWPE powder was found to be 0.954 g/cm³ as measured by helium gas pycnometry.

5.3.2 Results

In laser sintering, the powder particles are sintered together by heat supplied by a laser and therefore the part density strongly depends on the energy density as provided by the laser [32]. The mass density values are shown in Table 5.2 and the influence of laser energy density on the mass density of the sintered parts is presented in Figure 5.3, Figure 5.4 and Figure 5.5.

Table 5.2: Densities of laser sintered UHMWPE parts

Laser Power (watts)	Laser energy density (J/mm²)	Bulk density (g/cm³)	Skeletal density (g/cm³)	Relative density (%)
6	0.016	0.3353	0.9425	35.15 ±0.49
8	0.021	0.3682	0.9436	38.59 ±0.10
10	0.027	0.3748	0.9440	39.28 ±0.06
12	0.032	0.3550	0.9431	37.21 ±0.71

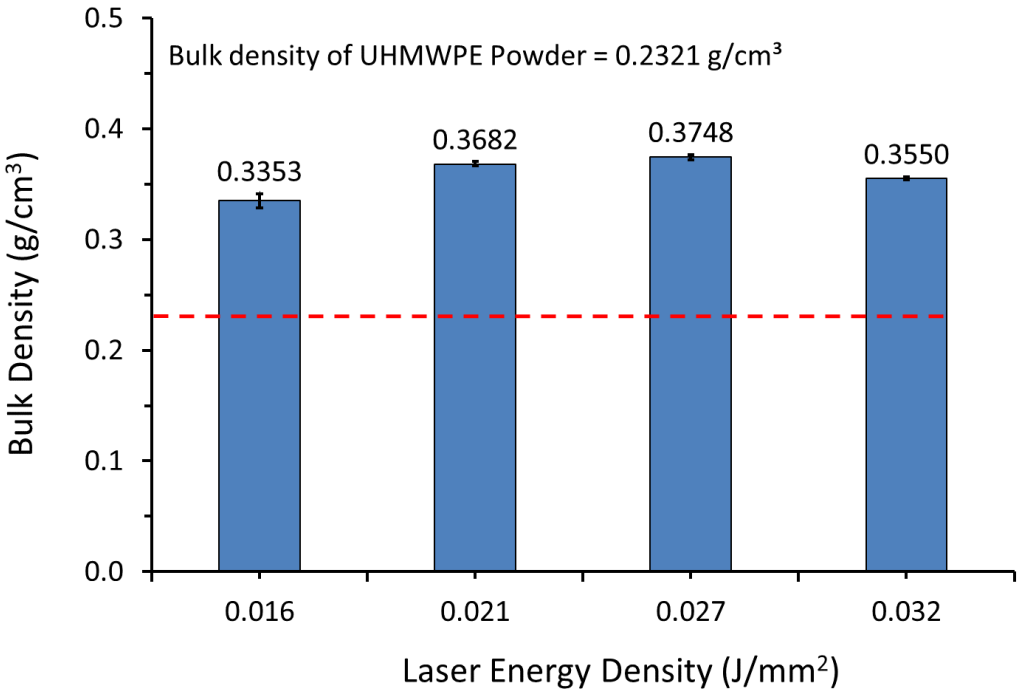

Figure 5.3: Average effect of energy density upon bulk density of UHMWPE parts

Laser sintered parts have achieved a bulk density in a range between nearly 0.34 – 0.38 g/cm^3 which is higher than the powder bulk density of 0.23 g/cm^3. On the other hand, the effect of energy density on skeletal density did not show any significant changes but all samples fell slightly below the true density of the powder measured by helium gas pycnometry.

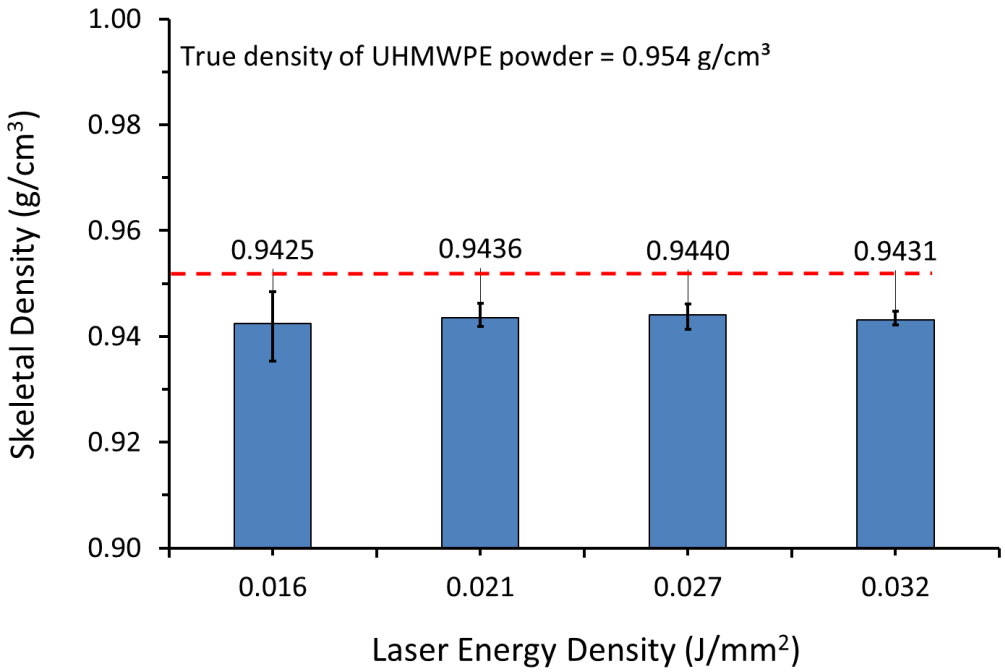

Figure 5.4: Average effect of energy density upon skeletal density of UHMWPE parts

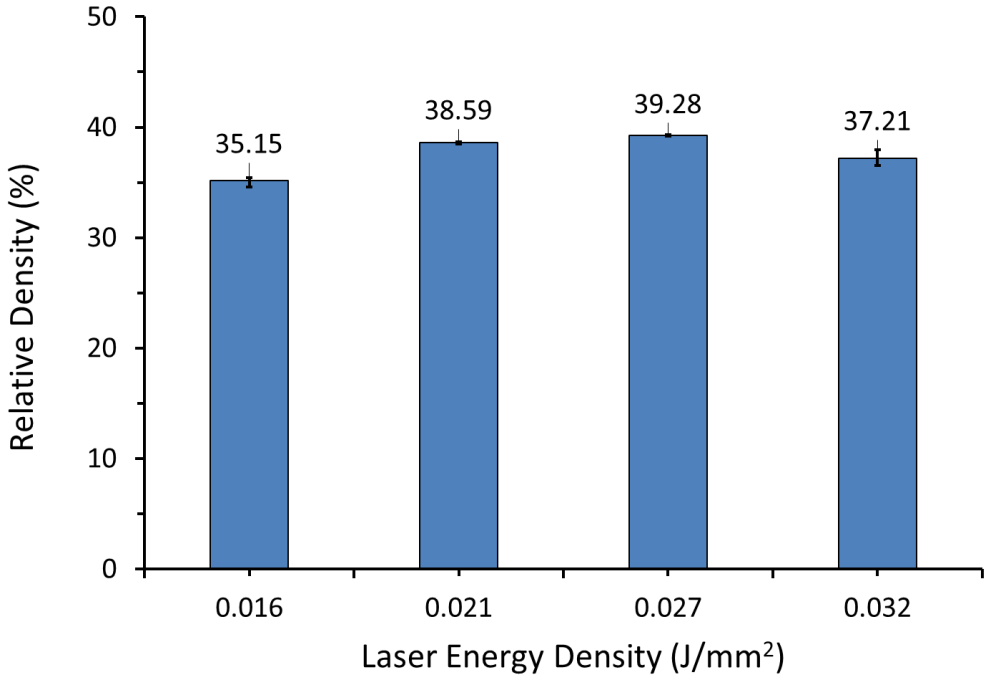

Figure 5.5: Average effect of energy density upon relative density of UHMWPE parts

A relative density of around 35% was achieved, with a laser energy density of 0.016 J/mm^2 (LP=6 watts). The peak relative density value of around 39% was achieved when laser energy density was maintained at 0.027 J/mm^2 (LP=10 watts). However, the relative density slightly decreased to around 37% when the laser energy density increased to 0.032 J/mm^2 (LP=12 watts). With a high energy density, thermal volatilisation of polymer can be more severe and the mass of parts decreased [33], which decreases the density of the parts indicating an increasing of porosity. Further increase in energy density would cause further reduction in density due to increased polymer degradation and expansion of the voids by trapped gases. In general, a low relative density of the UHMWPE fabricated parts has been observed for all sintered parts which indicates a high number of pores have been developed by the laser sintering process.

5.4 Part Dimensional Accuracy and Shrinkage

5.4.1 Methodology

To examine the effect of energy density on the dimensions of the laser sintered parts, three different measurements (length, width and thickness) of the parts were taken. Three individual measurements of each dimension were taken and then an average value was generated for each part. Four laser sintered parts were used for each set and then an average value for the sample length, width and thickness for each set was obtained. The dimensions were measured using Vernier callipers and compared to the dimensions of the input drawing.

5.4.2 Results

Results of the part dimensions measurements are listed in Table 5.3 and illustrated in Figure 5.6. The investigation shows that the variations in the length and width fluctuated with the energy density. However, the thickness of the sintered UHMWPE parts continually increased with the increasing laser energy density. Shrinkage in length and width was evident and only one single

experiment was there an increase in the width, this was observed at the highest energy density (i.e. 0.032 J/mm^2).

Table 5.3: Average dimensions of laser sintered UHMWPE parts

Laser Power (watts)	Laser energy density (J/mm^2)	Length (mm)	Width (mm)	Thickness (mm)
6	0.016	73.7 ±0.88	9.0 ±0.63	6.4 ±0.16
8	0.021	72.7 ±0.73	9.4 ±0.59	6.6 ±0.09
10	0.027	73.5 ±0.73	9.3 ±0.73	6.7.7 ±0.14
12	0.032	74.0 ±0.56	10.1 ±0.69	6.9 ±0.09

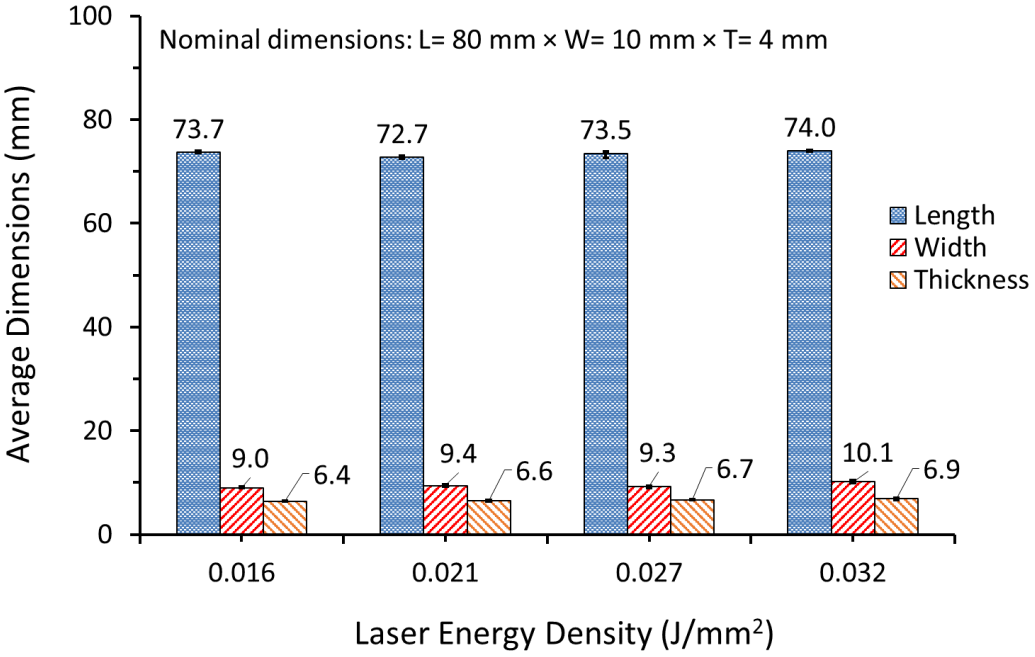

Figure 5.6: Average dimensions of laser sintered UHMWPE parts at different laser energy densities

Dimensional inaccuracy is a common occurrence when laser sintering polymer materials and it is still a major challenge [170]. These typical dimensional variations are due to inhomogeneous shrinkage during the building and cooling processes which leads to distortion in the sintered parts caused by stresses

[171]. Many factors may contribute to shrinkage but the main contributors are materials, process parameters, and the geometries of parts produced [172]. On the other hand, expansion in laser-sintered parts may also occur due to thermal inconsistencies within the powder bed. Goodridge *et al.* [61] highlighted the importance of pre-heating of the powder to avoid the curling phenomenon and also to achieve uniformity across the powder bed when sintering UHMWPE. In their study a Vanguard Laser Sintering machine from 3D System was used. This machine has two powder feed chambers fitted with a temperature controlled heater so that the powder can be heated before being spread across the build area. In our study, EOS P100 machine was used in which there is no facility to pre-heat the powder before the deposition over the build bed. Therefore, high thermal gradients were expected when sintering UHMWPE and hence the high shrinkage.

This shrinkage depends on the temperature at which the part is subjected to laser sintering. It is also affected by the length of time the powder bed retains heat (i.e. cooling), as well as the thickness of the powder layer [171].

It is widely acknowledged that part orientation is a significant factor that influences the dimensional accuracy of the part to be produced [172]. Part orientation has an effect on the material properties such as strength and shrinkage [173]. Goodridge *et al.* [61] produced sintered UHMWPE parts reporting dimensional accuracy of ±0.1mm with the parts being built in a vertical orientation (i.e. length being in the z-axis direction). In our study, the parts were placed in x-y plane and the thickness being in z-axis (Figure 5.1). Hopkinson and Sercombe [174] investigated the accuracy and the effect of part position on the shrinkage during indirect laser sintering of aluminium powder. They found that error in z-axis direction is more clearly apparent than in-plane errors. This phenomenon is known as ‘‘Z-growth” or “bonus-Z”, which occurs as a result of the laser penetrating beyond the specified depth of the part. Z-growth is an undesirable growth of the part in the z-axis which occurs during laser scanning of the first few layers. The powder below the part boundary

melts and sintered leading to out of tolerance part. It has been suggested that the effect of Z-growth could be minimised by reducing the laser energy density for the first few layers to ensure dimensional accuracy of the part [87, 170, 175].

5.5 Flexural Properties

5.5.1 Methodology

Flexural properties were examined by three-point bending tests (Figure 5.7). These samples were designed with a nominal dimension of 80 mm long, 10 mm wide and 4 mm thick. The flexural strength was directly measured using the sintered parts without any post processing other than bead blasting. Three specimens for each set of parameters were tested and the average values were reported. Flexural tests were performed on a Texture Analyser TA500 (TM Lloyd Instruments, UK) fitted with a 500 N load cell. All tests were performed at ambient temperature with a constant cross-head speed of 2mm/min and span length of 40mm.

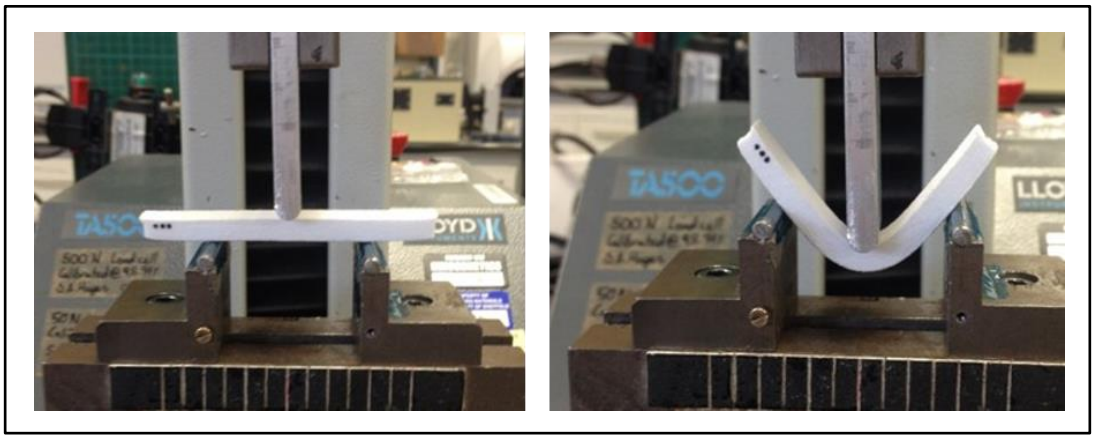

Figure 5.7: Flexural test was performed on a Texture Analyser TA500

After a significant deflection, the test samples take a V-shape, and load begins to drop. If the sample has not already failed and the load dropped to 40% then the test is stopped. In this study none of the sintered parts were ruptured during the three point bending tests but small cracks were observed on the bottom surface of some samples, at the centre-span, but they were not significant.

5.5.2 Results

Flexural strength was measured to evaluate the importance of energy density (i.e. laser power) in laser sintering. The average effect of laser energy densities upon the flexural properties is shown in Table 5.4 including the average values of the maximum flexural stress, strain and modulus. The values of these properties for any given set of samples were obtained by an average of three measurements and expressed as mean ± standard deviation.

Table 5.4: Flexural properties of laser sintered UHMWPE parts

Laser Power (watts)	6	8	10	12
Energy density (J/mm²)	0.016	0.021	0.027	0.032
Max. Load (N)	8.43 ± 1.89	12.67 ± 0.52	14.46 ± 0.60	12.71 ± 0.59
Max. Deflection (mm)	18.83 ± 3.29	22.64 ± 0.36	24.12 ± 1.28	22.87 ± 0.14
Max. Stress (MPa)	1.37 ± 0.30	1.82 ± 0.07	2.12 ± 0.05	1.61 ± 0.03
Max. Strain	0.45 ± 0.08	0.57 ± 0.01	0.60 ± 0.03	0.59 ± 0.02
Modulus (MPa)	32.12 ± 4.78	36.82 ± 3.00	46.86 ± 3.07	36.53 ± 1.67

Figure 5.8 shows the typical flexural stress-strain curve obtained by three point bend test analysis. The result revealed a less ductile behaviour for parts built at low laser energy densities than the parts built at higher laser energy density. The bonding between particles is due to the formation of necks between the particles. As the laser energy density increases these necks become thicker and stonger which leads to a more ductile behaviour with large plastic region in the stress–strain curve. This behaviour has been observed with laser sintering of other polymers [34]. However, at higher laser energy density, 0.032 J/mm^2 (LP=12 watts), showed a decrease in maximum

flexural stress and strain. Gill *et al.* observed this phenomena when processing SiC/Polyamide matrix composites by laser sintering and reported that with increasing energy density from the optimum, degradation of the polymer occurs, which results in a reduction in strength [35].

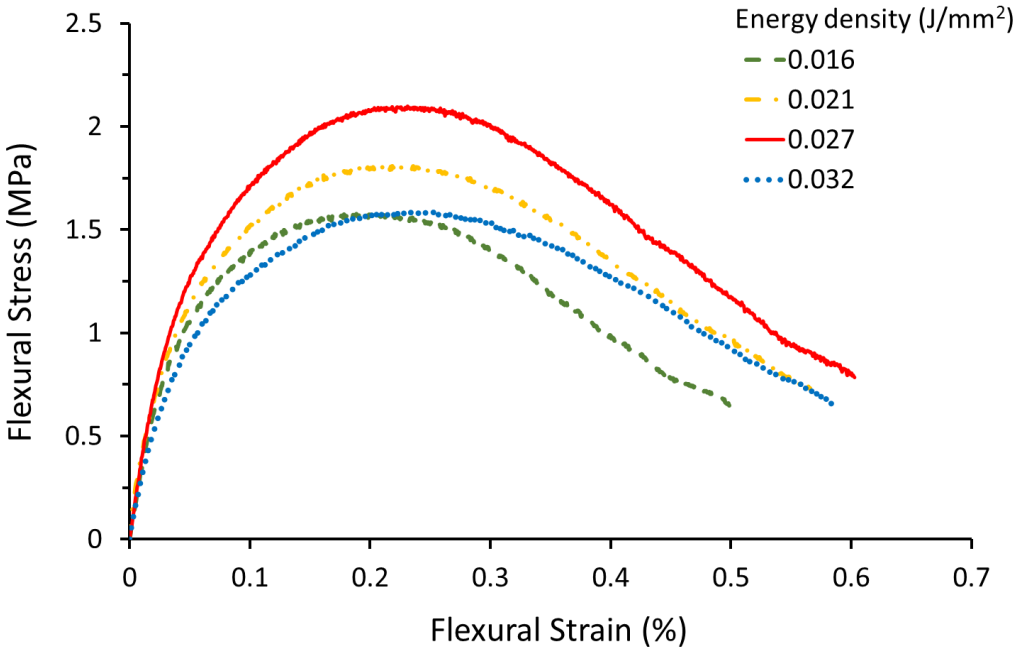

Figure 5.8: Flexural stress-strain curve of UHMWPE parts produced at different laser energy densities

The flexural properties of the sintered parts are presented in Figure 5.9, Figure 5.10 and Figure 5.11. The trend of flexural strength versus energy density is similar to that of the bulk density in Figure 5.3. Higher laser energy density increases the flexural strength of the UHMWPE parts, up to a limit. With increasing bulk density the flexural strength increases. The maximum value of the flexural strength is 2.12 ± 0.05 MPa at energy density of 0.027 J/mm^2 (LP=10 watts). Results show that flexural strength is influenced by laser energy density and good flexural strength is still achieved with energy density of 0.016 J/mm^2 (LP=6 watts). A slightly lower strength is observed at energy density of 0.032 J/mm^2 (LP=12 watts), due to a decrease in bulk density (Figure 5.3).

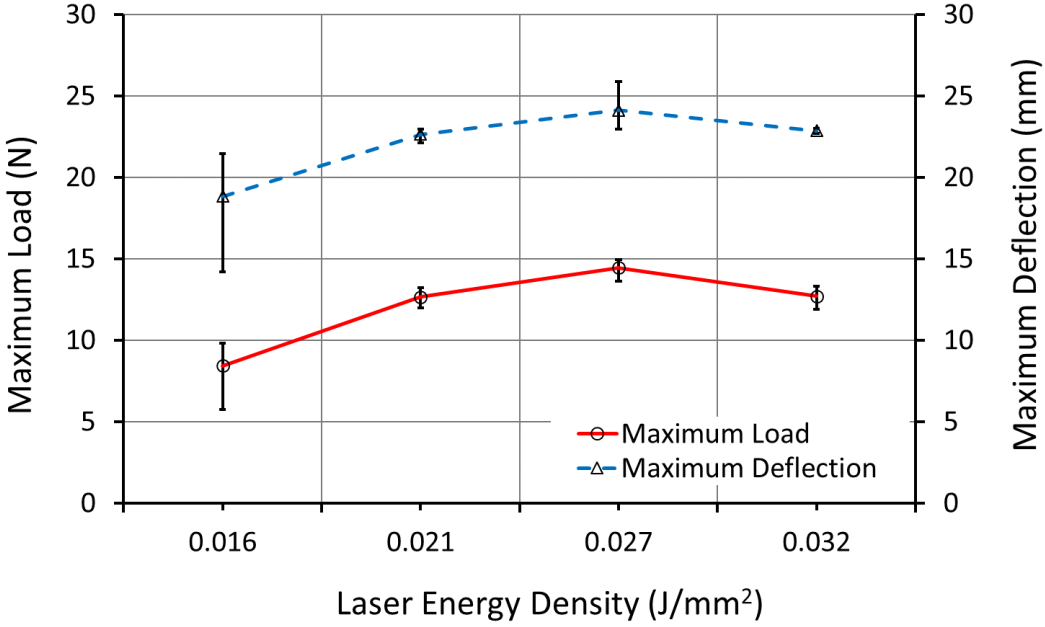

Figure 5.9: Effect of laser energy density on maximum flexural load and deflection

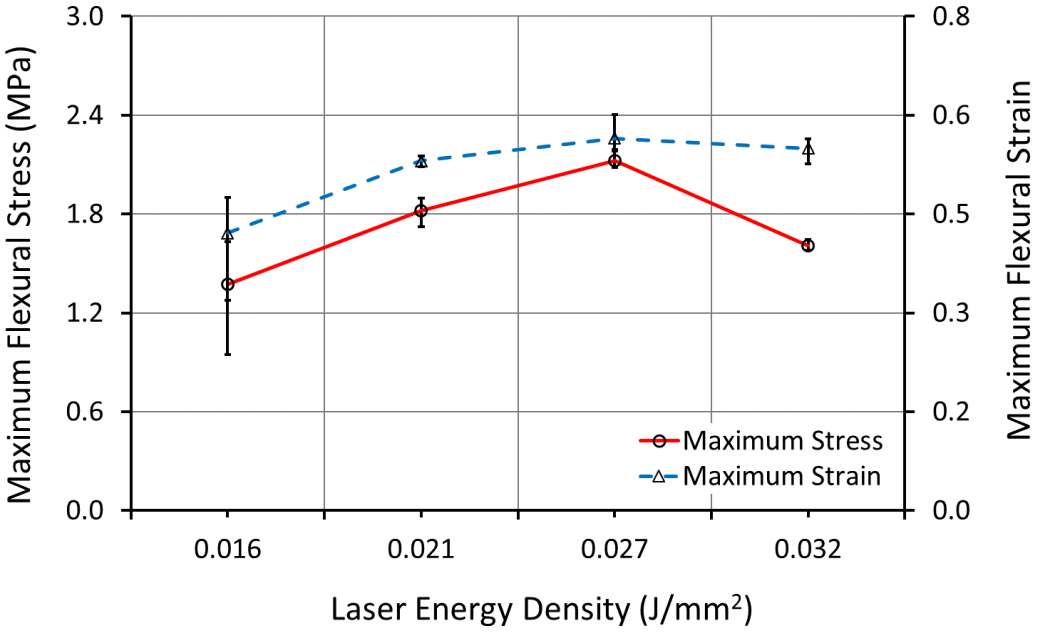

Figure 5.10: Effect of laser energy density on maximum flexural stress and strain

Figure 5.11 shows that the flexural modulus increased systematically with the increase of energy density. The peak flexural modulus value of 46.86 ± 3.07 MPa was achieved when laser energy density was maintained at about 0.027

J/mm^2 (LP=10 watts) and then began to drop at energy density of 0.032 J/mm^2 (LP=12 watts). This drop is probably due to thermal degradation caused by an excessive laser exposure of the powder causing the particles to degrade [34].

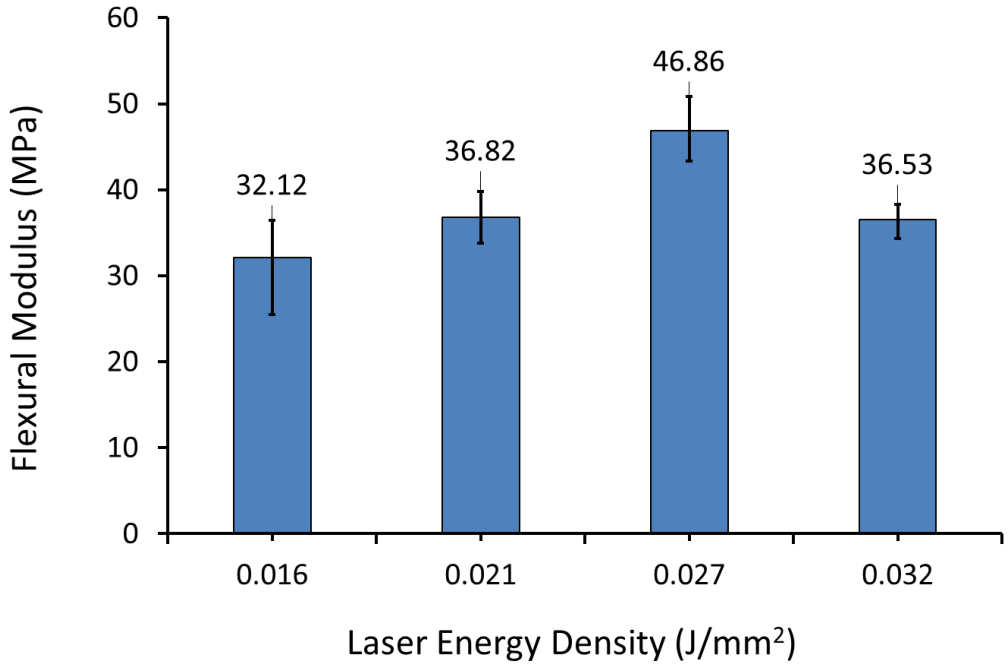

Figure 5.11: Effect of laser energy density on maximum flexural modulus

The results here show notable differences with the work carried out by Goodridge *et al.* [61] which studied the flexural properties of UHMWPE. The primary reason for this distinction is the significant difference in the manufacturing process between the present work and Goodridge *et al.* In their work the sintered parts were manufactured using Vanguard laser sintering machine equipped with temperature controlled heaters around the powder feed chambers. Pre-heating process of the powder is crucial in laser sintering and has significant effect in reducing the thermal gradients. Furthermore, Goodridge *et al.* used a vertical orientation when building the parts and this probably would minimise the dimension inaccuracy and shrinkage but may lead to a negative effect on strength.

Flexural strength and modulus vary directly with density and low density reduces maximum strengths due to high porosity. The flexural test results revealed that the flexural stress and modulus increase with increase in relative density as shown in Figure 5.12 and Figure 5.13.

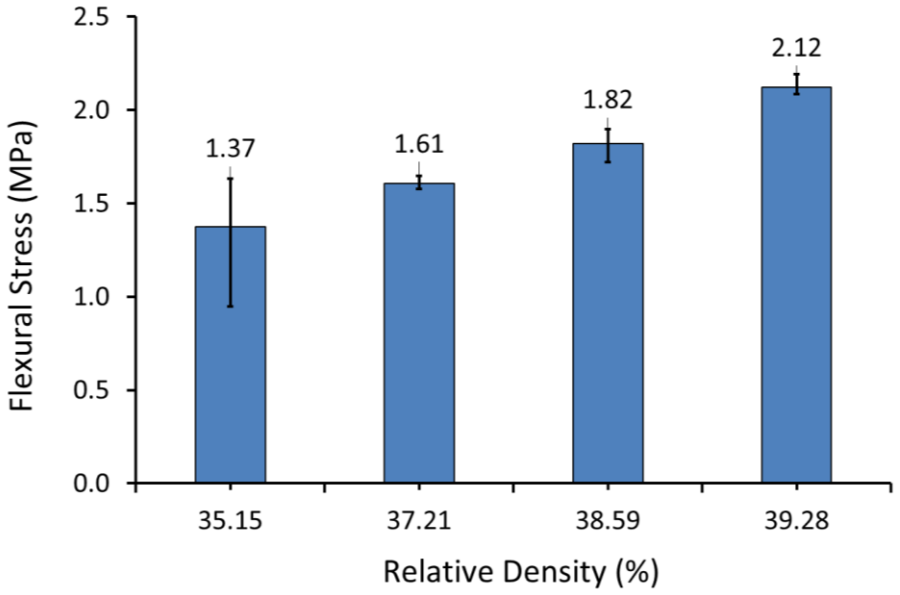

Figure 5.12: Flexural stress v Relative density for sintered UHMWPE parts

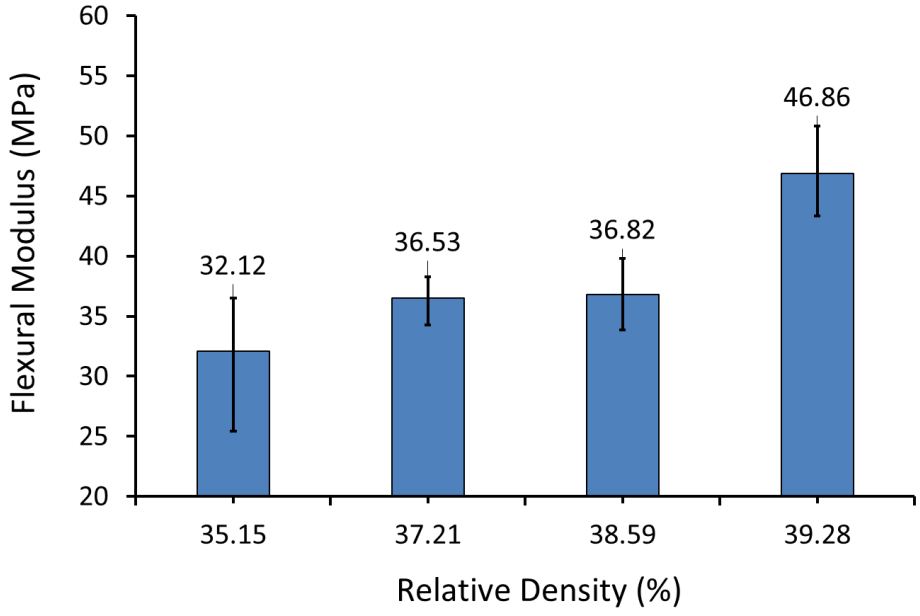

Figure 5.13: Flexural modulus v Relative density for sintered UHMWPE parts

5.6 Morphology of Sintered Parts

5.6.1 Methodology

Microstructure of the laser sintered samples was examined using a scanning electron microscope (Philips XL-20, Holland) at an accelerating voltage of 15 kV. Samples were cut out parallel to and 2-3 mm below the top surface, in the x-y plane, and then were mounted on a sample holder with adhesive tape. All samples were gold sputtered before the examination.

5.6.2 Results

Figure 5.14 shows representative SEM images of the surface of the porous sintered samples from the UHMWPE powder at a laser energy density of 0.016 J/mm^2 (LP=6 watts). The porous structure is seen to form between the powder agglomerations, forming irregular pores connected together and a heterogeneous distribution. Material properties are highly influenced by this porosity.

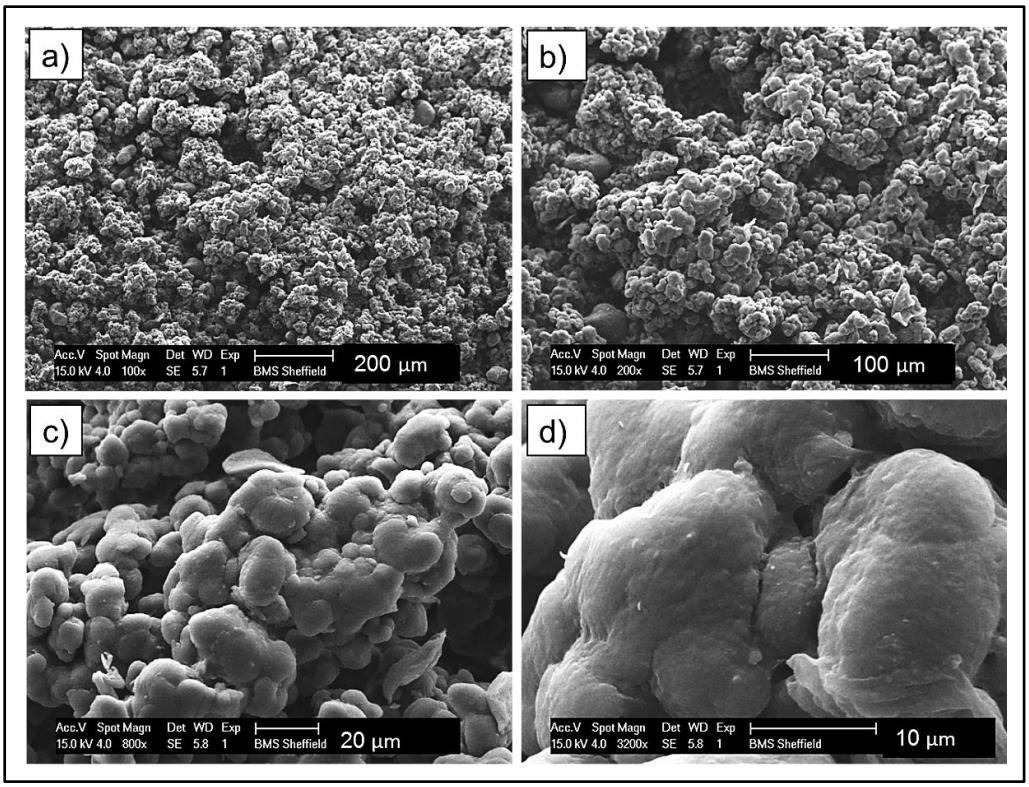

Figure 5.14: SEM micrographs of the sintered UHMWPE at laser power of 6 watts with magnifications: a) 100x, b) 200x, c) 800x and d) 3200x

5.7 Manufacture of Tensile Test Parts

The tensile test parts were designed according to the ASTM D638, type IV (Figure 5.15) and were manufactured using the laser sintering machine EOS Formiga P100 (Germany).

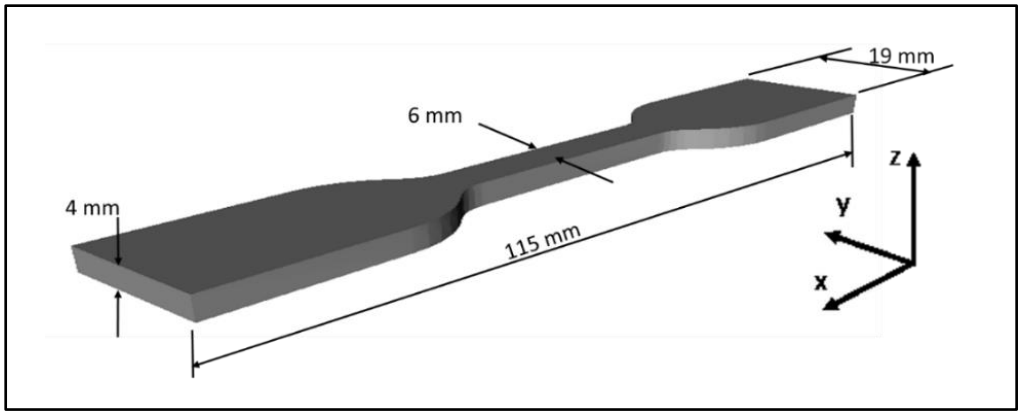

Figure 5.15: Schematic of the orientation of Tensile test parts in the build bed

The dimensions of the width and thickness at the gauge length of 33 mm were 6 mm and 4 mm respectively while the overall length of the parts was 115 mm. The tensile test parts were oriented in the x-y direction with the long axis parallel to the x-axis. Four sets of test specimens (six specimens in each set) were manufactured using different laser powers of 6, 8, 10 and 12 watts and all other parameters were kept constant as listed in Table 5.1.

Although the bed temperature was a degree above the melting temperature of the powder, it was found to be suitable in terms of powder spreading and multilayers sintering. The selected temperature does not always represent the absolute thermodynamic temperature. A slight variation is expected in the actual temperature of the bed during the sintering process due to the variation in the emissivity of polymeric materials.

All parts were built without applying scale factors for compensation of the inherent shrinkage during cooling. After fabrication the parts were removed from the part cake and cleaned manually then sandblasting and pressurised air were used to remove any trace of un-sintered powder.

Tensile test UHMWPE parts were successfully manufactured at laser powers of 6, 8, 10 and 12 watts and all parts were handled and cleaned without loss of definition (Figure 5.16).

Figure 5.16: Sintered UHMWPE part fabricated using 10 watts laser power

5.8 Tensile Properties

5.8.1 Methodology

The tensile properties were directly measured using the sintered parts without any post processing beyond bead blasting. An average and range were obtained over five tests for each set of parameters. Tensile tests were performed on a tensile testing machine (Tinius Olsen Ltd, UK) fitted with a 1000 N load cell and laser extensometer. All the tests were carried out at ambient temperature with a constant cross head speed of 5 mm/min. Three measurements were made of the thickness and width at different locations using Vernier callipers, one at the centre and one at each end of the reduced width section (i.e. gauge length). The average of the three measurements was used when calculating the cross sectional area.

The specimens were marked using two reflective tape strips at zero tension that are used to measure the elongation by the laser extensometer (Figure 5.17). Stress–strain data, Young's modulus, ultimate strength and elongation at break were generated by Tinius Olsen's Horizon software.

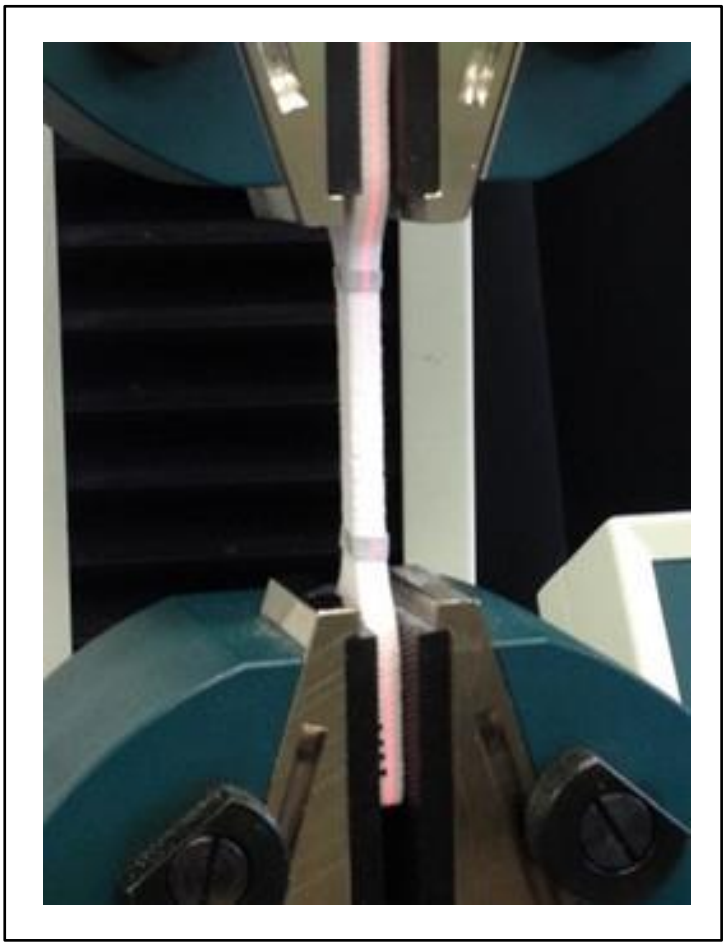

Figure 5.17: Tensile test specimen set up

Tensile strength was measured to examine the influence of laser energy density. Observation during tensile test showed that considerable elongation took place before crack formation began and this behaviour is a classic example of ductile failure in tensile test. Digital photographs of the specimens during the tensile tests are presented in Figure 5.18. A crack was formed on the surface of the specimen before breakage. The area where the crack formation occurred is marked using a red circle.

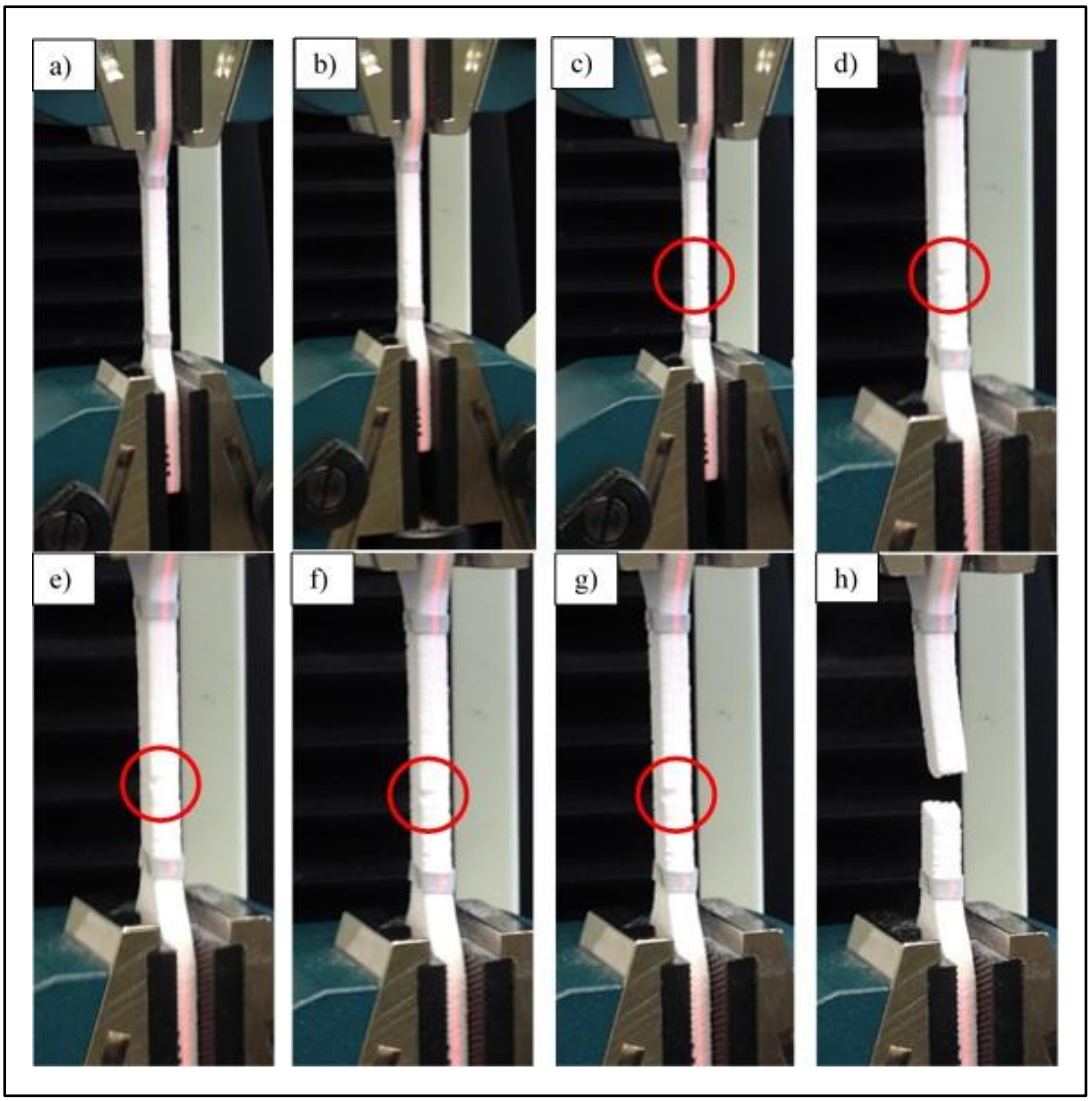

Figure 5.18: Tensile test of laser sintered UHMWPE parts produced with laser power of 10 watts.

5.8.2 Results

The effect of laser energy density upon the tensile properties is shown in Table 5.5 including the average values for the ultimate strength, Young's modulus, and elongation at break. The values of these properties for any given set of specimens were obtained by an average of five measurements and expressed as mean ± standard deviation.

Table 5.5: Average tensile properties values of laser sintered UHMWPE

Laser Power (watts)	Laser Energy Density (J/mm²)	Ultimate Tensile Strength (MPa)	Young's Modulus (MPa)	Elongation at break (%)
6	0.016	1.63 ±0.13	46.5 ±5.1	35.6 ±6.3
8	0.021	1.69 ±0.06	49.8 ±6.5	42.2 ±4.6
10	0.027	2.42 ±0.20	72.6 ±14.9	51.4 ±6.6
12	0.032	1.93 ±0.10	50.2 ±2.9	50.6 ±6.9

Stress-strain curves obtained by tensile test analysis are shown in Figure 5.19. The result revealed a less ductile behaviour for parts built at low laser energy densities than the parts built at higher energy density. The trend is the same as in Figure 5.8, where ductility increases with laser power up to 10 watts and then decreases. When sintering at higher laser energy densities, there is greater flow and the bonding necks between the particles are larger, resulting in stronger bonds which in turn leads to a more ductile behaviour with large plastic regions in the stress–strain curves as has been seen with laser sintering of other polymers [34]. The parts built at the higher laser energy density, 0.027 and 0.032 J/mm^2 (LP=10 and 12 watts respectively), showed a higher strength and modulus relative to the parts sintered at low laser energy density, 0.016 and 0.021 J/mm^2 (LP=6 and 8 watts).

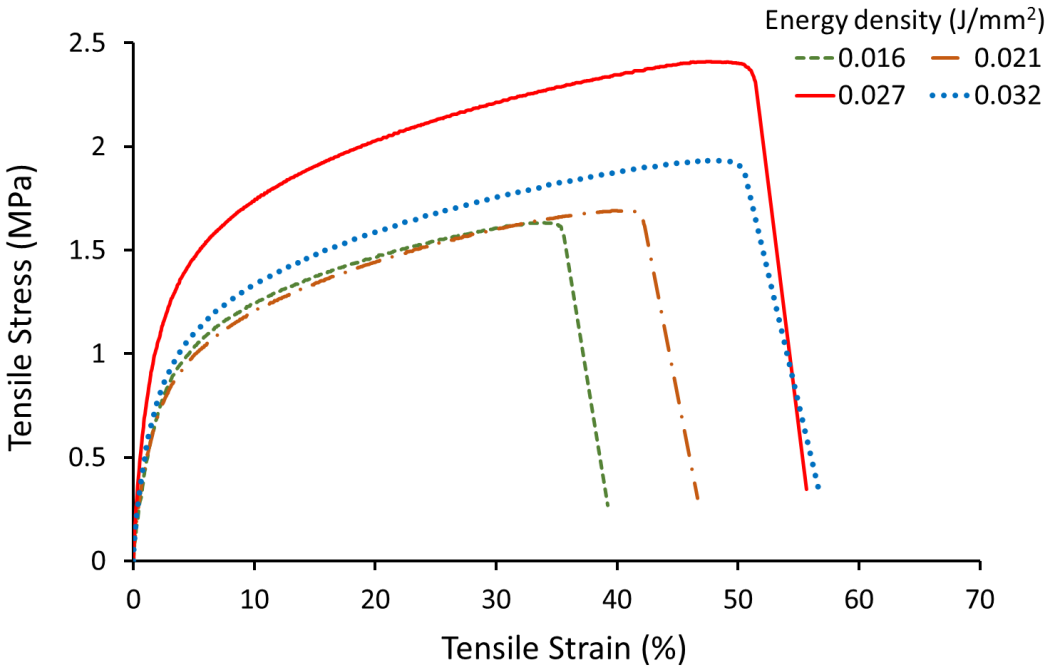

Figure 5.19: Stress–Strain curves for each of the tested laser power levels of the sintered parts (each profile represent an average of 5 tested samples).

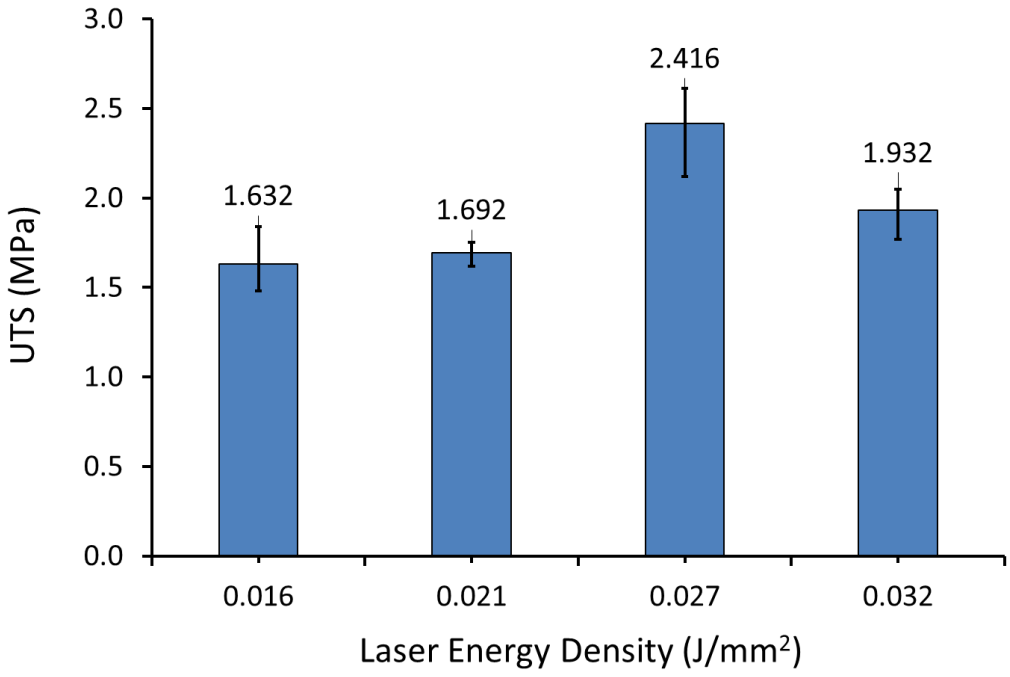

Figure 5.20: Effect of laser energy density on UTS of UHMWPE parts for laser powers of 6, 8, 10, 12 watts corresponding to 0.016; 0.021; 0.027 and 0.032 J/mm^2 respectively.

Laser sintered UHMWPE parts showed an average ultimate strength of 1.63 ±0.13 MPa. This was achieved at a laser energy density of 0.016 J/mm^2 (LP=6 watts), while a value of 2.42 ±0.20 MPa was achieved at a laser energy density of 0.027 J/mm^2 (LP=10 watts) as shown in Figure 5.20.

The relatively low value for the ultimate strength provides evidence of the weak bonding between UHMWPE particles which is probably due to incomplete fusion. As the laser energy density increased to 0.032 J/mm^2 (LP=12 watts), the UTS decreased. This phenomena was observed by Gill *et al.* when processing SiC/Polyamide matrix composites by laser sintering and they reported that degradation of the polymer occurs with increasing laser energy density from the optimum, which then results in a reduction in strength [35]. Caulfield *et al.* [34] observed similar phenomena with Nylon 12 (DuraForm^{TM} polyamide) and suggested this may be due to degradation of the polymer as a result of excessive exposure of the laser to the powder causing the particles to pyrolyse.

Figure 5.21 shows that the laser energy density used to create the parts had a strong influence on the resultant Young's modulus value. The highest modulus was 72.6 ±14.9 MPa at a laser energy density of 0.027 J/mm^2 (LP=10 watts) while the lowest modulus was 46.5 ±5.1 MPa at a laser energy density of 0.016 J/mm^2 (LP=6 watts).

The average elongation at break of the tested samples ranges from 35.6% to 51.4%. Figure 5.22 shows that the elongation increases with the increase in laser energy density and this can be attributed to the increase in fusion between particles, increasing part density [34]. This result shows that if the material integrity and interparticle bonding are enhanced by an adequate laser energy density; the material ductility increases and the material becomes less brittle. However, increasing above this optimum results in polymer degradation and a drop off in mechanical properties.

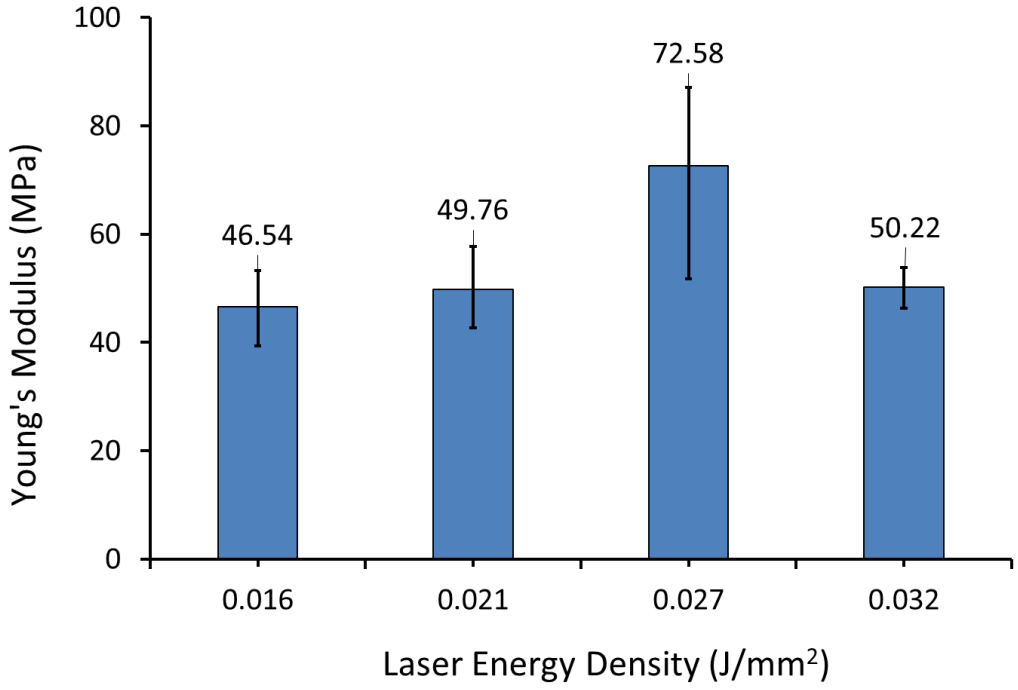

Figure 5.21: Effect of laser energy density on Young's Modulus of UHMWPE parts for laser powers of 6, 8, 10, 12 watts corresponding to 0.016; 0.021; 0.027 and 0.032 J/mm^2 respectively.

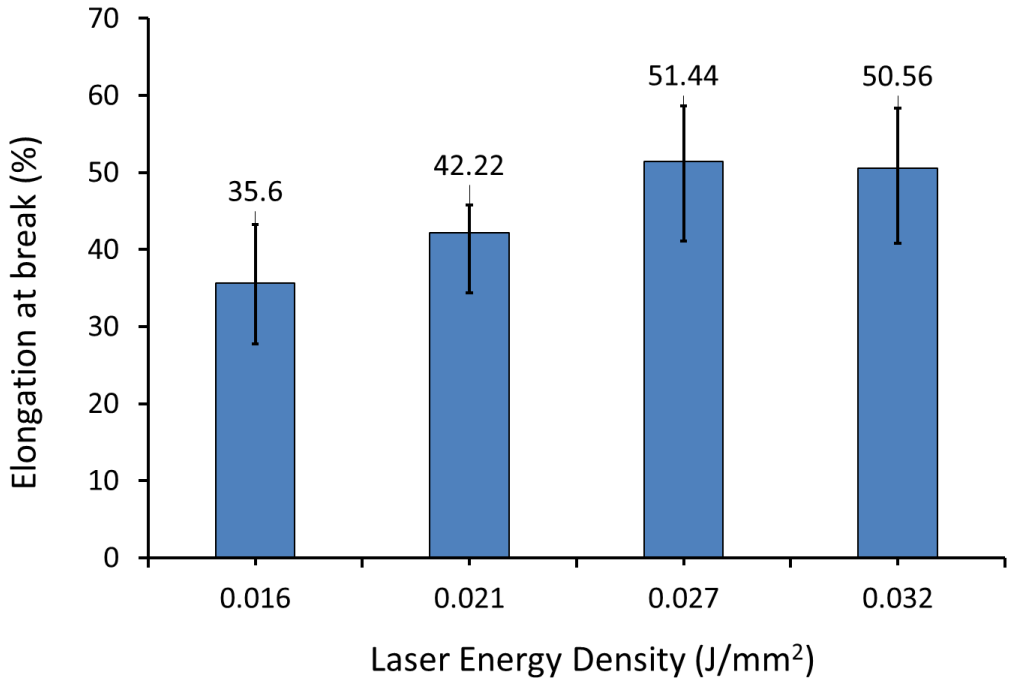

Figure 5.22: Effect of laser energy density on Elongation at break of UHMWPE parts for laser powers of 6, 8, 10, 12 watts corresponding to 0.016; 0.021; 0.027 and 0.032 J/mm^2 respectively.

5.9 Morphology of Fracture Surface

5.9.1 Methodology

The fracture morphology of the tensile test parts was observed using a scanning electron microscope (Philips XL-20, Holland) at an accelerating voltage of 15 kV. Samples were cut parallel to and 2-3 mm below the fracture surface. All samples were gold sputtered prior to observation.

5.9.2 Results

The SEM micrographs of the fractured surfaces of the tensile test specimens at laser energy densities of 0.016, 0.021, 0.027 and 0.032 J/mm^2 (6, 8, 10 and 12 watts respectively) are shown in Figure 5.23, Figure 5.24, Figure 5.25 and Figure 5.26, respectively.

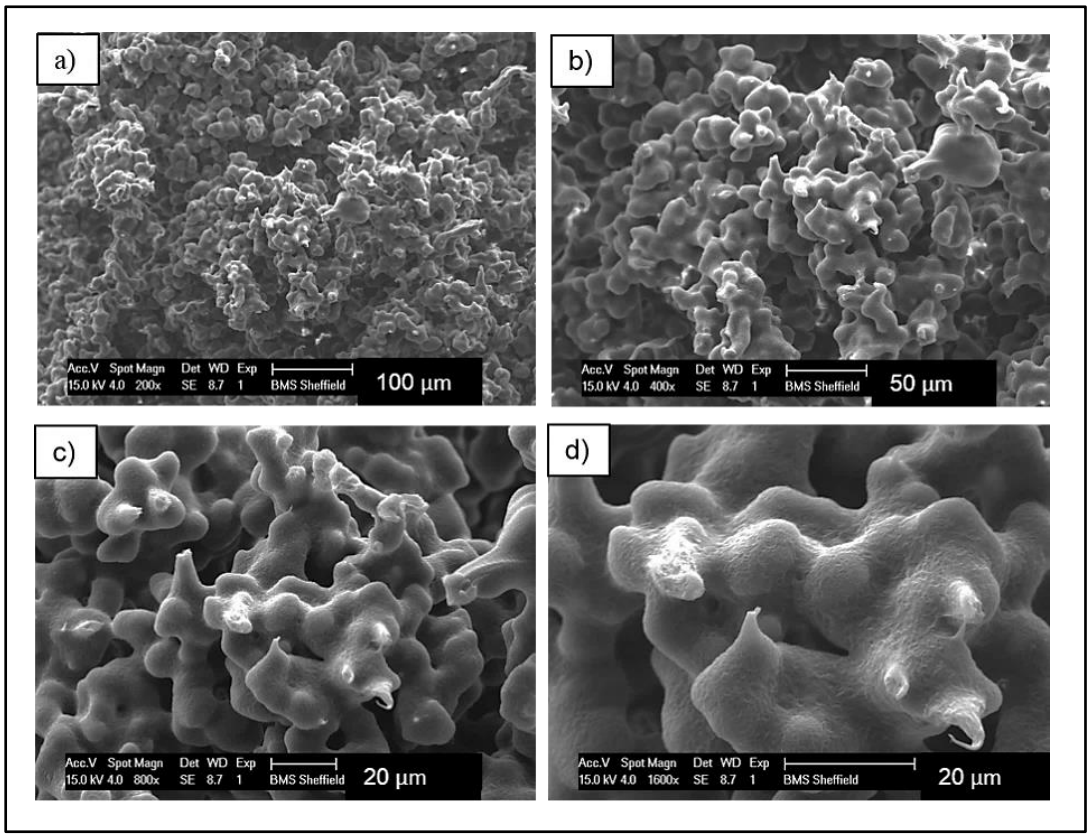

Figure 5.23: SEM micrographs of the fracture surface of tensile tested part of UHMWPE sintered at 6 watts with magnifications:
a) 200x, b) 400x, c) 800x and d) 1600x
The highest magnification clearly shows the neck between the particles, but also the relatively open large pores in the lowest magnification.

A high degree of sintering with large necks between the particles can be seen in all parts. The fracture surface micrographs show characteristic features of ductile failure with plastic deformation and fibrils on the surface which were produced by the separation of particles during the tensile test.

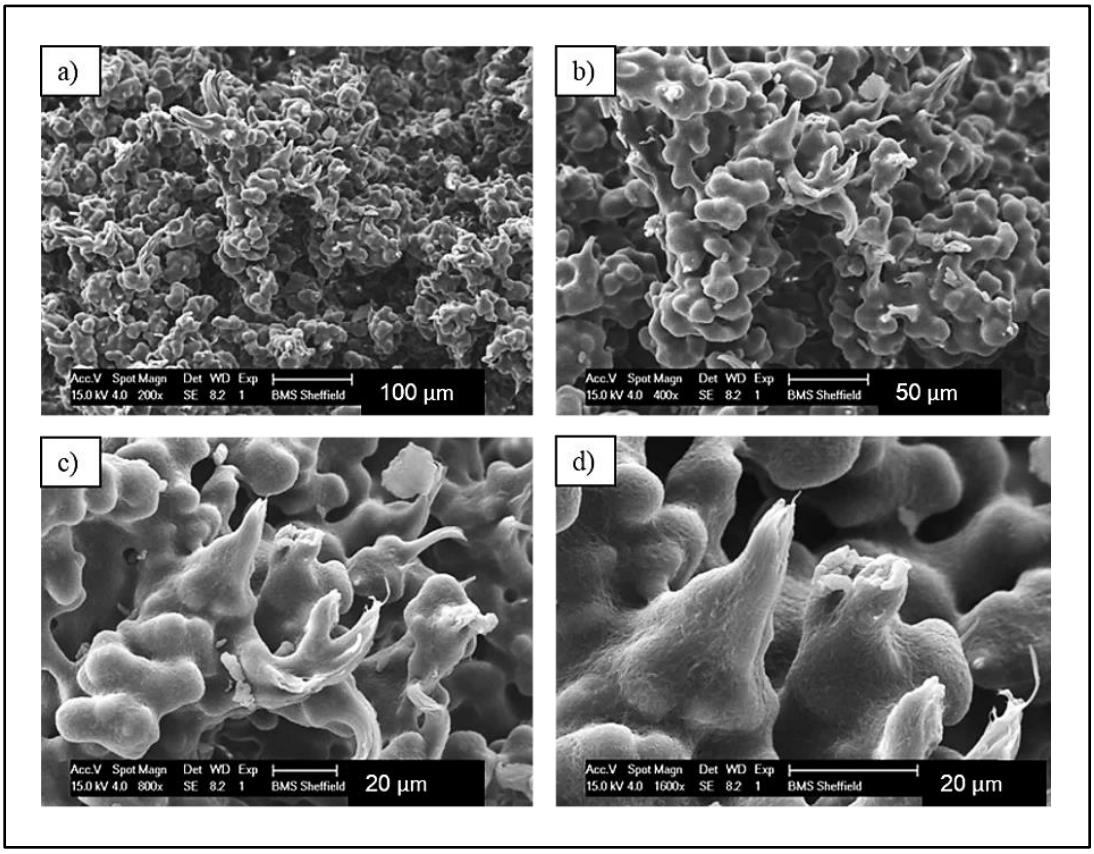

Figure 5.24: SEM micrographs of the fracture surface of tensile tested part of UHMWPE sintered at 8 watts with magnifications:
a) 200x, b) 400x, c) 800x and d) 1600x
Compared with the 6 watts sample there is less definition of the particles, but still the open pore structure.

The fibrils on the fracture surface of the parts laser sintered at an energy density of 0.027 J/mm^2 (LP=10 watts) appear larger than those parts laser sintered at 0.016 J/mm^2 (LP=6 watts) and corresponded to the higher elongation at break of the 0.027 J/mm^2 (LP=10 watts) parts.

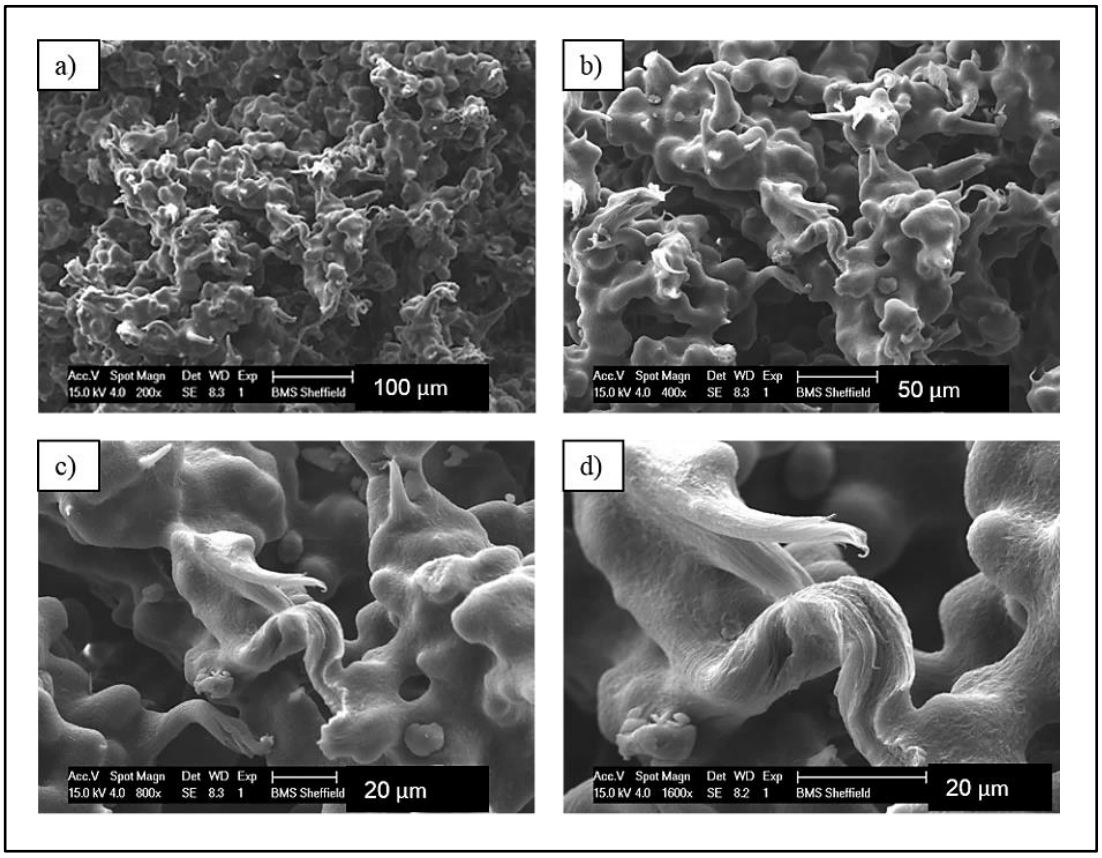

Figure 5.25: SEM micrographs of the fracture surface of tensile tested part of UHMWPE sintered at 10 watts with magnifications:
a) 200x, b) 400x, c) 800x and d) 1600x
Here the highest magnification shows very little of the particle structure, the surface is smoother showing improved particle sintering. However, the open pore structure is still maintained in the lowest magnification

Referring to section 5.8.1, during tensile tests, cracks were formed on the surface of the specimen before breakage. Crack initiation is normally followed by crack growth in which more fibrils undergo extensive plastic deformation until they rupture. This is evident from all micrographs.

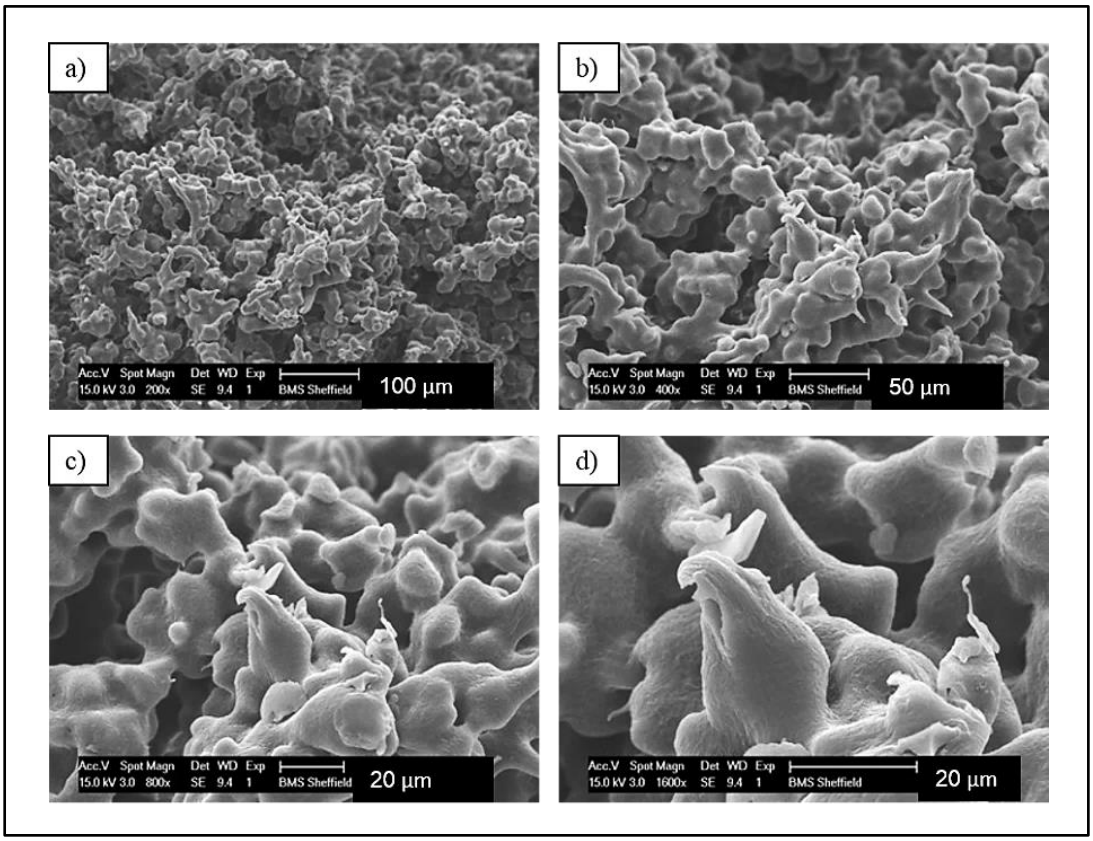

Figure 5.26: SEM micrographs of the fracture surface of tensile tested part of UHMWPE sintered at 12 watts with magnifications:
a) 200x, b) 400x, c) 800x and d) 1600x
Here, as in the 10 watts sample, there is good sintering.

5.10 Summary

Flexural test samples were fabricated successfully at various laser power using a commercial machine EOS Formiga P100 with a laser energy density ranges between 0.016 and 0.032 J/mm^2. The average flexural strength of the sintered parts increased with increase in laser energy density up to 0.027 J/mm^2 with a maximum value of the flexural strength of 2.12 ± 0.05 MPa. The highest Young's modulus value achieved was 46.86 ± 3.07 MPa when the laser energy density was maintained at about 0.027 J/mm^2.

The sintered parts achieved bulk density in a range of around 0.34 – 0.38 g/cm^3 which is higher than the bulk density of UHMWPE powder (i.e. 0.23 g/cm^3). Based on the findings of this investigation, shrinkage in the length and width was evident. The thickness of the sintered UHMWPE parts increased with the increase of laser energy density due to the widely known Z-growth phenomenon. The laser penetrates and fuses the powder particles beyond the specified depth causing a growth in the z-axis direction [87]. The dimensional inaccuracy is still a major challenge when laser sintering polymer materials.

Tensile test parts of UHMWPE were successfully manufactured by Laser Sintering across a range of build parameters. The sintered parts were mechanically tested at room temperature. The three mechanical parameters investigated, ultimate strength, modulus and elongation, exhibit a clear dependence on the sintering laser energy density. Minimum ultimate tensile strength of 1.63 ±0.13 MPa was achieved at laser energy density of 0.016 J/mm^2 (6 watts) while a maximum of 2.42 ±0.20 MPa was achieved at 0.027 J/mm^2 (10 watts). The same trend was reflected in the Young's modulus with average values in range between 46.5 ±5.1 and 72.6 ±14.9 MPa at laser energy density of 0.016 J/mm^2 and 0.027 J/mm^2, respectively. Maximum elongation of 51.4 % ±6.6 was achieved at laser energy density of 0.027 J/mm^2 (10 watts).

The mechanical and physical evaluations show that within a laser energy density range of 0.016-0.032 J/mm^2 (Laser power of 6–12 watts) there appears to be an optimum where strength and relative density reach a maximum, and ductility increases with laser energy density. However, with increasing energy density from the optimum, degradation of the polymer occurs, which results in a reduction in strength [35].

Chapter 6 Morphology Behaviour of Laser Sintered UHMWPE

6.1 Abstract

Porous structures have unique physical properties (mechanical, density, etc.) that are related to their low density and architecture. These properties open a wide range of potential applications, from biomedical scaffolds, packaging, thermal insulation, filtering, food and beverage, pharmaceuticals, automobile, military and aerospace industries [99].

This work describes the morphological characterisations of porous UHMWPE laser sintered parts, sintered under different conditions, to gain an insight into the correlation of process parameters and the morphology properties of these parts. Laser power was investigated as the primary control of the porosity of the structures. The difference in the porosity levels and the pores morphology between different laser sintered parts were reported. The relationships between laser power, porosity and mechanical properties were discussed.

The manufactured parts were characterised through porosity measurements and scanning electron microscopy (SEM). X-ray micro-computed tomography (micro-CT) was employed to evaluate the mean internal porosity as well as the size and spatial distribution of pores inside the structure of the UHMWPE parts. This was undertaken with the aim of developing a better understanding of the three-dimensional internal morphology of laser sintered UHMWPE parts. The porosity was then compared with the porosity measured using helium gas pycnometry.

The results showed a high level of porosity in the laser sintered UHMWPE parts with a range of 60-62% and 61-65% measured by micro-CT and helium gas pycnometry, respectively. There are no significant differences in the results obtained from both techniques. The results showed that flexural strength decreases with an increase in porosity of the sintered parts.

6.2 Introduction

Micro-computed tomography (micro-CT) technique is a promising quality control method in AM that is able to perform non-destructive dimensional measurements of the internal structure and porosity, which are of concern in AM [176]. Previous studies of AM parts have been investigating the pore size and the porosity distribution using micro-CT. Dupin *et al.* [32] used micro-CT in their work and reported that the laser power has a significant impact on the porosity of polyamide 12 sintered parts. Their results show that the open and closed porosities decrease when laser energy density increases. Rouholamin and Hopkinson [89] showed that micro-CT analysis can be used as a non-destructive technique to assess the morphology of nylon 12 and measure the porosity and pore size of the laser sintered parts.

In this study, X-ray micro-CT was used to evaluate the porosity as well as the size and spatial distribution of pores inside the structure. This research establishes relationships between manufacturing process parameters (i.e. laser power), porosity and with mechanical properties (i.e. flexural properties).

To the author's knowledge, no investigation has been reported related to the effect of process parameters on the porosity of laser sintered UHMWPE parts. The laser power was varied to investigate how this influences the mechanical properties and porosity of the structure. The difference in the porosity levels and the pore morphology between different laser sintered parts is studied.

6.3 Material Characterisation and Parts Manufacturing

6.3.1 Material

UHMWPE (GUR 2122), supplied as a powder by Celanese (Germany), was used in this work. The virgin powder has an average particle size of 125 µm (d50), and a size distribution range from 46.2 µm (d10) to 293 µm (d90), as measured

by laser light scattering using a Mastersizer 3000 (Malvern Instruments, UK) and the dry sample dispersion technique.

Detailed characterisation of UHMWPE powder has been reported earlier in section 4.3, Chapter 4.

6.3.2 Part Manufacture

The laser sintered UHMWPE parts were manufactured as described in section 5.2, 0 (Figure 6.1). These parts were produced at various laser powers of 6, 8, 10 and 12 watts. All other parameters were kept constant as listed in Table 5.1 (0).

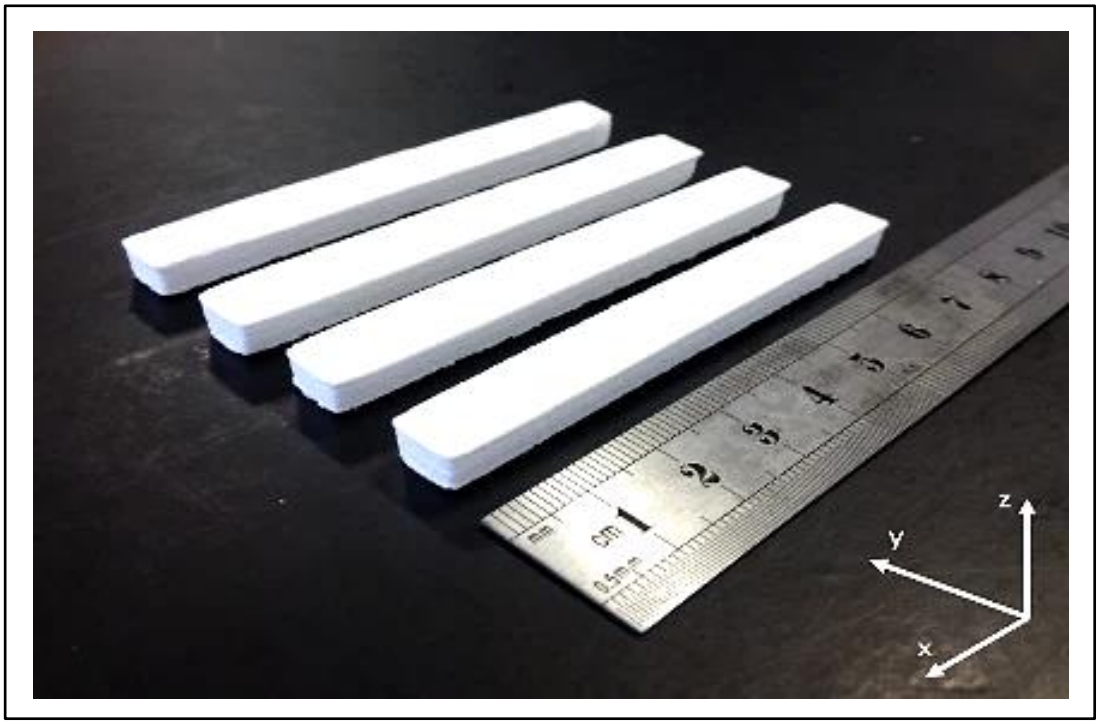

Figure 6.1: Laser sintered UHMWPE parts

6.4 Parts Characterisation Methods

Small rectangular specimens with approximately 10 mm length, 8 mm width and 6 mm thickness, were cut out, from the centre and the end, of the laser sintered rectangular parts as shown in Figure 6.2. Three samples (A, B, and C) were used for density measurements and two samples (A and C) for

morphology investigation. In this study, two methods were used to evaluate the porosity; micro-CT and helium gas pycnometry.

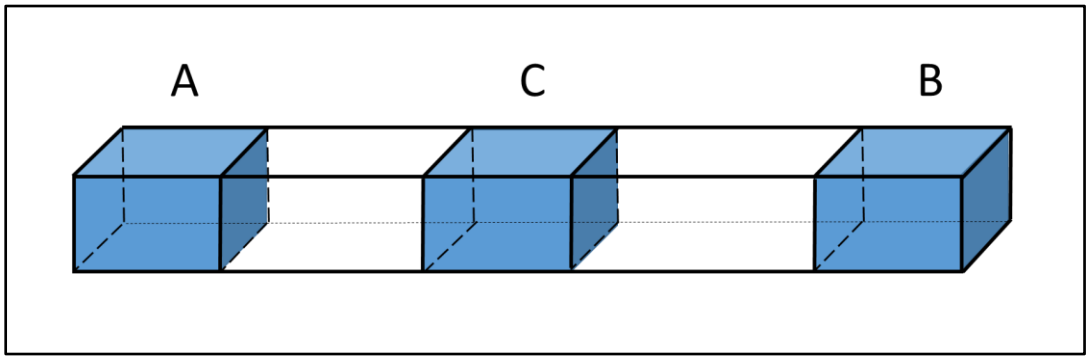

Figure 6.2: Density and morphology samples cut out from the laser sintered parts

6.4.1 X-ray micro-Computed Tomography Analysis

The micro-CT technique is described by Ho and Hutmacher [155]. The internal microstructure of the laser sintered UHMWPE parts was investigated using Skyscan 1172 (Bruker μCT, Belgium). The scanning conditions used were a current of 165 μA, voltage of 40 kV, pixel size of 5.9 μm, 360° rotation and 0.35° rotation step. Skyscan NRecon software (Bruker micro-CT, Belgium) was used to reconstruct cross-section images from tomography projection images obtained from the scanner. CTAn software (Bruker micro-CT, Belgium) was used for 3D morphological analysis of the micro-CT data (Figure 6.3).

A cylindrical region of interest (ROI) with a diameter of 5 mm and a height of 8 mm was chosen for the 3D porosity analysis for all samples. CTVox software was used to show 3D representations of the structure (Figure 6.4).

The morphological measurements in 3D and 2D are performed on segmented or binarised images (black and white). Image segmentation or "thresholding" is an important step in micro-CT analysis that has to be performed prior to 3D porosity measurement. The thresholding range is selected via the histogram and visual estimation by comparing the raw image to the binarised image. In binarised images white colour represents solid areas and the areas outside this selection are black and represent pores or spaces.

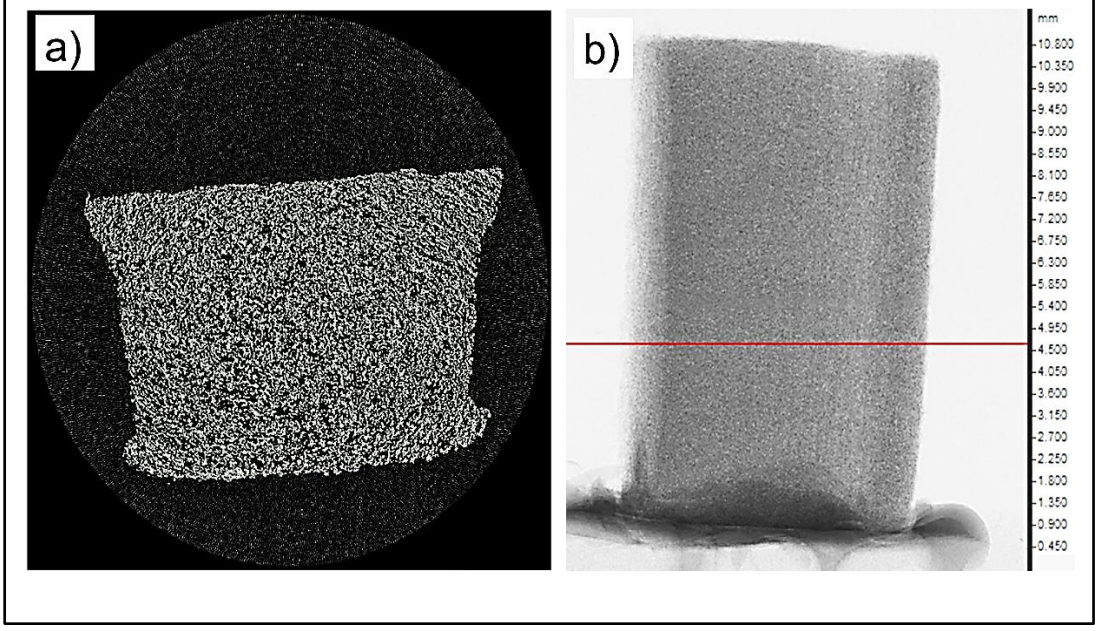

Figure 6.3: micro-CT images of laser sintered part at 6 watts:
a) Single 2D cross-section image (Pores in black)
b) Reconstructed images to form 3D part.
(Red line indicates the position of the 2D image)

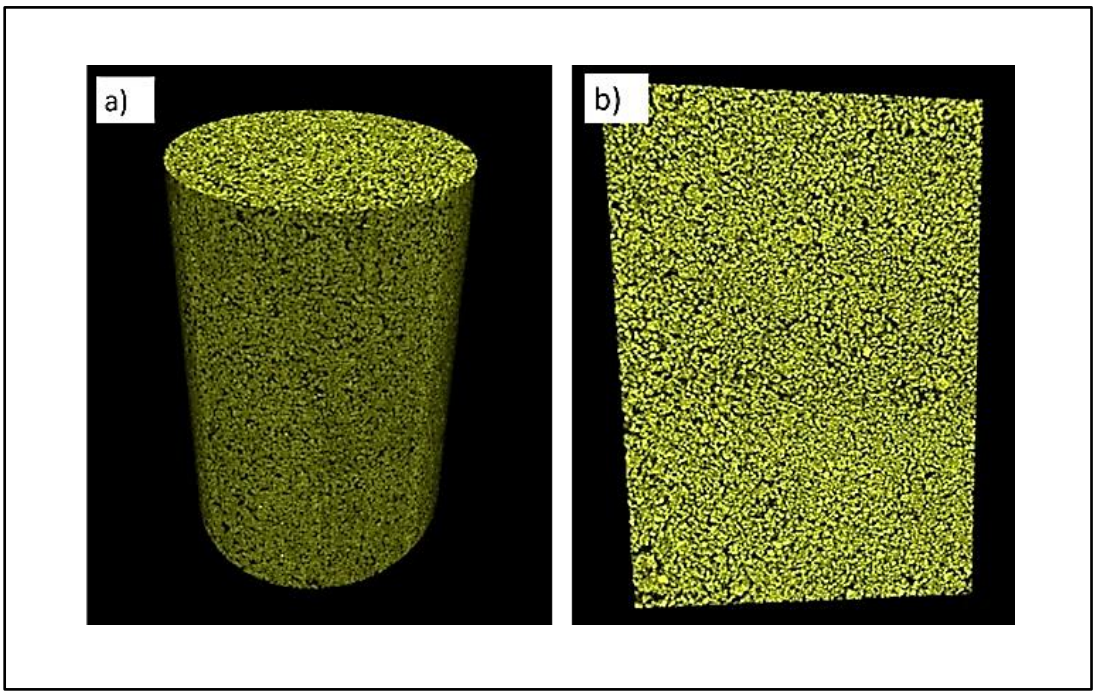

Figure 6.4: 3D representation of the part structure
a) ROI created by CTAn
b) Cross-section of the cylindrical ROI

Thresholding process affects the subsequent analysis and visualisation. Since the threshold for binarisation of the micro-CT images is selected manually, an overestimation or underestimation can be expected using this method. Thresholding is an inherent difficulty in micro-CT technique due to noise and reconstruction artefacts [155, 177-179].

The threshold used in this analysis was readily obtained for each individual sample with lower and upper grey values of 43 and 255, respectively.

6.4.2 Helium Gas Pycnometry

To determine the porosity of the sintered parts, the true density of UHMWPE powder (ρ_{Trure}), the bulk density (ρ_{Bulk}) and the skeletal density ($\rho_{Skeletal}$) of sintered parts must be known.

The bulk density of laser sintered parts was determined using a volumetric method as described in section 5.3.1, 0. The true density (or reference density) of the UHMWPE powder and the skeletal density of the sintered parts were determined using Helium Gas Pycnometer (Micromeritics AccuPyc II 1340, USA). The true density of the UHMWPE powder was determined to be 0.954 g/cm³.

The total, open and closed porosities were calculated using the following equations [32], [180]:

$$Total\ porosity = 1 - (\frac{\rho_{Bulk}}{\rho_{True}}) \times 100 \quad (10)$$

$$Open\ porosity = 1 - (\frac{\rho_{Bulk}}{\rho_{Skeletal}}) \times 100 \quad (11)$$

$$Closed\ porosity\ = Total\ porosity - Open\ porosity \quad (12)$$

The total porosity is a measure of the volume fraction of the sample not occupied by polymer. The open porosity is a measure of the porosity that is connected to the surface, and available for the helium gas to explore. The closed porosity is the porosity not open to the surface, the helium gas does not enter these regions.

6.4.3 Microstructure of Laser Sintered Parts

The external microstructure of the sintered parts was observed using a scanning electron microscope (Philips XL-20, Holland) at an accelerating voltage of 15 kV. All samples were gold sputtered before the observation to avoid charging.

6.5 Results and Discussion

6.5.1 Morphological Properties

Figure 6.5 and Figure 6.6 show a micro-CT image of a whole scanned sample and 2D images of the cross-section, respectively. These were produced using CTAn software with regions of different densities in different colours.

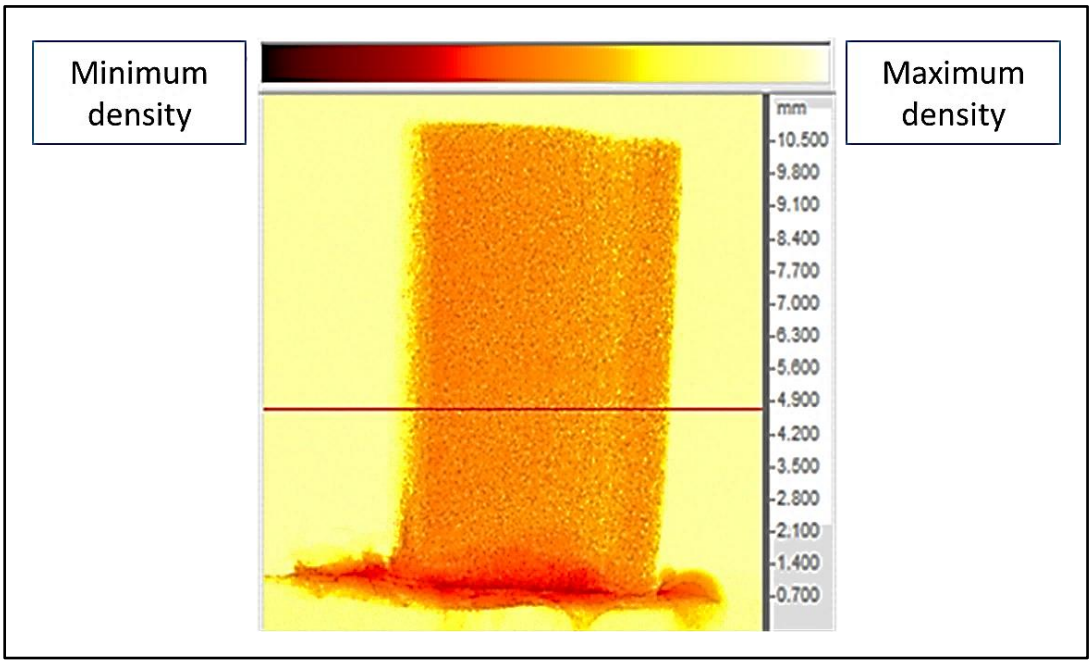

Figure 6.5: Reconstructed image of laser sintered sample produced by CTAn software

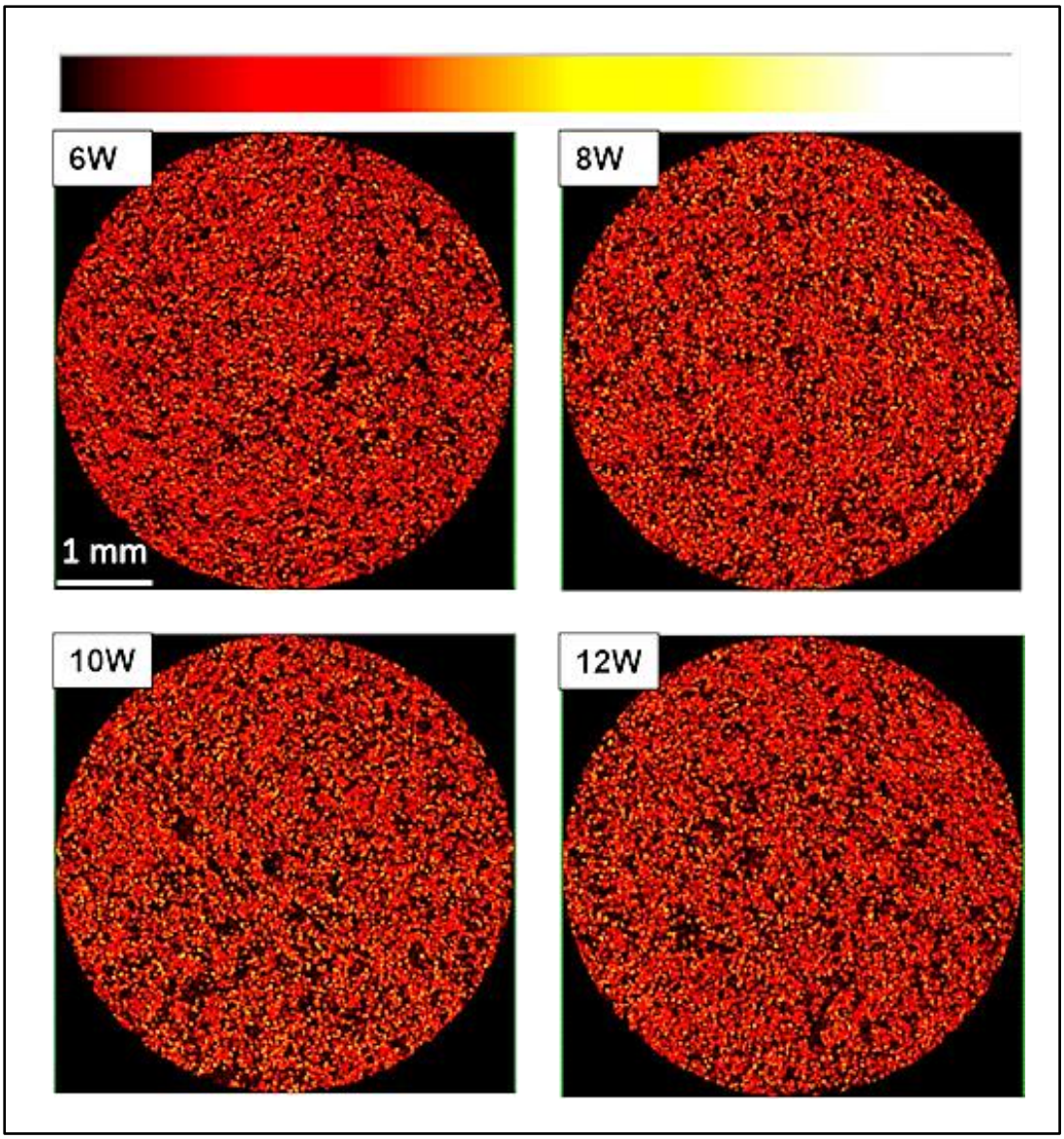

Figure 6.6: 2D images of cross section of UHMWPE parts produced at different laser powers

These images show that the density is varied from region to region in the 3D structure. The colour bar at the top of the image represent the variation in density with higher density areas are presented in white and areas with low density including the pores are presented in black.

The image in Figure 6.5, indicates a different density on the inside and in the outer area of the sintered part. The outer shell is more dense (yellow colour) than the inside of the part which is mainly in red to orange colour. Rüsenberg [153] indicated that the dense shell surrounding the part can be formed and

strongly influenced by the thickness of the sample and the cooling rate. Ajuku [77] also reported the same phenomenon and suggested that the short bursts of energy at the edges result in parts being much denser at the edges than at the centres.

Figure 6.6 shows the cross-section images of the sintered parts at different laser powers. The dominated colour mainly ranges between red and orange, which indicates a low and medium density. High volume of pores can be observed at all levels of laser power (pores are in black). However, there are yellow areas within the structure as an indication of high density elements.

Morphological properties of the 3D structure of the laser sintered UHMWPE parts, such as porosity, average pore diameter and pore size distribution were measured using micro-CT. In this study, two specimens were scanned for each laser power and the average results were obtained.

The effect of laser power on porosity of the sintered parts measured by helium gas pycnometry and micro-CT is shown in Table 6.1. Figure 6.7, Figure 6.8 and Figure 6.9 show the effect of laser power upon the total, open and closed porosities.

Table 6.1: Porosity measuerment of laser sintered UHMWPE parts

Laser Power (watts)	Helium Pycnometry			Micro-CT		
	Total porosity (%)	Open pores (%)	Closed pores (%)	Total porosity (%)	Open pores (%)	Closed pores (%)
6	64.85	64.42	0.43	61.44	61.43	0.01
8	61.41	60.98	0.43	60.30	60.29	0.01
10	60.72	60.30	0.42	60.67	60.66	0.01
12	62.79	62.36	0.43	61.84	61.83	0.01

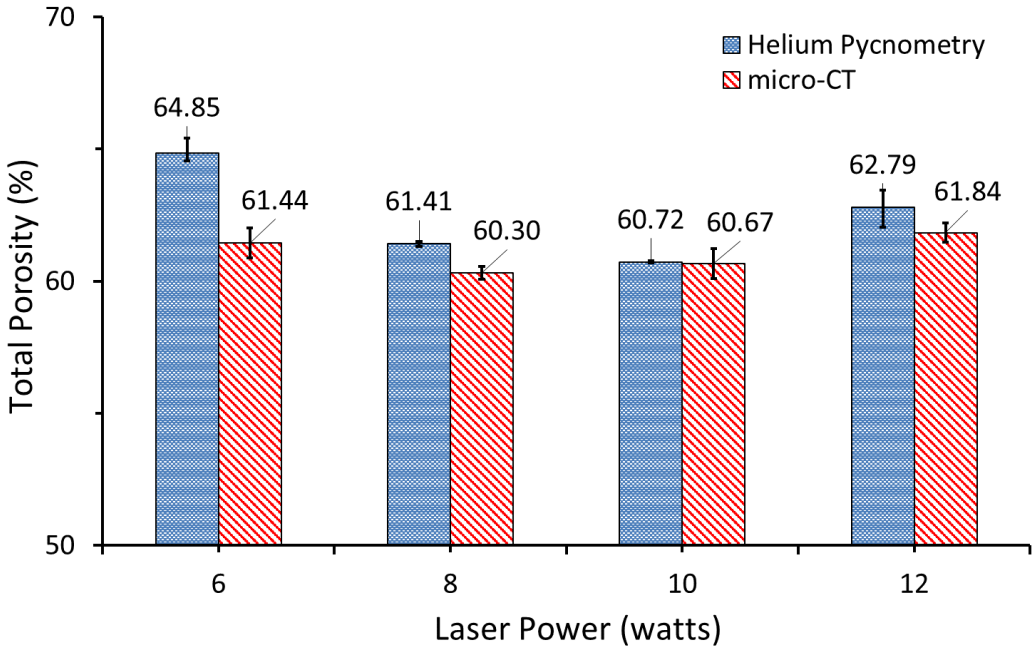

Figure 6.7: Effect of laser power upon the porosity of the UHMWPE parts

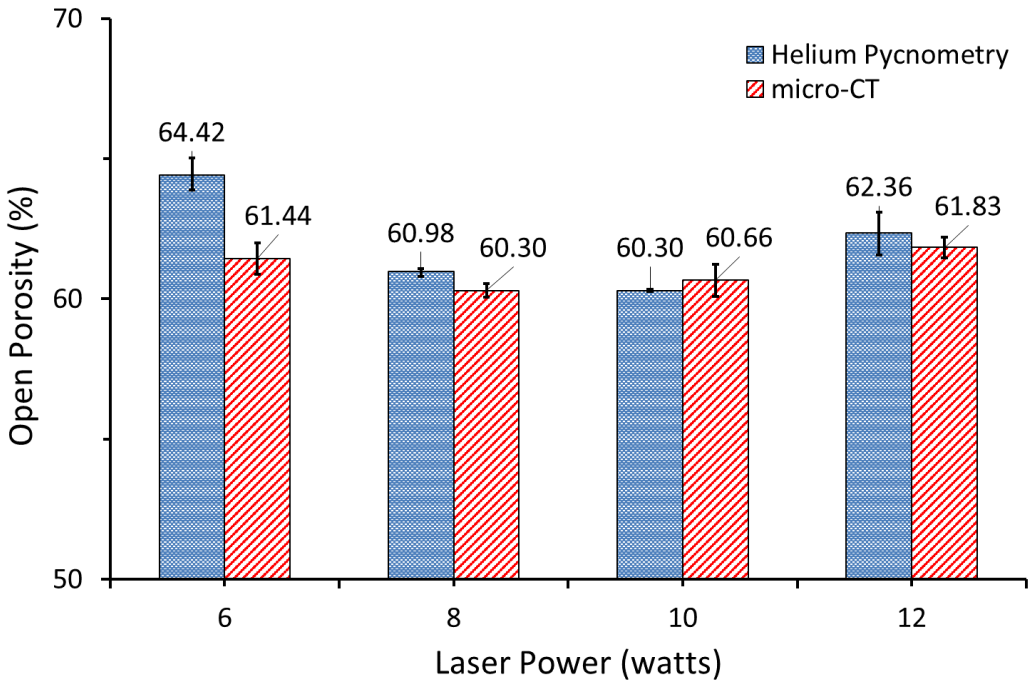

Figure 6.8: Average open porosity in UHMWPE parts

Figure 6.7 shows a slight decrease of the porosities as the laser power increased from 6 to 10 watts. However, further increase in laser power (i.e. 12 watts) showed a slight increase in porosity. Gill *et al.* reported that polyamide laser sintered parts built at higher energy density showed a reduction in porosity when compared to laser sintered parts built at lower energy density. With increasing energy density from the optimum, the porosity increases due to degradation of the polymer [35].

The change in the trend of total and open porosities (Figure 6.7 and Figure 6.8, respectively) measured by micro-CT technique is similar to the porosities measured using helium gas pycnometry method. There are no significant differences in the results obtained from both techniques and it is clear that results fit very well with each other.

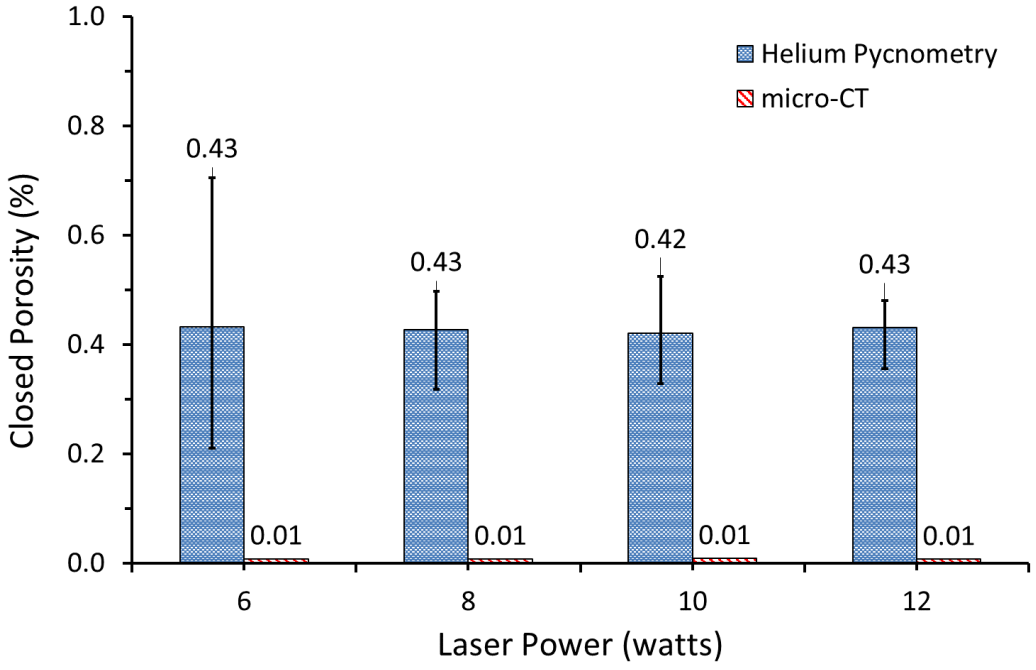

Figure 6.9: Average closed porosity in UHMWPE parts

The closed porosity (Figure 6.9) shows a similar trend with open porosity measured by helium gas pycnometry. However, this result does not fit well with the result of the closed porosity obtained by micro-CT technique. This is very likely due to the fact that the volume of the closed porosity is low, less

than 0.5%. It is interesting to note that all samples show a similar closed porosity, this suggest that the closed porosity is not influenced by processing and may be an inherent property of the UHMWPE. The fact that a negligible closed porosity is seen in the CT, suggest that the porosity is below the resolution of the instrument.

Figure 6.10 shows the effect of laser power on the average pore diameter.

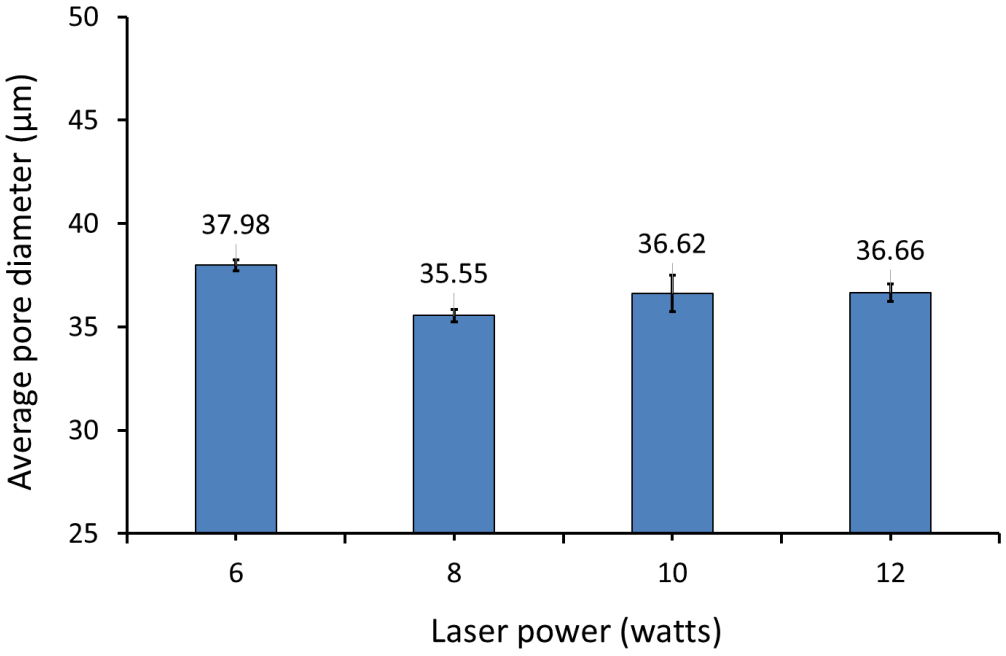

Figure 6.10: Average pore diameter of UHMWPE parts measured by micro-CT

UHMWPE structure shows a slightly larger pores at a laser power of 6 watts. However, the average pore diameter remains fairly constant with increasing laser power (i.e. 8, 10 and 12 watts). The 36.70 ±1.0µm overall average pore size is consistent with the SEM images shown in section 5.9.2, 0.

The cross-section (5 mm diameter) of the 3D micro-CT images in Figure 6.11 shows similar characteristics at all levels of laser power.

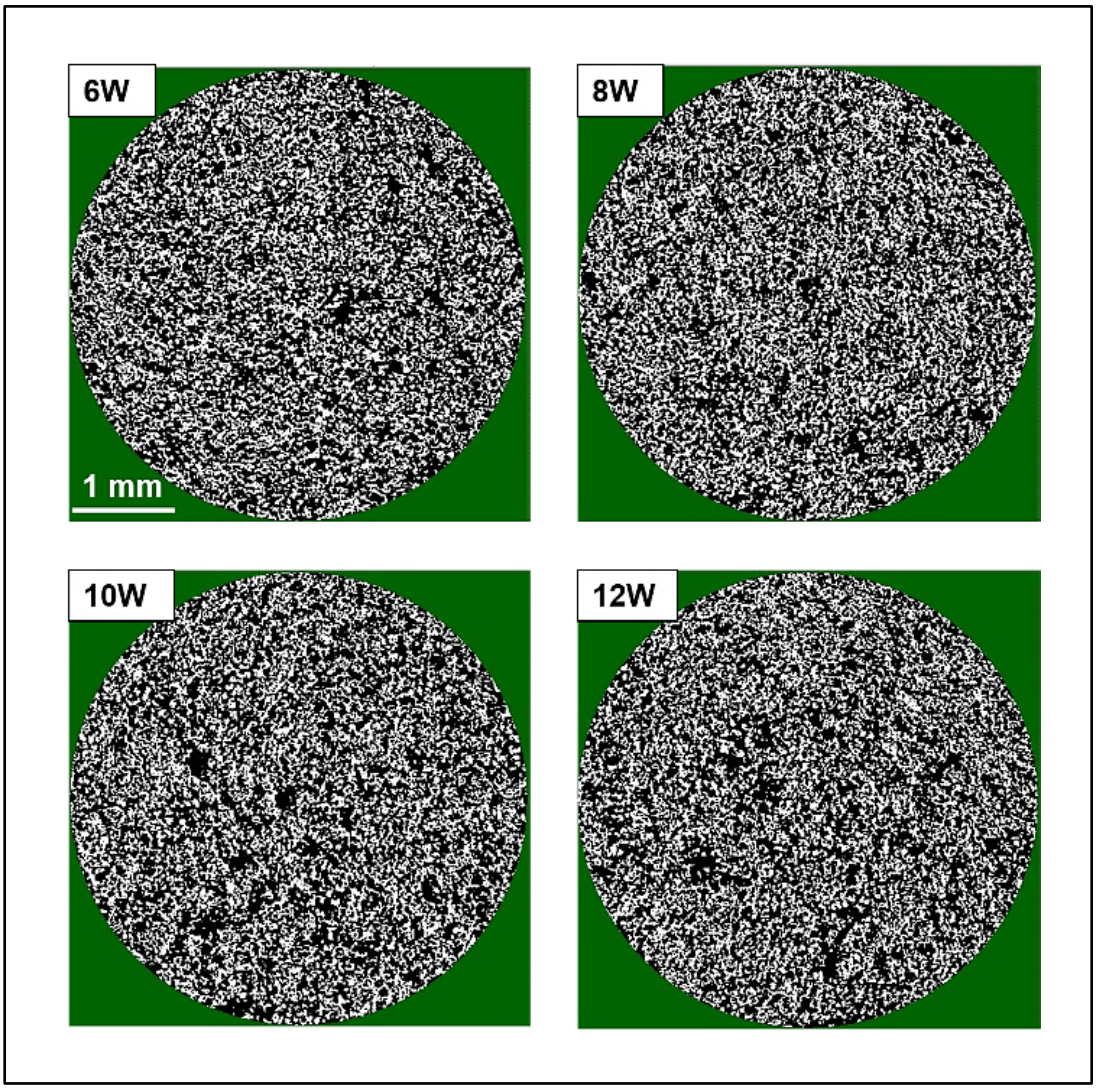

Figure 6.11: Cross-section of micro-CT 3D images of UHMWPE parts produced at different laser powers (Pores in black colour)

Figure 6.12 shows the pore diameter distributions of laser sintered parts at different laser powers. The volume of the pores with diameters in a range between 30 – 42 μm is the highest for all levels of laser power. Pore diameters larger than 42 μm and smaller than 89 μm are also present at all laser power levels and pore diameter larger than 89 μm can be seen clearly at laser power of 6 watts. However, the result shows that there is no statistically significant difference in the pore size distribution when the laser power is changed.

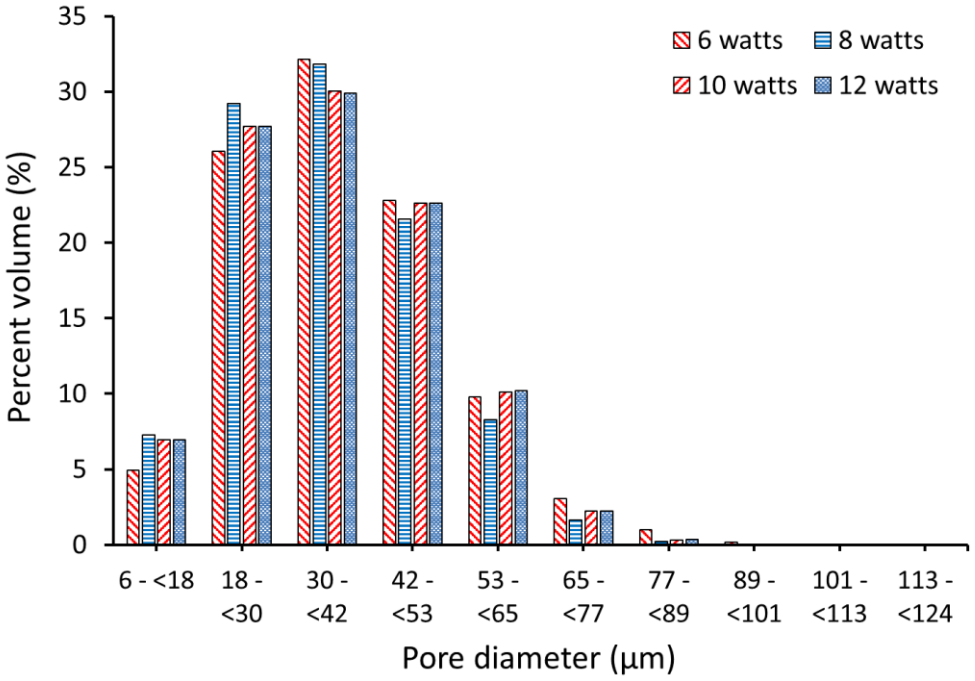

Figure 6.12: Pore size distribution of laser sintered UHMWPE parts produced at different laser powers

Figure 6.13 shows the result of the flexural stress, obtained from section 5.5.2, 0, which was plotted versus the porosity of laser sintered UHMWPE parts.

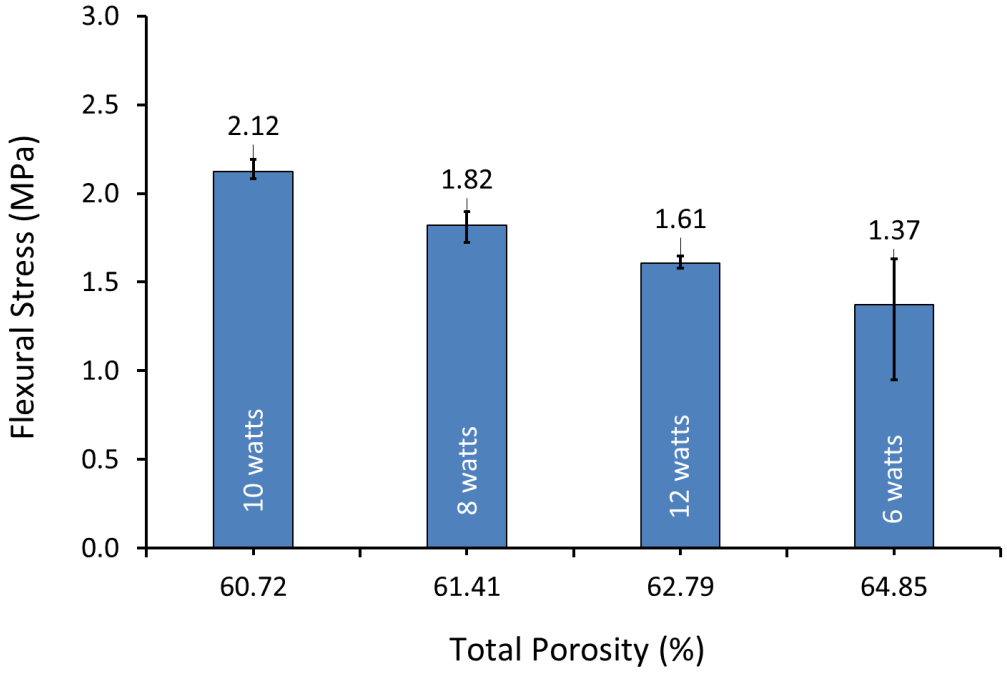

Figure 6.13: Flexural stress vs total porosity of laser sintered UHMWPE parts

The porosity results, obtained by helium gas pycnometry method, shows a typical change trend whereby the strength decreases as porosity increases. This behaviour was observed by Gill *et al.* when processing SiC/Polyamide matrix composites by laser sintering and reported that the strength of laser sintered parts decreases when the laser energy is insufficient to fully sinter the polymer, resulting in an increase in porosity [35].

6.5.2 Microstructure Observation

Figure 6.14 and Figure 6.15 show representative SEM images of the surface of the sintered UHMWPE parts at laser power of 6 and 8 watts respectively.

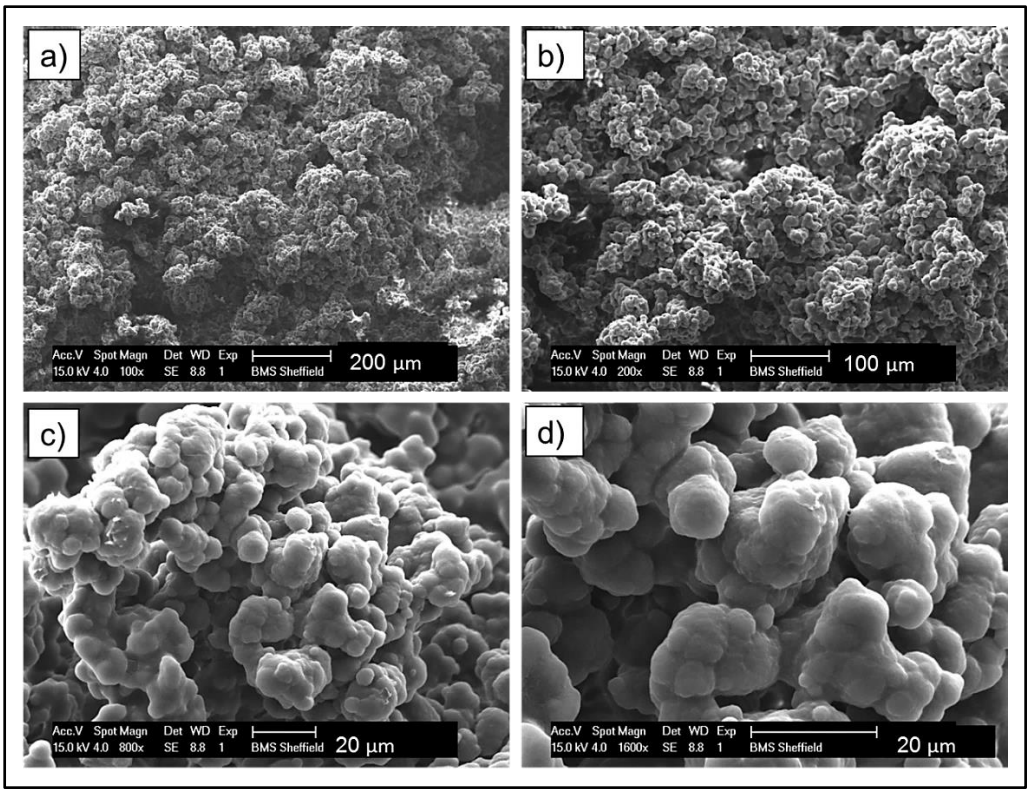

Figure 6.14: SEM micrographs of the sintered part of UHMWPE at laser power of 6 watts with magnifications: a) 100x, b) 200x, c) 800x and (d) 1600x

The porous structure can be seen in both samples but with different forms. The SEM observation showed that when the laser power increased from 6 to 8 watts, the laser sintered UHMWPE parts became denser with a higher degree of coalescence. It seems that the fusion of the polymer particles

becomes better with a more compact morphology when the laser power increases up to an optimum level [181].

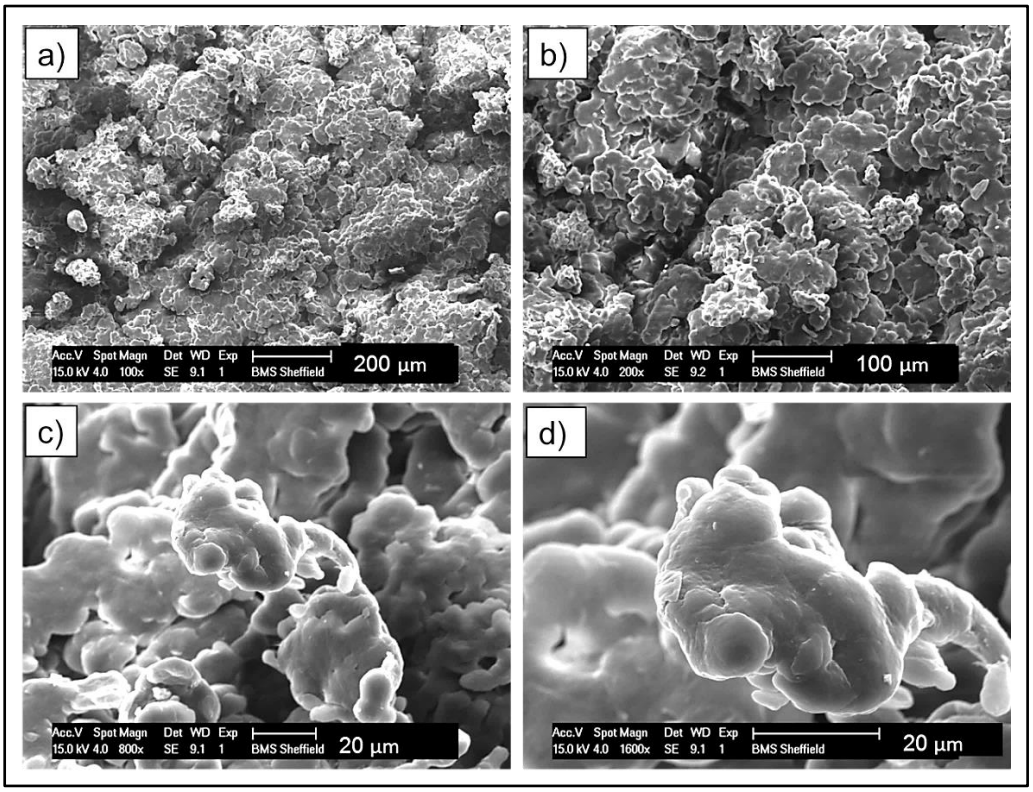

Figure 6.15: SEM micrographs of the sintered part of UHMWPE at laser power of 8 watts with magnifications: a) 100x, b) 200x, c) 800x and (d) 1600x

6.6 Summary

The following conclusions can be made for this study:

- The results show a high level of porosity in the laser sintered UHMWPE parts with a range of 60-62% and 61-65% measured by micro-CT and helium gas pycnometry, respectively. A slight decrease in porosity was observed when the laser power increased from 6 to 10 watts. Further increase in laser power to 12 watts showed a slight increase in porosity.

- The change in the trend of total and open porosities measured by the micro-CT technique is similar to the porosities measured by helium gas

pycnometry. There are no significant differences in the results obtained from both techniques. The results fit very well with each other demonstrating the suitability and reliability of micro-CT for morphology characterisation.

- UHMWPE parts have slightly larger pores at laser power of 6 watts and the average pore diameter remains fairly constant with the increase in laser power (i.e. 8, 10 and 12 watts).
- The porosity results, obtained by helium gas pycnometry, combined with the flexural measurements, showed that the flexural strength decreases as the porosity increases.

Chapter 7 Characterisation of AC-UHMWPE Composite Powder for Laser Sintering

7.1 Abstract

Composites of Activated Carbon (AC) and Ultra High Molecular Weight Polyethylene (UHMWPE) powders were prepared. They were characterised by a number of techniques in order to generate a better understanding of the material properties. This was undertaken so that the suitability and processing behaviour of AC-UHMWPE composite for Laser Sintering could be determined.

Previous investigation shows that the degree of control over the microstructure of the laser sintered parts depends on the process parameters, especially the properties of the powder. Particle size distribution and morphology influence the packing density of the powder, whereas the thermal behaviour and stability define the laser energy density required in laser sintering [17]. Understanding the thermal stability of AC-UHMWPE composite is essential for the simulation of laser sintering process.

Powdered composites were prepared with different ratios of UHMWPE and AC. The structure and properties of AC-UHMWPE composite were investigated. The prepared composite was characterised by light scattering and scanning electron microscopy (SEM), for particle size and morphology analysis; helium gas pycnometry for density measurement; differential scanning calorimetry (DSC) and thermal gravimetric (TGA) for thermal analysis, and X-ray diffraction (XRD) for crystallinity measurement.

7.2 Introduction

UHMWPE parts are widely used, in pure or blended form, in many applications such as food and beverage, foundry, chemical processing, mining, lumber, textile, paper, transportation and medical applications [104]. It is difficult to

process UHMWPE by conventional methods due to its high molecular weight [112, 182]. Therefore, powder processing techniques have been used as an alternative option to manufacture UHMWPE parts including powder compression moulding, ram extrusion and compaction followed by sintering [120, 161]. However, the limited processing options restrict the applications of UHMWPE [182]. The processing of UHMWPE can be enhanced by adding high thermally conductive fillers in to the UHMWPE matrix, such as carbon black, graphite, carbon nanotubes or activated carbon [104, 110, 183].

Activated carbon (AC) is an effective and reliable material in removing impurities and has a large adsorptive capacity. It has an attraction for a vast number of dissolved organics and chlorine. It can also be custom tailored to suit particular applications. AC is used in a wide range of applications including water and gas purification, air filters in gas masks and respirators, medicine, air pollution control, energy storage, fuel cells, batteries and many other applications [130, 132, 133, 184, 185]. AC is a widely available material at a very low cost and it can be used as an ideal filler or matrix material for a range of applications [104].

The aim of the characterisation process is to obtain a better understanding of the material requirements and provide a detailed insight on whether AC-UHMWPE composite powder can be a suitable material for laser sintering.

7.3 Materials

UHMWPE (GUR 2122), supplied as a powder by Celanese (Germany), was used in this work. Detailed characterisation of UHMWPE (GUR 2122) has been reported earlier in section 4.3, Chapter 4.

Powdered Activated Carbon (PAC) produced from coconut shell with a mesh size of 60x200 (250–75 µm) was supplied by Eurocarb Products Ltd (UK) and manufactured by high temperature steam activation in Sri Lanka. PAC product specification is listed in Table 7.1 as provided by the supplier (Eurocarb datasheet – YAO 60x200 AW).

Table 7.1: Powdered Activated Carbon (PAC) specification

Particle size (µm)	Bulk Density, Dry (g/cm^3)	Surface Area (m^2/g)	Ash content (%)	pH	Moisture content (%)
75 – 250	0.440-0.490	1250	1 (max)	6-8	5 (max)

7.4 Preparation of AC-UHMWPE Composites

The UHMWPE and AC powders were sieved separately to remove large agglomerated particles. UHMWPE powder was then dry mixed with AC using a tumbler mixer (Mixing station P1, EOS GmbH, Germany) for 60 minutes approximately. The mixing ratios used were 70% AC-30% UHMWPE, 80% AC-20% UHMWPE and 85% AC-15% UHMWPE (weight/weight). Sample labels are shown in Table 7.2.

Table 7.2: Powders sample labels

Sample labels	PE100	PE30	PE20	PE15	AC100
UHMWPE (%)	100	30	20	15	0
AC (%)	0	70	80	85	100

7.5 Characterisation Methods of AC-UHMWPE Composites

7.5.1 Powder Particle Size and Morphology

Both particle size and morphology of UHMWPE powder were reported in section 4.3.1, Chapter 4. The particle size of AC was determined and the microstructure of the AC-UHMWPE composite powder was investigated.

A Mastersizer 3000 (Malvern Instruments, UK) was used to determine the particle size of AC powder, by using laser diffraction method. The specimen was characterised by the dry powder dispersion method using air as the media. The distribution of the particle size was determined at a feed pressure of 3bar and 10 measurements were taken from the available specimen.

The microstructure of the AC-UHMWPE powder was examined using a scanning electron microscope (Philips XL-20, Holland) at an accelerating voltage of 13 kV. In order to prepare a sample for examination, a sample holder with adhesive tape, was dipped in the composite powder and then was shaken up to remove the excess leaving a small number of particles. The sample was gold sputtered before the examination.

7.5.2 Powder Density and Flow

The true density of AC, bulk and tapped densities of AC-UHMWPE powder were measured, and the powder flow was investigated.

The true density of AC powder was measured by helium gas pycnometer (Micromeritics AccuPyc II 1340, USA). The bulk and tapped densities and powder flow of AC powder were carried out as described in section 4.3.2, Chapter 4.

For the composite powders, densities were measured according to the rule of mixtures. This assumes that a composite property is the volume weighed average of the phases (matrix and dispersed phase) properties. Therefore, the composite density were calculated using the following equation [186]:

$$\rho_c = f \times \rho_{UHMWPE} + (1 - f) \times \rho_{AC} \qquad (13)$$

$\rho_c, \rho_{UHMWPE}\ and\ \rho_{AC}$ are the densities of the composite, UHMWPE and AC powders, respectively. $f\ and\ (1 - f)$ are the volume fractions of UHMWPE and AC powders respectively.

7.5.3 Differential Scanning Calorimetry (DSC)

The thermal properties of the composites powders were measured at a heating rate of 10°C/min by DSC method (Perkin Elmer DSC 8500) from 25 to 220°C under a nitrogen atmosphere. DSC curves of AC-UHMWPE composites were obtained under two thermal cycles and three samples were tested for each set of parameters. The weight of the samples was 7.1 mg on average.

7.5.4 Thermogravimetric Analysis (TGA)

This analysis was performed to determine the amount of UHMWPE and activated carbon used in the composites powders and to examine the influence of the composition on the thermal stability of the composites.

The TGA method was described in section 4.3.5, Chapter 4. The mass fraction percentages were calculated using the onset and delta Y methods as shown in Figure 7.1.

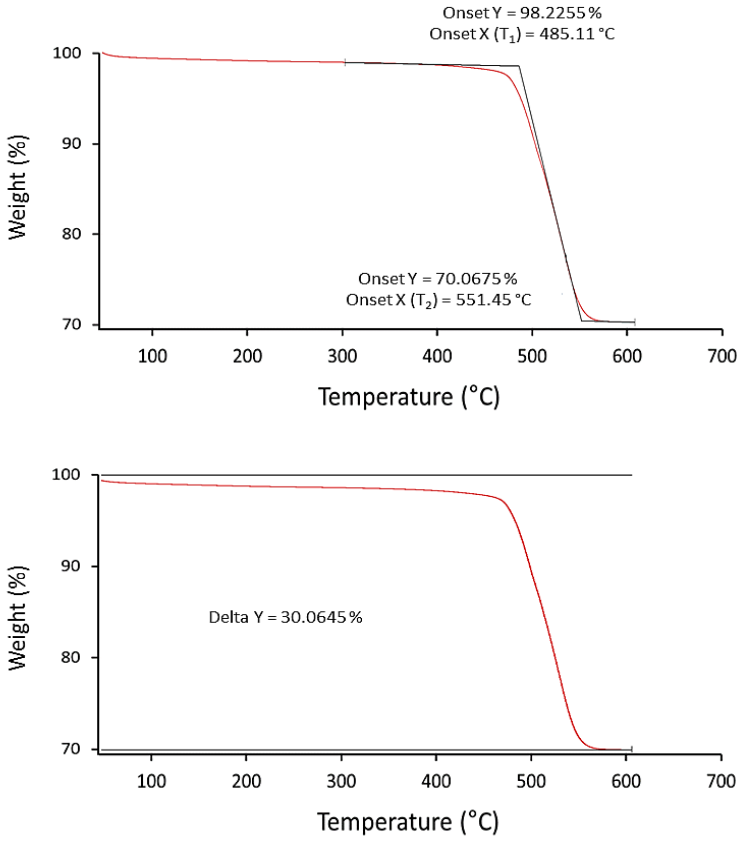

Figure 7.1: Onset temperature (top) and delta Y (bottom) calculation methods.
T_1 and T_2 are the initial and final onset decomposing temperatures, respectively.

The extrapolated onset temperature, which refers to the temperature at which the weight loss begins, is the intersection point of two lines drawn tangent to the two linear regions of the TGA curve, (Figure 7.1). The onset temperature was used because it is a reproducible temperature from the calculation. This temperature is also recommended to be used by both ASTM E1131 and ISO 11358 standards. The delta Y, the change in mass, was used to measure the "as run" sample and determine the mass fraction percentages.

7.5.5 X-Ray Diffraction Analysis (XRD)

XRD analysis was performed using a Bruker D8 Advance X-ray diffraction system, equipped with a Cu Kα radiation source with a wavelength, λ, of 0.15418 nm generated at 40 kV and 40 mA. AC-UHMWPE powder samples were mounted on the stage and scanned from 10° to 70° using a step size of 0.05° and time/step of 10 seconds. Two samples were tested.

7.5.6 Degree of Crystallinity

The estimated degree of crystallinity of AC-UHMWPE powder was determined using DSC and XRD methods. The effect of mass fraction of activated carbon on the overall crystallinity was investigated.

Differential Scanning Calorimetry: DSC was used to determine the overall degree of crystallinity of AC-UHMWPE composites. The degree of crystallinity (X_C) was calculated using the following equation [28, 30, 187]:

$$X_C(\%) = \left(\frac{\Delta H}{\Delta H_{100} \times (1-W_f)}\right) \times 100 \qquad (14)$$

Where ΔH is the melting enthalpy of the AC-UHMWPE composite powder, ΔH_{100} is the melting enthalpy of polyethylene containing 100% of crystallinity, which is 293 J/g [161] and W_f is the weight fraction of activated carbon. The average of three DSC measurements was used to determine the overall crystallinity of the samples.

X-ray diffraction: The diffraction peaks at around 15° - 30° of the AC-UHMWPE composites were a mixture of the diffraction peaks of neat UHMWPE and AC. The crystallinity was calculated using the area of crystalline peaks in the region of 2θ between 15 and 30° and the area of the diffuse background of the amorphous in this region, which was estimated using a Gaussian function (Figure 7.2). The crystallinity was then calculated using the following equation:

$$X_C(\%) = \frac{A_C}{A_C + A_A} \times 100 \qquad (15)$$

Where A_C represents the area of crystalline phase and A_A is the area of amorphous phase.

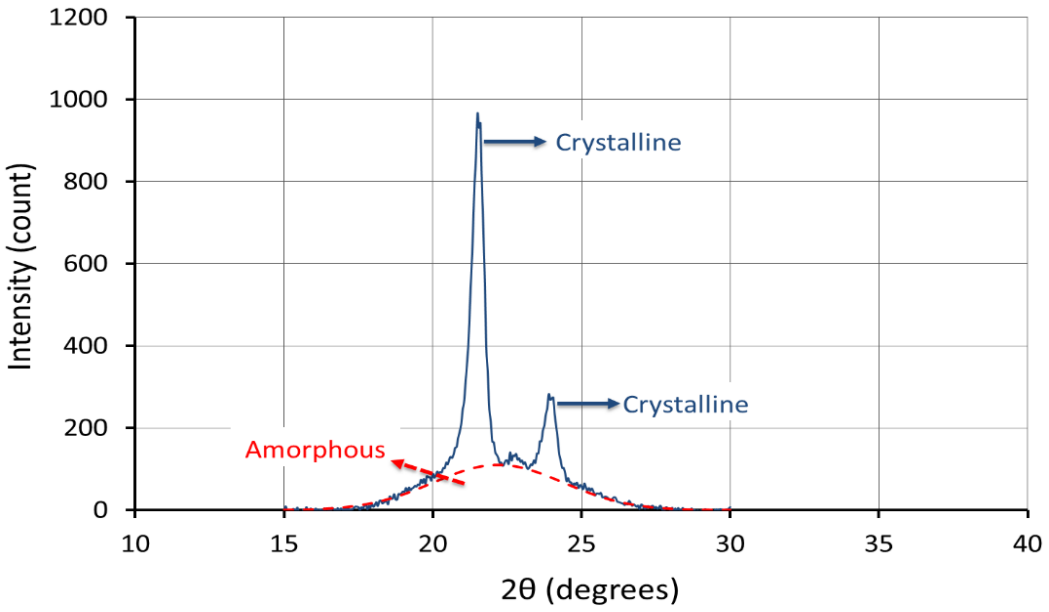

Figure 7.2: XRD data fitted with Gaussian function showing the amorphous fraction

7.6 Results and Discussion

7.6.1 Powder Particle Size and Morphology

The result presented in Figure 7.3 shows that the average particle size of AC used in this work was 196 µm (d_{50}), while 10% of the AC particles were larger than 344 µm (d_{90}) and 10% of the particles were less than 92.2 µm (d_{10}).

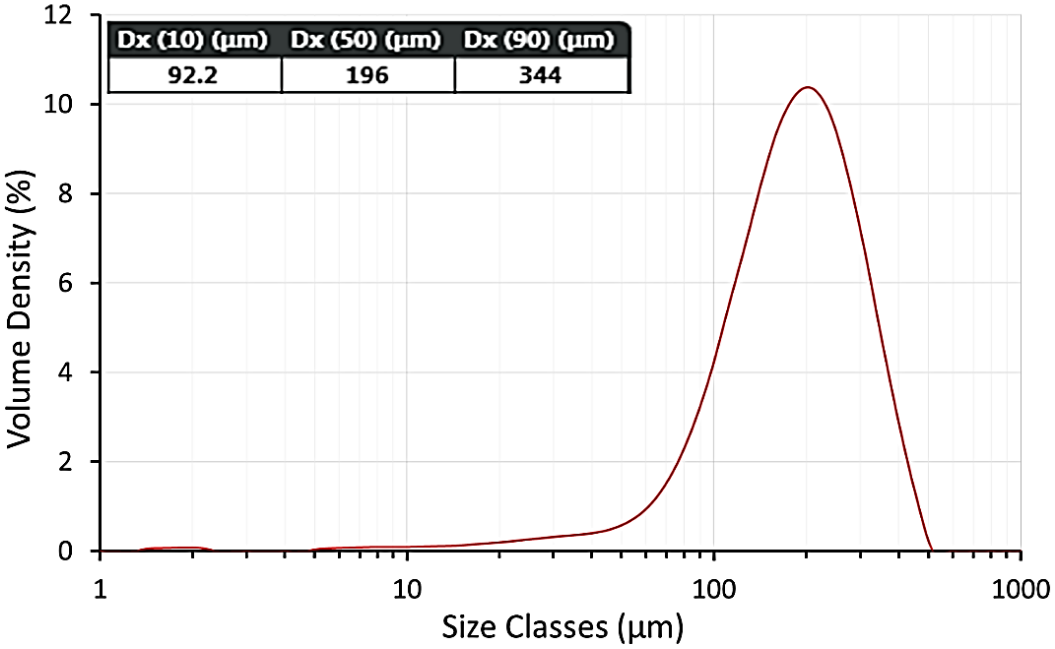

Figure 7.3: Particle size distribution of AC powder

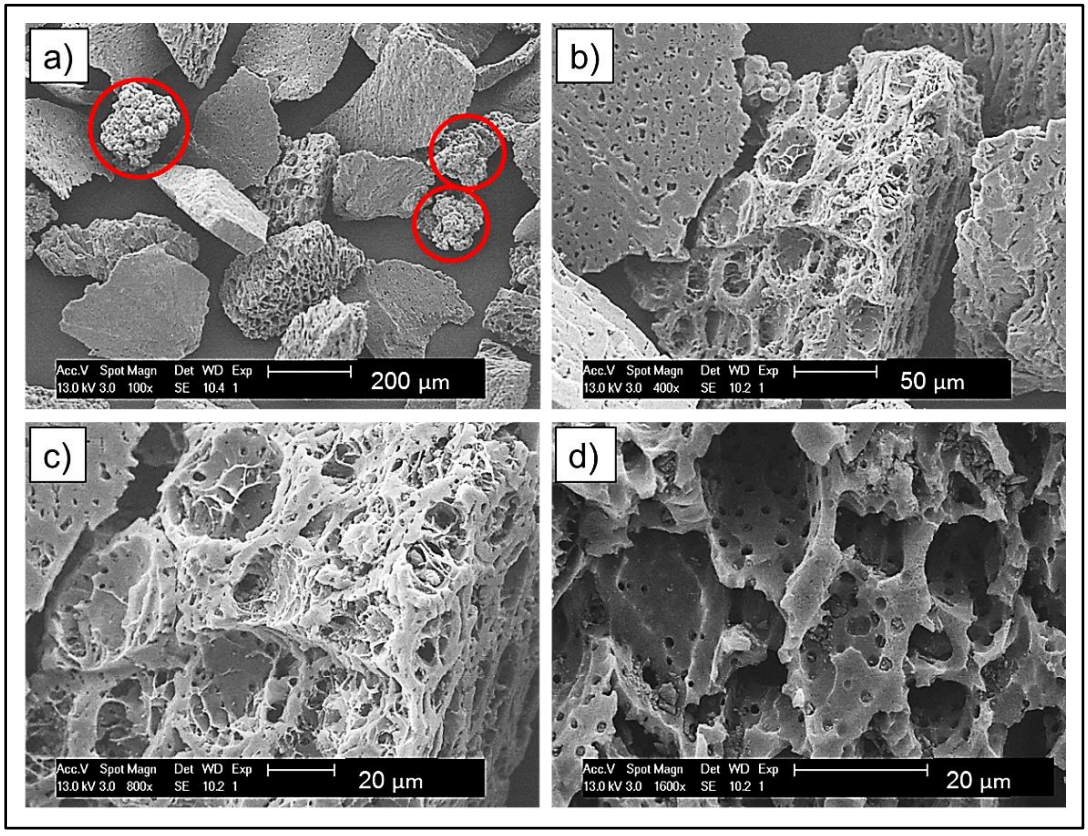

Figure 7.4: SEM images of un-sintered AC-UHMWPE powder
Magnifications: a) 100x, b) 400x, c) 800x and d) 1600x
(UHMWPE particles are highlighted in red circle)

SEM examination reveals the textural and morphological properties of AC powder. The highly porous particles have irregular shape with a wide variety of pores is present as shown in Figure 7.4. Well-developed large pores with honeycomb shapes could be observed on the surface of the particles.

7.6.2 Powder Density and Flow

The true density of AC powder was measured using helium gas pycnometer (Micromeritics AccuPyc II 1340, USA) and was found to be 2.1718 g/cm^3. The results of the measurements of the densities (true, bulk and tapped) and Hausner ratios are listed in Table 7.3.

Table 7.3: Densities and Hausner ratios of composite materials

Composite ratios	True density (g/cm^3)	Bulk density (g/cm^3)	Tapped density (g/cm^3)	Hausner ratio (HR)
PE100	0.954	0.2321	0.3236	1.39
PE30	1.8065	0.3170	0.4057	1.28
PE20	1.9282	0.3291	0.4175	1.27
PE15	1.9891	0.3352	0.4233	1.26
AC100	2.1718	0.3534	0.4409	1.25

Figure 7.5 shows that the bulk and tapped densities of the composites powders are increased with increasing amounts of activated carbon. This result was expected as the composite density is the product of the densities of UHMWPE and activated carbon (as per the rule of mixtures).

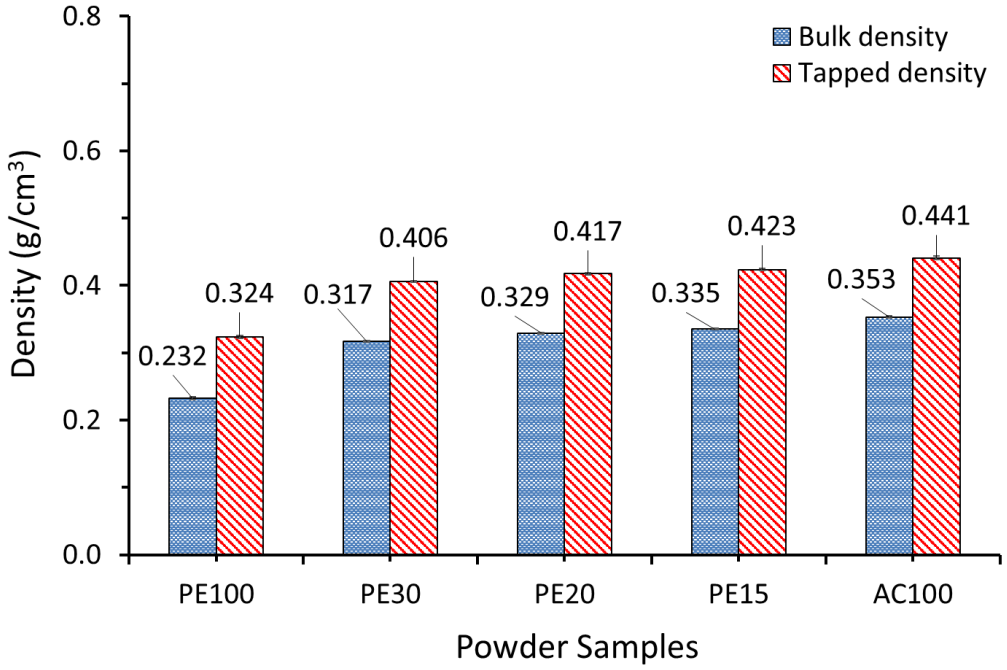

Figure 7.5: Bulk and tapped densities of AC-UHMWPE composites

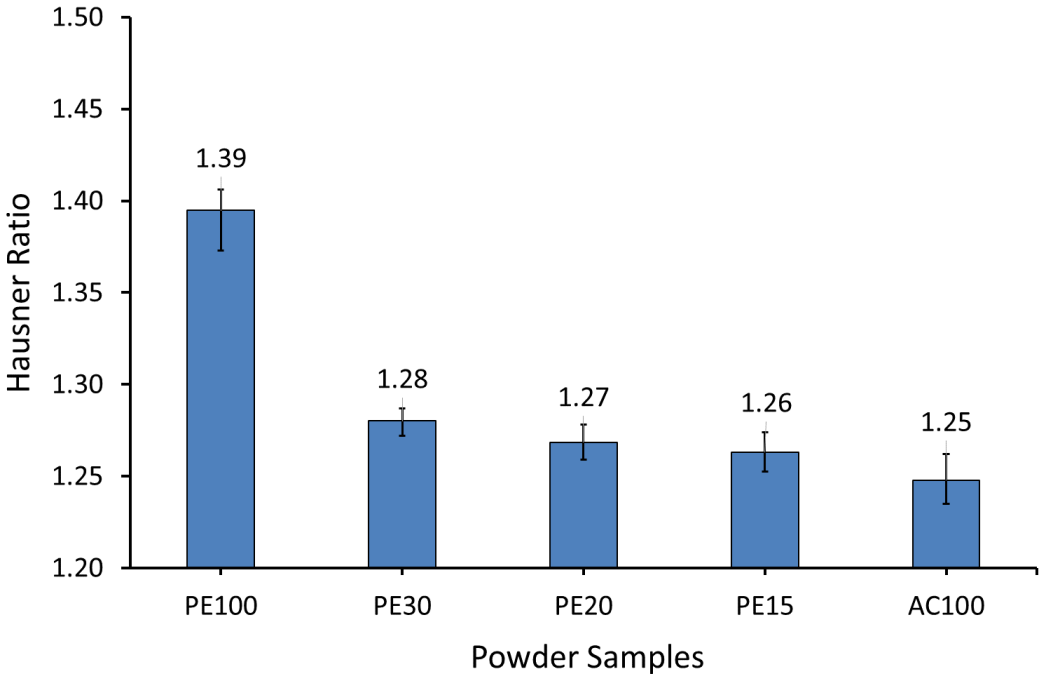

Figure 7.6: Hausner ratios of AC-UHMWPE composite powders

Based on the criteria of distinguishing between cohesive and non-cohesive powder, which was explained in section 4.2.2.2, Chapter 4, the Hausner ratio of the powders was calculated for PE30, PE20, PE15 and AC100 and were found

to be 1.28, 1.27, 1.26 and 1.25 respectively (Table 7.3). The results in Figure 7.6 indicates that the AC powder has high flow and the addition of AC has improved the flow of UHMWPE (original HR = 1.39). This improvement was observed during spreading and distribution of the powder in the laser sintering machine.

The flow of powder could be influenced by the powder particle size. Coarse powders flow easier than fine powders [19]. This influence was evident in this case as the particle size of AC was bigger than the size of UHMWPE particles. Previous study suggested that the flow of the powder increases with the increase of particle size but above the optimum the flow does not show any improvement [21].

7.6.3 Differential Scanning Calorimetry

The thermal properties of the neat UHMWPE and the AC-UHMWPE composite powders are summarised in Table 7.4 (melt and crystallisation peaks) and the DSC curves of the first and second thermal cycling are presented in Figure 7.7 and Figure 7.8, respectively.

Table 7.4: Thermal properties of neat UHMWPE and composite powders

Sample ID	1st Thermal cycle		2nd Thermal cycle	
	Melting point peak (°C)	Crystallisation point peak (°C)	Melting point peak (°C)	Crystallisation point peak (°C)
PE100	141.24	117.27	133.98	117.18
PE30	140.43	118.64	132.94	118.51
PE20	139.58	118.63	132.56	118.52
PE15	139.35	118.76	132.52	118.61

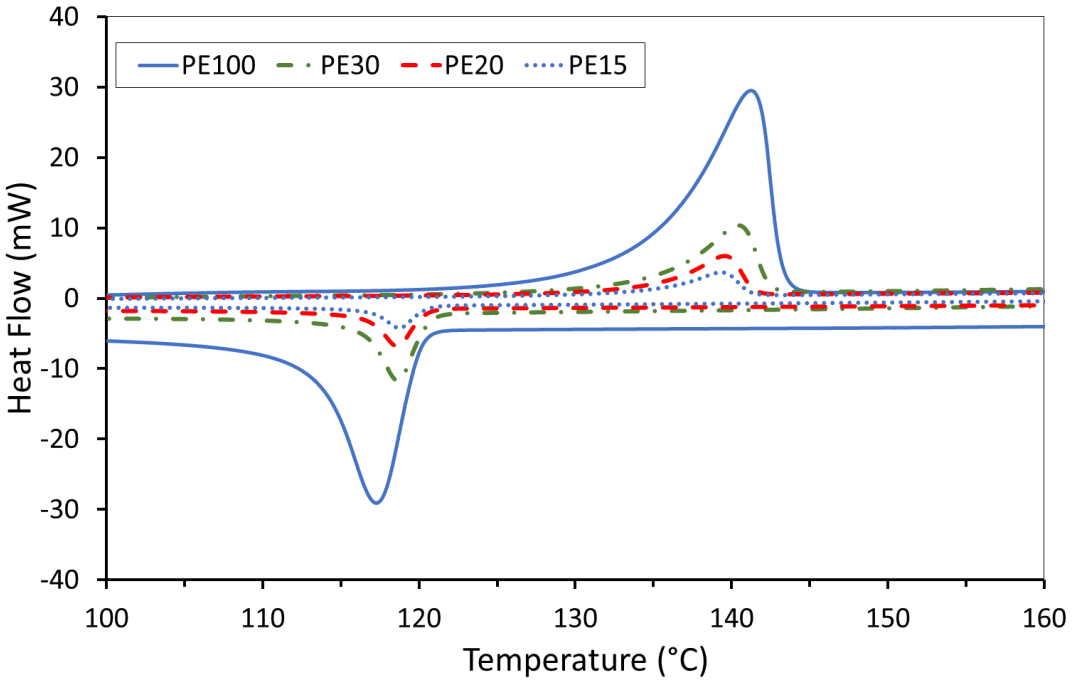

Figure 7.7: DSC curves of the neat UHMWPE and AC-UHMWPE composites (1st Run)

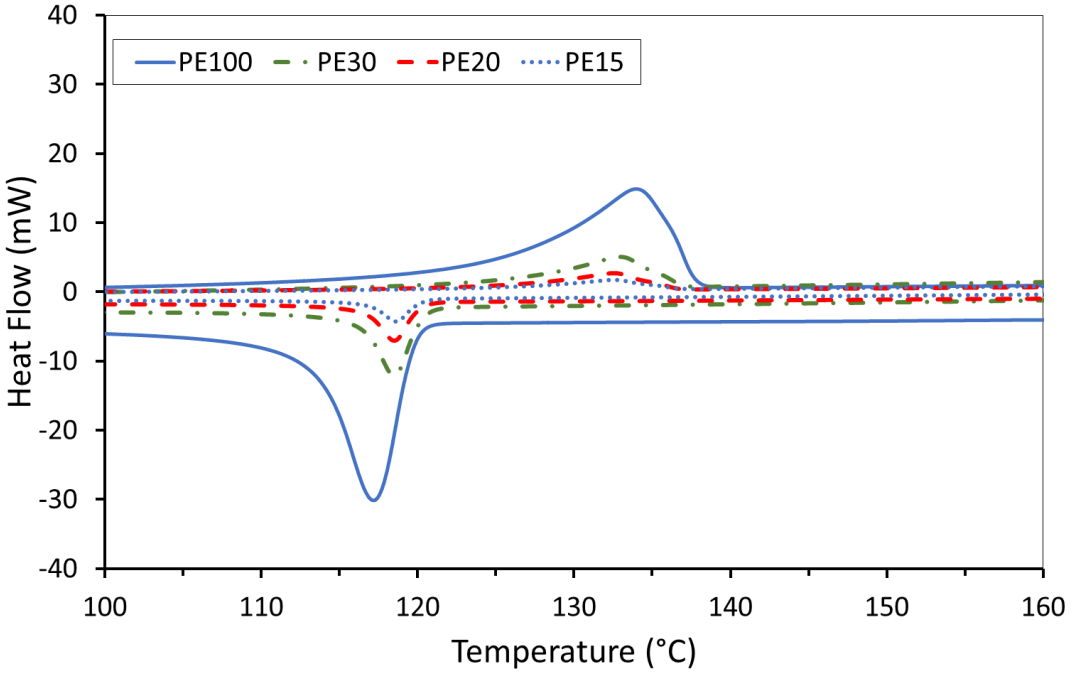

Figure 7.8: DSC curves of the neat UHMWPE and AC-UHMWPE composites (2nd Run)

The results show that the intrinsic thermal properties of UHMWPE powder are not significantly affected by the introduction of activated carbon. A slight change was observed but it is most likely due to measurement error. This result indicates that there was no interaction occurred between the UHMWPE and AC materials at the targeted temperature. However, the crystallisation peaks of AC-UHMWPE composites are less sharp compared to neat UHMWPE, indicating gradual crystallisation kinetics for these composite powders [22].

7.6.4 Thermogravimetric Analysis

TGA curves of neat UHMWPE and AC-UHMWPE composites are presented in Figure 7.9 and the corresponding thermal characteristic data are listed in Table 7.5.

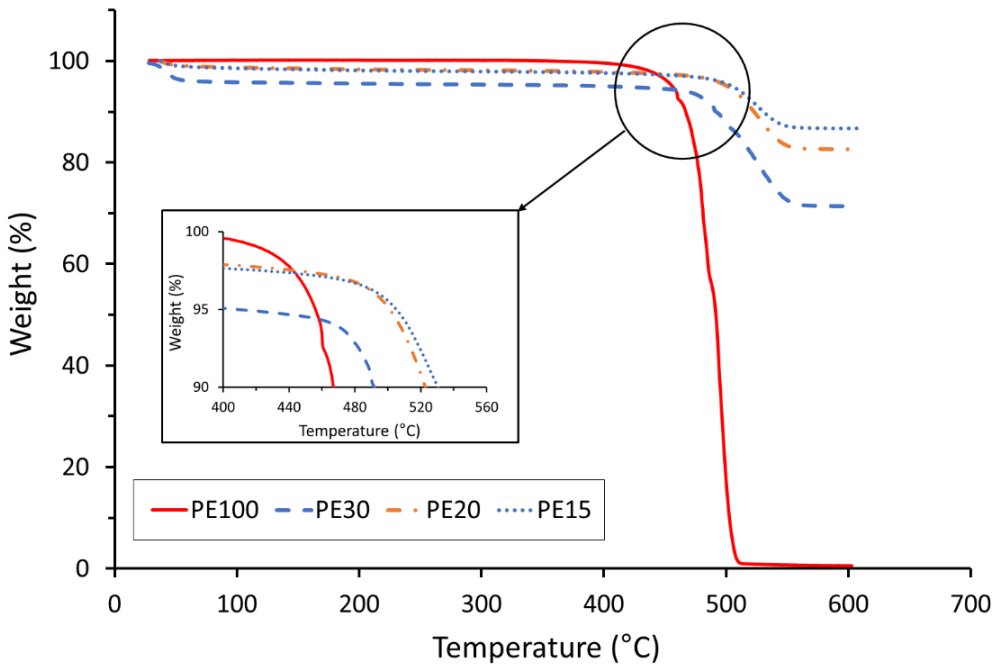

Figure 7.9: TGA results for AC-UHMWPE composite powders

The thermal degradation of the neat UHMWPE starts at around 478°C. The results show that the onset of mass loss is considerably shifted to higher temperatures for the AC-UHMWPE composites. For the composites containing 15 and 20% of UHMWPE, this shift was around 20°C.

This suggests that the thermal stability of the AC-UHMWPE has increased with the increase in the activated carbon content, as shown in Figure 7.10. Activated carbons can preferentially adsorb the volatile degraded UHMWPE components during the degradation process. This could delay the mass loss and retard the thermal degradation, resulting in a higher degradation temperature of the composites compared to that of the neat UHMWPE.

Table 7.5: TGA analysis thermal data of neat UHMWPE and AC-UHMWPE composites

Sample ID	Onset Temperature (°C)		UHMWPE mass (%)		
	T_1*	T_2*	Theory	Actual (Delta Y)	Actual (Onset)
PE100	478.84	503.92	100	99.48	98.75
PE30	483.36	543.09	30	31.70	26.39
PE20	498.18	547.61	20	17.35	15.01
PE15	497.03	545.03	15	13.33	10.77

** T_1 and T_2 are the initial and final decomposing temperatures respectively.*

The sample mass of the composites remained constant at temperatures above 550°C (Figure 7.9), effectively allowing a verification of the actual UHMWPE content. As can be seen in Figure 7.11, there is a slight disagreement between the intended and actual UHMWPE weight fractions. The reason for the observed disagreement is related to the inconsistency caused by the manual mixing technique and the sampling, by using a scoop, and the small amount of powder used when preparing TGA samples. This issue would be less evident when using mechanical mixing, such as tumbling mixers with larger quantities of powders.

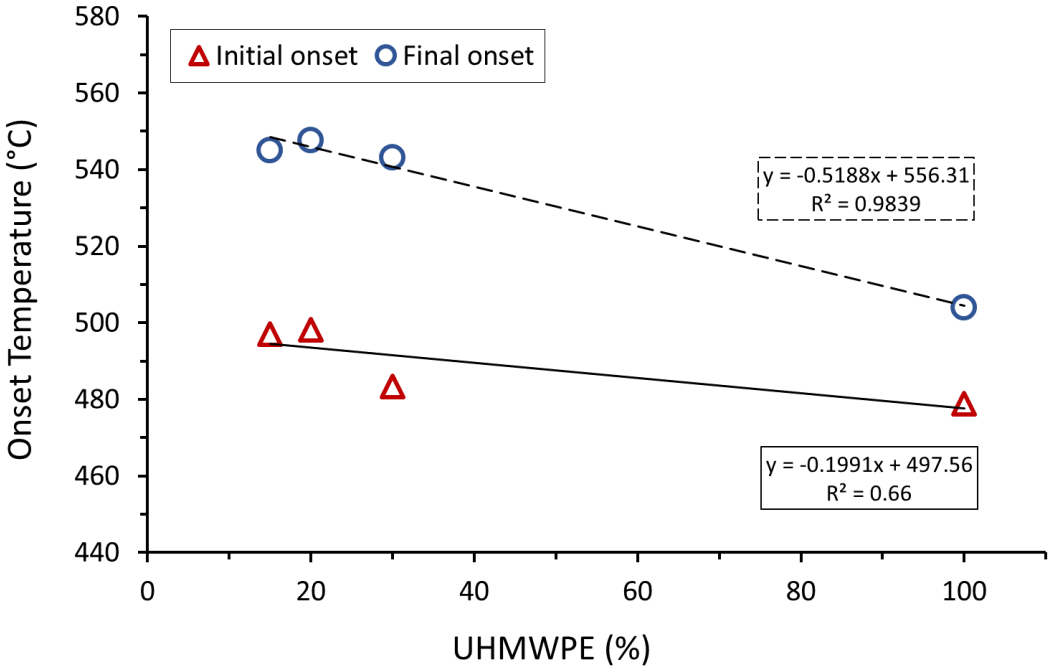

Figure 7.10: Effect of AC addition on thermal stability of UHMWPE

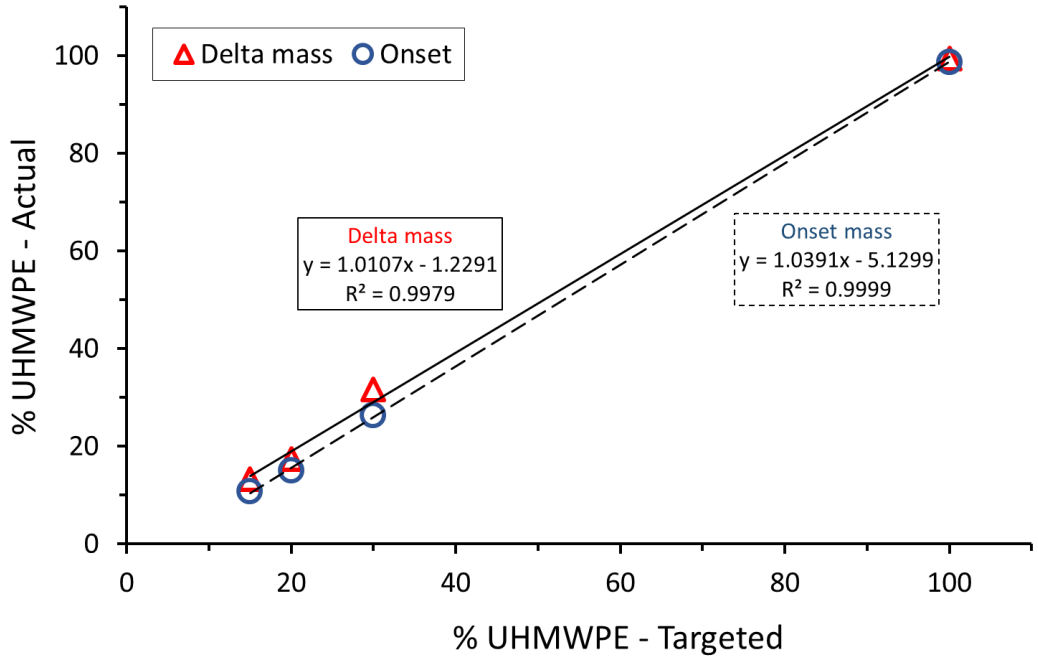

Figure 7.11: Actual UHMWPE weight fractions in the composite powders measured by TGA

7.6.5 X-Ray Diffraction Analysis

The XRD spectrum for UHMWPE and AC powders is shown in Figure 7.12. The XRD pattern of AC shows broad peaks and the absence of sharp peaks suggests a predominantly amorphous structure, which is a typical characteristic of AC [188, 189]. Two broad peaks were observed at 2θ = 22.9° and 2θ = 44.15° which correspond to the reflections of (002) and (101) planes, respectively [190].

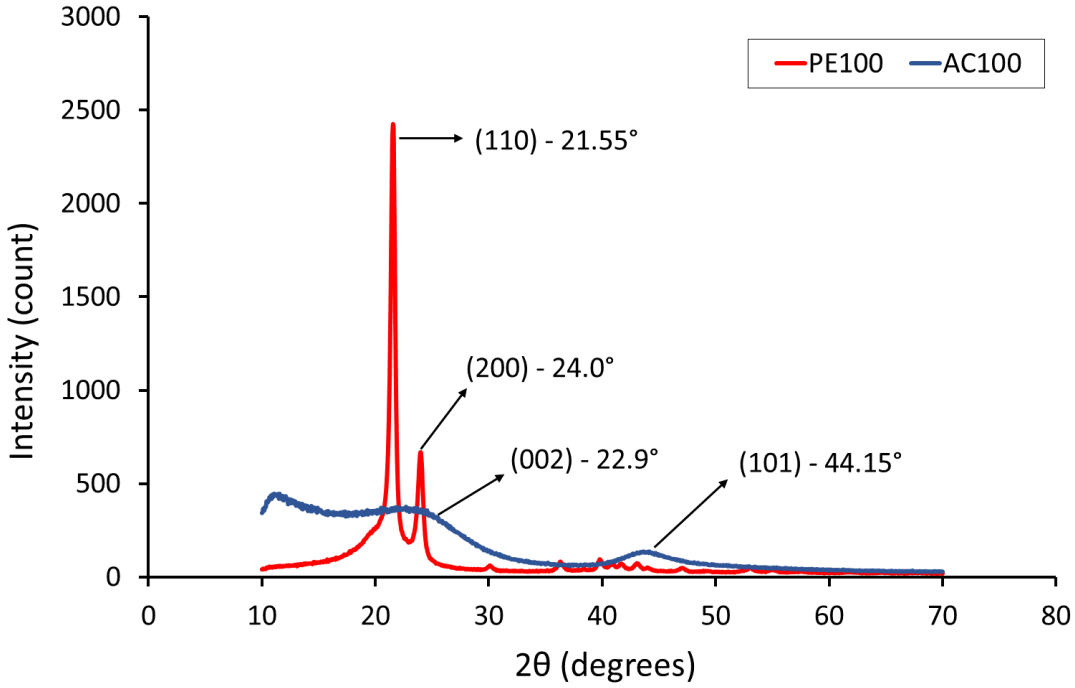

Figure 7.12: XRD profile of neat UHMWPE and activated carbon powders

The XRD patterns of AC-UHMWPE composites PE30, PE20 and PE15 are shown in Figure 7.13. Two sharp peaks can be observed at 2θ = 21.5° and 24.05°, which were assigned to the (110) and (200) crystal planes, respectively [165]. The broad range of 2θ angles covering between 16–26° occurred as a result of the amorphous phase [31]. The sharp peaks of (110) and (200) crystal planes were 21.5°, 21.5°, 21.55° and 24.05°, 24°, 24° for PE30, PE20 and PE15 respectively, The XRD profiles of the AC-UHMWPE composites show a new weak and wide diffraction peak near 2θ = 43.0°, which is assigned to the (101) diffraction

planes of graphitic carbon coming from activated carbon and confirming its amorphous state [182].

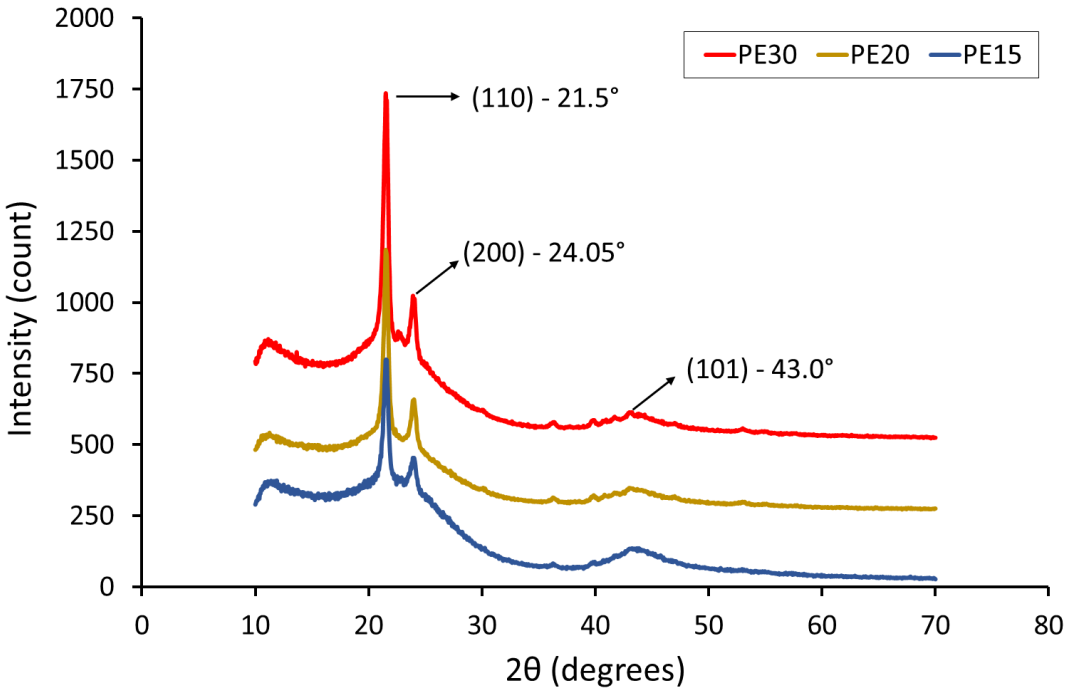

Figure 7.13: XRD profile of AC-UHMWPE composite powders

The results show that there is no noticeable difference in the XRD patterns of the AC-UHMWPE composites (PE30, PE20 and PE15) and no obvious shift of diffraction peak positions can be observed. This result suggests that the ratio of the unprocessed AC-UHMWPE composite does not affect the microstructure of the composite materials.

7.6.6 Degree of Crystallinity

The estimated degree of crystallinity of AC-UHMWPE powder was determined using DSC and XRD methods. The effect of mass fraction of activated carbon on the overall crystallinity was investigated.

DSC measurements were performed to determine the crystallinity of the AC-UHMWPE composite powders (i.e. PE30, PE20 and PE15). Figure 7.14 shows that the crystallinity of the first heating cycle has increased slightly with the decrease of the mass fraction of activated carbon. All the data was normalised

for the mass of UHMWPE. This result was unexpected since the tests were performed on untreated powders (virgin powders). The composite powders were mixed mechanically and no interaction should occur between the materials of the composite under the specified test temperature and therefore the crystallinity of untreated AC-UHMWPE composites should remain unchanged with the change of the composite content ratios.

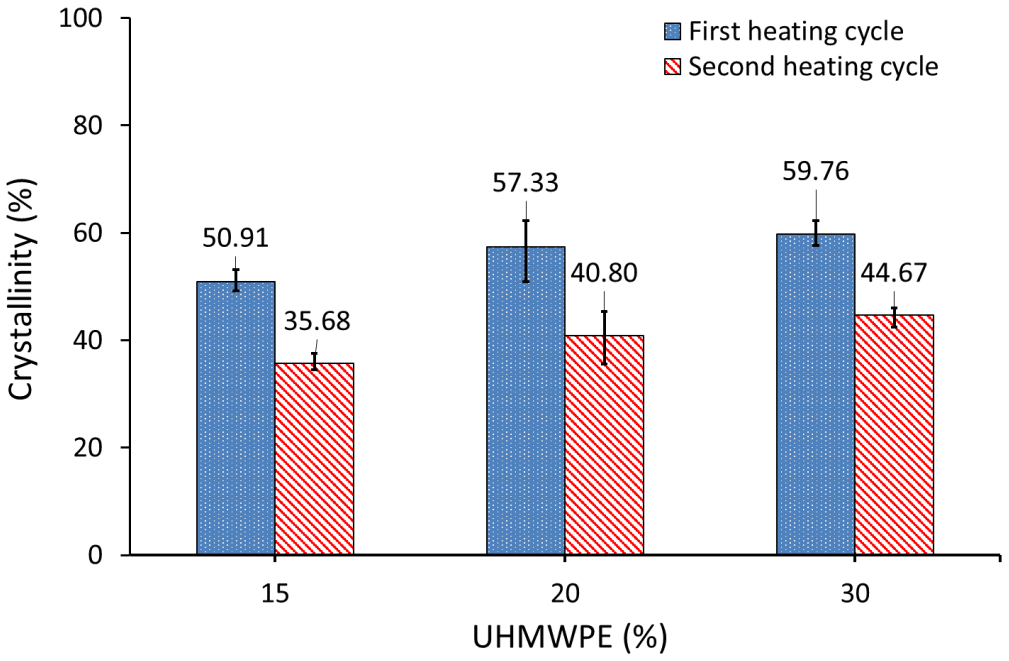

Figure 7.14: Degree of crystallinity of AC-UHMWPE composites measured by DSC

One of the reasons for the observed disagreement could be related to the inconsistency caused by the manual mixing method and sampling error when preparing DSC samples. However, these changes in crystallinity could be also influenced by the high thermal conductivity of the activated carbon and un-uniform temperature distribution across the DSC pan. The key to obtaining good data in this scenario lies in minimising the effect of un-uniform temperature distribution and this can be done by coating the aluminium pan with a thin coating of silicon oil before placing the powder in the pan.

The composite powder samples were placed directly in the DSC pan, after coating with a thin layer of a silicone oil to improve the thermal contact

between the pan and the test sample. The pan on the reference side was coated as well with the silicone oil.

Figure 7.15 shows that the degree of crystallinity of AC-UHMWPE composites did not change, in the first heating cycle, with the change of the mass fraction of activated carbon. This result has confirmed our initial prediction regarding the crystallinity behaviour of untreated AC-UHMWPE composites. However, the degree of crystallinity in the second heating cycle of AC-UHMWPE composites decreased with increasing the mass fraction of activated carbon.

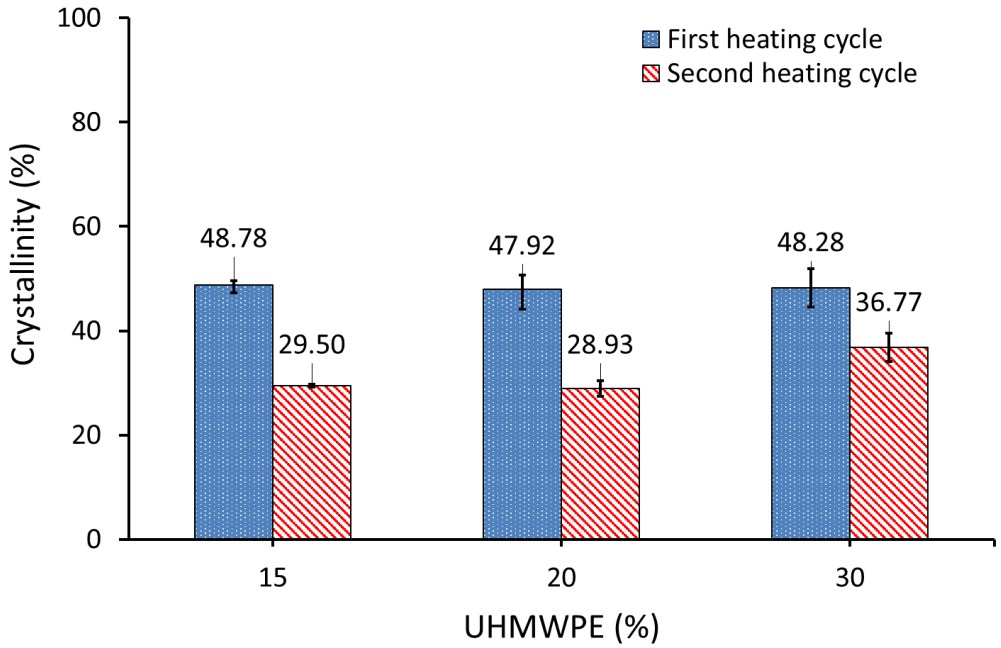

Figure 7.15: Degree of crystallinity of AC-UHMWPE composites measured by DSC. DSC pan was coated with silicone oil

Table 7.6 shows the degree of crystallinities of AC-UHMWPE composite powders calculated from the first heating (X_{C1}) and second heating (X_{C2}) cycles of the DSC, and also the crystallinity obtained by XRD measurements (X_{C3}). The degree of crystallinity of the neat UHMWPE (PE100) was decreased from 57.45% to 48.28% (using DSC) and from 67.80% to 61.35% (using XRD) for AC-UHMWPE composite with 70% AC and 30% UHMWPE (PE30). The three AC-UHMWPE composite samples (i.e. PE30, PE20 and PE15) showed

statistically insignificant changes in crystallinity confirming that the change in the composition ratio of untreated composite does not have a significant effect on the degree of crystallinity. This slight change is most likely due to sampling or measurement error since there is no mechanism or process that took place and affect the crystallinity of the composite powders.

Table 7.6: Degree of crystallinity of neat UHMWPE and AC-UHMWPE composite powders

Sample ID	Crystallinity (%) - DSC		Crystallinity (%) - XRD
	X_{C_1}	X_{C_2}	X_{C_3}
PE100	57.45 ±3.70	43.10 ±1.24	67.80 ±8.50
PE30	48.28 ±3.70	36.77 ±3.86	61.35 ±3.65
PE20	47.92 ±3.40	28.93 ±1.51	57.15 ±2.95
PE15	48.78 ±1.34	29.50 ±0.31	56.10 ±0.20

From the degree of crystallinity values presented in Table 7.6, it was observed that the crystallinities calculated from XRD and DSC are not in good agreement. The average values of the XRD results were higher than that of the DSC (first heating cycle) by 10.35%, 13.07%, 9.23% and 7.32% for the PE100, PE30, PE20 and PE15 powders, respectively. The degree of crystallinity values calculated using DSC and XRD may differ from one another due to a number of reasons including the sample size and the random selection of the sample from the bulk powder used in DSC, and also the differences in the way the background and amorphous scattering are determined in XRD which introduces some subjectivity to the calculation. Generally, the crystallinity measured by XRD method shows higher values compared to DSC method. This is a widely known issue in polymer systems as these methods measure two different properties [163].

7.7 Laser Sintering Trials of AC-UHMWPE Composite

A commercial laser sintering system EOS Formiga P100 was used to manufacture test samples from AC-UHMWPE powder. Before sintering the test samples, a range of processing conditions were attempted so that suitable parameters can be obtained for processing the parts. Based on the experience gained from sintering UHMWPE, laser power of 8 watts and laser scan speed at 2500 mm/s with a range of powder bed temperatures starting from 135, 125, 120, 117.5, 115 and 110°C were initially attempted in order to find the suitable bed temperatures to achieve a good powder flow and produce multilayer parts. Since the removal chamber temperature does not have significant effect on the process as well as the parts quality, therefore it was set to the same temperature as the bed temperature for all trials. A layer thickness of 0.1 mm, laser count of 2 (double scan) and hatch spacing of 0.15 mm were fixed for all trials. The laser sintering parameters selected for the initial trials are listed in Table 7.7. The composite virgin powder was used for the initial trial was PE30 powder with 70% AC and 30% UHMWPE by weight (70:30 AC-UHMWPE).

Table 7.7: Laser sintering parameters of the initial trials

Parameter	Unit	Initial Range
Laser Power	watts	8
Bed Temperature	°C	110, 115, 117.5, 120, 125, 135
Removal Chamber Temperature	°C	110, 115, 117, 120, 125, 135
Laser Scan Speed	mm/s	2500
Hatch Spacing	mm	0.15
Laser Count	-	2 (double scan)
Layer Thickness	mm	0.1

The laser sintering process and sintered parts of the initial trials were assessed visually and also by manual handling of the parts. A bed temperature ranges between 110˚C and 120˚C were found to be suitable in terms of spreading of powder, reducing the effect of curling, producing multilayer parts, ease of powder removal and cleaning,. However, observations during laser sintering showed that the composite powder flows much better at bed temperatures of 117.5 ˚C and 120˚C. Additionally, powder removal was easier at these temperatures.

Figure 7.16 shows AC-UHMWPE test parts were produced with good definition and good mechanical properties.

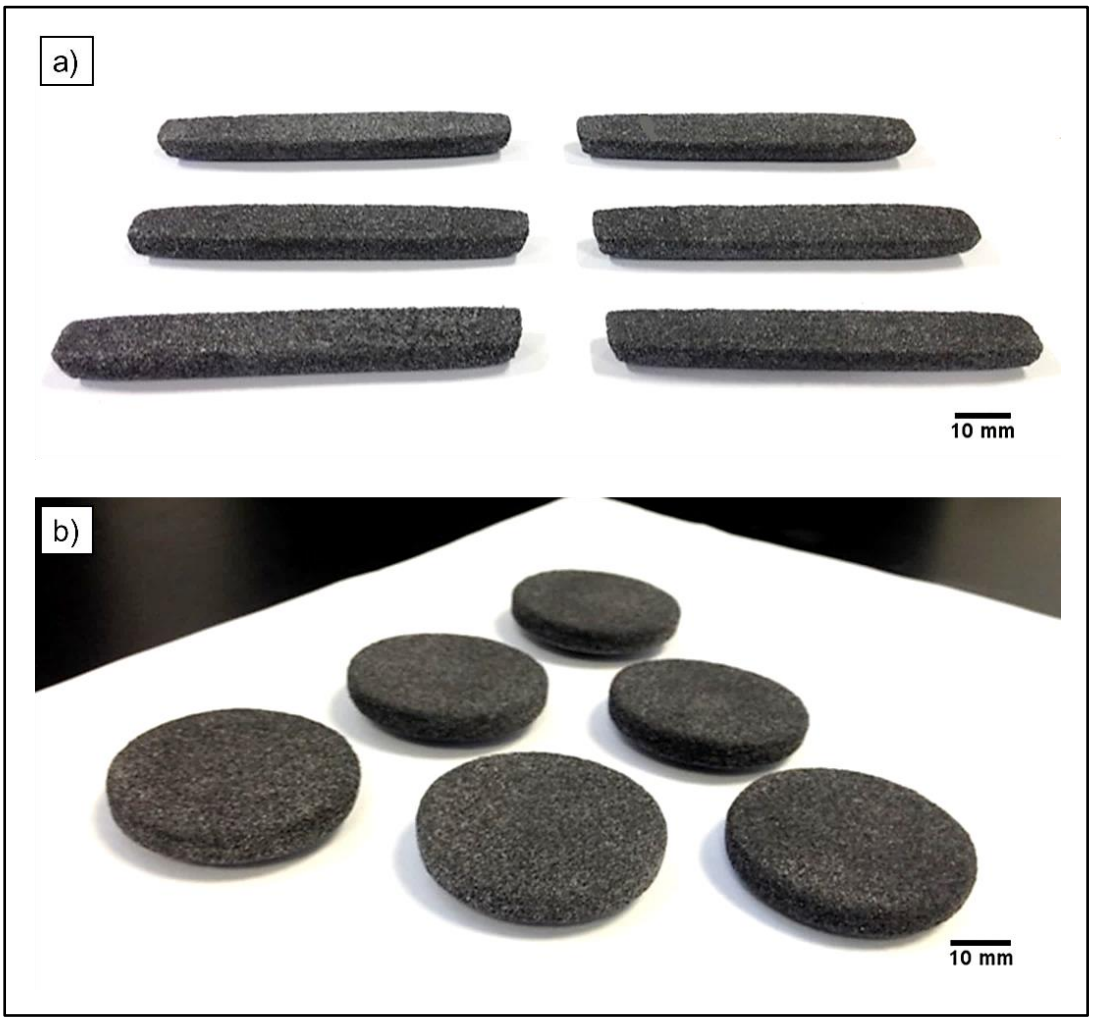

Figure 7.16 : AC-UHMWPE test samples produced at laser power of 8 watts
a) Three point bend samples, b) Water flow rate test samples

After identifying the suitable bed temperature, new sets of samples were produced with laser powers of 6, 8, 10 and 12 watts in order to establish the range of laser powers that can be used and worked with to produce well-defined multilayer parts with a good strength. The laser sintering parameters selected for this test are listed in Table 7.8. A fixed bed temperature of 117.5 ˚C was selected for all samples.

Laser sintered parts with a length of 80 mm, width of 10 mm and thickness of 4 mm (according to ISO 178), were built in x-y orientation with the long axis parallel to the x-axis, width parallel to the y-axis and thickness parallel to z-axis (i.e. build direction) as illustrated in Figure 5.1, in chapter 5.

Table 7.8: Laser sintering parameters used to identify suitable laser powers range of the initial trials

Parameter	Unit	Initial Range
Laser Power	watts	6, 8, 10, 12
Bed Temperature	°C	117.5
Removal Chamber Temperature	°C	117
Laser Scan Speed	mm/s	2500
Hatch Spacing	mm	0.15
Laser Count	-	2 (double scan)
Layer Thickness	mm	0.1

Laser sintered AC-UHMWPE parts were successfully manufactured using various laser powers. Sintered parts were manufactured with well-defined structure and good mechanical properties (Figure 7.17).

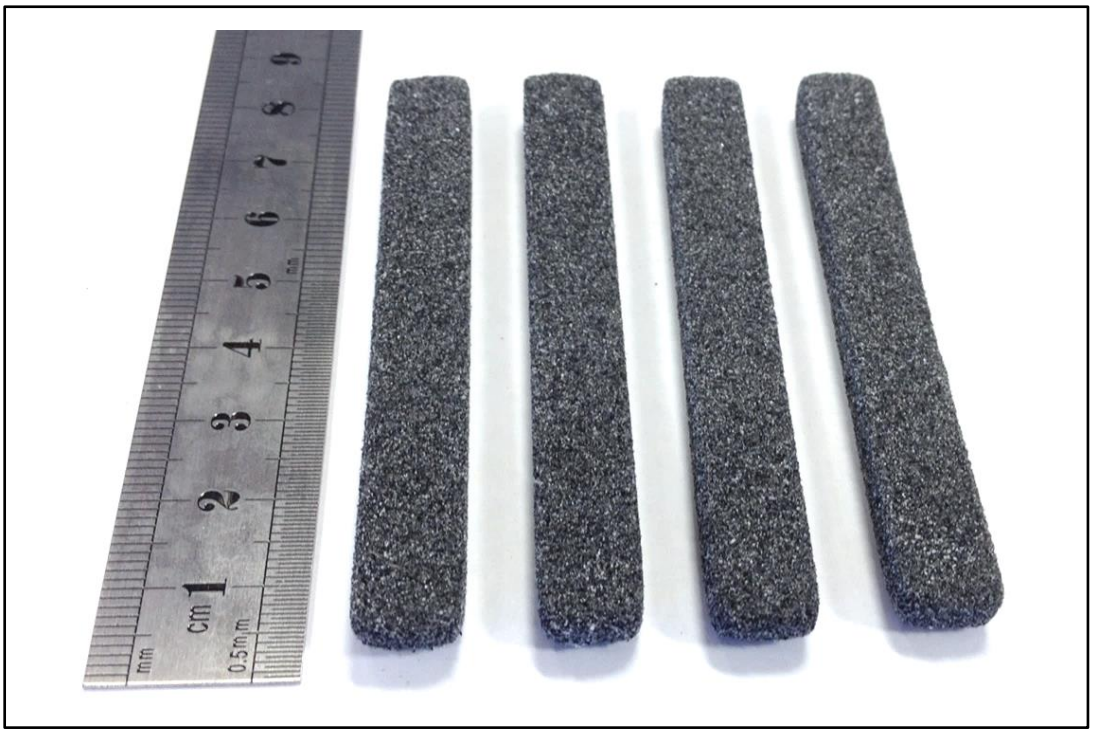

Figure 7.17 : Laser sintered flexural test samples produced at laser power of 12 watts

7.7.1 Relative Density

Relative density is the ratio of the bulk density of the parts to the density of the material composing the parts (i.e. theoretical density or true density of the powder) and was calculated as described in section 5.3, 0.

Results presented in Figure 7.18 shows the relative density of 70:30 AC-UHMWPE samples produced at laser powers of 6, 8, 10 and 12 watts and a bed temperature of 117.5°C. Results showed statistically insignificant changes in the relative density with the change in laser power in the range between 6 and 12 watts. This result suggests that the density of the laser sintered AC-UHMWPE parts is mainly governed by the matrix (i.e. activated carbon) and the changes in laser power did not alter the overall density of the parts significantly.

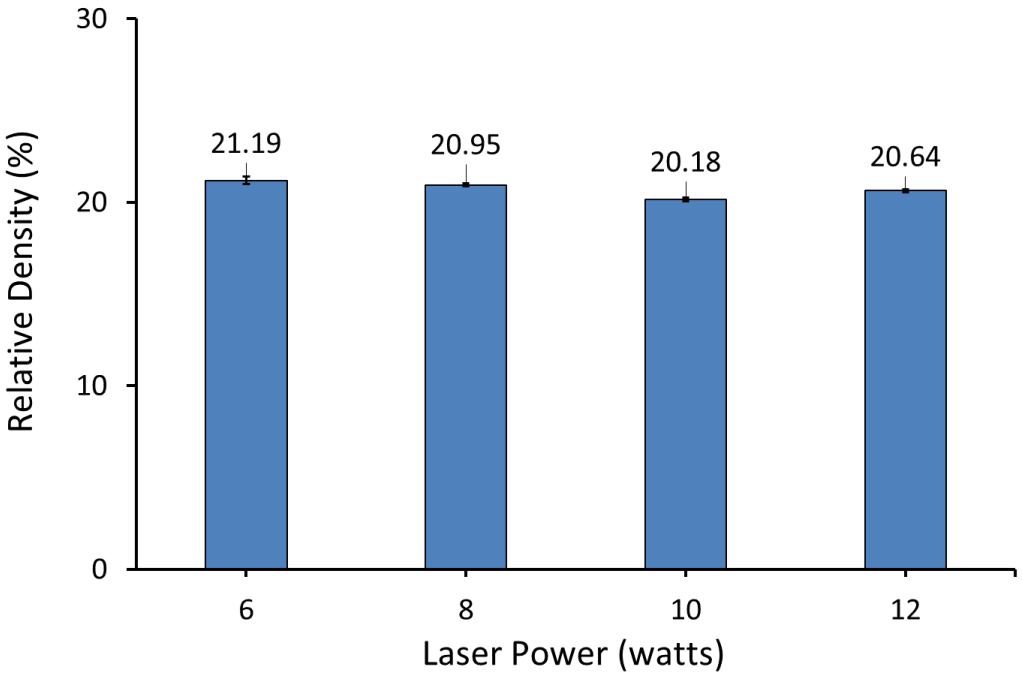

Figure 7.18 : Relative density of 70:30 AC-UHMWPE produced at various laser powers and bed temperature of 117.5°C

7.7.2 Mechanical Properties

Flexural tests were performed on a Texture Analyser TA500 (TM Lloyd Instruments, UK) fitted with a 50 N load cell. All tests were performed with a constant cross-head speed of 0.4mm/min and span length of 40mm.

Figure 7.19 and Figure 7.20 show the maximum flexural stress and strain of 70:30 AC-UHMWPE samples, respectively, produced at laser powers of 6, 8, 10 and 12 watts and a bed temperature of 117.5°C. The results suggest that the flexural stress remains unchanged within the range of laser power between 6 and 12. However, a slight drop in flexural stress can be observed at laser power of 10 watts and it is likely due to statistical variation.

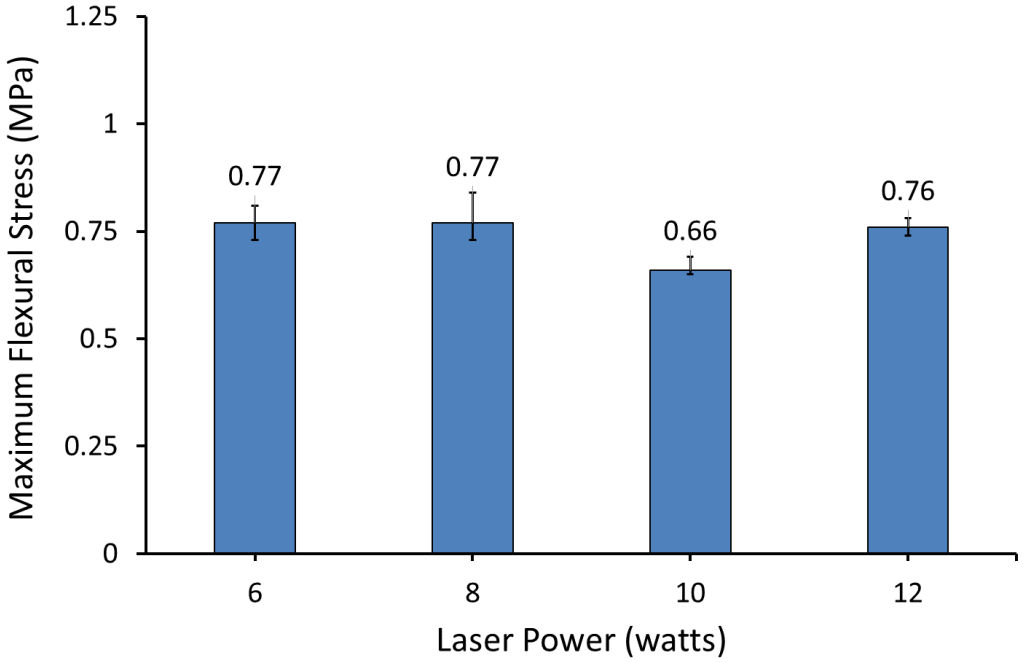

Figure 7.19 : Maximum Flexural Stress of 70:30 AC-UHMWPE produced at various laser powers and bed temperature of 117.5°C

Similarly, Figure 7.20 shows that the average flexural strain remains unchanged within the range of laser power between 6 and 12 watts.

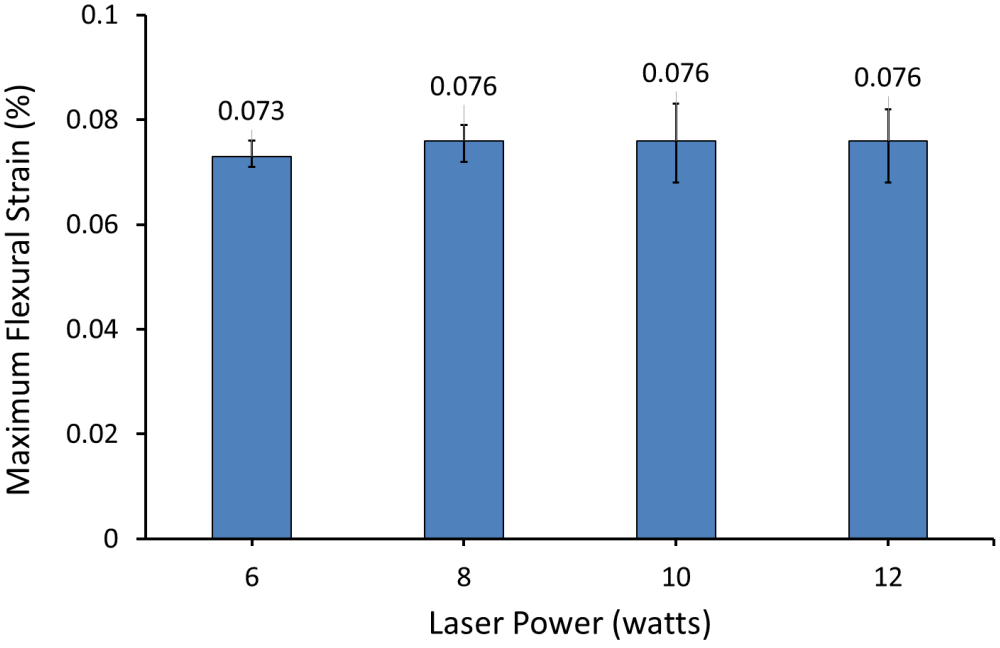

Figure 7.20 : Maximum Flexural Strain of 70:30 AC-UHMWPE produced at various laser powers and bed temperature of 117.5°C

A flexural strain with an overall average of 0.075 ±0.002% was achieved. This result showed statistically insignificant changes in the flexural strain with the change in laser power, at the specified range. Using different laser powers did not alter the overall flexural strain of the sintered parts significantly.

7.8 Summary of AC-UHMWPE Powder Characterisation

AC powder has a broad range of particle size with an average of 196 µm (d_{50}), which was larger than the average particle size of UHMWPE (i.e. 125 µm). According to the supplier's datasheet, the AC powder has a particle size range of 75 – 250 µm. The SEM examination revealed that the highly porous particles have irregular shape with a rough surface. The Hausner ratio of the powders was calculated for PE30, PE20, PE15 and AC100 and were found to be 1.28, 1.27, 1.26 and 1.25, respectively. The results indicate that the AC has high powder flow and the addition of AC has improved the flow of UHMWPE.

The flow and packing is influenced by the shape and the friction between particles. Since the friction increases with the increase in the surface area of the powder, then using coarser particles would induce better flow than fine powders due to the high inter particle friction between the particles of the fine powders [188].

The DSC results show that the intrinsic thermal properties of UHMWPE powder are not significantly affected by the introduction of activated carbon, indicating that no interaction occurred between the UHMWPE and AC materials at the targeted temperature.

The TGA results revealed that the onset of mass loss is considerably shifted to higher temperatures for the AC-UHMWPE composites. For the composites containing 15% and 20% of UHMWPE, this shift was around 20°C. This suggests that the thermal stability of the AC-UHMWPE has increased with the increase in the content of the activated carbon. Activated carbons can preferentially

adsorb the volatile degraded UHMWPE components during the degradation process. This could delay the mass loss and retard the thermal degradation, resulting in a higher degradation temperature of the composites compared to that of the neat UHMWPE. The result clearly shows that the temperature window is wide enough and favourable for laser sintering.

There is no noticeable difference in the XRD patterns of the AC-UHMWPE composites and no obvious shift of diffraction peak positions was observed. This suggests that the ratio of the unprocessed AC-UHMWPE composite does not affect the microstructure of the composite materials.

The degree of crystallinity of the neat UHMWPE was decreased from 57.45% to 48.28% (using DSC) and from 67.80% to 61.35% (using XRD) for 70:30 AC-UHMWPE composite powder. The three AC-UHMWPE composite samples (i.e. PE30, PE20 and PE15) showed statistically insignificant changes in the trend confirming that the change in the composition ratio of untreated composite does not have a significant effect on the degree of crystallinity. However, a slight change was observed and it is most likely due to sampling or measurement error.

Laser sintering is well suited process to manufacture a variety of composite materials including non-standard LS materials (i.e. off-the-shelf powders). However, powder characteristics and properties, such as particle size, shape and powder flow, can greatly influence the quality of the parts produced as well as the processing of the powder [191].

Laser sintered 70:30 AC-UHMWPE parts were successfully manufactured using various laser powers. Sintered parts were manufactured with well-defined structure and good mechanical properties.

Chapter 8 Characterisation of Laser Sintered AC-UHMWPE Composites

8.1 Introduction

Carbon-based materials and polymer matrix composites are emerging materials as fillers for Laser Sintering (LS) to enhance the properties of the produced parts. A successful attempt has been made to laser sinter a complex carbon/carbon composite components using a mixture of carbon fibre (CF) and phenolic resin [94]. Yan *et al.* reported that the PA12-CF composite has a lower bed temperature in the LS process, denoting a lower energy is required and a better efficiency of material reutilisation [28]. In line with other studies, Yan *et al.* result proves that the addition of carbon fibres can highly improve the flexural modulus and strength of sintered parts. A significant improvement has been observed, with the addition of a small quantity of nanofiller, compared to the main polymer's mechanical, electrical and thermal properties [192]. Goodridge *et al.* used a 3% (wt) PA12-Carbon nanofibre (CNF) composite and reported that the laser sintered parts of nanocomposites exhibited higher dynamic mechanical properties by 22% than those of the base PA-12 parts [95].

Bai *et al.* studied the dynamic mechanical properties of a PA12-Carbon nanotube (CNT) nanocomposite for laser sintering [192]. The results demonstrated that CNTs have a significant improvement in the elastic modulus of the laser-sintered parts, compared to that of neat PA-12. In another study, Bai *et al.* reported that PA12-CNT parts with 0.1 wt% CNT showed improved impact, tensile and flexural properties without affecting elongation at break, compared to that of neat PA-12 [80]. Similarly, Salmoria *et al.* showed high values for the flexural modulus and ultimate strength for the PA-12/MWCNTs (multi-walled carbon nanotubes) composite when compared to PA-12 parts. The fatigue test carried out by Salmoria *et al.* showed also an improvement in the stiffness of the composite with the addition of MWCNTs [96].

Bipolar plates are critical component of Polymer Electrolyte Membrane (PEM) fuel cell that converts electrochemical energy into electricity. Graphite composite bipolar plates were laser sintered successfully using a mixture of graphite powder and phenolic binder [97]. The phenolic binder melts by laser and binds the graphite particles. Similar work was conducted by Chen *et al.* and the finished LS bipolar plate showed outstanding mechanical strength and surface finish but the dimensional accuracy and shrinkage remain as a challenge [188]. Graphite materials, such as natural and synthetic graphite, carbon fibre, and carbon black were investigated by Guo *et al.* using laser sintering to fabricate bipolar plates [193]. The study shows that natural graphite improves electrical conductivity and CFs considerably improve flexural strength. On the other hand, carbon black (nano-sized), which covers the particles surface of natural graphite, has a negative effects on flexural strength and electrical conductivity. While synthetic graphite reduces electrical conductivity and slightly decreases flexural strength. Bourell *et al.* reported that the CF addition (26% volume) to the graphite powder and phenolic binder composite has increased the flexural strength of the finished laser-sintered parts, but the electrical conductivity was lowered [194].

Athreya *et al.* was successfully processed PA-12 reinforced with 4% (wt) of carbon black (CB) parts by LS [98]. In this study, Athreya *et al.* reported a reduction in the flexural modulus and indicated that this reduction was occurred as a result of the formation of a segregated structure in the nanocomposite and a weak interface between the polymer and the filler. Athreya *et al.* also reported in another study that the mechanical properties of laser sintered PA-12/CB parts were lower than that of the PA-12 laser sintered parts [88]. Athreya suggested this behaviour was due to lack of dispersion of CB nanoscale particles in the polymer matrix, as well as the high porosity in the PA-12/CB sintered parts. Additionally, the tensile modulus of the PA-12/CB laser sintered parts was lower than the flexural modulus which was due to insufficient bonding between successive layers during sintering, which can be worsen by the presence of a porous CB nano-filler.

Porous materials have been widely used in many applications and are mostly produced using powder technology to achieve desired mechanical properties [195]. In this study, a novel UHMWPE polymer binder and coconut shell activated carbon powder composite has been processed by a laser sintering technique. AC-UHMWPE composites containing 15, 20, 30 wt% of UHMWPE concentrations were prepared and laser sintered at various levels of laser power and part bed temperature. The understanding of the effects of process parameters and composition on the microstructural properties, such as porosity, and the mechanical behaviour of porous materials are far from satisfactory.

This work studies the morphological and mechanical behaviour of AC-UHMWPE parts produced by laser sintering. The characterisation of the porous structures was conducted using three techniques; Helium Gas Pycnometry, micro-CT and Mercury Porosimetry and detailed information was obtained on density, porosity and pore size distribution. Mechanical properties such as maximum flexural stress and modulus were obtained. Thermal behaviour and crystallinity were examined using DSC, TGA and XRD techniques. The external microstructure of the laser sintered AC-UHMWPE parts was observed using a scanning electron microscope. 3D images of the laser sintered parts were constructed using micro-CT technique to show 3D representations of the laser sintered AC-UHMWPE structure.

8.2 Parts Manufacturing

Laser sintered parts with a length of 80 mm, width of 10 mm and thickness of 4 mm (according to ISO 178), were built using a commercial laser sintering machine (EOS P100, Germany). The test parts were oriented in the x-y direction with the long axis parallel to the x-axis, width parallel to the y-axis and thickness parallel to z-axis (i.e. build direction) as shown in section 5.2, 0.

In order to examine the effect of laser power, bed temperature and composite composition on the material characteristics and mechanical properties of the

laser sintered AC-UHMWPE parts, laser powers of 8 and 12 watts and bed temperatures of 117.5°C and 120°C were selected for processing AC-UHMWPE with ratios of 85:15, 80:20 and 70:30. All other parameters were kept constant as listed in Table 8.1. After building, all the parts were left in the machine for two to three hours and then were removed and left for cooling in the laboratory for 24 hours. Then the parts were cleaned gently by a brush to remove the un-sintered powder.

Table 8.1: Laser sintering parameters used for manufacturing of AC-UHMWPE parts

Parameter	Unit	Values
UHMWPE content	%	15, 20, 30
Laser Power	watts	8, 12
Laser Energy Density	J/mm²	0.021, 0.032
Bed Temperature	°C	117.5, 120
Removal Chamber Temperature	°C	117, 120
Laser Scan Speed	mm/s	2500
Hatch Spacing	mm	0.15
Laser Count	-	2 (double scan)
Layer Thickness	mm	0.1

Laser sintered AC-UHMWPE parts were successfully manufactured using laser powers of 8 and 12 watts and bed temperatures of 117.5°C and 120°C with composition ratios of 85:15, 80:20 and 70:30.

All samples were labelled as listed in Table 8.2. The sample's label consists of three parts in format of "*PEnn-nnn.n-nn*":

1. *PEnn*: content of UHMWPE (%)
2. *nnn.n*: bed temperature (°C)

3. *nn*: laser power (watts)

Table 8.2: Sample labels of laser sintered AC-UHMWPE parts

Sample ID	UHMWPE (%)	Bed Temperature (°C)	Laser Power (watts)
PE15-117.5-8	15	117.5	8
PE15-117.5-12	15	117.5	12
PE15-120-8	15	120	8
PE20-117.5-8	20	117.5	8
PE20-117.5-12	20	117.5	12
PE20-120-8	20	120	8
PE30-117.5-8	30	117.5	8
PE30-117.5-12	30	117.5	12
PE30-120-8	30	120	8

8.3 Characterisation Methods

8.3.1 Relative Density

The relative density is defined as the part bulk density related to the true density of the material(s) composing the part and was calculated using Equation (9) as shown in section 5.3.1, 0. Three samples with approximately 10 x 8 x 6.5 mm^3 were cut out from the rectangular laser sintered AC-UHMWPE parts and used for bulk density measurements. The rectangular test samples were made by laser sintering with process parameters as listed in Table 8.2. The bulk density of the samples was calculated by measuring dimensions, using a Vernier calliper, and weights, using a mass balance accurate to 0.001 g. The average density value of three samples was taken as the bulk density of the laser sintered AC-UHMWPE composite parts. The true density of AC and

UHMWPE powders were measured by helium gas pycnometer (Micromeritics AccuPyc II 1340, USA). The true density of the composite powders were estimated based on the rule of mixtures approach as described in section 7.5.2, Chapter 7.

8.3.2 Porosity

The characteristics of a porous material depend on the size, shape and arrangement of the pores, and they are also affected by the porosity and composition of the material itself. Three methods were considered to determine the porosity of laser sintered AC-UHMWPE parts and these are Helium Gas Pycnometry, micro-CT and Mercury Intrusion Porosimetry.

8.3.2.1 *Helium Gas Pycnometry*

The porosity of the sintered parts was determined by measuring the true density of AC-UHMWPE powder (ρ_{Trure}), the bulk density (ρ_{Bulk}) and the skeletal density ($\rho_{Skeletal}$) of sintered AC-UHMWPE parts. The true density of the composite powders were estimated based on the rule of mixtures approach as described in section 7.5.2, Chapter 7. The skeletal density of the sintered parts were determined using helium gas pycnometer (Micromeritics AccuPyc II 1340, USA). The bulk density of laser sintered parts was determined using a volumetric method as described in section 5.3.1, 0. Then the total, open and closed porosity were calculated using Equations (10), (11) and (12) as shown in section 6.4.2, Chapter 6. Three samples for each set of parameters were tested and the average values were reported.

8.3.2.2 *X-ray micro-Computed Tomography (micro-CT)*

The microstructure of the laser-sintered AC-UHMWPE parts was investigated using Skyscan 1172 (Bruker µCT, Belgium). A current of 165 µA, voltage of 40 kV, pixel size of 5.9 µm, 360° rotation and 0.35° rotation step, were used. Cross-section images were reconstructed from tomography projection images, obtained from the scanner, using Skyscan NRecon software (Bruker micro-CT,

Belgium). 3D morphological analysis of the micro-CT data was carried out using CTAn software (Bruker micro-CT, Belgium). A cylindrical region of interest, diameter of 5 mm and height of 4 mm, was chosen for the 3D porosity analysis for all samples. Three samples for each set of parameters were tested and the average values were reported.

Image thresholding is a crucial step in micro-CT analysis that has to be performed prior to 3D modelling. The thresholding range is selected via the histogram of the images and visual estimation as shown in Figure 8.1.

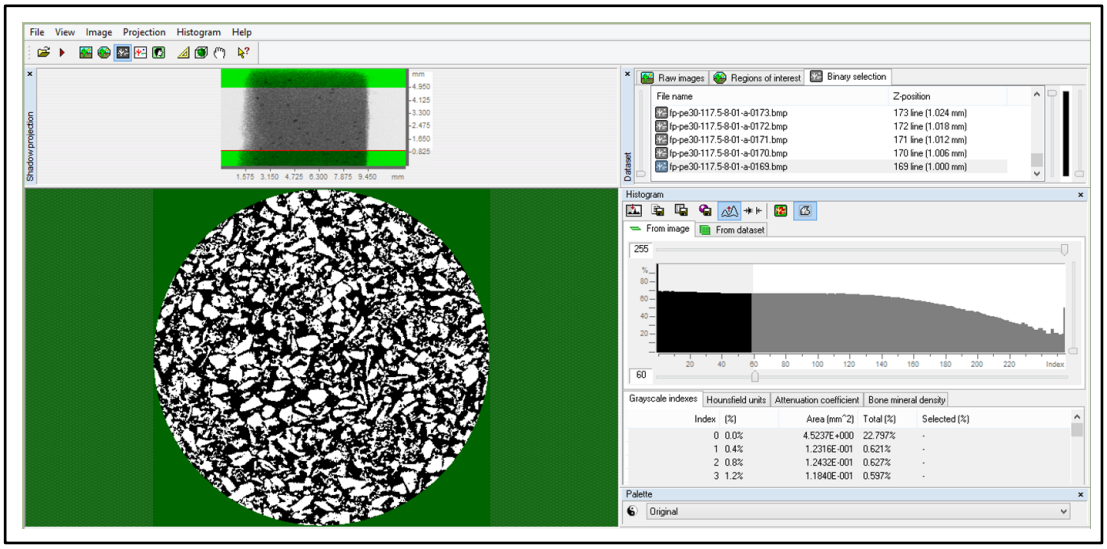

Figure 8.1 : CTAn software window displays 2D image (left) and the threshold histogram (right). The lower and upper grey threshold selected for all samples are set to 60 and 255, respectively

When a structure made up of multiple materials, the ranges of the thresholding overlap, making the digital separation of these materials difficult [155]. The threshold used in this analysis was readily obtained for each individual sample with lower and upper grey values of 60 and 255, respectively.

8.3.2.3 *Mercury Intrusion Porosimetry*

Mercury Intrusion Porosimetry (MIP) is a useful characterisation method for porous materials. Pores between about 3.5 nm and 500 µm can be investigated. Porosity, pore size distribution, and density can be measured [196].

MIP tests were performed on the Micromeritics AutoPore V 9600 Version 1.02 porosimeter (Micromeritics Instrument, USA) to determine the porosity and pore size distribution. The porosimeter operates in a pressure range of approximately 0.0007 to 206.84 MPa (0.10 to 30000 psi) over a pore diameter range of approximately 0.006 to 1800 μm. The mercury porosity was defined as the percentage of the bulk volume of sample intruded by mercury at a maximum pressure of 206.84 MPa and a 130° contact angle. Two samples of each selected set of laser sintered AC-UHMWPE parts were used and these are PE15-117.5-12, PE20-117.5-12 and PE30-117.5-12.

A sample of approximately 0.10-0.20 g was first weighed and placed in a penetrometer. The penetrometer was assembled and weighed prior to testing and the values were used in the calculations. The penetrometer with the sample is placed into the mercury filling device and a vacuum apparatus is used to remove air from the cell and the sample. A low pressure was then used and the mercury was introduced into the penetrometer until it was filled and the sample was completely covered. Pressure was gradually increased causing the intrusion of mercury into the large pores. Mercury filled penetrometer was removed and weighed to measure the amount of mercury held, and then was placed to the high pressure compartment and pressure was stepwise increased to a final pressure of 206.84 MPa (30000 psi).

8.3.3 Mechanical Properties

Mechanical properties were examined using three-point bending tests, which were performed on a Texture Analyser TA500 (TM Lloyd Instruments, UK) fitted with a 50 N load cell. All tests were conducted at ambient temperature with a constant cross-head speed of 0.4mm/min and span length of 40mm. The flexural strength was directly measured using the laser sintered AC-UHMWPE parts without any post processing. Three samples for each set of parameters were tested and the average values were reported.

8.3.4 Differential Scanning Calorimetry

The thermal property of the laser sintered AC-UHMWPE parts were measured at a heating rate of 10°C/min by differential scanning calorimetry (Perkin Elmer DSC 8500) from 25 to 220°C under a nitrogen atmosphere. The weight of the samples was 5.9 mg on average. The samples were held for 1 minute at 220°C before the cooling cycle started. The results were then analysed using the Pyris™ software. The peaks were identified and the temperatures of these peaks were then labelled as melting or crystallisation temperatures. DSC curves of AC-UHMWPE parts were obtained under two thermal cycles and three samples were analysed for each set of parameters.

8.3.5 Thermogravimetric Analysis

TGA was performed using TGA analyser (Pyris 1 TGA, PerkinElmer, USA) to investigate the thermal stability of laser sintered AC-UHMWPE parts. Approximately, ten milligrams of the material was placed in a ceramic crucible and was heated from 25°C to 600°C under nitrogen atmosphere at a heating rate of 10°C /min. One sample for each set of parameters was tested.

8.3.6 XRD Analysis

A Bruker D8 Advance X-ray diffraction system, equipped with a Cu Kα radiation source with a wavelength (λ) of 1.5418 nm generated at 40 kV and 40 mA, was used for XRD analysis. Laser sintered AC-UHMWPE samples were mounted on the stage and scanned from 10° to 70° using a step size of 0.05° and time/step of 10 seconds. Two samples for each set of parameters were tested.

8.3.7 Degree of Crystallinity

DSC and XRD measurements were conducted to determine the crystallinity of the laser sintered AC-UHMWPE parts (samples are listed in Table 8.2). Equation (14), in section 7.5.6, Chapter 7, and Equations (7), in section 4.2.6, Chapter 4, were used to calculate the degree of crystallinity using DSC and XRD methods, respectively.

8.3.8 Morphology

X-ray micro-CT technique is a useful tool that can be used to visualise the structure of the laser sintered AC-UHMWPE parts. A cylindrical region of interest (diameter of 5 mm and height of 4 mm) was specified for the 3D images analysis. CTVox software was used to show 3D representations of the laser sintered AC-UHMWPE structure.

The external microstructure of the laser sintered AC-UHMWPE parts was observed using a scanning electron microscope (Philips XL-20, Holland) at an accelerating voltage of 13 kV. Samples of 2-3 mm thick were cut out from the cross section of the rectangular laser sintered parts and then were mounted on a sample's holder with an adhesive tape. All samples were gold sputtered before the observation to avoid charging.

8.4 Results and Discussion

8.4.1 Relative Density of Laser Sintered Parts

The effect of laser power and bed temperature on the relative densities of the laser sintered AC-UHMWPE parts is shown in Figure 8.2 and Figure 8.3.

Figure 8.2 shows that the relative density of the 70:30 AC-UHMWPE parts is higher than that of the 85:15 and 80:20 AC-UHMWPE parts produced at the same laser power and bed temperature. The laser sintered 70:30 AC-UHMWPE parts, produced at laser power of 8 watts and bed temperature of 117.5°C, have an average relative density of 20.95 ±0.08%, while the laser sintered 80:20 and 85:15 AC-UHMWPE parts have an average relative density of 17.74 ±0.18% and 16.49 ±0.40%, respectively. The increase in the UHMWPE content from 15% to 30% showed a density increase of 4.46%. This is a small increase in relative density, however, mechanical properties are known to be very sensitive even to small changes [195].

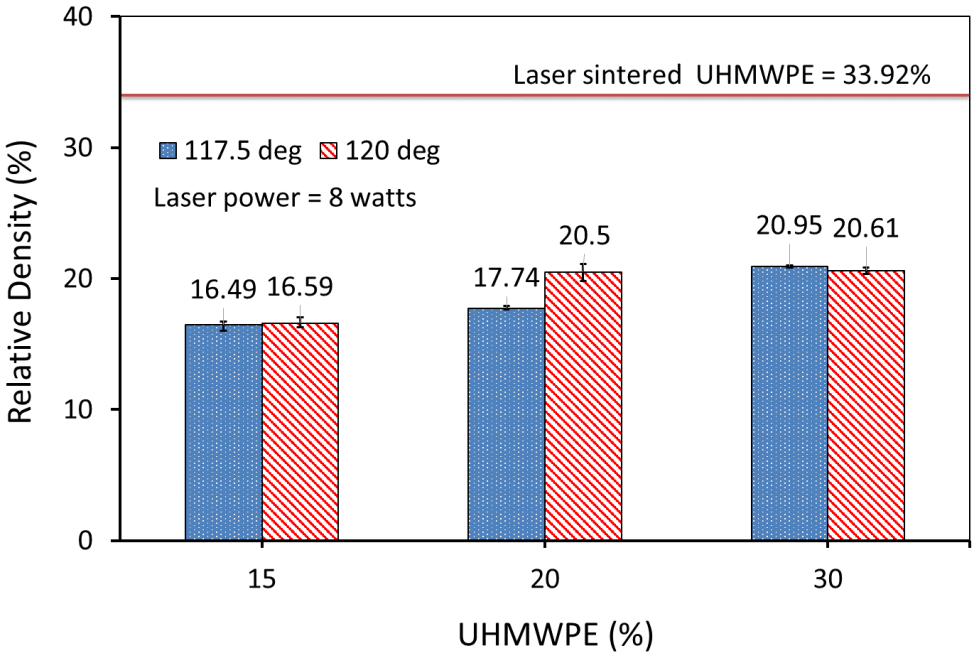

Figure 8.2 : Relative density of AC-UHMWPE with different UHMWPE % content produced at laser power of 8 watts and bed temperatures of 117.5°C and 120°C. (Three samples for each condition and the error bar represents the range of the data)

The effect of laser power and bed temperature on the relative density of the parts produced at the same UHMWPE content was not apparent. For example, the relative densities of parts produced with 85:15 AC-UHMWPE and laser power of 8 watts were 16.49 ±0.40% and 16.59 ±0.42% at bed temperature of 117.5°C and 120°C, respectively (Figure 8.2).

Similar behaviour was observed with parts produced at a fixed bed temperature of 117.5°C and laser powers of 8 and 12 watts, as shown in Figure 8.3. This result suggests that the effects on relative density are not driven by the laser power and bed temperature within the applied ranges.

The results show that UHMWPE content had the most obvious impact on relative density (Figure 8.4). The relative density of the laser sintered AC-UHMWPE parts is still considerably lower from that of laser sintered neat UHMWPE parts, which has a relative density of 33.92%.

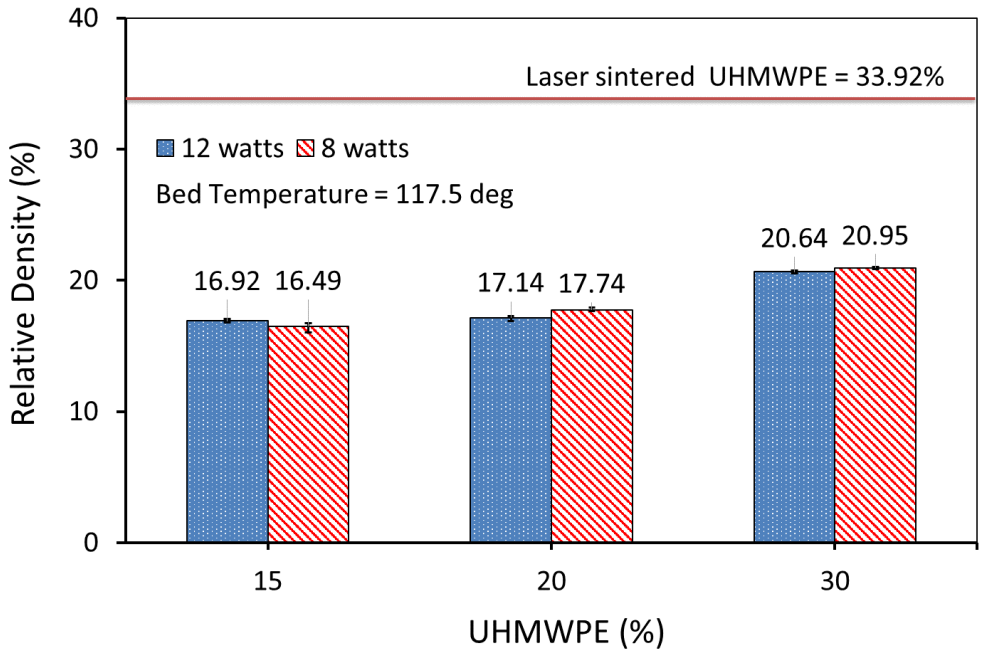

Figure 8.3 : Relative density of AC-UHMWPE with different UHMWPE % content produced at laser power of 8 and 12 watts and bed temperature of 117.5°C. (Three samples for each condition and the error bar represents the range of the data)

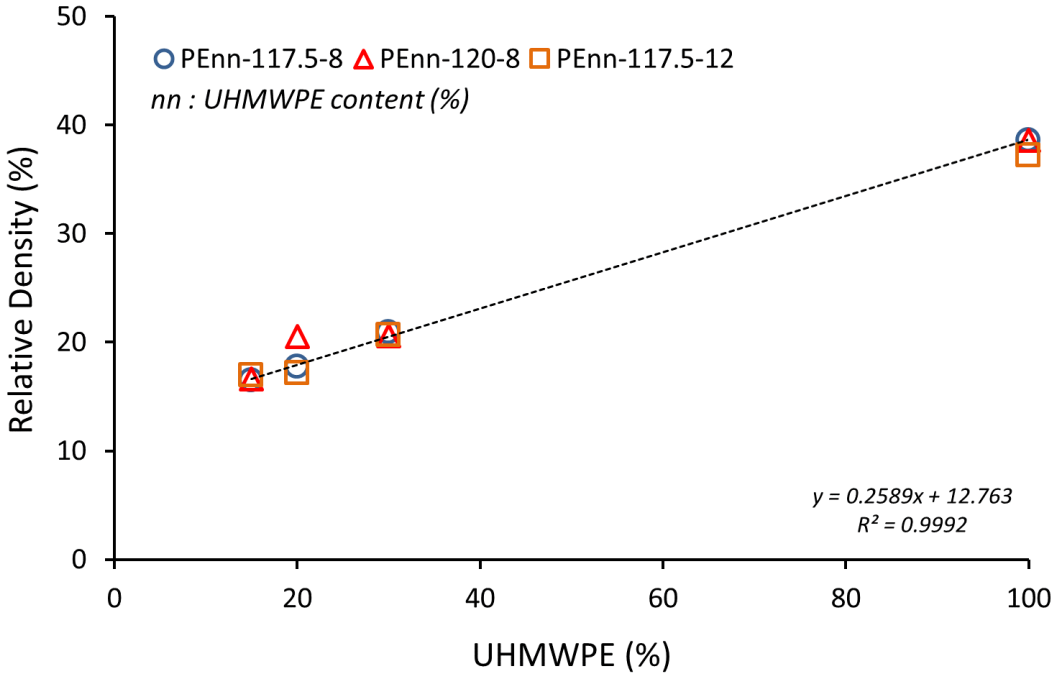

Figure 8.4 : Relative density of AC-UHMWPE produced at different UHMWPE % content and process parameters (Three samples for each condition). Note: 100% UHMWPE samples were produced at bed temperature of 142°C and included in this graph for comparison purposes.

8.4.2 Porosity of Laser Sintered Parts

8.4.2.1 *Helium Gas Pycnometry*

The porosity of laser sintered parts of AC-UHMWPE was determined by measuring the bulk density of the parts as well as the density of the raw materials (powders), which was measured by helium pycnometry.

Figure 8.5 and Figure 8.6 show the results of total porosity versus the composition of laser sintered AC-UHMWPE parts produced at different bed temperatures and laser powers, respectively. The results show that the porosity did not change significantly when bed temperature and laser power were changed. However, a slight reduction in porosity of approximately 4% has been observed when the UHMWPE content increased from 15% to 30% in both cases (compared with an expected change of 0.7% by the rule of mixtures of the composite powder, note that the total porosity of UHMWPE and AC powders was 75.67% and 83.73%, respectively).

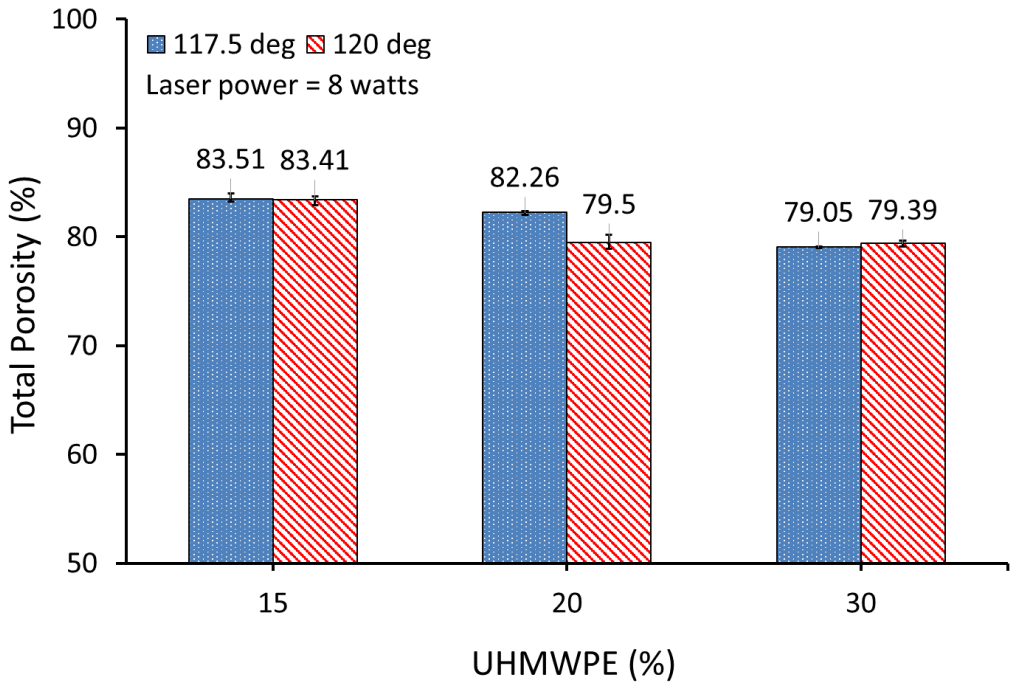

Figure 8.5 : Total porosity of AC-UHMWPE with different UHMWPE % content produced at laser power of 8 and bed temperatures of 117.5°C and 120°C. (Three samples for each condition and the error bar represents the range of the data)

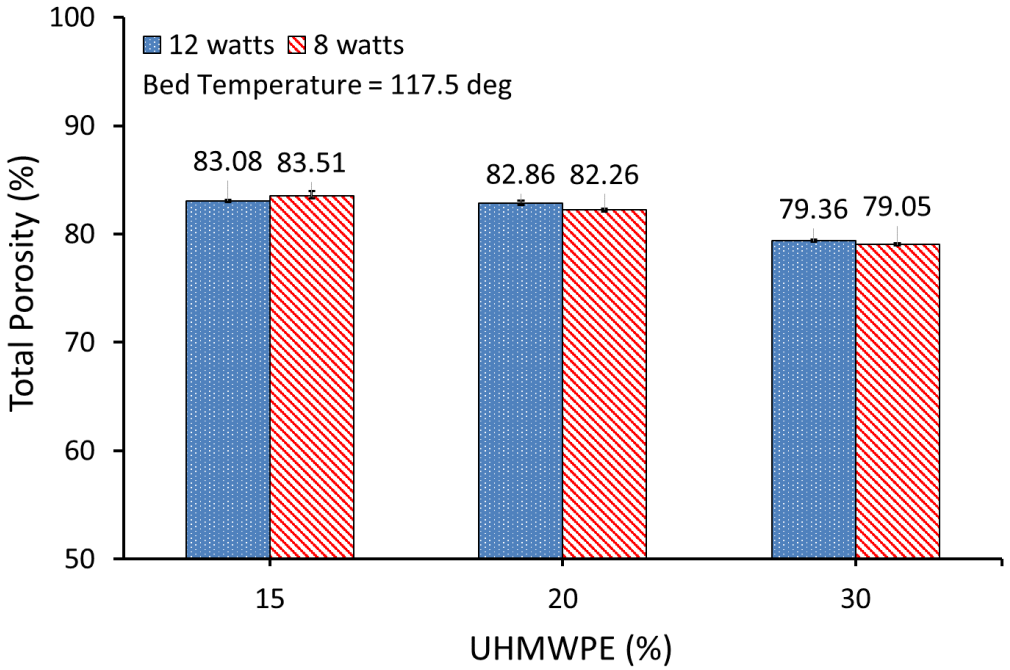

Figure 8.6 : Total porosity of AC-UHMWPE with different UHMWPE % content produced at laser power of 8 and 12 watts and bed temperature of 117.5°C. (Three samples for each condition and the error bar represents the range of the data)

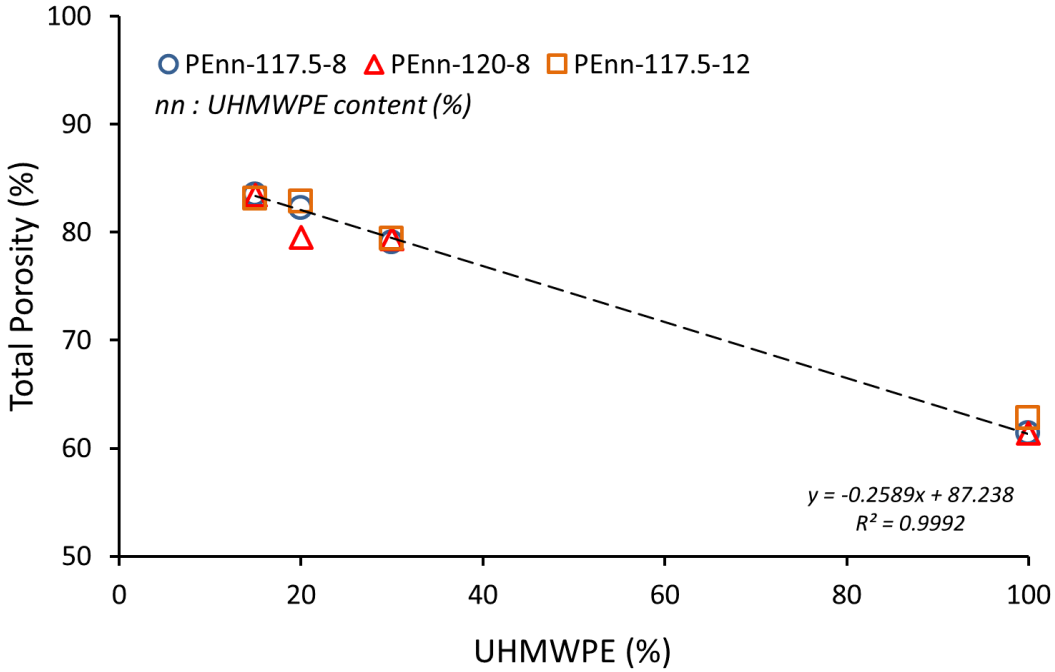

Figure 8.7 : Total porosity of AC-UHMWPE produced at different UHMWPE % content and process parameters (Three samples for each condition). Note: 100% UHMWPE samples were produced at bed temperature of 142°C and included in this graph for comparison purposes.

This result suggests that the porosity decreases with the increase in UHMWPE content (Figure 8.7) and the effects on porosity are not driven by bed temperatures and laser powers within the range of parameters analysed. For both cases nearly the same porosities could be achieved.

Figure 8.8 and Figure 8.9 show the evaluation of the open and closed porosities of laser sintered AC-UHMWPE, respectively.

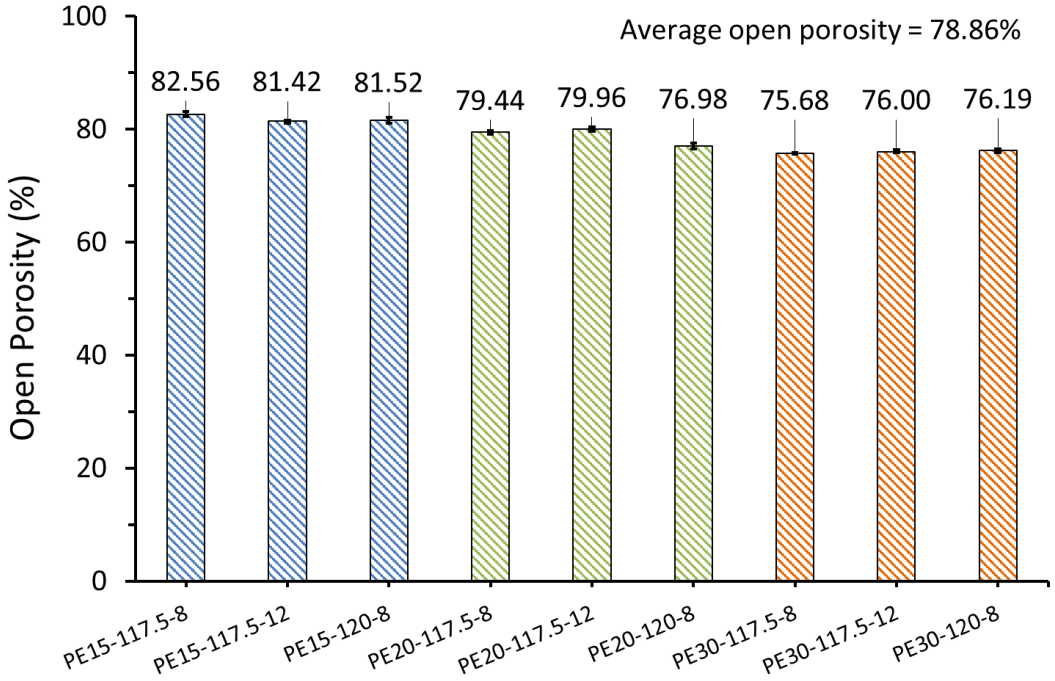

Figure 8.8 : Open porosity of laser sintered AC-UHMWPE parts measured using Helium Gas Pycnometry. (Three samples for each condition and the error bar represents the range of the data)

The overall average open porosity decreases by 5.88% when the UHMWPE content increased from 15% to 30% (from 81.83 ±0.63% to 75.96 ±0.26) and the closed porosity increased by 1.81% (from 1.50 ±0.50% to 3.31 ±0.10). Laser sintered AC-UHMWPE parts present higher open porosity and lower closed porosity at low levels of UHMWPE content. The values of closed porosity are higher for 70:30 AC-UHMWPE parts compared to the 80:20 and 85:15 AC-UHMWPE parts.

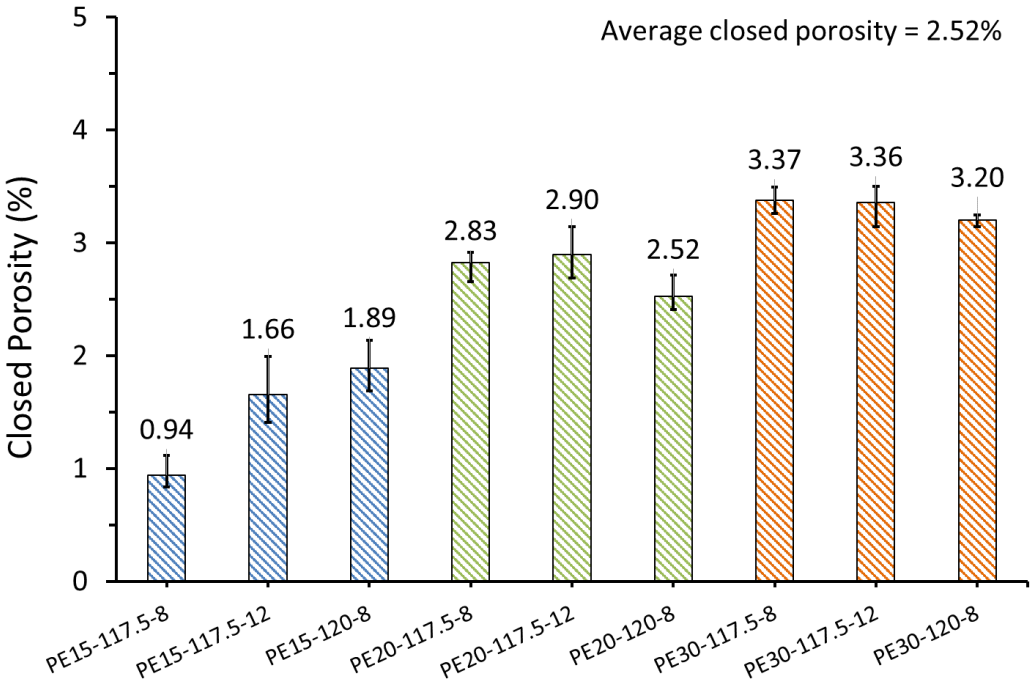

Figure 8.9 : Closed porosity of laser sintered AC-UHMWPE parts measured using Helium Gas Pycnometry. (Three samples for each condition and the error bar represents the range of the data)

These results can be explained by the fact that increasing the amount of UHMWPE raises the coalescence process between UHMWPE particles resulting more dense parts with a slight increase in closed porosity.

8.4.2.2 *X-ray micro-Computed Tomography (micro-CT)*

A comparison between micro-CT and Helium pycnometry is presented in Figure 8.10. The average total porosity measured by micro-CT and helium pycnometry were 56.50 ±1.84% and 81.38 ±1.98%, respectively.

There are noticeable differences between these two methods. The porosities measured by micro-CT do not fit very well with the helium pycnometry porosity values. The helium pycnometry gives significantly higher values than micro-CT by an average of 24.88%.

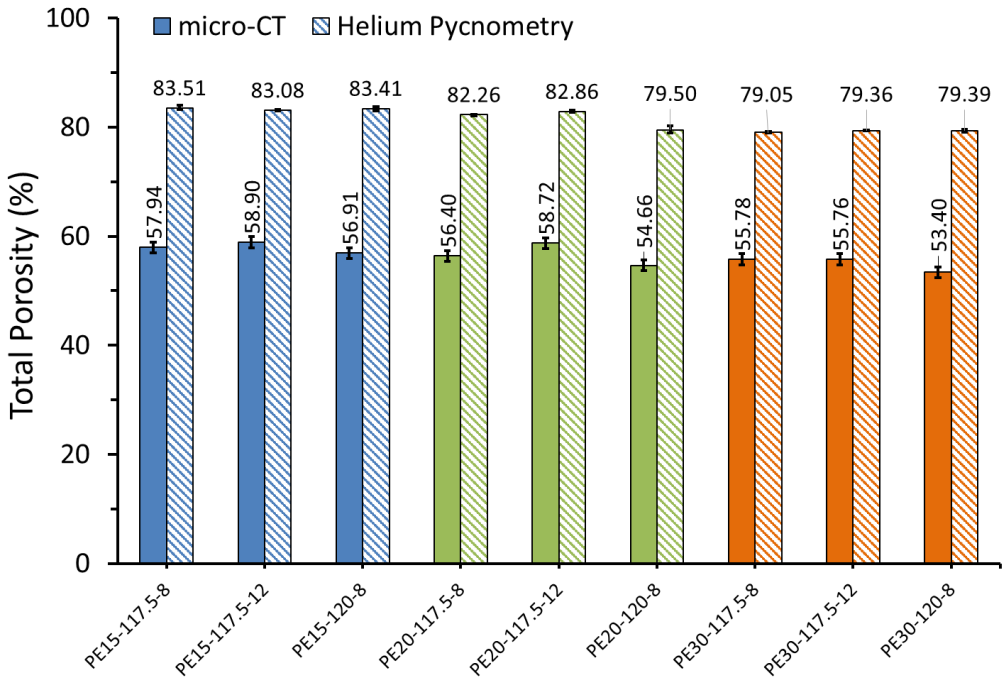

Figure 8.10 : Total porosity of laser sintered AC-UHMWPE measured using micro-CT and Helium gas pycnometry with average porosities of 56.50 ±1.84% and 81.38 ±1.98%, respectively.
(Three samples for each condition)

There could be many reasons for this discrepancy. Among these reasons, probably is the sub-microstructure of the AC-UHMWPE composite particles, which have fine pores inside that could be detected by the helium pycnometry, but are not discerned by micro-CT image analysis. Additionally, low resolution of the X-ray system and the grey threshold value of the analysis software result in a loss of small pores and consequently in low porosity values. The drawbacks of the micro-CT approach are attributed to the loss of the underlying geometry of the particles as well as the conversion of the grayscale images into binary matching images. These issues are sensitive to the greyscale threshold that is used to separate the pixels between the solid and pore phases [178].

Figure 8.11 presents the pore size distribution of laser sintered AC-UHMWPE samples measured by micro-CT technique, summarising the estimated values of percentage pore volumes with regard to different pore diameters.

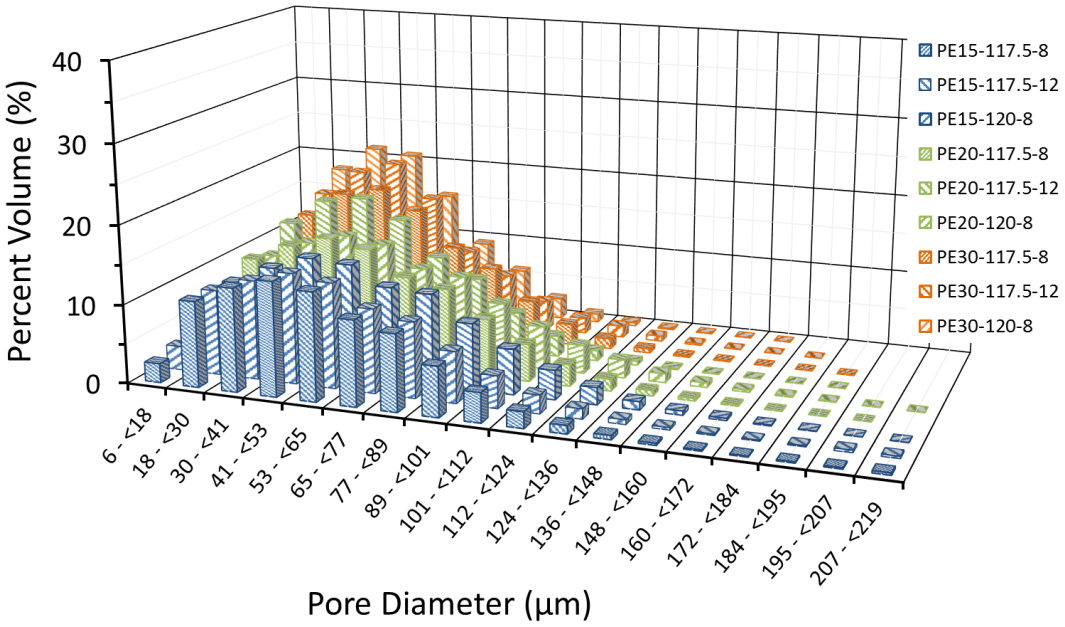

Figure 8.11 : Pore size distribution of laser sintered AC-UHMWPE parts measured using micro-CT (Three samples for each condition).

The results show that the pore size distribution is closely related to the composition ratio of the AC-UHMWPE. The samples with 30% UHMWPE, show narrower pore size distributions and the majority of the pores having diameters between 30 to 77 µm with a peak of pores volume ranges between 30 – 41 µm. AC-UHMWPE samples of 85:15 and 80:20 show a wider distribution which peaks at pore diameter ranges between 41 – 53 µm and exhibit large pores with a diameter between approximately 100 to 200 µm compared to 70:30 AC-UHMWPE samples.

The results suggest that the pore size distribution broadens with the reduction in UHMWPE content. This is partly due to the presence of the large AC particles, which results in the formation of large pores in the structure without small pores. Figure 8.12 shows the particle size distribution of the AC and UHMWPE powders.

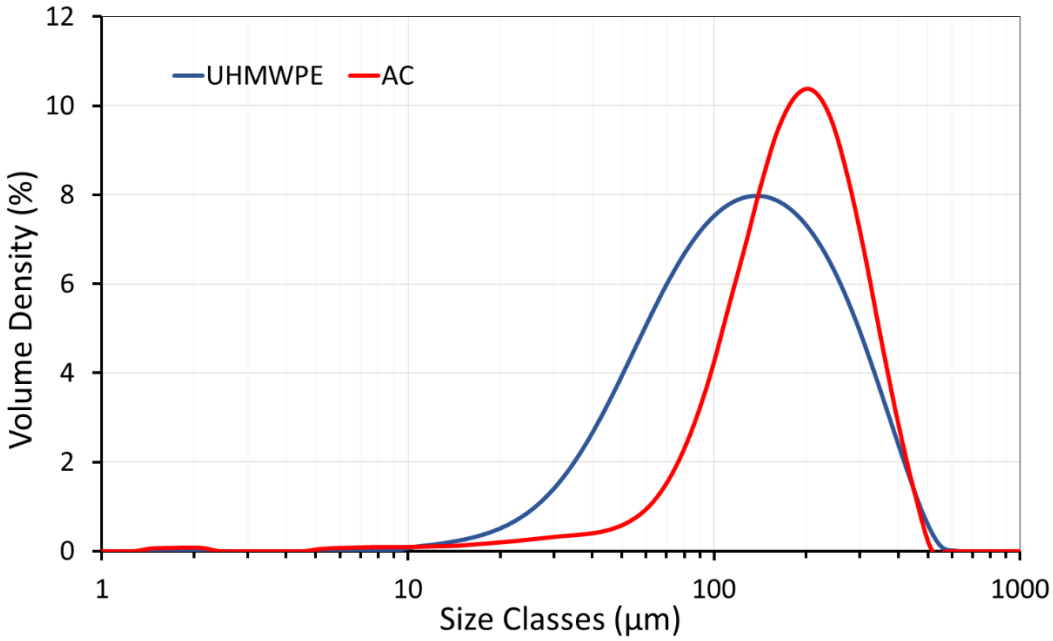

Figure 8.12: Particle size distribution of AC and UHMWPE powders

The average pore diameters of the laser sintered AC-UHMWPE parts presented in Figure 8.13.

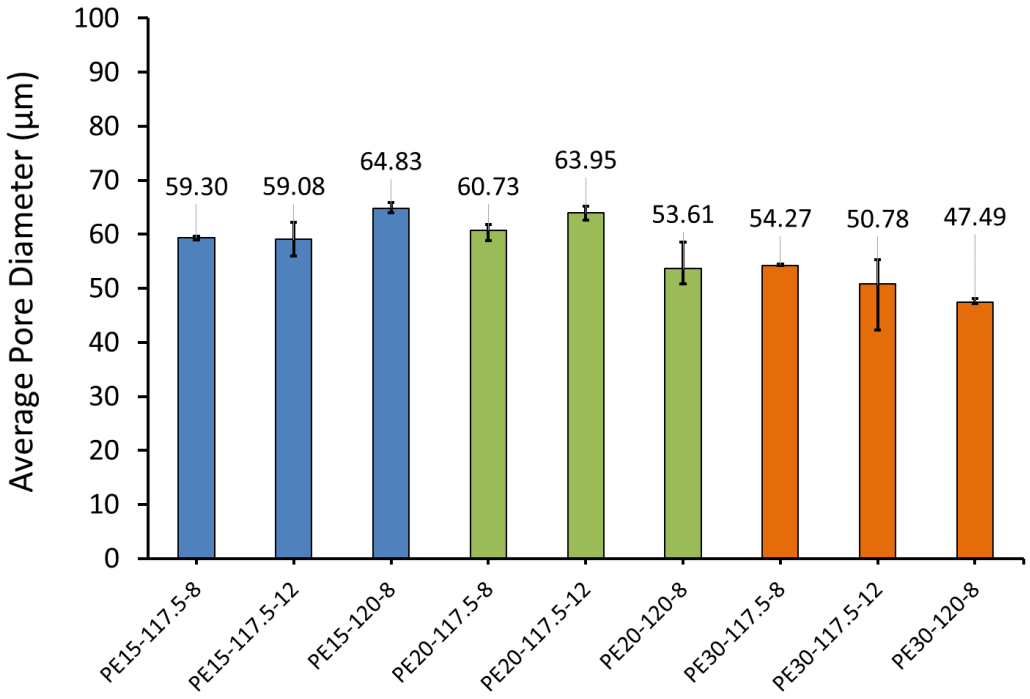

Figure 8.13 : Average pore diameter of laser sintered AC-UHMWPE parts measured using micro-CT (Three samples for each condition).

The average pore diameters were determined as 61.07, 59.43 and 50.85 µm for laser sintered parts with AC-UHMWPE composition of 85:15, 80:20 and 70:30, respectively. A slight decrease in pore size can be observed with the increase in UHMWPE content. Compared to the neat UHMWPE, the overall average of pore diameter was 36.70 ±1.0µm, as measured by micro-CT technique.

As indicated earlier in regard of the pore size distribution, similarly the increase in pore size is probably due to the formation of large pores resulting from the large particles of activated carbon.

8.4.2.3 *Mercury Porosimetry*

The characterisation of pore structures, in terms of porosity and pore size distribution, was performed using mercury intrusion pycnometry technique. Three groups of laser sintered AC-UHMWPE samples were tested and analysed. The groups of samples selected for this analysis were PE15-117.5-12, PE20-117.5-12 and PE30-117.5-12. These samples were manufactured at a bed temperature of 117.5°C and a laser power of 12 watts with different ratios of AC-UHMWPE (i.e. 85:15, 80:20 and 70:30).

Figure 8.14 shows that the porosity measured by mercury intrusion differs slightly between the three groups of samples analysed. The overall average porosity of all samples is 63.34% with a standard deviation of ±1.99%, this compares with 70.23 ±0.94% and 65.70 ±0.70% for un-sintered UHMWPE and AC powder, respectively, as measured by mercury porosimetry.

This method gives slightly higher porosity values than that of micro-CT (with overall average porosity of 56.50%), but lower porosity values than that of helium pycnometry. Only open pores that are connected to the surface can be measured and the completely closed pores are not accounted for. Mercury is forced into the porous samples by pressure and the mercury volume penetrating the pores is measured as a function of applied pressure. Higher pressure is needed to overcome mercury resistance against intrusion into

smaller pores [177]. Low porosity values can be attributed to the fact that some pores cannot be intruded by mercury including closed pores [155].

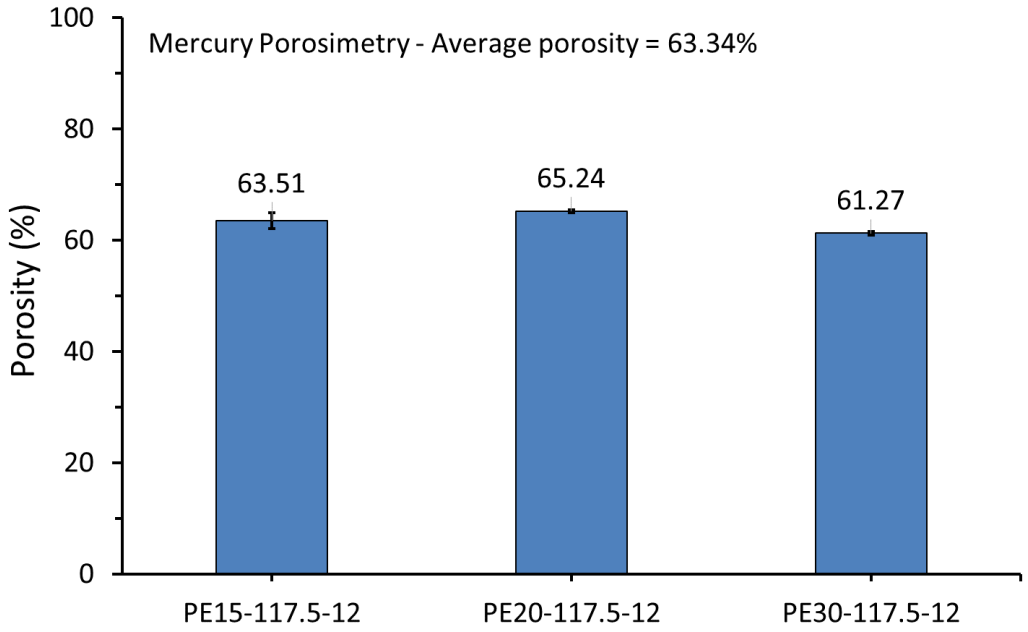

Figure 8.14 : Porosity of laser sintered AC-UHMWPE parts measured using Mercury Porosimetry (Two samples for each condition).

Figure 8.15 shows a typical log differential intrusion curve of pore size distributions for a laser sintered AC-UHMWPE samples. The results show that 85:15 and 80:20 AC-UHMWPE samples have similar pore size distributions with a peak of pore size of approximately 69 µm and dominant range of pores between 48 – 88 µm. The pore size distribution curve of 70:30 AC-UHMWPE samples was shifted to lower values with a peak of pore size of approximately 47 µm and dominant range of pores between 31 – 62 µm.

This result suggests that the pore size decreases with increasing UHMWPE content in the laser sintered AC-UHMWPE parts. Additionally, a reduction in the area under the curves can be observed with increasing the UHMWPE content, indicating that the porosity decreases with the UHMWPE content [197].

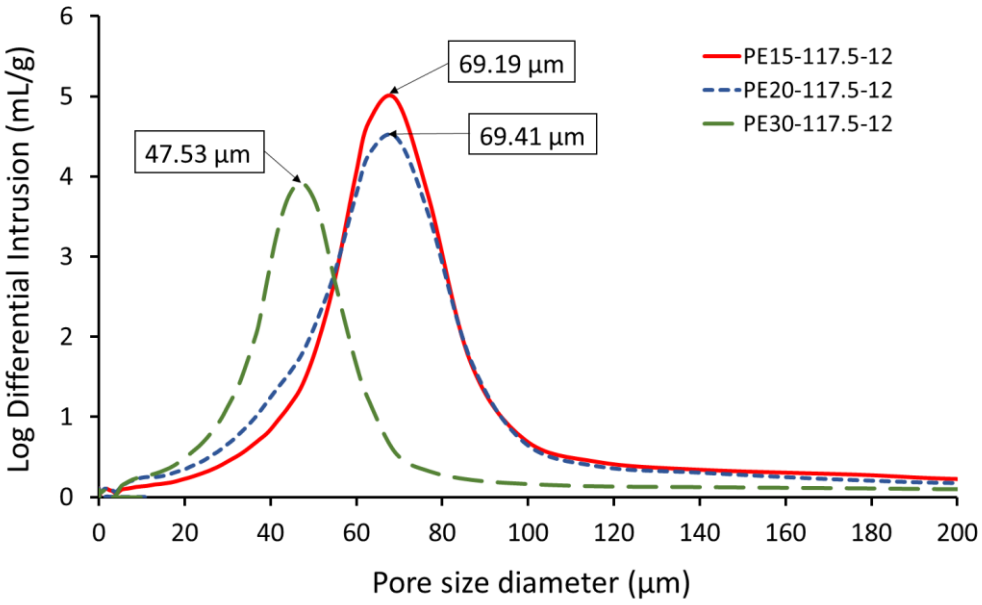

Figure 8.15 : Pore size distribution of laser sintered AC-UHMWPE parts measured using mercury intrusion

8.4.3 Mechanical Properties

8.4.3.1 *Flexural Stress*

Flexural strength was measured to determine the effects of the laser sintering parameters and the composition of the composite on the mechanical properties of the laser sintered AC-UHMWPE parts. The average effect of the bed temperature and laser power upon the flexural strength are shown Figure 8.16 and Figure 8.17, respectively.

The result in Figure 8.16 shows that the maximum flexural strength of AC-UHMWPE composites increased with increasing the UHMWPE content at different bed temperatures and laser power of 8 watts. The flexural strength of the 70:30 and 80:20 AC-UHMWPE parts increases by 99% and 77%, respectively at bed temperature of 117.5°C and by 70% and 46% at bed temperature of 120°C as compared with 85:15 laser sintered parts. The increase in strength could be explained by the increase in the amount of the binding material which induces higher bonding between UHMWPE particles in the matrix yielding to increasing the flexural strength.

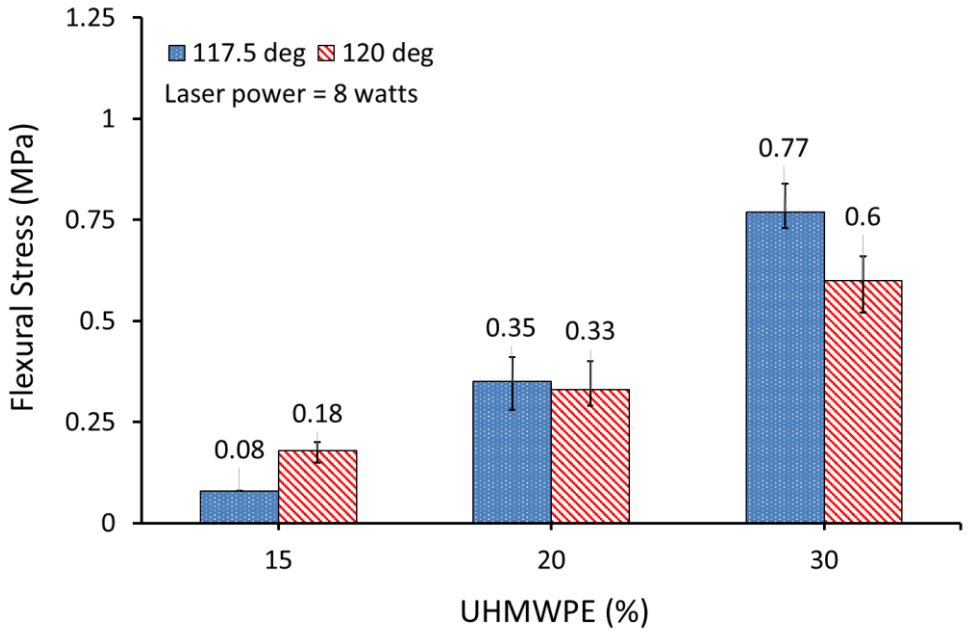

Figure 8.16 : Flexural stress of AC-UHMWPE with different UHMWPE % content produced at laser power of 8 and bed temperatures of 117.5°C and 120°C (Three samples for each condition and the error bar represents the range of the data)

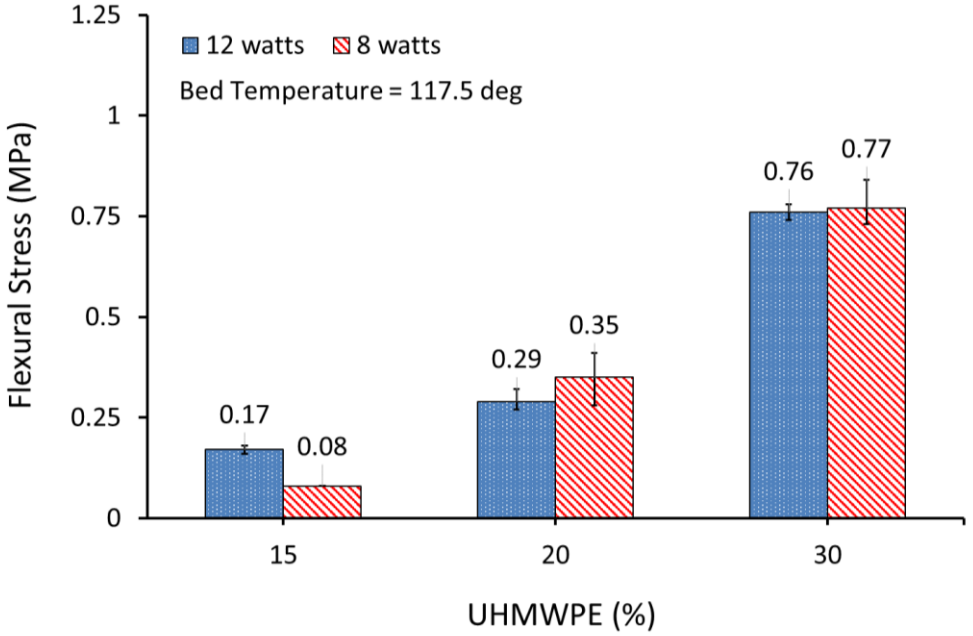

Figure 8.17 : Flexural stress of AC-UHMWPE with different UHMWPE % content produced at laser power of 8 and 12 watts and bed temperature of 117.5°C (Three samples for each condition and the error bar represents the range of the data)

A similar behaviour was observed with the flexural stress produced at different laser powers as shown in Figure 8.17. However, the effect of laser power and bed temperature on flexural stress of the parts produced at the same UHMWPE content, did not have a significant impact, except 85:15 laser sintered parts. Parts with reduced amount of binder (85:15 AC-UHMWPE) and produced at laser power of 8 watts and bed temperature of 117.5°C were generally weak and difficult to handle comparing to the parts produced at higher laser power and bed temperature.

A slight variation in the flexural stress was observed between all parts produced at different process parameters but with the same UHMWPE content, which very likely results from errors when measuring the dimensions of the samples geometrically because of the surface roughness.

Generally, the flexural stress behaviour was similar to that of the relative density. It can be concluded that the effects on flexural stress are not driven by the laser power and bed temperature within the range of parameters analysed. For both cases, nearly the similar values of flexural stresses could be achieved for parts produced at the same UHMWPE content.

8.4.3.2 *Flexural Modulus*

The flexural tests results show that the modulus of the AC-UHMWPE composite material is proportional to the UHMWPE content as depicted in Figure 8.18 and Figure 8.19.

The stiffness of the 80:20 and 70:30 AC-UHMWPE parts increases by 68% and 85%, respectively at bed temperature of 117.5°C and by 26% and 87% at bed temperature of 120°C as compared with 85:15 laser sintered parts (Figure 8.18). A similar behaviour was observed with the modulus shown in Figure 8.19. This increase in the modulus was attributed to the increase of the stiffness of the matrix due to the increase of the UHMWPE content that binds the structure of matrix together.

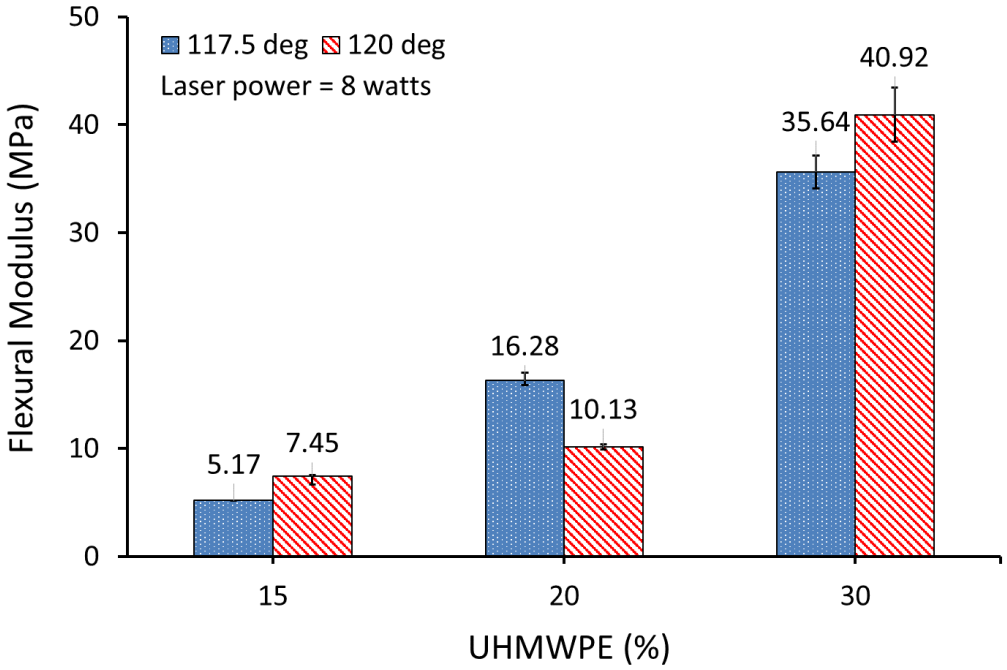

Figure 8.18 : Flexural modulus of AC-UHMWPE with different UHMWPE % content produced at laser power of 8 and bed temperatures of 117.5°C and 120°C.
(Three samples for each condition and the error bar represents the range of the data)

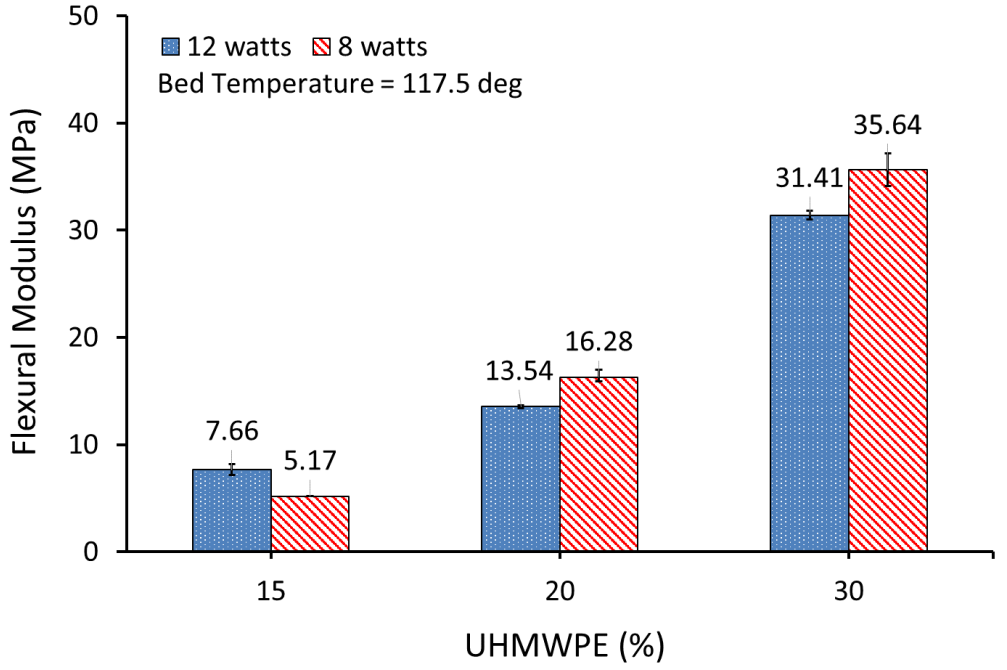

Figure 8.19 : Flexural modulus of AC-UHMWPE with different UHMWPE % content produced at laser power of 8 and 12 watts and bed temperature of 117.5°C.
(Three samples for each condition and the error bar represents the range of the data)

Variations in the values of flexural modulus were observed between all parts produced at different process parameters and the same UHMWPE content. The average of these variations ranges from a minimum of 12.38%, for 70:30 AC-UHMWPE samples, to a maximum of 31.56%, for 85:15 AC-UHMWPE samples, which were produced at different bed temperatures and constant laser power (Figure 8.18), or at different laser powers and constant bed temperature (Figure 8.19). Parts produced with a higher UHMWPE content exhibit smaller variation (i.e. 70:30 AC-UHMWPE samples). A well-defined structure can be formed with a higher content of binder, which in turn facilitates the flow of material by increased and improved fusion of the polymer particles producing a well-defined geometry. It is well known that the flexural modulus is highly sensitive to the geometry of the samples and therefore if there is any slight error when measuring the dimensions of the samples geometrically, due to the surface roughness, would have a considerable effect on the value of the flexural modulus.

8.4.4 Differential Scanning Calorimetry

The melt and crystallisation peaks of the laser sintered AC-UHMWPE parts are summarised in Table 8.3 and a comparison of the peak temperatures between different AC-UHMWPE parts are presented in Figure 8.20 and Figure 8.21.

Table 8.3: Thermal properties of neat UHMWPE and composite powders

Sample ID	1st Thermal cycle		2nd Thermal cycle	
	Melting point peak (°C)	Crystallisation point peak (°C)	Melting point peak (°C)	Crystallisation point peak (°C)
PE15-117.5-8	136.92	121.27	135.17	121.18
PE15-117.5-12	136.05	120.67	134.12	120.62
PE15-120-8	136.30	120.74	134.47	120.66
PE20-117.5-8	135.83	120.50	134.44	120.43
PE20-117.5-12	135.55	120.39	134.35	120.28

PE20-120-8	136.47	120.66	134.65	120.56
PE30-117.5-8	136.62	120.80	135.19	120.61
PE30-117.5-12	136.13	120.51	134.98	120.48
PE30-120-8	137.57	121.13	135.79	121.00

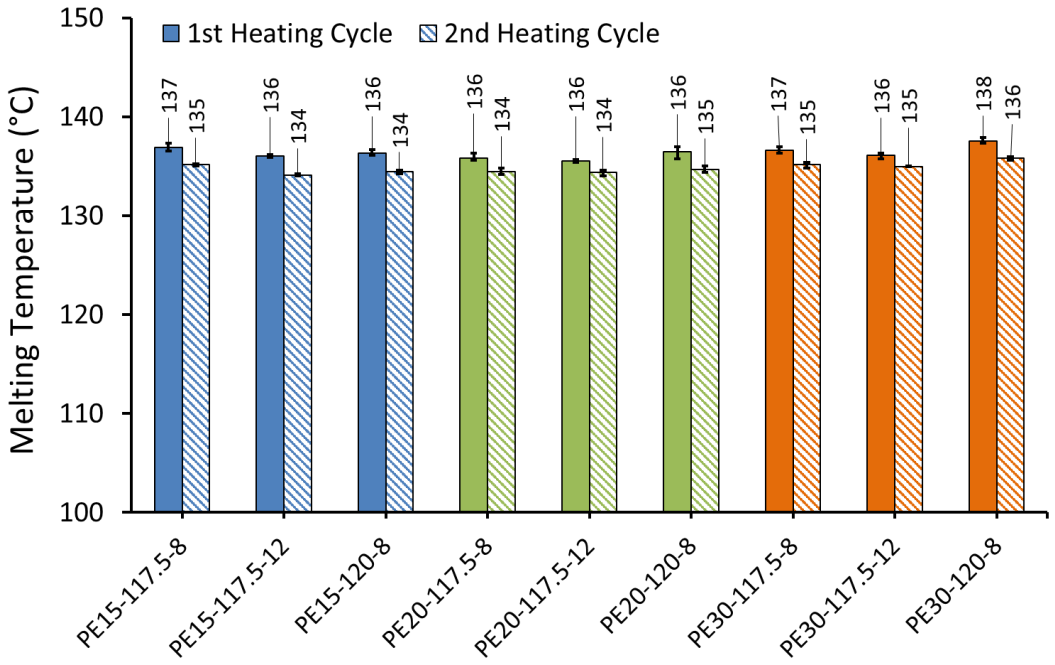

Figure 8.20 : Melting peak temperatures of laser sintered AC-UHMWPE composites produced with different UHMWPE % content, laser powers and bed temperatures

The results show that the peak temperatures for melting and crystallisation remain constant for all samples indicating that the intrinsic thermal properties of the laser sintered AC-UHMWPE parts are not affected by the composition ratio of the AC-UHMWPE composite, laser power or bed temperature. There was no interaction occurred between the UHMWPE and AC materials after the application of the heat generated by the laser beam.

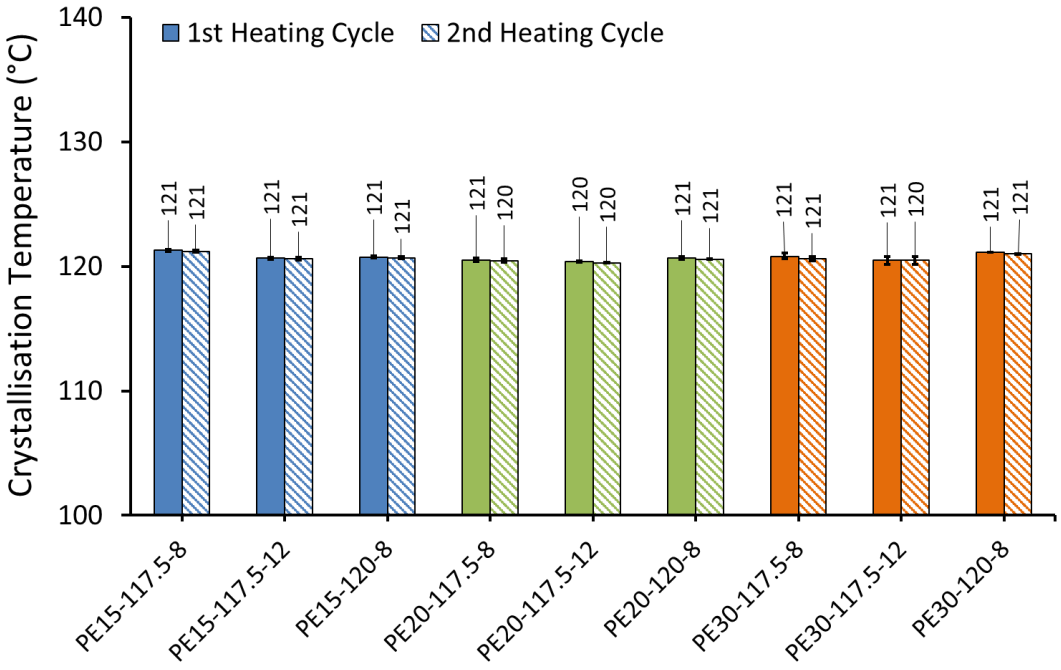

Figure 8.21 : Crystallisation peak temperatures of laser sintered AC-UHMWPE composites produced with different UHMWPE % content, laser powers and bed temperatures

Since the sintered parts were treated by a laser and subsequently the thermal history of the virgin powder has changed, then the first heating cycle of the sintered parts can be a representative of the second heating cycle of the un-sintered powder. Therefore a valid comparison can be made to examine the thermal behaviour of the sintered parts. On this basis, the results show that the average of the melt temperatures in the first heating cycle of the laser sintered parts was slightly increased to 136.44°C compared to the average of the melt temperatures in the second heating cycle of the un-sintered AC-UHMWPE powders, which was 132.67°C (refer to Table 7.4, Chapter 7). While the average of the crystallisation temperatures in the first heating cycle of the sintered parts was slightly increased to 120.89°C compared to the average of the crystallisation temperature in the second heating cycle of the un-sintered AC-UHMWPE powders, which was 118.55°C (refer to Table 7.4, Chapter 7).

Although there is an insignificant difference in the melting and crystallisation temperatures of all samples, the first heating cycle of the laser sintered parts

and the second heating cycle of the composite powder correspond well to each other. Therefore, consolidating AC-UHMWPE composite powders by laser did not alter the thermal properties significantly.

8.4.5 Thermogravimetric Analysis

Table 8.4 lists the initial and final decomposition temperatures of the AC-UHMWPE composite powders and the laser sintered parts. Figure 8.22 shows the thermal stability of the laser sintered AC-UHMWPE parts.

Table 8.4: TGA analysis thermal data of laser sintered AC-UHMWPE parts

Sample ID	Onset Temperature (°C)		
	T_1*	T_2*	ΔT
PE15	497.03	545.03	48.00
PE15-117.5-8	499.29	548.58	49.29
PE15-117.5-12	499.54	550.22	50.68
PE15-120-8	496.31	546.34	50.03
PE20	498.18	547.61	49.43
PE20-117.5-8	497.36	552.09	54.73
PE20-117.5-12	494.04	548.59	54.55
PE20-120-8	496.53	546.49	49.96
PE30	483.36	543.09	59.73
PE30-117.5-8	480.77	547.91	67.14
PE30-117.5-12	485.11	551.45	66.34
PE30-120-8	479.79	551.04	71.25

** T_1 and T_2 are the initial and final onset decomposing temperatures, respectively.*

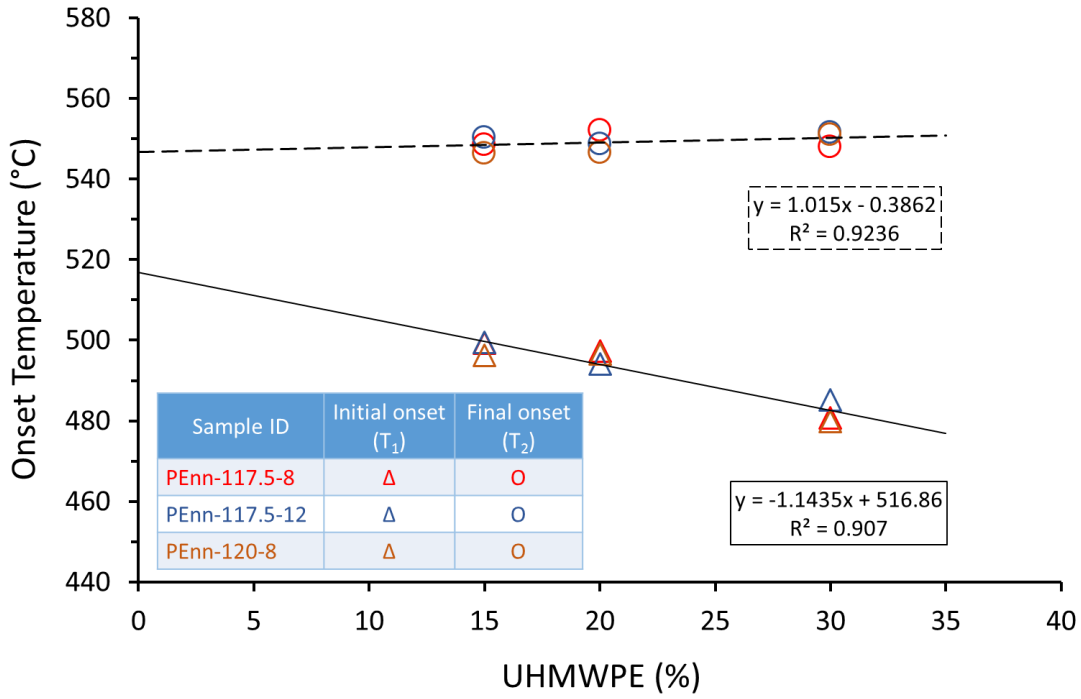

Figure 8.22 : Thermal stability of laser sintered AC-UHMWPE composite parts
T_1 and T_2 are the initial and final onset decomposing temperatures, respectively.

The results show an average of initial decomposition temperatures of approximately 498°C, 495°C and 482°C were observed for 85:15, 80:20 and 70:30 AC-UHMWPE parts, respectively. The initial decomposition temperatures of the sintered parts decreased significantly with the increase in UHMWPE content but the final decomposition temperatures remained relatively constant with a slight increase with UHMWPE content.

This behaviour was reflected on the difference between the initial and final decomposition temperatures of laser sintered parts. The difference between the initial and final decomposition temperatures increased slightly compared to the AC-UHMWPE powders at the same ratio of composition. The average increase was 2°C, 3.65°C and 8.51°C for 85:15, 80:20 and 70:30 AC-UHMWPE parts, respectively. This indicates that the decomposition rate was slowed down after the application of the laser energy. During the sintering process, a cross linking may occur as a result of the high thermal energy applied and subsequently the molecular weight of the polymer increases. This increase may restrict the mobility of the molecules and slows down the degradation

process. Additionally, the spreading of the polymer onto the AC particles and the strong bonds between the UHMWPE particles could delay the degradation process.

The thermal stability curves of the laser sintered AC-UHMWPE parts produced at different laser power and bed temperature compared to the un-sintered composite powders are presented in Figure 8.23, Figure 8.24 and Figure 8.25. All samples were tested without pre-drying as the physical moisture uptake of the composite powders and the laser sintered AC-UHMWPE parts can occur quickly. The results have not been adjusted for the moisture content. The final mass was not the same for all samples due to sampling error.

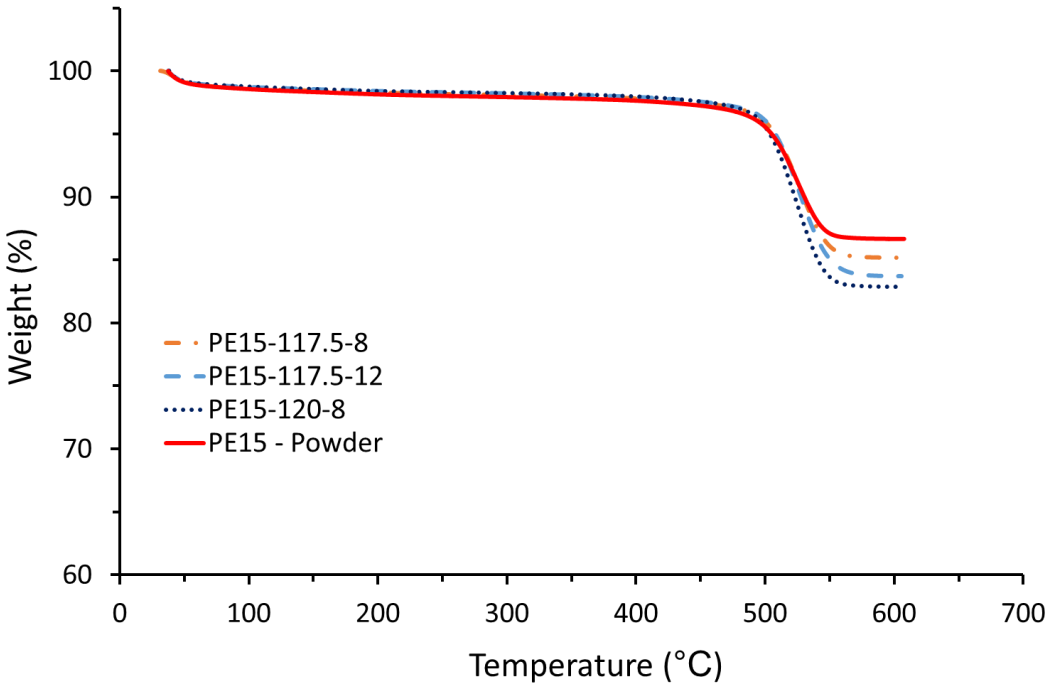

Figure 8.23 : TGA curves of laser sintered AC-UHMWPE parts with 85:15 AC-UHMWPE produced at different laser powers and bed temperatures

The TGA curves in Figure 8.23 show that the thermal decomposition behaviour of laser sintered AC-UHMWPE parts is similar to that of the un-sintered AC-UHMWPE powders with a ratio of 85:15 AC-UHMWPE, except that the initial decomposition temperatures were slightly higher.

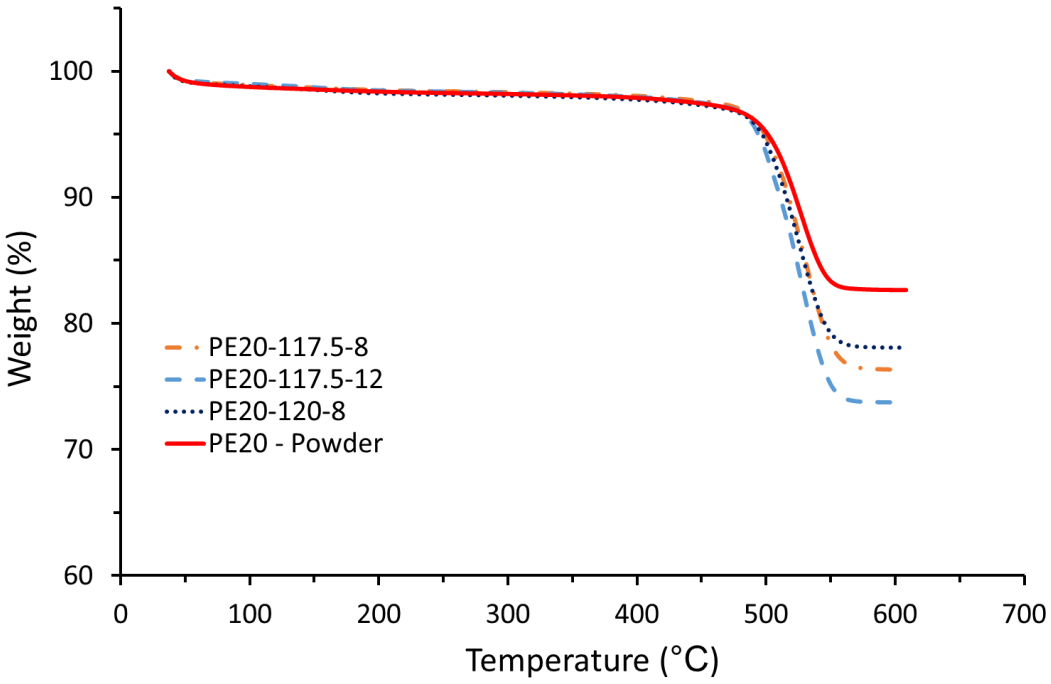

Figure 8.24 : TGA curves of laser sintered AC-UHMWPE parts with 80:20 AC-UHMWPE produced at different laser powers and bed temperatures

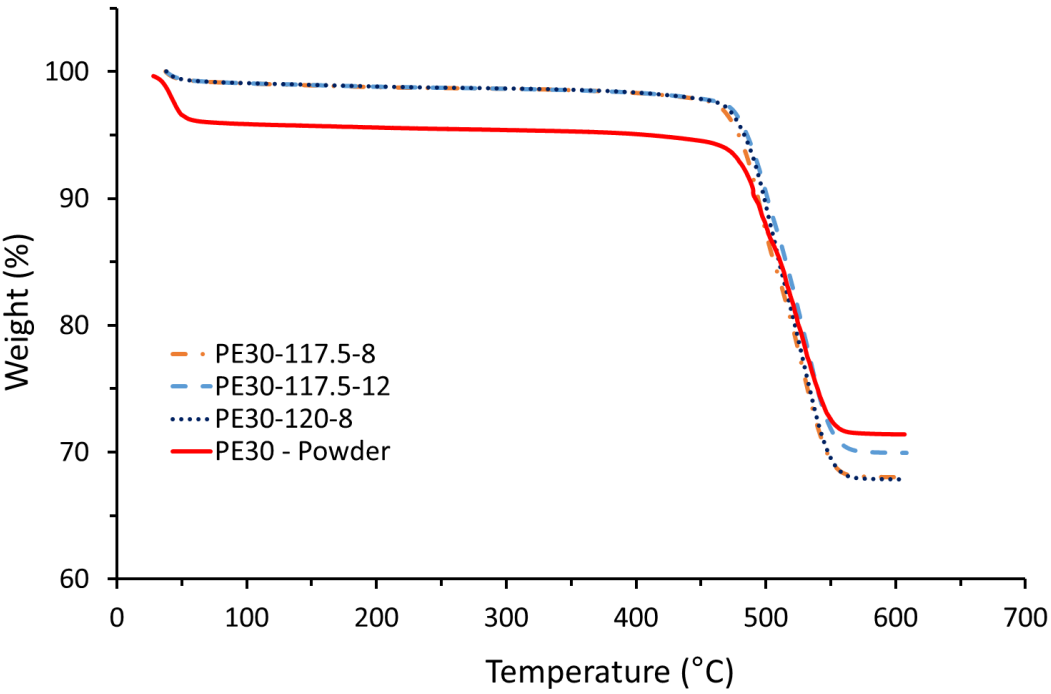

Figure 8.25 : TGA curves of laser sintered AC-UHMWPE parts with 70:30 AC-UHMWPE produced at different laser powers and bed temperatures

Applying different laser powers or bed temperatures appeared to have no effect on the decomposition behaviour. Similar behaviour was observed with 80:20 and 70:30 AC-UHMWPE samples as shown in Figure 8.24 and Figure 8.25.

However, the TGA curves of the laser sintered AC-UHMWPE parts, produced at the same laser power and bed temperature but with different composition ratios, were shifted to a higher temperature when the activated carbon ratio increased indicating a higher thermal stability (Figure 8.26).

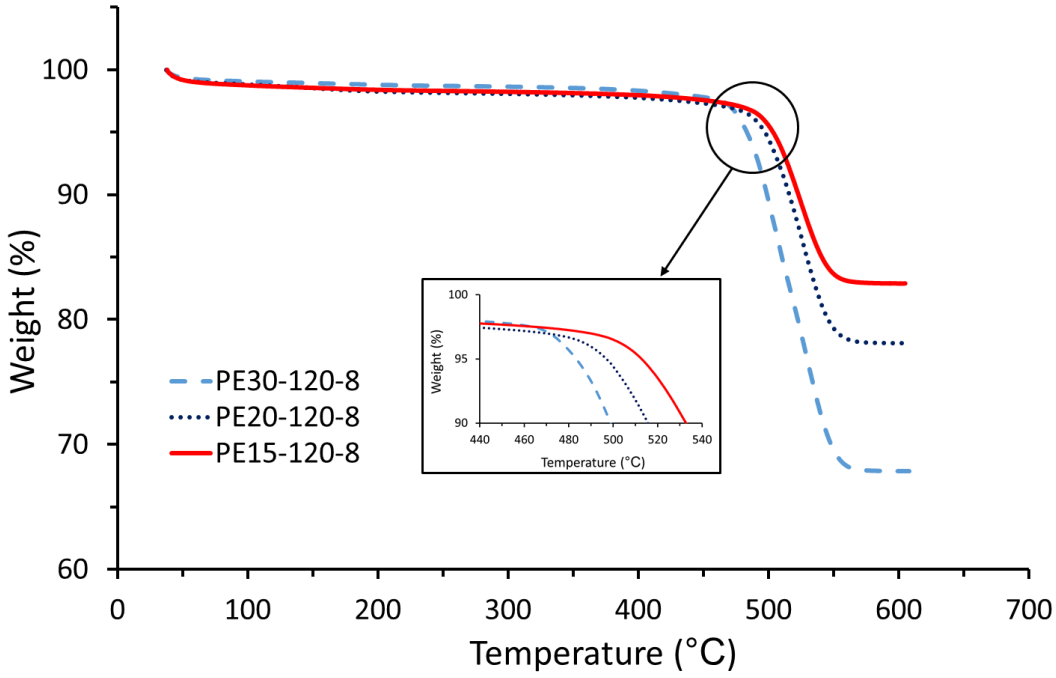

Figure 8.26 : TGA curves of laser sintered parts with 85:15, 80:20 and 70:30 AC-UHMWPE produced at laser power of 8 watts and bed temperature of 120°C

The TGA analysis of laser sintered AC-UHMWPE showed a stable weight of the samples up to about a minimum of 480°C (sample PE30-120-8), independent of the processing history. The weight loss of the UHMWPE occurs in a narrow temperature range with a single step weight loss. This behaviour is a typical depolymerisation reaction [198]. The final decomposition temperature were slightly shifted to higher temperatures with increasing of activated carbon and increased on average by 3.35, 1.45 and 7.04°C for laser sintered parts of 85:15,

80:20 and 70:30 AC-UHMWPE, respectively compared to un-sintered composite powders.

The shift in the decomposition temperatures, which was observed between the laser sintered parts produced at the same process parameters with different composition ratios, could be attributed to the increase of the adsorption of the volatile degraded UHMWPE components with increasing of activated carbon. This could delay the mass loss and retard the thermal degradation, resulting in a higher degradation temperatures.

At temperatures above 546°C, for samples with 85:15 and 80:20 AC-UHMWPE, and 551°C, for samples with 70:30 AC-UHMWPE, the mass remained constant for all samples, effectively allowing a verification of the actual UHMWPE content in the laser sintered composites. Figure 8.27 shows that there is a slight disagreement between the intended and actual UHMWPE weight fractions due to the small size of the samples used in this analysis.

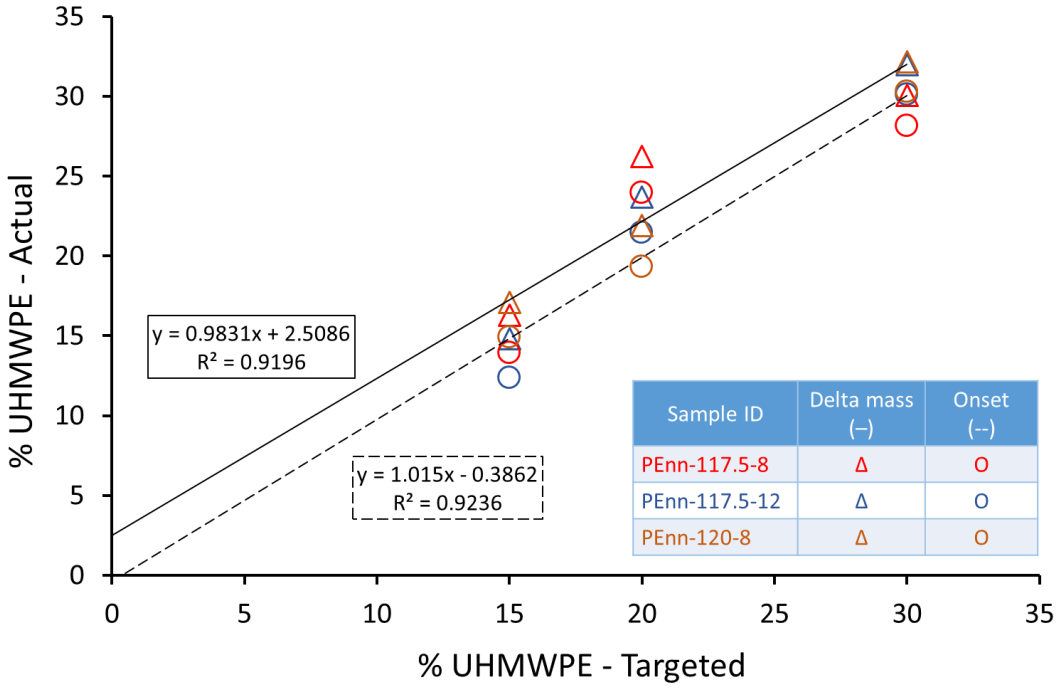

Figure 8.27: Actual weight fractions of UHMWPE in the laser sintered AC-UHMWPE composite parts measured by TGA

8.4.6 XRD Analysis

The XRD patterns of the laser sintered AC-UHMWPE parts and the composite powders are shown in Figure 8.28, Figure 8.29 and Figure 8.30 for 70:30, 80:20 and 85:15 AC-UHMWPE, respectively.

The diffraction peaks centred at 2θ = 21.6 and 24.0° correspond to the (110) and (200) planes of the UHMWPE, respectively [199]. The XRD profiles of the laser sintered AC-UHMWPE composites show a weak and wide diffraction peak near 2θ = 43.0°, which is assigned to the (101) diffraction planes of graphitic carbon coming from activated carbon and confirming its amorphous state [182]. This is a similar peak to that of the un-sintered composite powders.

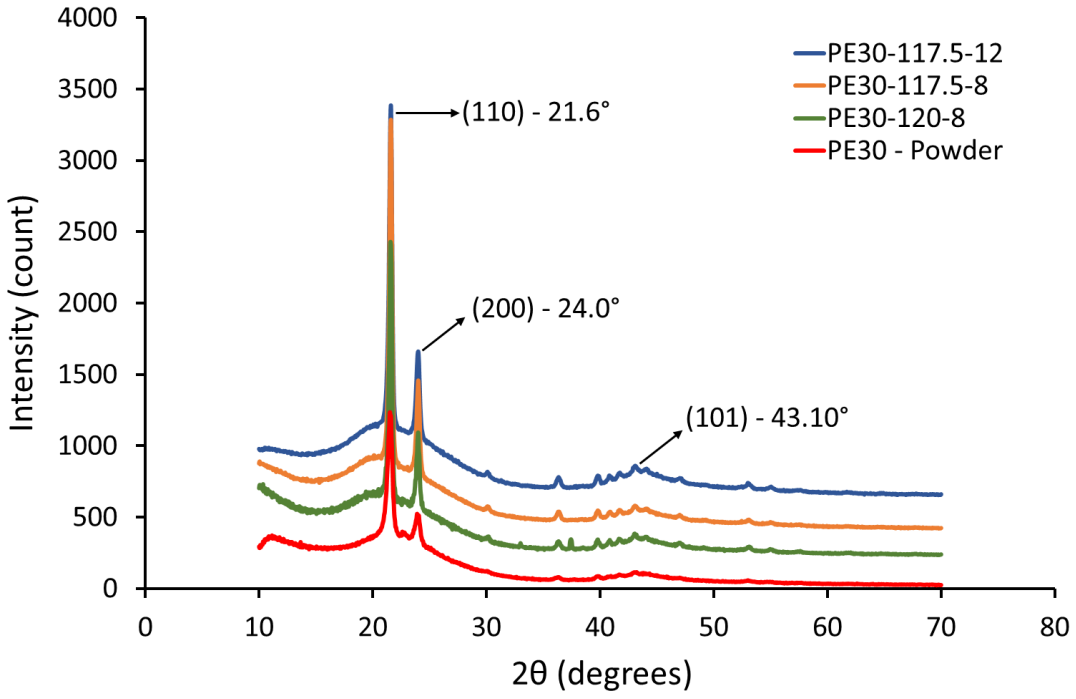

Figure 8.28: XRD profile of laser sintered 70:30 AC-UHMWPE composite parts produced at different laser powers and bed temperatures

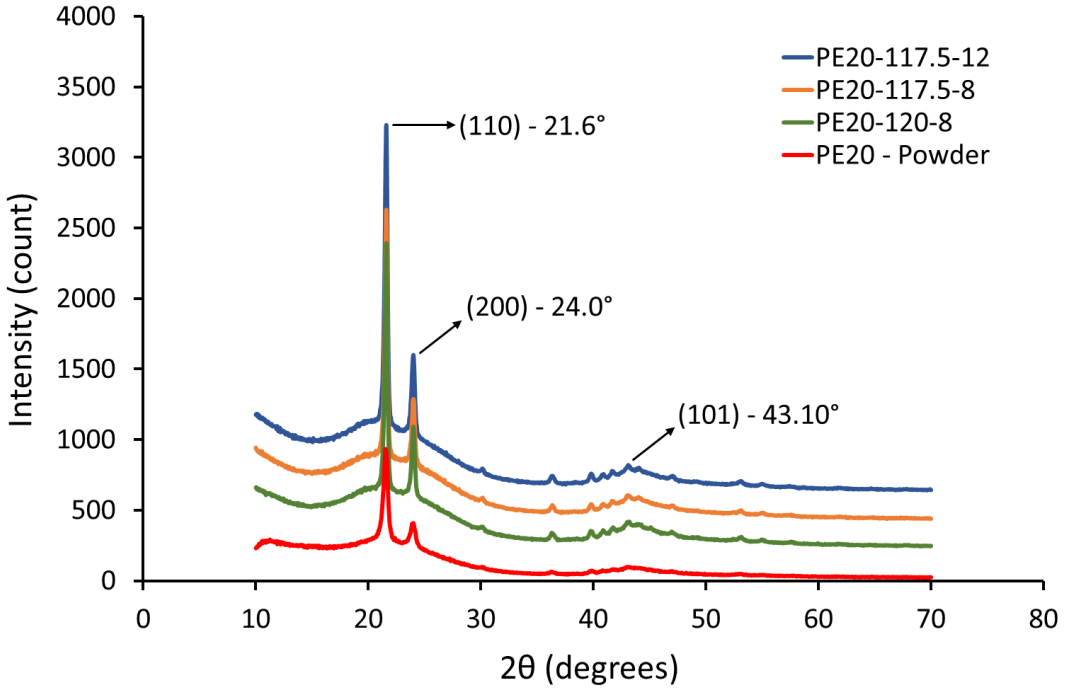

Figure 8.29: XRD profile of laser sintered 80:20 AC-UHMWPE composite parts produced at different laser powers and bed temperatures

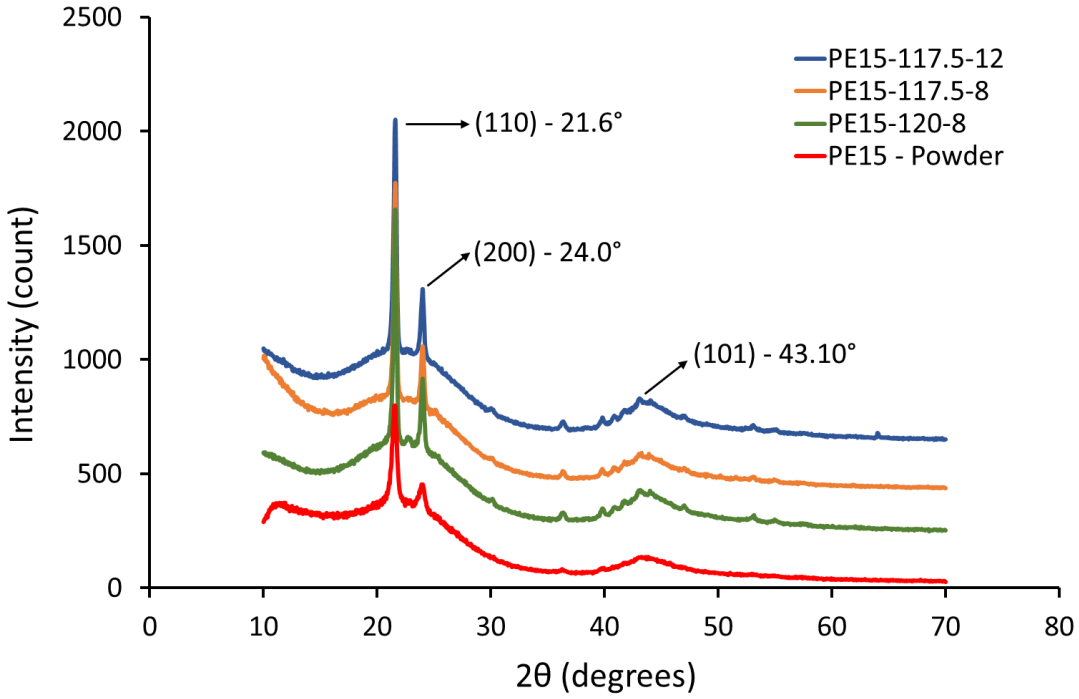

Figure 8.30: XRD profile of laser sintered 85:15 AC-UHMWPE composite parts produced at different laser powers and bed temperatures

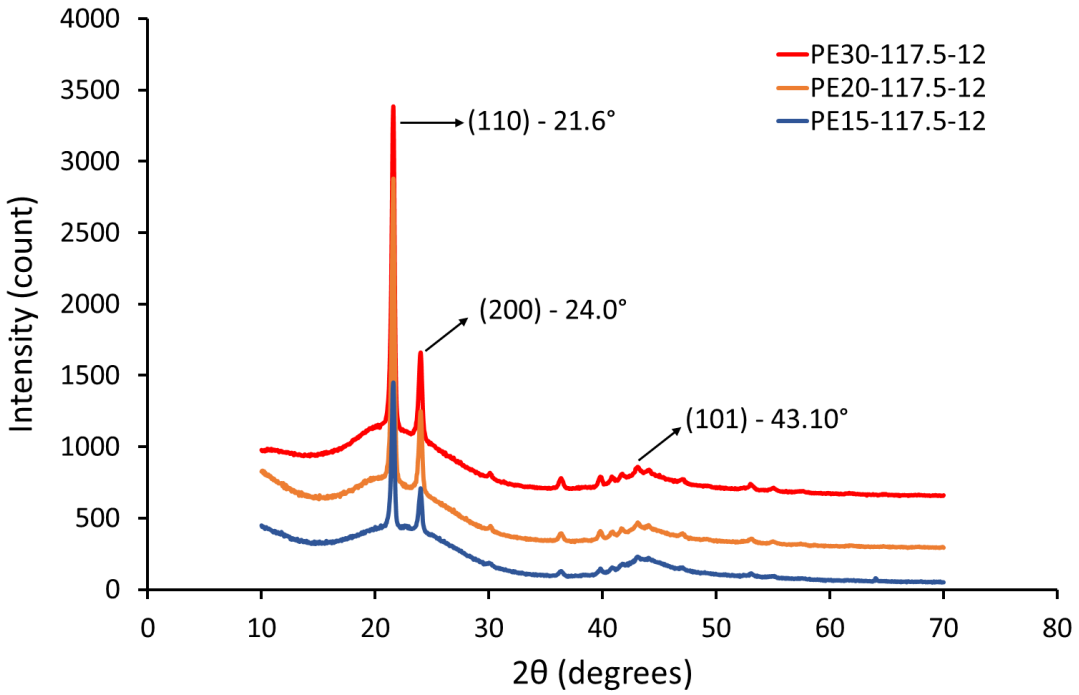

Figure 8.31: XRD profile of laser sintered 70:30, 80:20 and 85:15 AC-UHMWPE composite parts produced at laser power of 12 watts and bed temperature of 117.5°C

No significant changes were observed in the XRD patterns. Nevertheless, the intensity of the (110), (200) and (101) peaks are larger compared to the starting composite powders. The highest increase in the peak size was for (110) plane, indicating a significant growth of the crystallites along the (110) plane direction [200]. The result also shows (Figure 8.31) that the content of activated carbon in the composites affected the degree of crystallinity but had little effect on the crystallite structure. Increasing the content of activated carbon in the composites only led to decrease the intensity of the peaks without changing the crystal structure.

8.4.7 Degree of Crystallinity

Table 8.5 lists the degree of crystallinities of laser sintered AC-UHMWPE composite parts calculated from the first heating (X_{C1}) and second heating (X_{C2}) cycles of the DSC, and also the crystallinity obtained by XRD measurements (X_{C3}).

Table 8.5: Degree of crystallinity of laser sintered AC-UHMWPE parts

Sample ID	Crystallinity - DSC (%)		Crystallinity - XRD (%)
	X_{C1}	X_{C2}	X_{C3}
PE15-117.5-8	38.18 ±3.52	38.45 ±0.91	39.85 ±2.85
PE15-117.5-12	41.76 ±1.96	41.94 ±4.29	40.35 ±3.25
PE15-120-8	47.46 ±5.74	44.85 ±2.61	42.90 ±4.00
PE20-117.5-8	48.50 ±1.36	47.68 ±1.36	45.60 ±2.20
PE20-117.5-12	47.98 ±1.80	50.38 ±2.32	49.15 ±0.75
PE20-120-8	45.70 ±3.75	41.70 ±4.76	44.80 ±1.30
PE30-117.5-8	42.48 ±0.92	33.20 ±1.16	53.45 ±0.95
PE30-117.5-12	43.13 ±4.70	38.45 ±2.90	52.70 ±3.80
PE30-120-8	48.49 ±2.50	43.90 ±3.87	55.90 ±4.20

The average crystallinity in the first heating cycle of the DSC of all samples was measured at a minimum of 38% and a maximum of 48.5% approximately, and 40% and 56% as measured by XRD. The crystallinity measured by XRD method shows slightly higher values compared to DSC as expected.

The average crystallinity in the DSC first heating cycle of the laser sintered parts increased significantly compared to the average crystallinity in the DSC second heating cycle of the un-sintered AC-UHMWPE powders. The overall average crystallinity of the laser sintered AC-UHMWPE parts increased to approximately 42%, 47% and 45% compared to the average crystallinity of the un-sintered composite powder measured at approximately 30%, 29% and 37% for 85:15, 80:20 and 70:30 AC-UHMWPE, respectively.

The increase in crystallinity in the laser sintered parts as compared with starting powder can be attributed to the relatively slower rate of cooling of the parts during and after the consolidation process. Double laser scan was used

during laser sintering process and this could contribute to the slow cooling rate.

The effects of laser power and bed temperature on the crystallinity of the laser sintered AC-UHMWPE parts produced with different UHMWPE content, are shown in Figure 8.32 and Figure 8.33 as measured by DSC.

The average of crystallinity of laser sintered AC-UHMWPE samples produced at different bed temperatures and a constant laser power (Figure 8.32) was approximately 43%, 47% and 46% for AC-UHMWPE samples with 85:15, 80:20 and 70:30 AC-UHMWPE, respectively (normalised by the amount of UHMWPE). While the average crystallinity of the AC-UHMWPE samples produced at different laser powers and a constant bed temperature was approximately 40%, 48% and 43% for AC-UHMWPE samples with 85:15, 80:20 and 70:30 AC-UHMWPE, respectively (Figure 8.33).

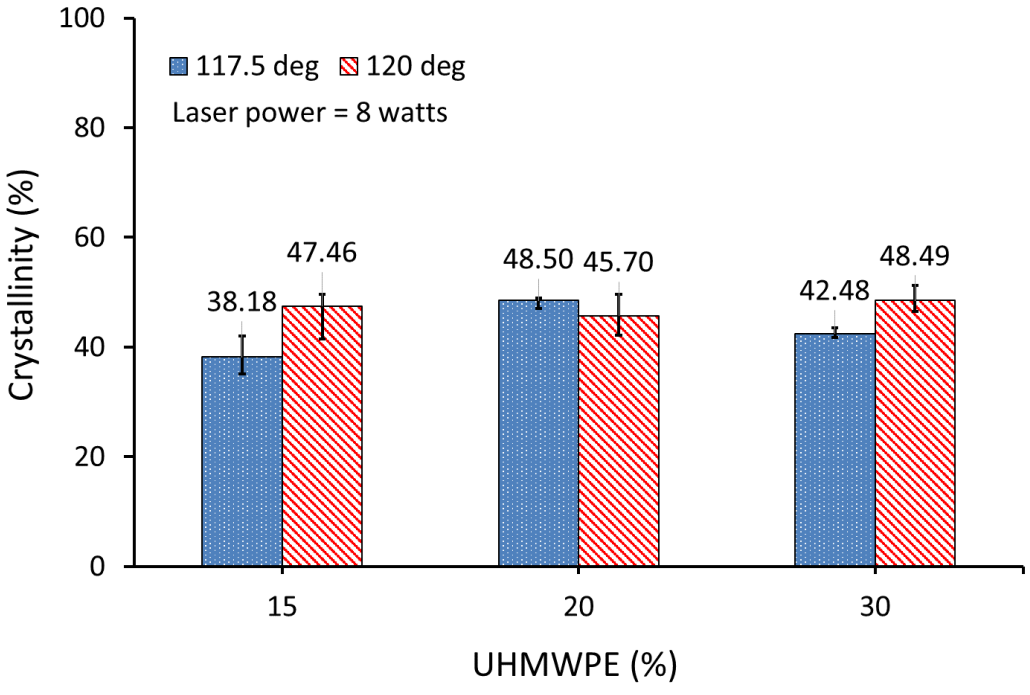

Figure 8.32 : Degree of crystallinity (DSC) of AC-UHMWPE with different UHMWPE % content produced at laser power of 8 watts and bed temperatures of 117.5°C and 120°C. (Normalised by the amount of UHMWPE)
(Three samples for each condition and the error bar represents the range of the data)

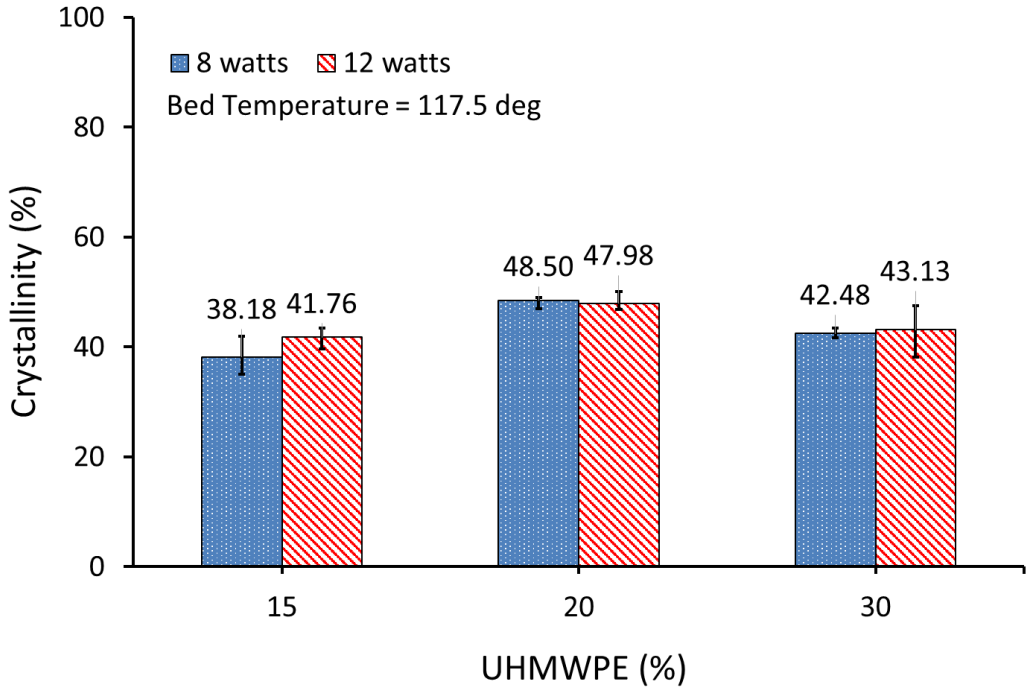

Figure 8.33 : Degree of crystallinity (DSC) of AC-UHMWPE with different UHMWPE % content produced at laser power of 8 and 12 watts and bed temperature of 117.5°C. (Normalised by the amount of UHMWPE)
(Three samples for each condition and the error bar represents the range of the data)

The results of DSC analysis do not show a clear pattern of change in crystallinity with the changes in laser power and bed temperature. Therefore, stronger conclusions cannot be drawn in this case as the DSC results do not show statistically significant changes in crystallinity values.

Unlike the DSC analysis, the XRD result shows a decrease in crystallinity of the laser sintered parts with increasing of activated carbon content as shown in Figure 8.34. Activated carbon has a very high thermal conductivity compared to UHMWPE polymer. Therefore, the thermal conductivity of the composite was improved by the addition of activated carbon and consequently the cooling rate was increased. Thus a decreased in crystallinity is expected in the laser sintered AC-UHMWPE parts with increasing AC content.

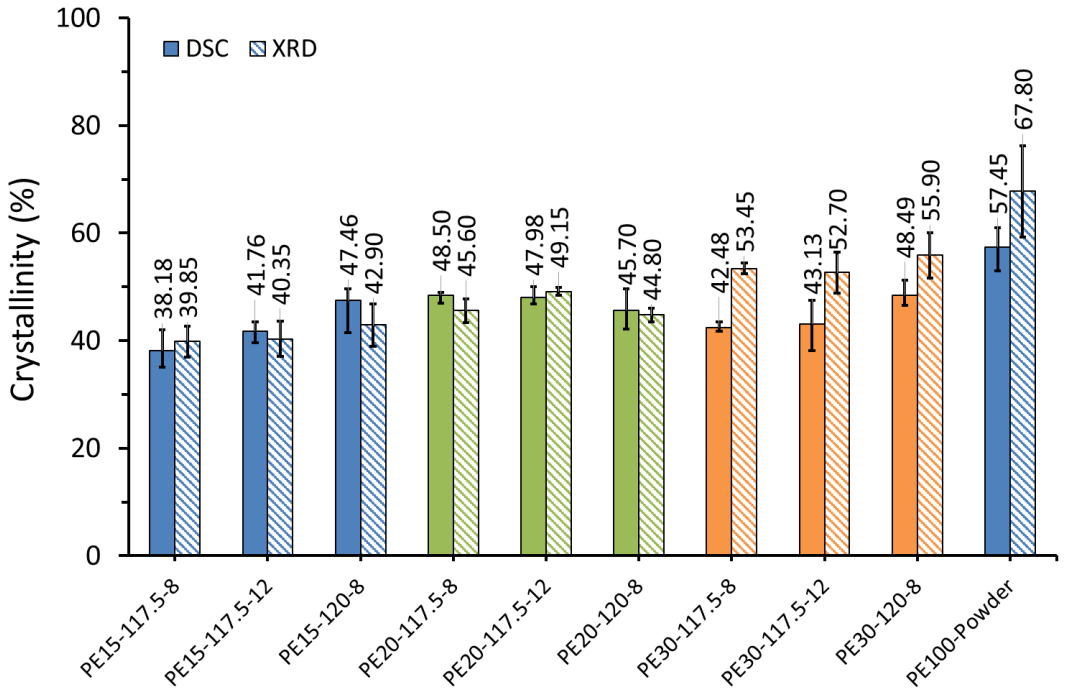

Figure 8.34 : Comparison between the crystallinity of laser sintered AC-UHMWPE composites measured by DSC (first heating cycle) and XRD methods

8.4.8 Morphology of Laser Sintered AC-UHMWPE Parts

Figure 8.35 and Figure 8.36 show the surface of the laser sintered parts produced with 80:20 and 70:30 AC-UHMWPE, respectively at a laser power of 8 watts and a bed temperature of 120°C.

SEM images revealed that UHMWPE particles were embedded between activated carbon particles and well fused and combined tightly to each other. This structure gives a sufficient support to withstand the stress transferred from the sintered UHMWPE to activated carbon particles. The images also show that the pores of activated carbon were not filled with UHMWPE and the surface of activated carbon was not covered with the UHMWPE.

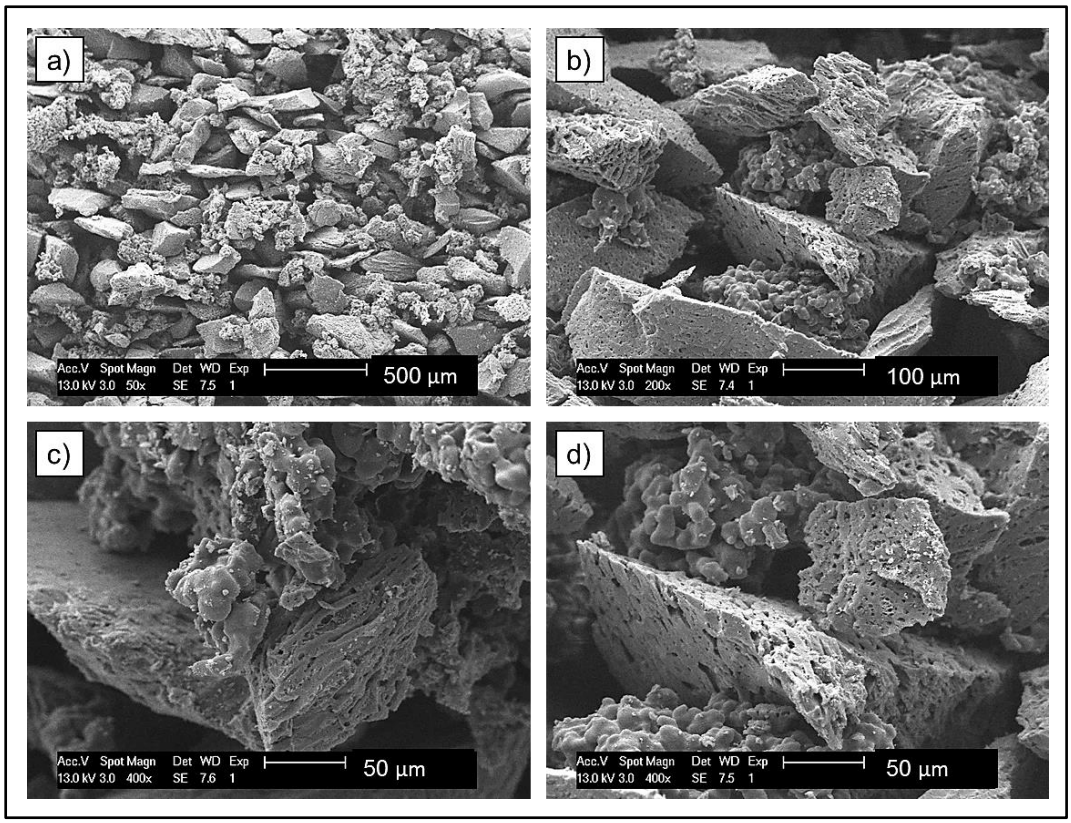

Figure 8.35: SEM micrographs of laser sintered AC-UHMWPE part (PE20-120-8) Magnifications: a) 50x, b) 200x, c) 400x and d) 400x

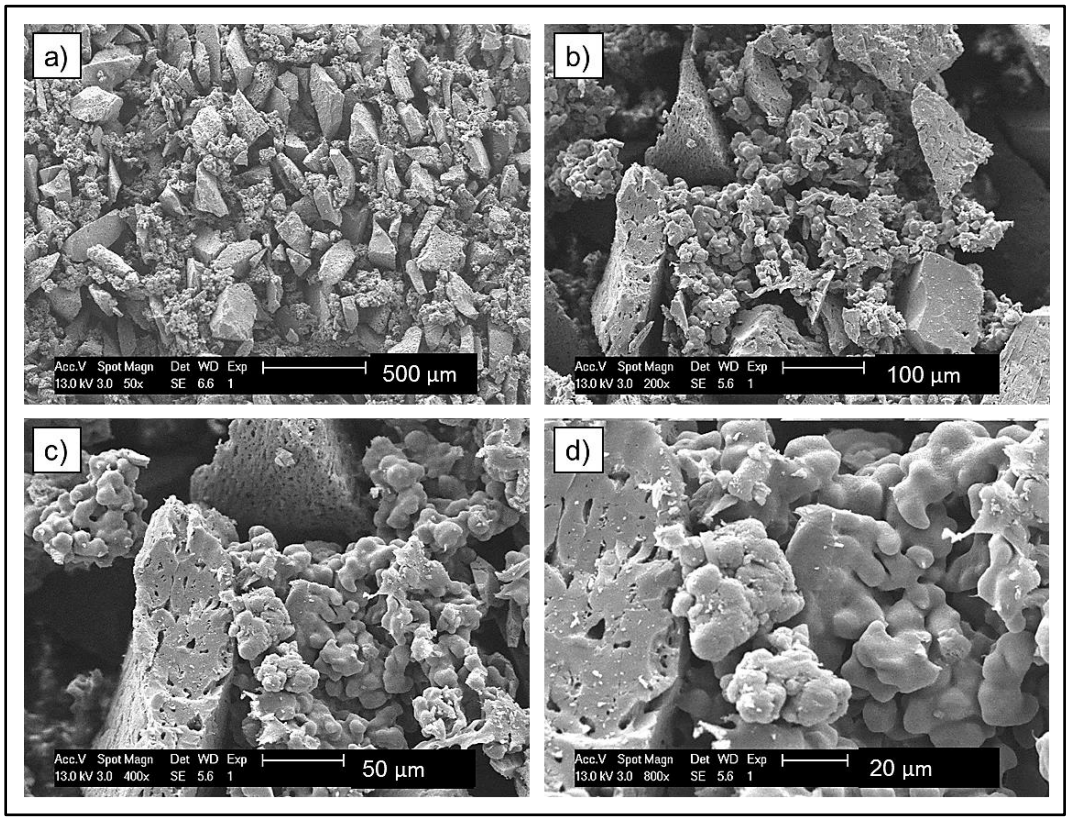

Figure 8.36: SEM micrographs of laser sintered AC-UHMWPE part (PE30-120-8) Magnifications: a) 50x, b) 200x, c) 400x and d) 800x

The structures in both 80:20 and 70:30 AC-UHMWPE appeared to be in a similar form. However, higher content of UHMWPE induces higher bonding between UHMWPE particles in the matrix yielding to improvement of the mechanical properties of the laser sintered AC-UHMWPE composites. The flexural strength of the 70:30 and 80:20 AC-UHMWPE parts, produced at fixed laser power of 8 watts, increases by 99% and 77%, respectively at bed temperature of 117.5°C and by 70% and 46% at bed temperature of 120°C as compared with 85:15 laser sintered parts.

X-ray micro-CT 3D images of laser sintered AC-UHMWPE are shown in Figure 8.37. The micro-CT images revealed that the sintered parts produced are formed from loosely, but fairly uniformly packed layers. The particles are closely packed and the particles of activated carbon and UHMWPE can easily be distinguished. UHMWPE particles are joined together and holding the structure with different pores in the parts can be observed.

Since high compact forces are not applied during the spreading of powder in laser sintering process, the particles are not deformed leading to increase in porosity and decrease in density. Both loosely packed layers, that form interconnected porosity, and also tightly packed layers, that form porosity which takes the form of sealed holes, exist in the parts. There is flattening of contact surfaces due to the large and long particles of activated carbon.

The combination of small UHMWPE particles and larger activated carbon particles has the benefit of better packing but small pores are evident regardless of the composition ratio of the composite powders.

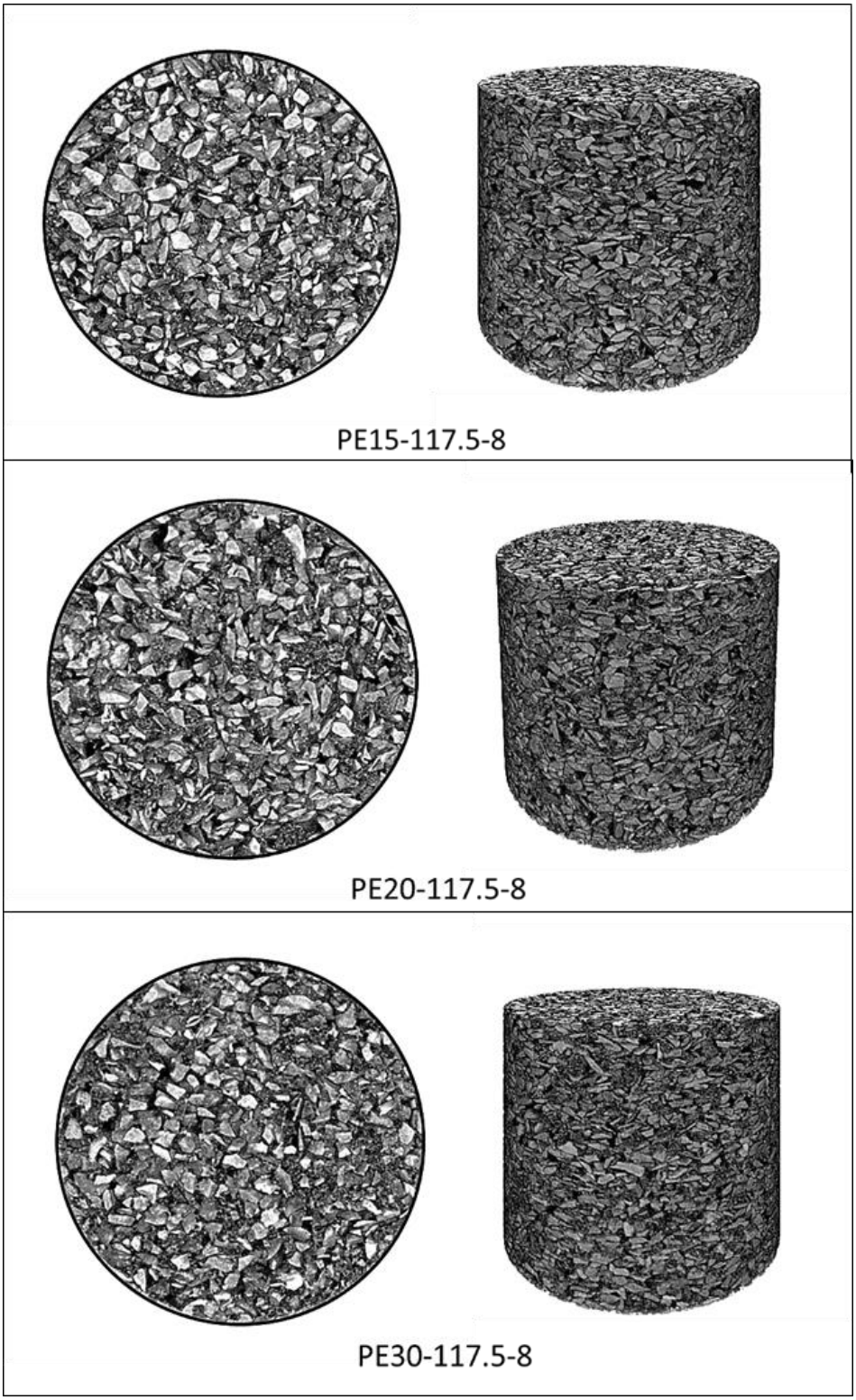

Figure 8.37 : micro-CT 3D images of laser sintered AC-UHMWPE with different UHMWPE content produced at laser power of 8 watts and bed temperature of 117.5°C. Cylindrical region of interest with a diameter of 5 mm and a height of 4 mm.

8.5 Design of Experiments (DoE)

A three-level full factorial design with three replicates was created and the properties to be evaluated were bulk density, porosity and flexural strength of the laser sintered AC-UHMWPE parts. The laser sintered AC-UHMWPE parts were manufactured using laser powers of 8 and 12 watts and bed temperatures of 117.5°C and 120°C with composition ratios of 85:15, 80:20 and 70:30. Table 8.6 shows the parameter levels used in the experiments. The samples highlighted in red have not been manufactured since this study was not an attempt to optimise the parameters used in laser sintering of AC-UHMWPE parts. Minitab 17, a statistical software, was used to analyse the experimental results.

Table 8.6: Design of experiments of the three level full factorial design

	Sample ID	UHMWPE (%)	Bed Temperature (°C)	Laser Power (watts)
Level 1	PE15-117.5-8	15	117.5	8
	PE15-117.5-12	15	117.5	12
	PE15-120-8	15	120	8
	PE15-120-12	15	120	12
Level 2	PE20-117.5-8	20	117.5	8
	PE20-117.5-12	20	117.5	12
	PE20-120-8	20	120	8
	PE20-120-12	20	120	12
Level 3	PE30-117.5-8	30	117.5	8
	PE30-117.5-12	30	117.5	12
	PE30-120-8	30	120	8
	PE30-120-12	30	120	12

The significance of the laser sintering parameters were evaluated using the Analysis of Variance (ANOVA). The ANOVA full report is listed in Appendix B.

In ANOVA analysis, the main parameters or/and its interactions are significant factors when their P-value is less than 0.05. In this study, the ANOVA results show that the content of UHMWPE (%) and bed temperature have the most significant effect on density with a P-Value of 0.00 and 0.045, respectively. Figure 8.38 and Figure 8.39 show the effect of process parameters and the interaction between these parameters on the mean of bulk density, respectively.

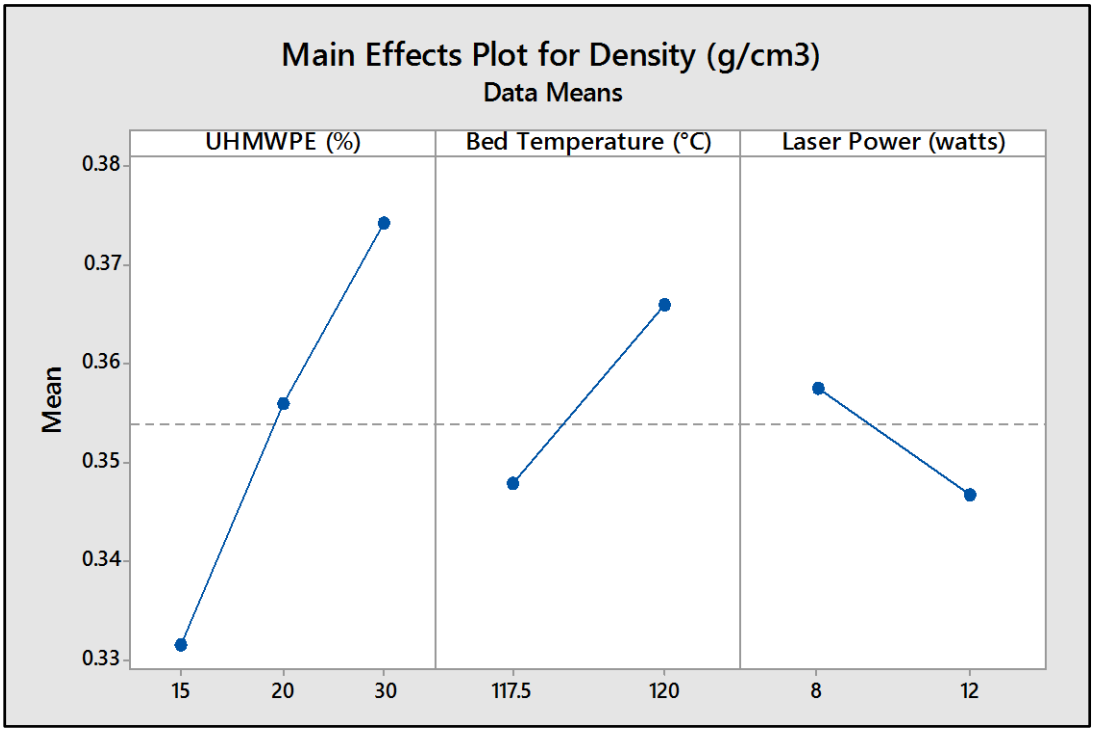

Figure 8.38: Effect of process parameters on bulk density

Higher density can be achieved when the content of UHMWPE in the AC-UHMWPE composite is higher (i.e. 30% UHMWPE). Similarly, the density of parts produced at a bed temperature of 120°C was higher than that of the parts produced at 117.5°C. Unlike bed temperature, the increase in laser power results in a decrease in density. However, the effect of laser power does not appear to be significant.

The interaction plot in Figure 8.39 shows that higher density can be achieved when the parts are produced at 30% UHMWPE content with a laser power of 8 and 12 watts and a indicating a significant effect of UHMWPE content on density. However, no clear interaction between the laser power and bed temperature can be observed as the plot shows the higher density can be achieved at laser power of 8 watts and bed temperature of 120°C. Nevertheless, the percentage of UHMWPE content has clearly significant effect on density.

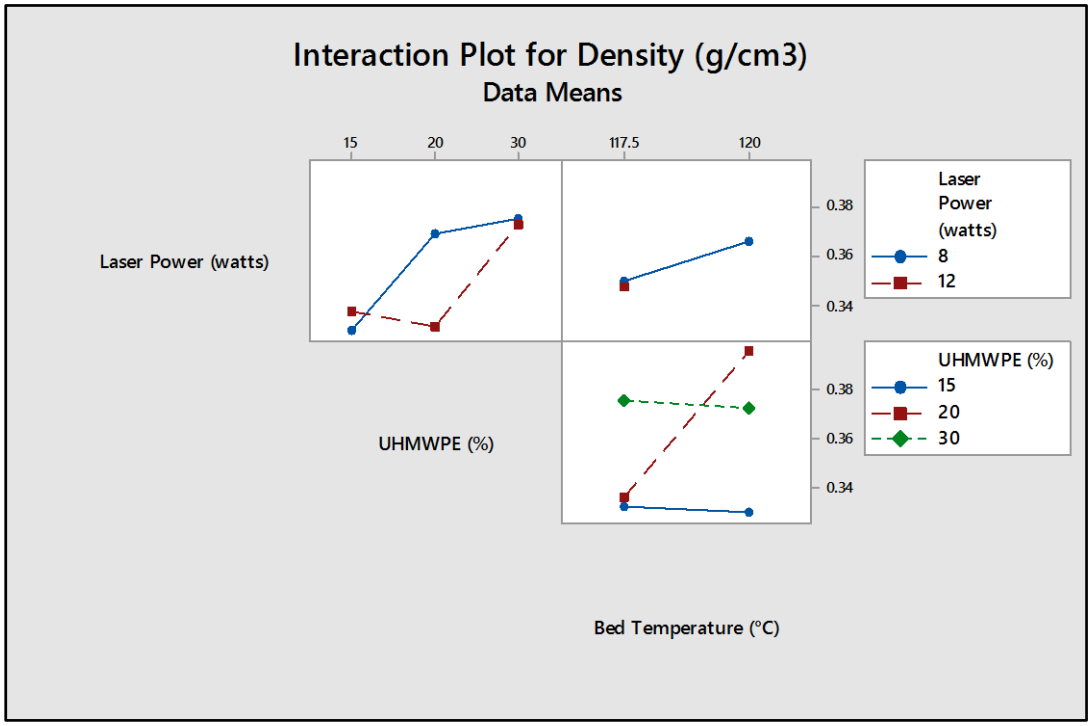

Figure 8.39: Interaction effect of process parameters on bulk density

The ANOVA analysis shows that the porosity of the laser sintered AC-UHMWPE parts have similar behaviour to that of the density. The content of UHMWPE (%) and bed temperature have the most significant effect on porosity with a P-Value of 0.00 and 0.051, respectively. Figure 8.40 and Figure 8.41 show the effect of process parameters and the interaction between these parameters on the mean of the porosity, respectively.

The results show that higher porosity can be achieved at 15% UHMWPE content. Similarly, low bed temperature results in a slight increase in porosity. Unlike bed temperature, the increase in laser power results in a slight increase in porosity.

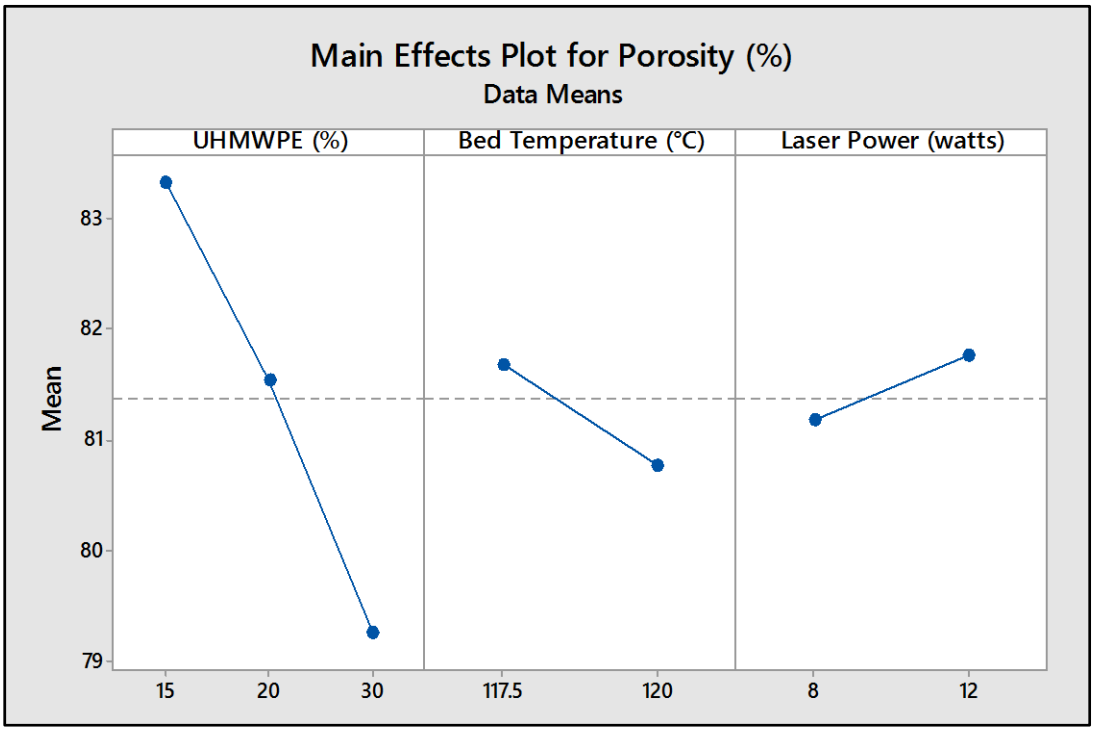

Figure 8.40: Effect of process parameters on porosity

The interaction plot in Figure 8.41 there is no clear interaction between the laser power and bed temperature on porosity. However, similar to density, the percentage of UHMWPE content has clear effect on porosity which decreases with the increasing of the UHMWPE content.

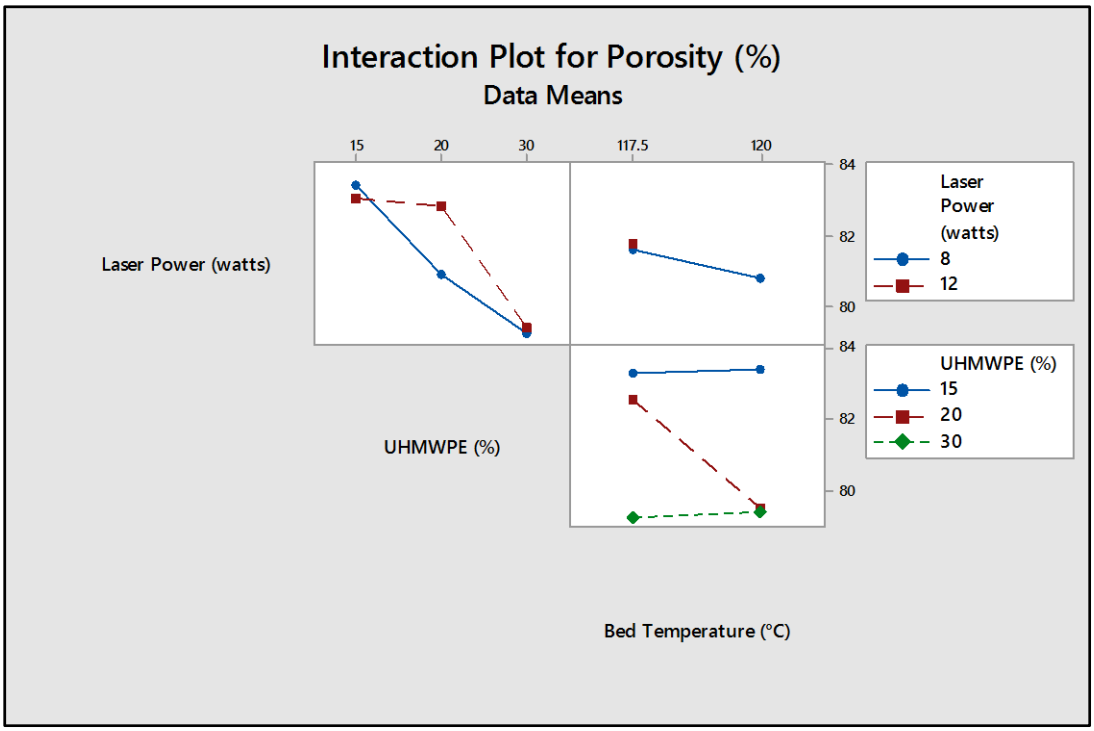

Figure 8.41: Interaction effect of process parameters on porosity

Figure 8.42 and Figure 8.43 show that the UHMWPE content is the dominant factor that effect the mechanical properties (i.e. Flexural stress).

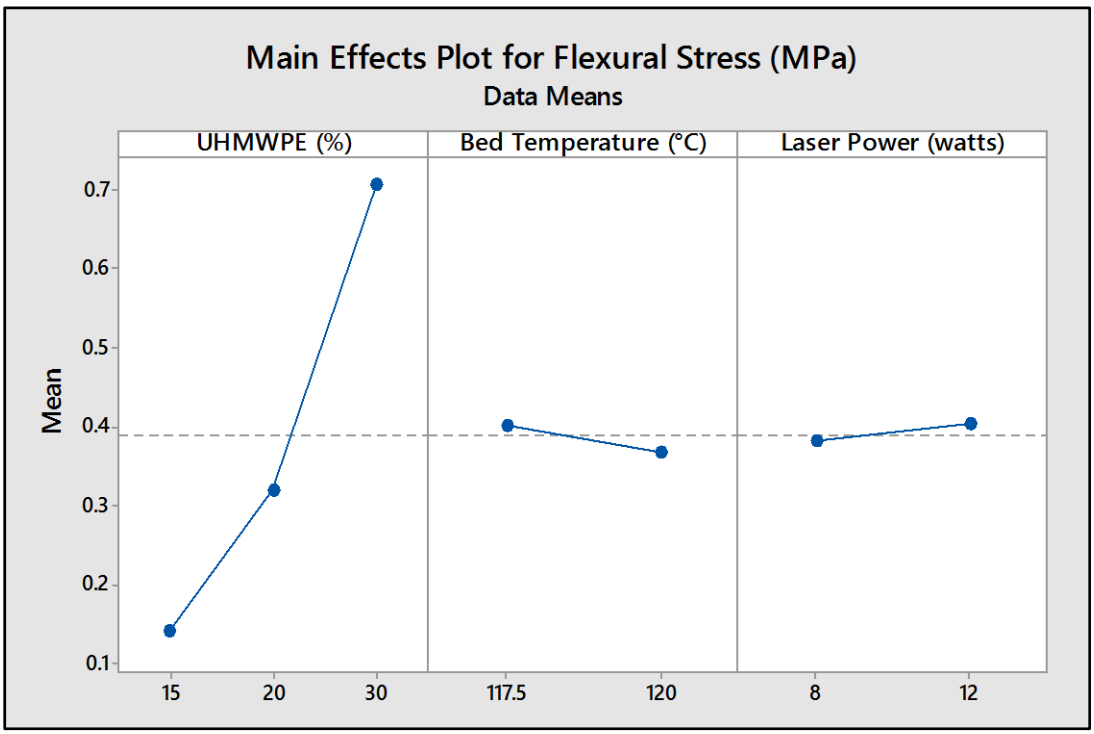

Figure 8.42: Effect of process parameters on flexural stress

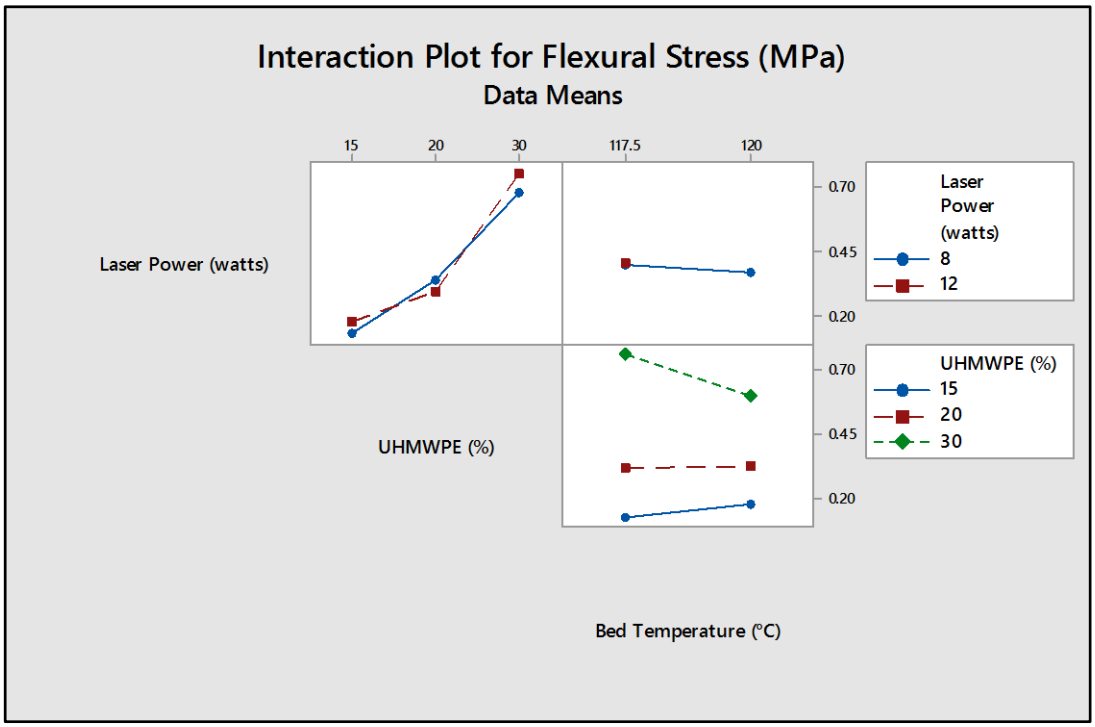

Figure 8.43: Interaction effect of process parameters on flexural stress

The ANOVA analysis indicates that the P-Value of the effect of % UHMWPE, bed temperature and laser power were 0.00, 0.364 and 0.839, respectively which confirms the previous findings in section 8.4.3.

8.6 Summary

Laser sintered AC-UHMWPE parts were successfully manufactured using laser powers of 8 and 12 watts and bed temperatures of 117.5°C and 120°C with composition ratios of 85:15, 80:20 and 70:30 AC-UHMWPE. However, samples PE15-117.5-8 exhibited weak physical and mechanical properties compared to other sets of samples manufactured. These samples were too fragile to be manually handled.

8.6.1 Relative Density

An average relative density of approximately 20.95 ±0.08%, 17.74 ±0.18% and 16.49 ±0.40% was achieved for laser sintered AC-UHMWPE parts with

compositions of 70:30, 80:20 and 85:15 AC-UHMWPE, respectively. These parts were produced at a fixed laser power of 8 watts and bed temperatures of 117.5°C and 120°C. Compared to the pure UHMWPE and AC powders, the relative densities were 24.33 ±0.23% and 16.27 ±0.09%, respectively. Based on the rule of mixtures, the relative densities of the PE30, PE20 and PE15 un-sintered composite powders were 17.55 ±0.06%, 17.07 ±0.07% and 16.85 ±0.07%, respectively.

Similar behaviour was observed with parts produced at a fixed bed temperature of 117.5°C and laser powers of 8 and 12 watts. The result suggests that the effects on relative density are not driven by the laser power and bed temperature within the range of parameters analysed. However, the UHMWPE content had the most obvious impact on relative density where an increase in the UHMWPE content from 15% to 30% showed a density increase by 4.46%.

8.6.2 Porosity Analysis

Two fluid techniques were used in addition to micro-CT, helium pycnometry and mercury intrusion porosimetry to evaluate the porosity in laser sintered AC-UHMWPE. Table 8.7 shows a porosity comparison between these three techniques.

Table 8.7: Total porosities of laser sintered AC-UHMWPE parts

Sample ID	Porosity (%)		
	Helium Gas	Mercury Porosimetry	Micro-CT
PE15-117.5-8	83.51 ±0.40	-	57.94 ±5.80
PE15-117.5-12	83.08 ±0.12	63.51 ±2.01	58.90 ±5.65
PE15-120-8	83.41 ±0.42	-	56.91 ±0.60
PE20-117.5-8	82.26 ±0.18	-	56.40 ±0.76
PE20-117.5-12	82.86 ±0.20	65.24 ±0.37	58.72 ±0.57

PE20-120-8	79.50 ±0.66	-	54.66 ±1.92
PE30-117.5-8	79.05 ±0.08	-	55.78 ±1.00
PE30-117.5-12	79.36 ±0.10	61.27 ±0.48	55.76 ±0.22
PE30-120-8	79.39 ±0.26	-	53.40 ±0.31

The results show that the porosity did not change significantly when bed temperature and laser power were changed. The average total porosity of the 85:15 AC-UHMWPE was 83.51% and 83.41% (measured by helium gas) for the samples produced at a fixed laser power of 8 watts and bed temperature of 117.5°C and 120°C, respectively. Similarly, the average total porosity of the 85:15 AC-UHMWPE was 83.08% and 83.51% (measured by helium gas) for the samples produced at a fixed bed temperature of 117.5°C and a laser power of 12 watts and 8 watts, respectively. However, a slight reduction in porosity (by 4% approximately) has been observed when the UHMWPE content increased from 15% to 30%. This result suggests that the porosity decreases with the increase in UHMWPE content and the effects on porosity are not driven by bed temperatures and laser powers within the range of parameters analysed.

Compared to micro-CT analysis, higher porosity values were obtained from helium pycnometry and mercury intrusion porosimetry techniques. Pores inside the composite material particles are difficult to be discerned on the micro-CT images. Nevertheless, the trends of the porosity values among all samples were obtained with reasonable agreement by all techniques. Generally, the porosity measured using helium pycnometry is high in comparison with the mercury intrusion and micro-CT techniques. Helium can penetrate effectively into structures and finest pores impenetrable to other fluids due to its very small molecular volume [155, 195].

Additionally, measuring the dimensions of the samples geometrically, when measuring the bulk density to calculate porosity by helium, may result in error

because of surface roughness as well as the difficulty in taking accurate linear dimensions [155].

8.6.3 Mechanical Properties

The flexural strength of the 70:30 and 80:20 AC-UHMWPE parts, produced at a fixed laser power of 8 watts, increases by 99% and 77%, respectively at bed temperature of 117.5°C and by 70% and 46% at bed temperature of 120°C as compared with 85:15 AC-UHMWPE laser sintered parts. The increase in strength is attributed to the increase in the amount of the binding material which induces higher bonding between UHMWPE particles in the matrix yielding to increasing the flexural strength.

The pattern of change in flexural stress appeared to be similar to that of the relative density. The effects on flexural stress are not driven by the laser power and bed temperature within the range of parameters analysed. However, the UHMWPE content had the most obvious impact on flexural stress and an increase in the UHMWPE content yielded to improvement of the mechanical properties of the laser sintered AC-UHMWPE parts.

8.6.4 Thermal Behaviour

The results of DSC analysis show that the peak temperatures for melting and crystallisation remain constant for all samples indicating that the intrinsic thermal properties of the laser sintered AC-UHMWPE parts are not affected by the composition ratio of the AC-UHMWPE composite, laser power or bed temperature. This indicates that there was no interaction occurred between the UHMWPE and AC materials after the application of the heat generated by the laser beam.

The results of TGA analysis show that the thermal decomposition behaviour of laser sintered AC-UHMWPE parts is similar to that of the un-sintered AC-UHMWPE powders with the same ratio of AC-UHMWPE composition. Applying different laser powers or bed temperatures appeared to have no effect on the

decomposition behaviour. This behaviour was observed for 85:15, 80:20 and 70:30 AC-UHMWPE parts. However, an average of initial decomposition temperatures of approximately 498°C, 495°C and 482°C were observed for 85:15, 80:20 and 70:30 AC-UHMWPE parts, respectively. It can be concluded that the initial decomposition temperatures increased significantly with the decrease in UHMWPE content indicating a higher thermal stability.

8.6.5 Degree of Crystallinity

The average crystallinity of the DSC first heating cycle of the laser sintered parts increased significantly compared to the average crystallinity of the DSC second heating cycle of the un-sintered AC-UHMWPE powders. The overall average crystallinity of the laser sintered AC-UHMWPE parts increased to approximately 42%, 47% and 45% compared to the average crystallinity of the un-sintered composite powder measured at approximately 30%, 29% and 37% for 85:15, 80:20 and 70:30 AC-UHMWPE, respectively.

The average of crystallinity of laser sintered AC-UHMWPE samples produced at different bed temperatures and a constant laser power was approximately 43%, 47% and 46% for AC-UHMWPE samples with 85:15, 80:20 and 70:30 AC-UHMWPE, respectively. While the average crystallinity of the AC-UHMWPE samples produced at different laser powers and a constant bed temperature was approximately 40%, 48% and 43% for AC-UHMWPE samples with 85:15, 80:20 and 70:30 AC-UHMWPE, respectively. The DSC results do not show statistically significant changes in crystallinity values with the change in laser powers and bed temperatures. Therefore, a clear pattern of change in crystallinity is difficult to establish.

The XRD result shows that increasing the content of activated carbon in the composites only led to decrease the intensity of the peaks without changing the crystal structure. This indicates that a decrease in crystallinity of the laser sintered parts occurred with increasing of activated carbon content. Activated carbon has a high thermal conductivity compared to UHMWPE polymer.

Therefore, the thermal conductivity of the composite was improved by the addition of activated carbon and consequently the cooling rate was increased. Thus a decreased in crystallinity is expected in the laser sintered AC-UHMWPE parts with increasing AC content.

It can be concluded that the addition of activated carbon in the composites affects the degree of crystallinity but has a little effect on the crystallite structure.

8.6.6 Design of Experiments

The design of experiments and ANOVA analysis confirmed that the UHMWPE content has a statistically significant effect on bulk density, porosity and flexural strength of the laser sintered AC-UHMWPE parts compared to the laser power and bed temperature.

Chapter 9 Manufacture of Activated Carbon Filters using Laser Sintering

9.1 Introduction

Portable water purification systems are used to provide safe drinking water. These systems can be used in remote villages and disaster zones and can purify water from potential pathogens like typhoid, cholera, dysentery and diarrhoea.

Unilever plc, a fast-moving consumer goods company, spent five years developing a solution for water purification and the result was in-home water purifier "Pureit". This system provides a drinking water without the need for gas, electricity or a pressurised water supply and relies on gravity for its operation. One of the main components in this system is Activated Carbon filter (ACF) [4].

The composite materials used in manufacturing "Pureit" AC filters are Activated carbon (AC), as a matrix, and Ultra High Molecular Weight Polyethylene (UHMWPE), as a binder. However, there are other conventional polymeric binders used in manufacturing of carbon filters such as Low Density Polyethylene (LDPE), Ethylene Vinyl Acetate copolymer (EVA) and High Density Polyethylene (HDPE) [201].

AC is one of the most commonly used materials for water filtration. AC is an effective and reliable material in removing impurities and has an enormous adsorptive capacity, an attraction for a wide variety of dissolved organics and chlorine and also an ability to be custom-tailored to suit specific applications. AC is used in a wide range of applications including water and gas purification, air filters in gas masks and respirators, medicine, air pollution control, energy storage, fuel cells, batteries and many other applications [130, 132, 133, 184, 185].

UHMWPE parts is widely used, in virgin or blended form, in the food and beverage, chemical processing, foundry, paper, mining, textile, lumber and

transportation industries [104]. This polymer is difficult to process by the conventional methods due to its high molecular weight. However, the processing of UHMWPE can be enhanced by adding high thermally conductive fillers in to the UHMWPE matrix, such as carbon black, graphite, carbon nanotubes or activated carbon [104, 110, 183].

The adsorbent AC and the binder UHMWPE powders are traditionally dry mixed together and compacted in a mould. The mixture is then heated above the melting point of the binder and kept at that temperature for a period of time. After completion, the mould is left to cool down and the unit filter is then removed from the mould [7, 201-203].

The current process of manufacturing AC filters have some drawbacks including low-production efficiency due to its long heating and cooling time, high energy consumption, limited mould life, and most importantly it does not allow the free-control of microstructures causing inefficient performance.

The current challenges are to provide varieties of complex geometry in shorter cycles of product development, combined with a desire to further reduce costs and improve quality. Therefore, it would be desirable to provide an advanced technology of manufacturing the activated carbon filters used in “Pureit” systems that decreases manufacturing time, save material and increases durability and performance. One possible way to achieve this goal is through the use of state-of-the-art technology such as Additive Manufacturing.

This work has been motivated to substantiate that there are many areas where Additive Manufacturing technology can be applied with shorter production time, reduced cost, improved product quality, and good control of the internal geometry in comparison with the conventional way of manufacturing the AC filters.

9.2 Characterisation of Pureit Activated Carbon Filter

The physical properties and material characteristics of the Pureit AC filter have been investigated. This characterisation can be useful to assess the results and compare it with the 3D printed AC filters.

9.2.1 Bulk Density and Porosity

The average densities and porosities of the Pureit AC filter are listed in Table 9.1 and a comparison of the porosity measured in different methods is shown in Figure 9.1.

Table 9.1: Densities and porosities of Pureit AC filter. (Three samples were tested)

Property		Unite	Value
Density	Bulk	g/cm³	0.4860 ±0.01
	Skeletal	g/cm³	1.6199 ±0.05
	Relative	%	25.20 ±0.33
Total Porosity	Helium gas pycnometry	%	74.80 ±0.33
	Mercury porosimetry	%	55.69 ±2.00
	Micro-CT	%	47.14 ±2.24

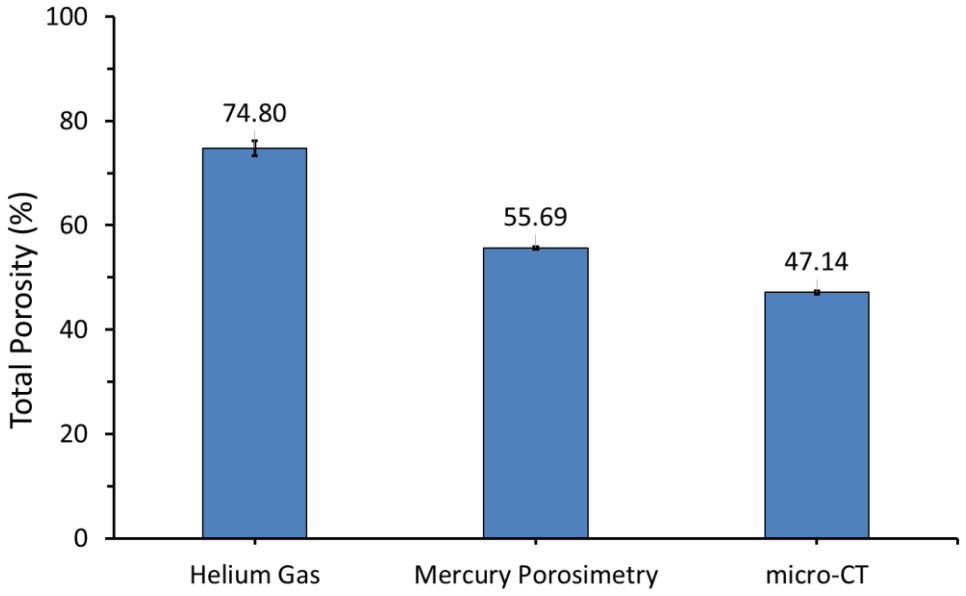

Figure 9.1 : Average porosity of Pureit AC filter measured by different methods

There are noticeable differences in porosity values measured by Helium gas pycnometry, Mercury porosimetry and micro-CT scanning methods. The Helium pycnometry gives significantly higher values than mercury and micro-CT. The reasons for this discrepancy were discussed in chapter 8.

Figure 9.2 shows the log differential intrusion curve of pore size distribution of the Pureit AC filter measured using mercury intrusion porosimetry.

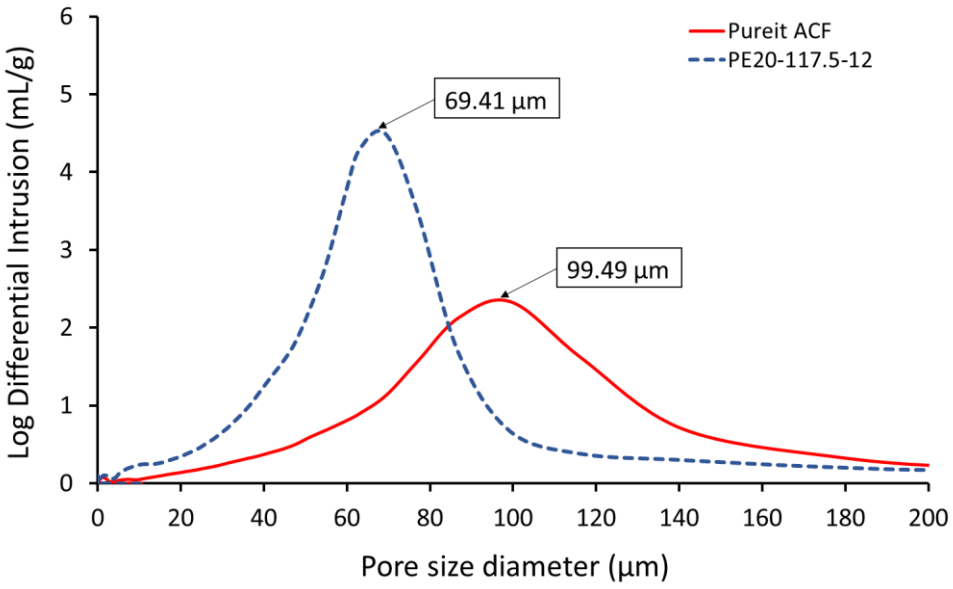

Figure 9.2 : Pore size distribution of Pureit AC filter and laser sintered 80:20 AC-UHMWPE parts measured using mercury intrusion

The results show that the pore size distribution of the Pureit AC filter is wide with a peak of pore size of approximately 99 µm. Whereas the 80:20 AC-UHMWPE laser sintered parts show a narrow pore size distribution and shifted to lower values with a peak of pore size of approximately 69 µm. The wide pore size distribution can be attributed by many factors, including the random stacking and irregular shape of the pores, as well as the manufacturing process.

9.2.2 Differential Scanning Calorimetry

The thermal properties of the Pureit AC filter were measured at a heating rate of 10°C/min by differential scanning calorimetry, using Perkin Elmer DSC 8500,

from 25 to 220°C under a nitrogen atmosphere. The samples were held for 1 minute at 220°C before the cooling cycle started. DSC curves of Pureit AC filter were obtained under two thermal cycles and three samples were analysed.

The melt and crystallisation peaks of the Pureit AC filter are summarised in Table 9.2 and the DSC curves are presented in Figure 9.3.

Table 9.2: Thermal properties of Pureit AC filter

Sample ID	1st Thermal cycle		2nd Thermal cycle	
	Melting point peak (°C)	Crystallisation point peak (°C)	Melting point peak (°C)	Crystallisation point peak (°C)
ACF-01	136.80	120.91	135.75	120.78
ACF-02	137.45	120.98	135.63	120.91
ACF-03	136.65	120.88	135.55	120.85

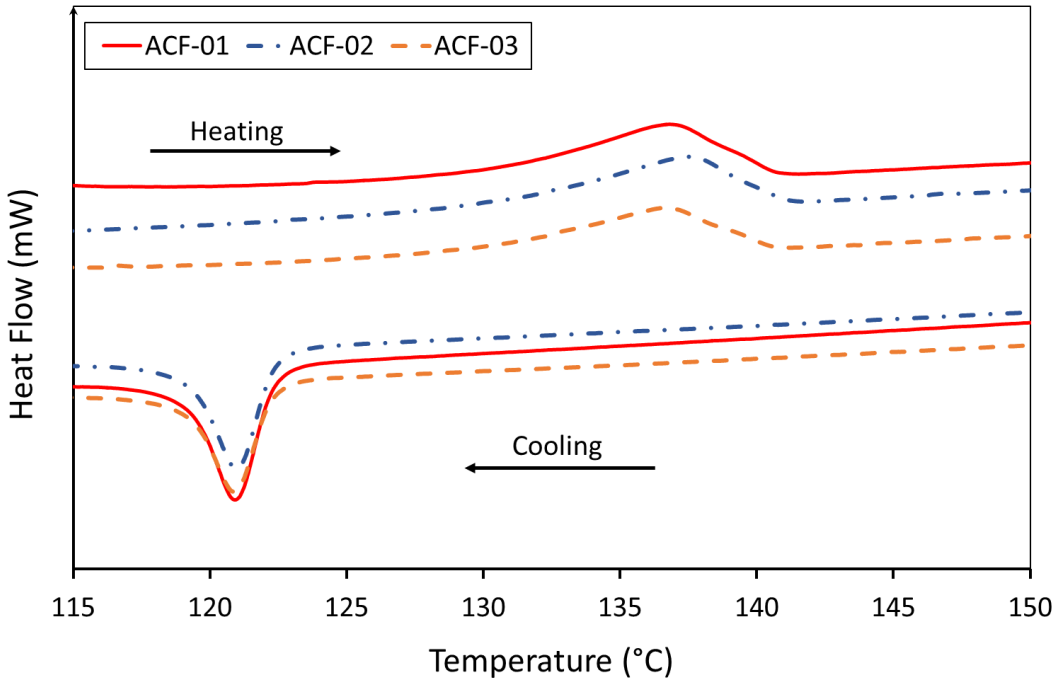

Figure 9.3 : DSC curves of Pureit ACF (Heating cycle of 1st Run)
Graphs were shifted vertically for clarity purposes

The average of the melt temperatures in the first heating cycle (i.e. 136.97°C) of the Pureit AC filter is slightly higher than the average of the melt

temperatures in the second heating cycle (i.e. 135.64°C) by approximately 1°C. While the average of the crystallisation temperatures in the first heating cycle (i.e. 120.92°C) remains almost constant compared to the average of the crystallisation temperature in the second heating cycle (i.e. 120.85°C).

The thermal behaviour of Pureit AC filter appeared to be similar to that of the laser sintered AC-UHMWPE parts. The average of the melt and crystallisation temperatures in the first heating cycle of the laser sintered parts were 136.44°C and 120.89°C, respectively.

9.2.3 Thermogravimetric Analysis

A total of six samples were cut out from Pureit AC filter as shown in Figure 9.4. Three samples were taken from the top part, closer to the outer shell of the filter, and the other three samples were taken from the bottom part, around the centre area. Approximately, ten milligrams of the material was placed in a ceramic crucible and was heated from 25°C to 600°C under nitrogen atmosphere at a heating rate of 10°C/min.

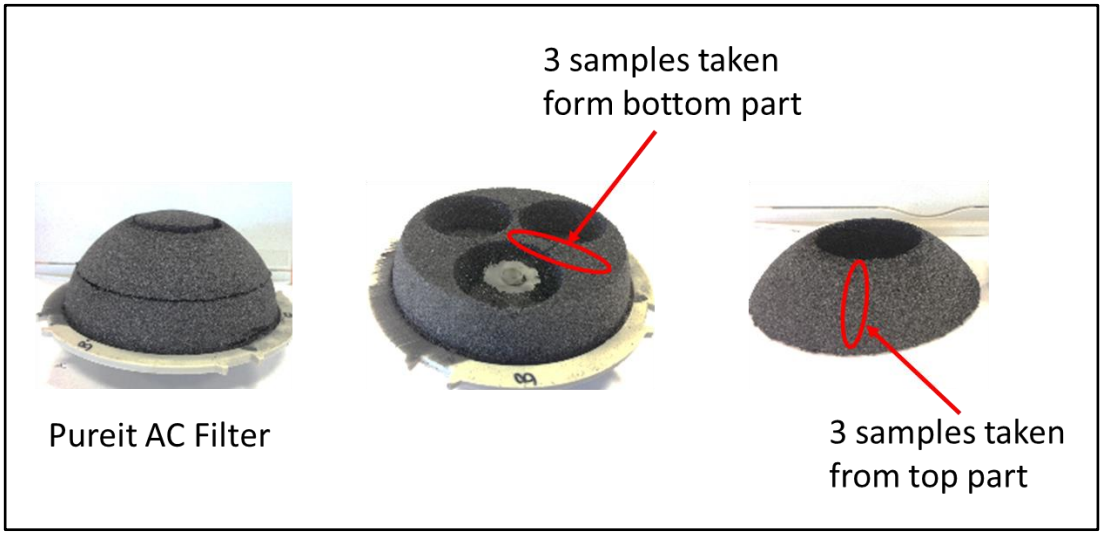

Figure 9.4 : TGA samples preparation

The TGA thermal stability curves of the Pureit AC filter are shown in Figure 9.5 and the initial and final decomposition temperatures are listed and shown in Table 9.3 and Figure 9.6, respectively.

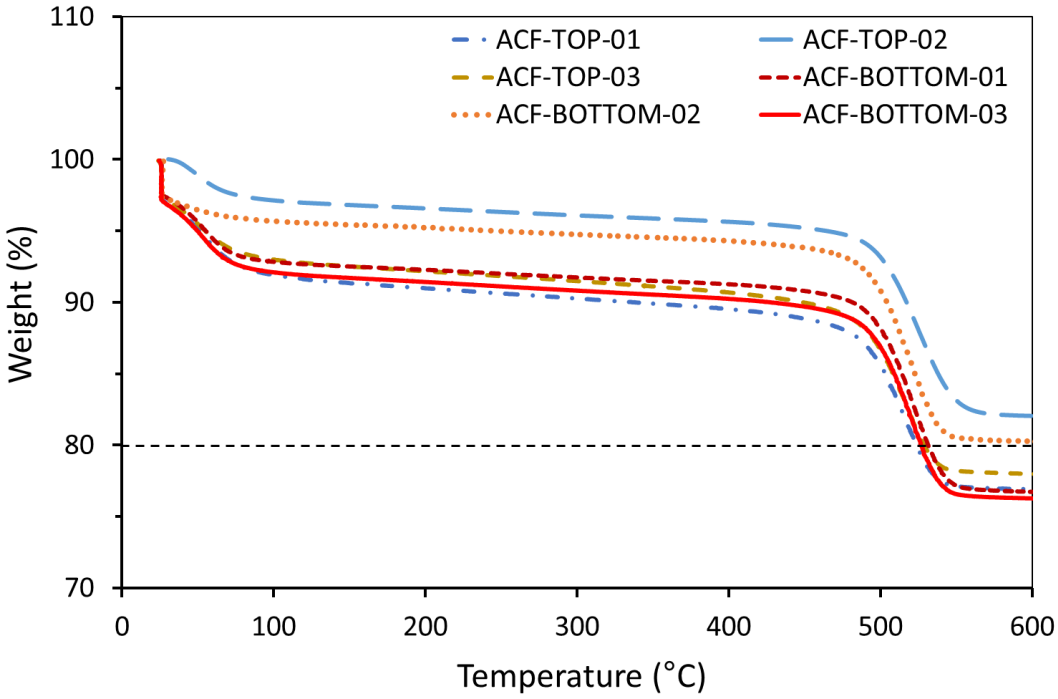

Figure 9.5 : TGA curves of Pureit AC filter

Table 9.3: TGA thermal data of Pureit AC filter

Sample ID	Onset Temperature (°C)	
	T_1*	T_2*
ACF-TOP-01	488.98	535.50
ACF-TOP-02	495.77	548.09
ACF-TOP-03	488.31	535.20
ACF-BOTTOM-01	493.65	541.50
ACF-BOTTOM-02	491.47	538.84
ACF-BOTTOM-03	492.91	540.58

** T_1 and T_2 are the initial and final onset decomposing temperatures respectively.*

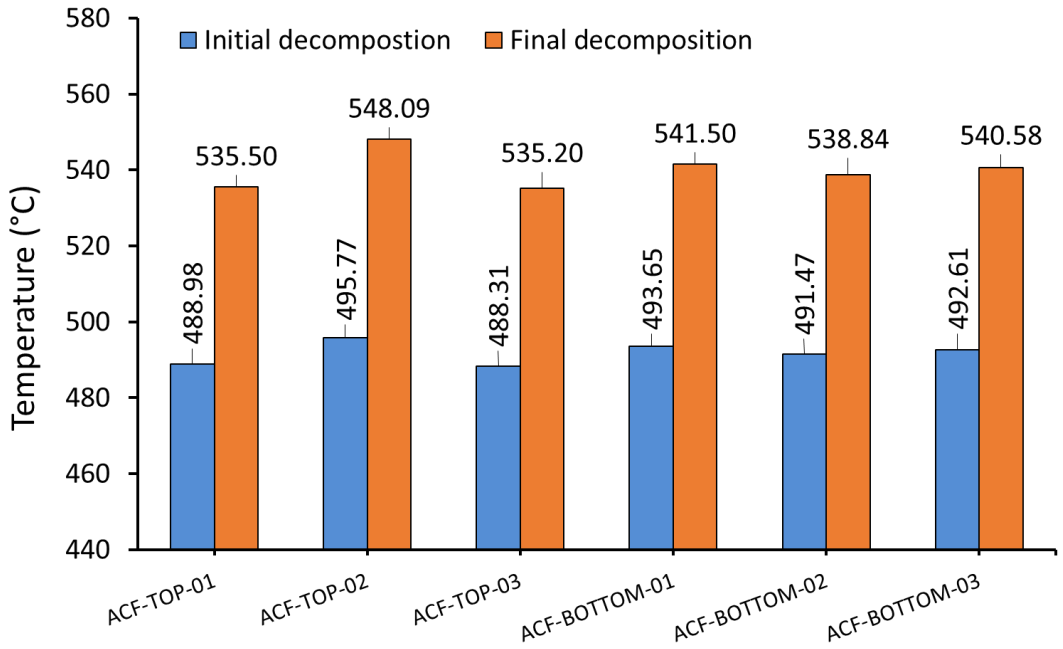

Figure 9.6 : Thermal stability of Pureit AC filter

The results show an average of initial decomposition temperatures of approximately 491.02 ±4.13°C and 492.58 ±1.09°C were observed for the samples cut out from the top and bottom of the Pureit AC filter, respectively. While an average of final decomposition temperatures of approximately 539.60 ±7.36°C and 540.31 ±1.35°C were observed for the samples cut out from the top and bottom of the Pureit AC filter, respectively. This result indicates that no significant differences in the initial and final decomposition temperatures can be observed between the samples cut out from the top and bottom of the Pureit AC filter.

Figure 9.7 shows the actual weight fractions of UHMWPE in Pureit AC filter. An average weight of 12.94 ±0.95% and 21.82 ±2.37% were observed using onset and delta mass methods, respectively. The result shows that here is a disagreement between the intended and the actual UHMWPE weight fractions in the Pureit AC filter. These differences are attributed by the small size of the samples used in this analysis and measurement errors.

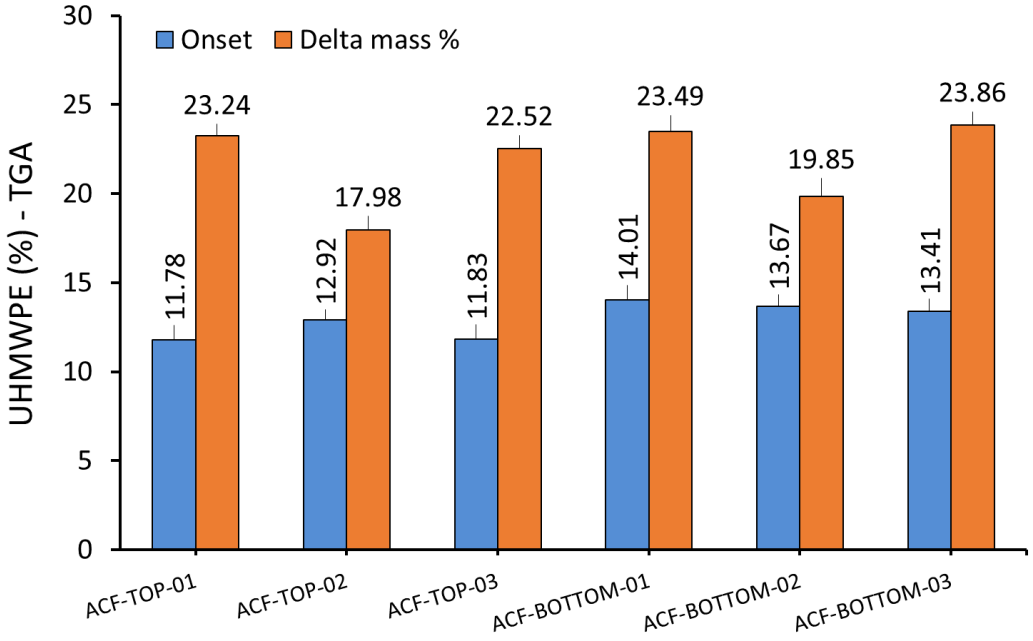

Figure 9.7 : Actual weight fractions of UHMWPE in Pureit AC filter measured by TGA

9.2.4 XRD Analysis

A Bruker D8 Advance X-ray diffraction system, equipped with a Cu Kα radiation source with a wavelength (λ) of 1.5418 nm generated at 40 kV and 40 mA, was used for XRD analysis. Samples were mounted on the stage and scanned from 10° to 70° using a step size of 0.05° and 10 seconds per step.

The XRD patterns of the Pureit AC filter and the laser sintered parts with 80:20 AC-UHMWPE produced at different laser powers and bed temperatures are shown in Figure 9.8.

The results show that the diffraction peaks of Pureit AC filter are similar to that of the laser sintered parts with 80:20 AC-UHMWPE. However, the intensity of the (110) and (200) peaks of the laser sintered parts are larger compared to the Pureit AC filter. The highest increase in the peak size was for (110) plane, indicating a significant growth of the crystallites along the (110) plane direction [200].

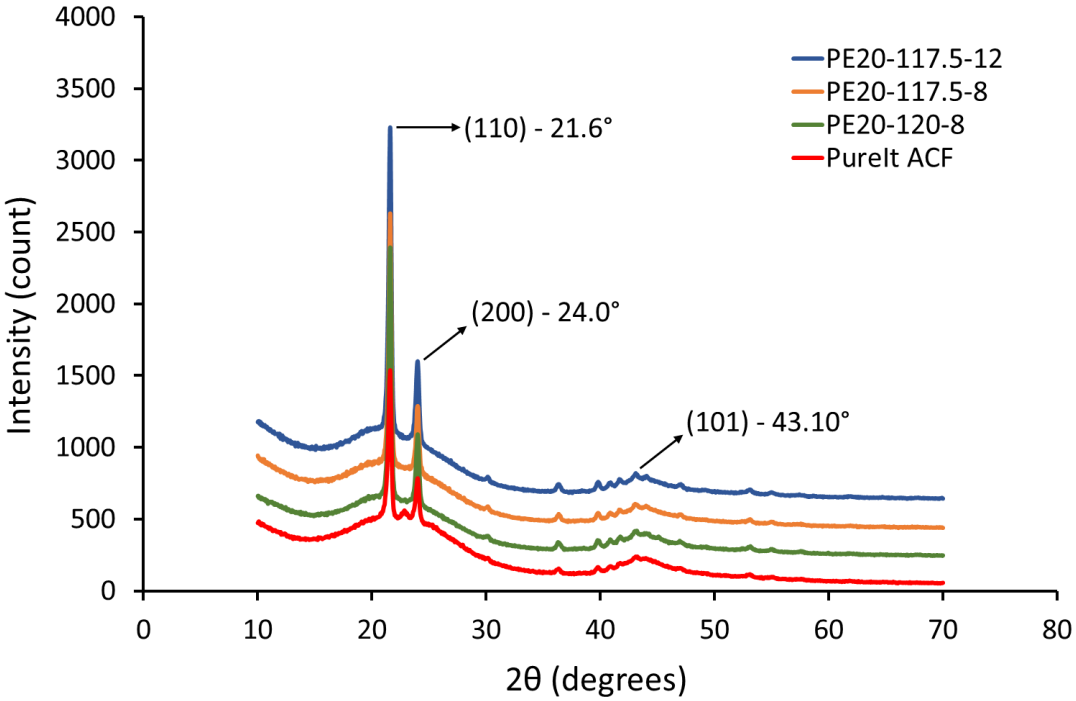

Figure 9.8 : XRD profile of Pureit AC filter compared to laser sintered 80:20 AC-UHMWPE parts produced at different laser powers and bed temperature

9.2.5 Degree of Crystallinity

The average crystallinity of the Pureit AC filter samples was calculated at 22.13 ±2.06% and 37.45 ±0.92% as measured by DSC (first heating cycle) and XRD methods, respectively. The crystallinity measured by XRD method shows higher values compared to DSC. Figure 9.9 shows that the crystallinity of Pureit AC filter is significantly lower than the average crystallinity of the laser sintered parts with 80:20 AC-UHMWPE. The long exposure to heat when manufacturing the Pureit AC filters by the conventional process (heated at 250°C for 2.5 hours) has a negative influence on crystallinity and could result in the degradation of the UHMWPE binder.

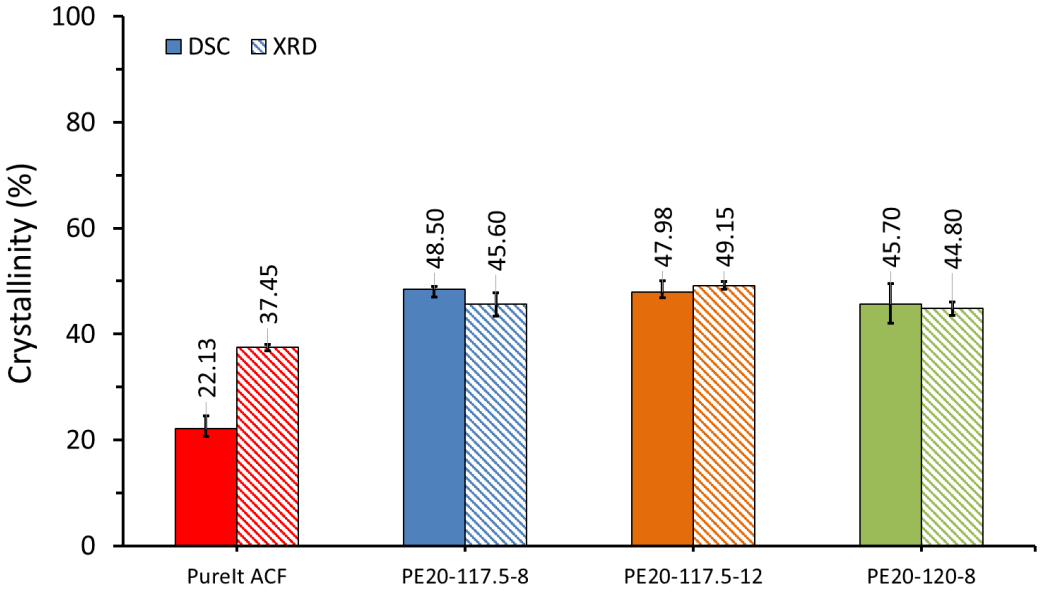

Figure 9.9 : Crystallinity of Pureit AC filter compared to laser sintered 80:20 AC-UHMWPE parts produced at different laser powers and bed temperature measured by DSC (first heating cycle) and XRD methods

9.2.6 Morphology of Pureit AC Filter

X-ray micro-CT images of the Pureit AC filter are shown in Figure 9.10 and Figure 9.11.

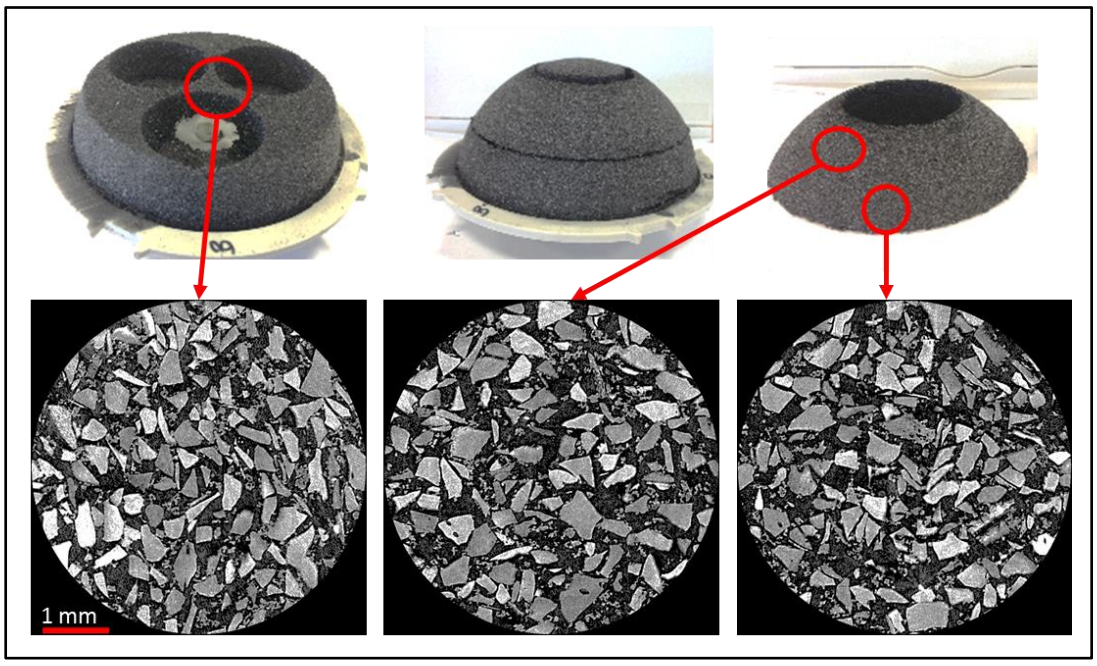

Figure 9.10 : micro-CT images of Pureit ACF

The micro-CT images in Figure 9.11 (a) revealed that large particles of the Intermediate Activated Carbon (IAC) are dominating the structure of the Pureit AC filter. The specification of the IAC powder is listed in Table 9.5. The activated carbon particles are not closely packed and can easily be distinguished. Unlike the Pureit AC filter, the sintered parts, shown in Figure 9.11 (b), are formed from fairly uniformly packed layers and the composite particles are closely packed.

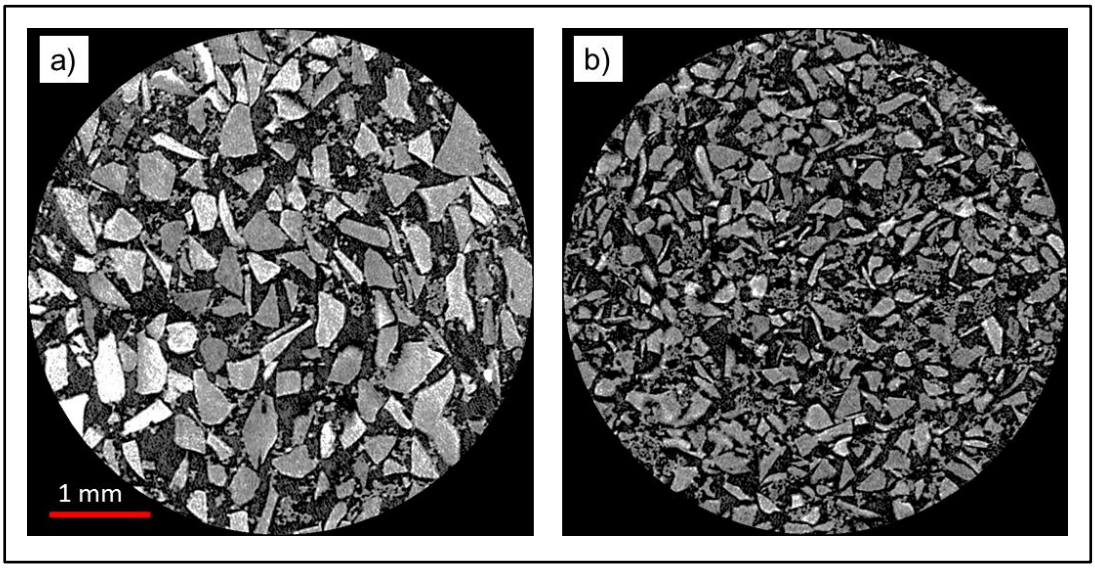

Figure 9.11 : micro-CT images of a) Pureit ACF and b) laser sintered 80:20 AC-UHMWPE part produced at a laser power of 8 watts and bed temperature of 117.5°C

Figure 9.12 shows that the particles of the UHMWPE binder are joined together and holding the structure with different pores can be observed.

These images reveal that the high temperature used in manufacturing the Pureit AC filters, caused a complete melting of the UHMWPE particles resulting in more flow over the activated carbon particles and may block some of the pores.

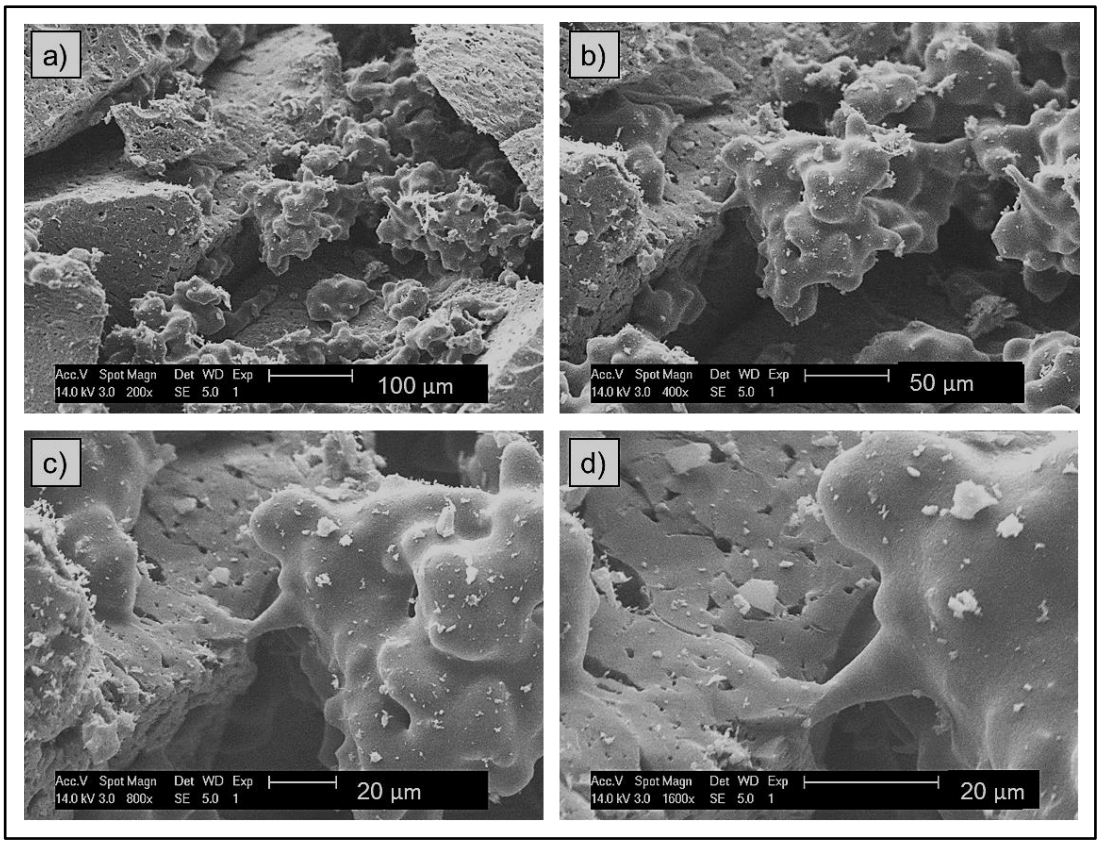

Figure 9.12: SEM micrographs of Pureit AC filter
Magnifications: a) 200x, b) 400x, c) 800x and d) 1600x

9.3 Materials and AC-UHMWPE Composite Preparation

The UHMWPE powder used in the manufacturing of the laser-sintered AC-UHMWPE parts was GUR 2122 (Celanese, Germany). More details about this material were described earlier in section 4.2, Chapter 4.

The Powdered Activated Carbon (PAC) used in this study was a coconut shell based activated carbon produced by high temperature steam activation (Eurocarb Products Limited, Bristol, UK), with a particle size ranges between 75-250 µm. The product specification is listed in Table 9.4.

The UHMWPE and AC powders were sieved separately to remove any large agglomerated particles. UHMWPE powder was then dry mixed with AC using a tumbler mixer (Mixing station P1, EOS GmbH, Germany) for 60 minutes approximately to accomplish uniform mixing. The mixing ratios used were

70:30, 80:20 and 85:15 AC-UHMWPE (weight/weight). The blended composite was left in the oven overnight at 50°C for drying before processing by laser sintering.

Table 9.4: Product specification of PAC powder (Eurocarb YAO60x200AW datasheet)

Properties	Technical Details	
	Unit	Value
Particle Size (ASTM D2862)	µm	5% max: +250 90% min: 75-250 5% max: -75
Carbon Tetrachloride Adsorption (ASTM D3467)	%	60 min.
Apparent Density, Dry (ASTM D2854)	g/cm^3	0.440 – 0.490
Iodine Number (AWWA B604)	-	1150 min. 1200+ typical
Surface Area (BET method N_2)	m^2/g	1250 typical
Ash (ASTM D2866)	%	1 max.
pH	-	6-8
Moisture Content (ASTM D2867)	%	5 max.

Pureit filters made by conventional process are usually manufactured from 80:20 AC-UHMWPE composite powder. The 80% AC is a mixture of 50:50 (w/w) PAC and Intermediate Activated Carbon (IAC). The IAC used in the manufacturing of Pureit filters is a coconut shell based activated carbon produced by high temperature steam activation, with a particle size ranges between 250-500 µm. The product specification is listed in Table 9.5.

Table 9.5: Product specification of IAC powder as supplied by Unilever

Properties	Technical Details	
	Unit	Value
Particle Size (ASTM D2862)	µm	5% max: +500 90% min: 250-500 5% max: -250
Carbon Tetrachloride Adsorption (ASTM D3467)	%	60 min.
Apparent Density, Dry (ASTM D2854)	g/cm^3	0.45 – 0.52
Iodine Number (AWWA B604)	-	1150 min.
Surface Area (BET method N_2)	m^2/g	1250
Ash (ASTM D2866)	%	3 max.
pH	-	6-7
Moisture Content (ASTM D2867)	%	5 max.

9.4 Manufacture of Experimental 3D printed AC Filters

AC filters are manufactured in different shapes based on the application and the design of the water purification systems. These filters can be shaped as a right circular cylinder with a hollow bore through (tube-shaped). In this case, the flow of water is directed in a radial direction through the wall of the tube (either outwardly or inwardly). Dome-shaped filters are also used to provide higher surface area for water flow. In these filters, the water flows through the top and sides of the dome into the inner space of the dome. Other shapes were used as AC filters may include a flat circular disc, square disc, low height tapered flat disc, solid cylinder and solid cone or a hollow cone [7, 201, 203].

In this study, it was decided to manufacture flat disc-shaped filters with a diameter of 40mm and a thickness of 4mm for a water flow test at the laboratory of the University of Sheffield. Hollow cylinder shaped filters with a height of 50mm and outer and inner diameters of 40mm and 10mm respectively, were fabricated using laser sintering and then physical properties and performance were evaluated at the Unilever R&D facilities in Bangalore, India. Both types of 3D printed filters were manufactured using PAC powder only as it is not feasible to use IAC powder due to the large particle size.

9.4.1 Disc-shaped filters

Laser sintered filters were built using a commercial laser sintering system (EOS P100, Germany). The test parts were oriented in the x-y direction with the thickness parallel to z-axis (i.e. build direction).

In order to examine the effect of laser power, bed temperature and composite composition on the material characteristics and water flow of the laser sintered AC-UHMWPE filters, laser powers of 8 and 12 watts and bed temperatures of 117.5°C and 120°C were selected for processing AC-UHMWPE with ratios of 85:15, 80:20 and 70:30. All other parameters were kept constant as listed in Table 9.6. After sintering, all the parts were left in the machine for two to three hours and then were removed and left for cooling in the laboratory for 24 hours. The parts then were cleaned gently by a brush to remove the un-sintered powder.

Table 9.6: Laser sintering parameters used for manufacturing of disc-shaped filters

Parameter	Unit	Values
UHMWPE content	%	15, 20, 30
Laser Power	watts	8, 12
Laser Energy Density	J/mm^2	0.021, 0.032

Bed Temperature	°C	117.5, 120
Removal Chamber Temperature	°C	117, 120
Laser Scan Speed	mm/s	2500
Hatch Spacing	mm	0.15
Laser Count	-	2 (double scan)
Layer Thickness	mm	0.1

All samples were labelled as listed in Table 9.7. The sample's label consists of four parts in format of "*WF-PEnn-nnn.n-nn*":

1. *WF: Disc-shaped filter*
2. *PEnn: content of UHMWPE (%)*
3. *nnn.n: bed temperature (°C)*
4. *nn: laser power (watts)*

Table 9.7: Sample labels of laser sintered AC-UHMWPE disc-shaped filters

Sample ID	UHMWPE (%)	Bed Temperature (°C)	Laser Power (watts)
WF-PE15-117.5-8	15	117.5	8
WF-PE15-117.5-12	15	117.5	12
WF-PE15-120-8	15	120	8
WF-PE20-117.5-8	20	117.5	8
WF-PE20-117.5-12	20	117.5	12
WF-PE20-120-8	20	120	8
WF-PE30-117.5-8	30	117.5	8
WF-PE30-117.5-12	30	117.5	12
WF-PE30-120-8	30	120	8

9.4.2 Cylinder-shaped filters

Cylinder-shaped filters were built using a commercial laser sintering system (EOS P100, Germany). After sintering, all the filters were left in the machine overnight to cool and then were removed and cleaned gently by a brush to remove the un-sintered powder.

The 3D printed filters were oriented in the x-y direction in the part bed with the height parallel to z-axis, which were labelled as “Vertical”. For the filters oriented with the width parallel to z-axis were labelled as “Horizontal”. Orientating the filter in the minimum z-height results with a minimum build time. If the part can be oriented in the part bed so that the longest side is in the x-y direction then the time and cost needed to produce the part are greatly reduced. Additionally, orientation is one of the most important factors in determining the quality and the properties of the final part [173]. In the x-y direction the powder particles fuses homogeneously, while in the z-direction there is a possibility of insufficient bonding between the layers and the degree of necking between particles is reduced. This is due to the fact that the powder particles in the previous layer are cooled slightly while waiting for the second layer to be consolidated [81]. This can lead to relatively a higher porosity value with bigger average pore sizes [204] and also a density reduction in that direction [34, 77, 103].

The effects of laser power, bed temperature and composite composition on the material characteristics and water flow of the laser sintered AC-UHMWPE filters were considered for this study. The filters were manufactured using the process parameters listed in Table 9.8. The laser scan speed, hatch spacing, and layer thickness were kept constant at 2500 mm/s, 0.15 mm, and 0.1 mm, respectively, with a double scan count.

The sample’s label consists of six parts in format of “*ACF-PEnn-nnn.n-nn-x-y*”:

1. *ACF: cylinder-shaped filter*
2. *PEnn: content of UHMWPE (%)*

3. *nnn.n: bed temperature (°C)*
4. *nn: laser power (watts)*
5. *x: orientation of the filter in the part bed. H: horizontal, V: vertical*
6. *y: powder condition. U: 100% used powder. If not shown in the label then powder is 100% virgin powder*

Table 9.8: Sample labels of laser sintered AC-UHMWPE cylinder-shaped filters

No.	Sample ID	UHMWPE (%)	Bed Temperature (°C)	Laser Power (watts)
1	ACF-PE30-117.5-8-V	30	117.5	8
2	ACF-PE20-120-8-V	20	120	8
3	ACF-PE20-120-12-H	20	120	12
4	ACF-PE20-120-12-V	20	120	12
5	ACF-PE20-125-8-H	20	125	8
6	ACF-PE20-125-12-H	20	125	12
7	ACF-PE20-120-8-12-V	20	120	8-12*
8	ACF-PE20-120-12-8-V	20	120	12-8**
9	ACF-PE20-120-12-8-H	20	120	12-8**
10	ACF-PE20-120-8-12-H-U	20	120	8-12*
11	ACF-PE20-120-8-12-V-U	20	120	8-12*
12	ACF-PE20-120-12-8-H-U	20	120	12-8**
13	ACF-PE20-120-12-H	20	120	12
14	ACF-PE17.5-120-8-H	17.5	120	8
15	ACF-PE17.5-120-12-H	17.5	120	12
16	ACF-PE17.5-120-16-H	17.5	120	16

** 5mm thick Inner shell was sintered at laser power of 8 watts and 10mm thick outer shell was sintered at 12 watts.*
*** 5mm thick Inner shell was sintered at laser power of 12 watts and 10mm thick outer shell was sintered at 8 watts.*

Functional graded structures have been used before in laser sintering to produce components with varying mechanical properties from the same material [81]. A drug delivery device matrix has been successfully produced by laser sintering with varying porosity and density to optimise drug loading and diffusion rate. A circular disc with varying porosity was manufactured with an outer shell being denser (using a laser power of 4 watts) and acting as diffusion barrier region while an inner shell more porous centre (using a laser power of 3 watts) acts as a drug encapsulation region [205].

In this work, a number of trials have been made to control the structural gradients of the 3D printed filters. It is widely known in Laser Sintering that higher laser power, up to a certain limit, would produce a dense structure due to a high sintering degree. By using a variation of laser power, a partial melting of the powder and hence geometrically undefined porosity can be achieved. The schematic diagram in Figure 9.13 shows the basic idea of creating the gradients by controlling the laser power.

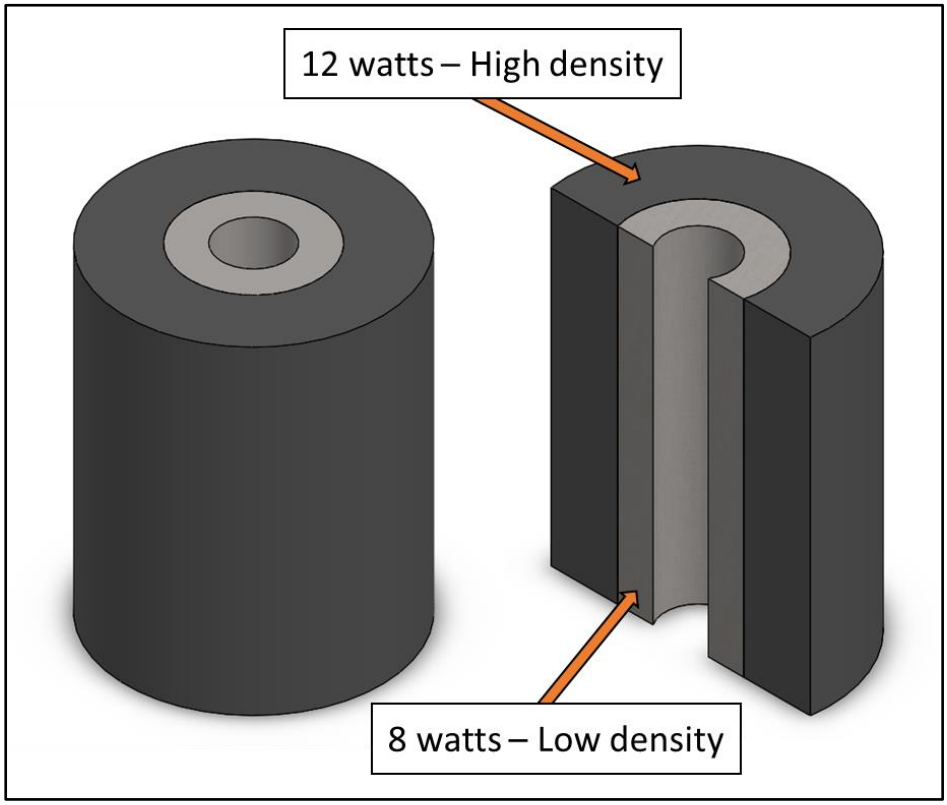

Figure 9.13 : Structural gradients controlled by laser powder

The objectives of this study is highlighted in Table 9.9. Physical properties will be determined by bulk density and porosity, while performance will be determined by the flow rate and turbidity removal. For the purposes of comparison, filters with 80:20 PAC-UHMWPE and 80:20 IAC-UHMWPE were also manufactured by Unilever, Bangalore using the conventional process.

Table 9.9: Objectives of the designed experiments for cylinder-shaped filters

Objectives	UHMWPE (%)	Samples number*
Preliminary trials. Compare physical properties and performance of 3D printed filter with filters made by conventional process	30	1
Evaluate the effect of laser power on physical properties and performance of 3D printed filters	20	2, 4
Evaluate the effect of different bed temperatures and orientation of filters in part bed on physical properties and performance	20	3, 4, 5, 6
Evaluate the effect of laser gradient and orientation of filters in part bed on physical properties and performance	20	7, 8, 9
Investigate the feasibility of manufacturing 3D printed filters from 100% used powder	20	10, 11, 12
Repeatability	20	3, 4, 13
Investigate the feasibility of manufacturing 3D printed filters with reduced binder content	17.5	14, 15, 16
Compare the flow characteristics for the disc-shaped and cylinder-shaped filters	20	Variable

** Sample number is referenced from Table 9.8*

Images of successfully manufactured 3D printed AC-UHMWPE filters using laser sintering are shown in Figure 9.14 and Figure 9.15.

Figure 9.14 : 3D printed disc-shaped filters using laser sintering

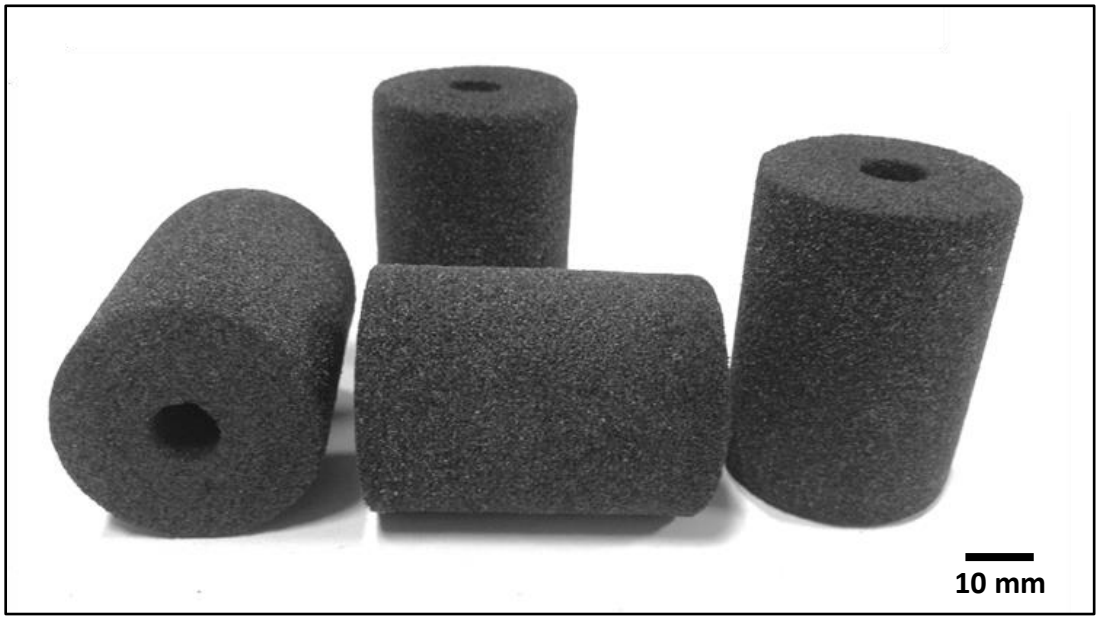

Figure 9.15 : 3D printed cylinder-shaped filters using laser sintering

9.5 Water Flow Rate - Experimental Procedure of 3D printed Disc-Shaped Filters

The experimental setup of the flow measurement conducted at the University of Sheffield laboratory is shown in Figure 9.16. The rig consists of five major components and these are; a 3D printed disc-shaped filter, reservoir of water, a beaker for collection of discharged filtrate from the filter, electronic balance and communication software. The accumulated mass of water discharged is transmitted automatically from the balance at predetermined time intervals and was recorded every two seconds until the last drop of water is discharged through the filter. Then the data is imported to an Excel spreadsheet and a diagram of the water discharge and time was plotted and the flow rate is calculated. The flow rate experiments were conducted consecutively six times, one after the other, on each of the four filters manufactured at different laser powder, bed temperature and composition ration of the composite. The average of the cumulative discharge of these four filters was then taken. Flow experiments were performed at constant room temperature and pressure and a potable tap water was used in these experiments.

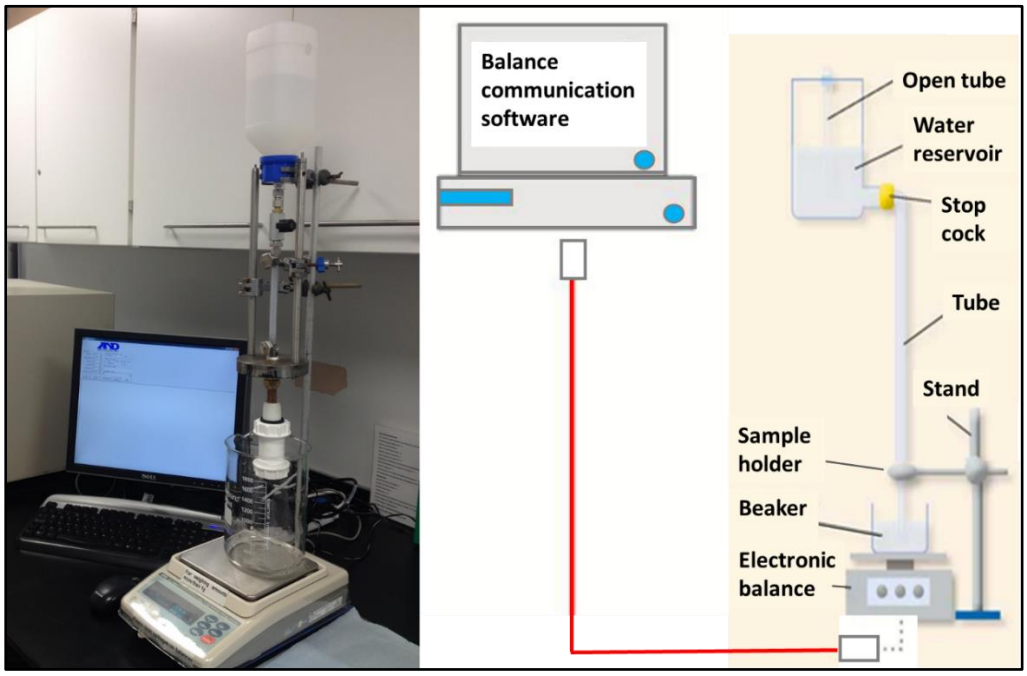

Figure 9.16 : Flow rate laboratory experiment set-up
Left) actual set-up, Right) schematic diagram

9.6 Results and Discussion of 3D Printed Filters

The effects of manufacturing process parameters on water flow rate of the disc-shaped filters were examined. The flow data were normalised to account for the thickness variation of the 3D printed discs and also to be comparable with the 3D printed cylinder-shaped filters. Therefore, a nominal wall thickness of 15 mm was used which represents the wall thickness of the cylinder-shaped filters.

9.6.1 Effects of Laser Power and Bed Temperature on Flow Rate of the Disc-shaped Filters

Figure 9.17 and Figure 9.18 show that the average flow rate of the disc-shaped filters decreases with increasing of the fraction weight of UHMWPE (wt%). The samples manufactured with 85:15 AC-UHMWPE show a higher flow rate compared to the samples manufactured with 80:20 and 70:30 AC-UHMWPE. However, the samples manufactured at laser power of 12 watts and bed temperature of 117.5°C show a higher flow rate compared to the samples manufactured at 8 watts and the same bed temperature (Figure 9.17). Similarly, the samples manufactured at a bed temperature of 120°C show a higher flow rate compared to the samples manufactured at bed temperature of 117.5°C and laser power of 8 watts (Figure 9.18).

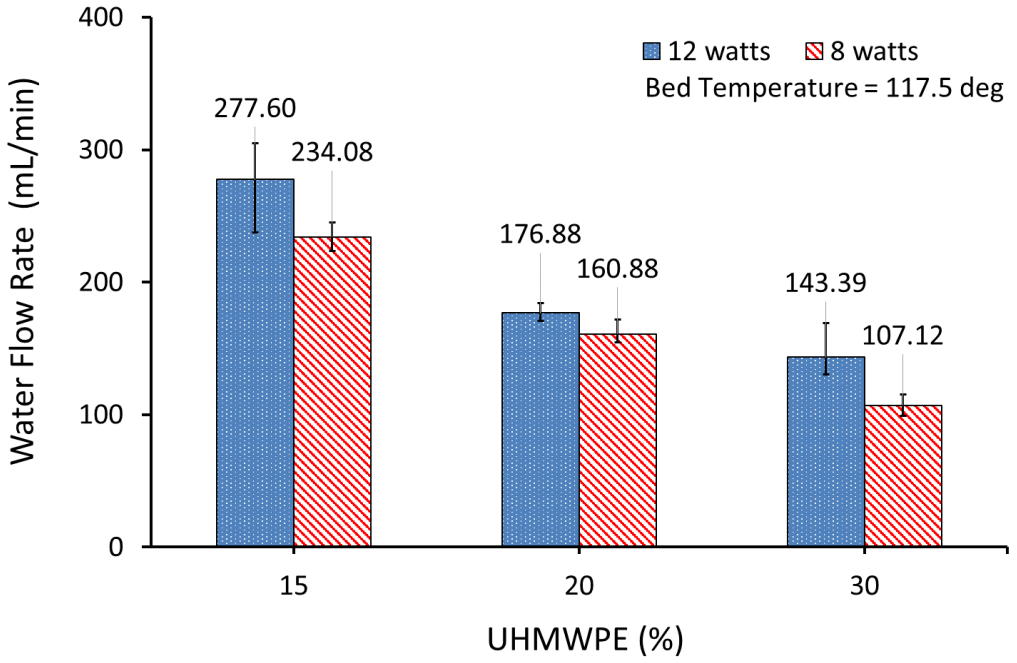

Figure 9.17 : Water flow rate of disc-shaped filters produced at laser power of 8 and 12 watts and bed temperature of 117.5°C with different UHMWPE content. (Four samples for each condition and the error bar represents the range of the data)

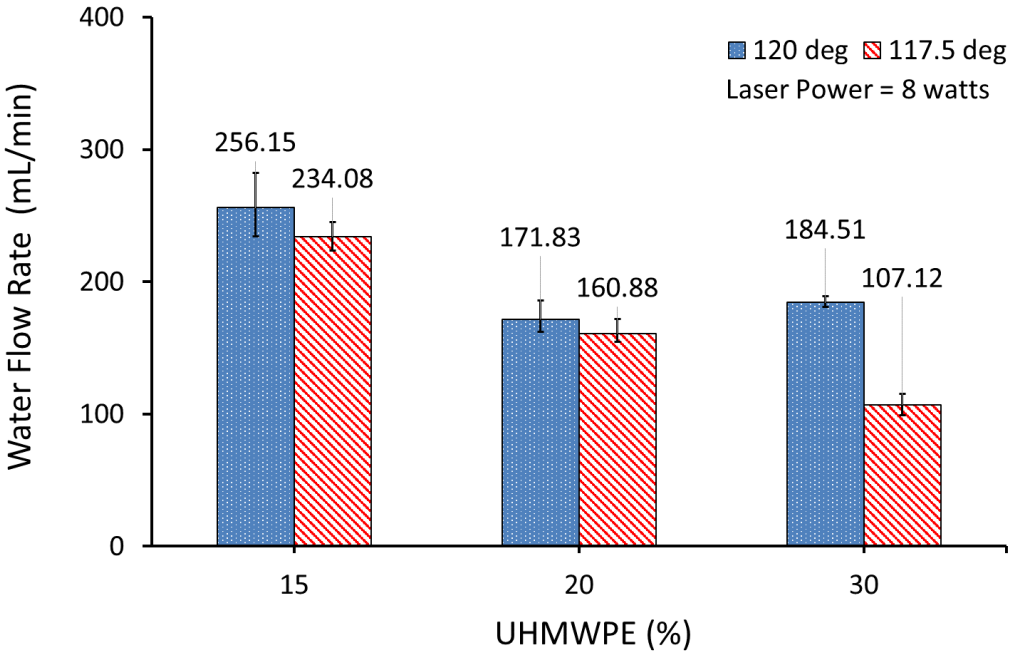

Figure 9.18 : Water flow rate of disc-shaped filters produced at laser power of 8 and bed temperatures of 117.5°C and 120°C with different UHMWPE content. (Four samples for each condition and the error bar represents the range of the data)

The results indicate that the flow rate is substantially influenced by the weight fraction of UHMWPE in the AC-UHMWPE composite. It can also be observed that the flow rate increased with the high energy input generated either by the laser power or by the bed temperature.

However, when additional samples were made at 20% UHMWPE, no systematic relationship was observed between the flow rate and the processing parameters. Figure 9.19 shows that the flow rate fluctuates with the changes in laser power and bed temperature with an overall average of approximately 161 ±14 mL/min.

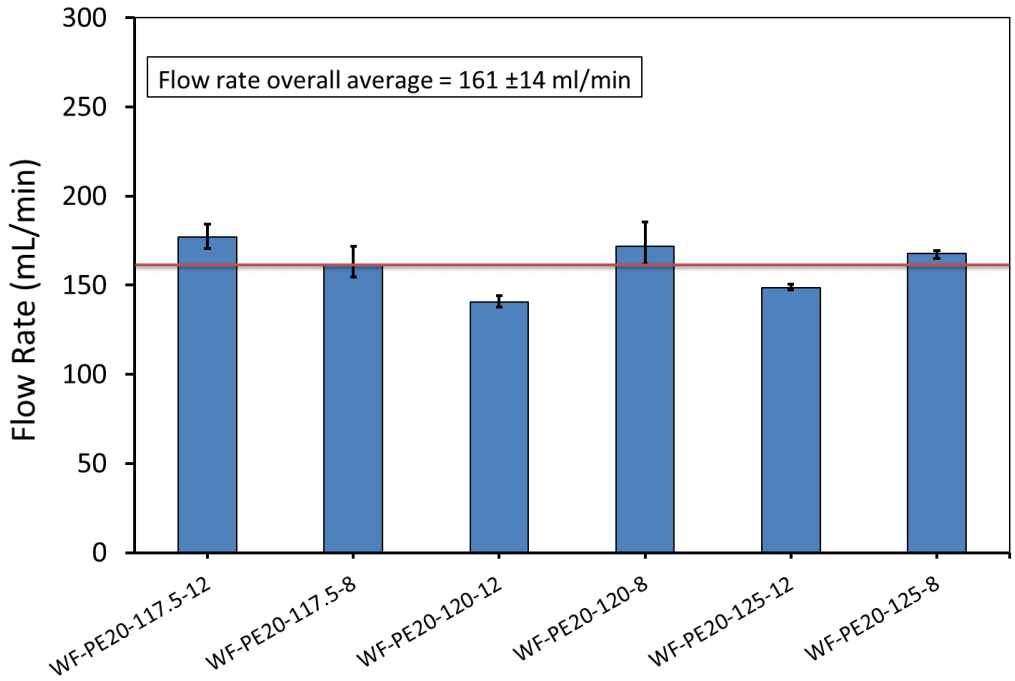

Figure 9.19 : Water flow rate of disc-shaped filters produced at different laser powers and bed temperatures with 80:20 AC-UHMWPE (Four samples for each condition and the error bar represents the range of the data)

9.6.2 Prediction of Water Flow Rate in Porous Media

Many models have been developed to describe the flow through porous media in order to predict and calculate the pressure drop of fluids passing through these porous media. These models are often based on empirical studies. Ergun

equation is one of the most widely used model to predict flow through packed bed [206]:

$$\frac{\Delta P}{L} = 150\ \frac{(1\ -\varepsilon)^2}{\varepsilon^3}\frac{\mu U}{D^2{}_p} + 1.75\ \frac{1-\varepsilon}{\varepsilon^3}\ \frac{\rho U^2}{D_p} \qquad (16)$$

Where:

ΔP: pressure drop of packed bed, Pa

L: height of packed bed, m

ε: porosity fraction

μ: dynamic viscosity of the fluid, kg/(m-s)

U: superficial bed velocity, m/s

D_p: particle diameter, m

ρ: density of the fluid, kg/m^3

Ergun model describes the permeability as a function of the mean particle size and porosity of the porous granular media. It assumes that packed bed is formed by a non-consolidated bed of spherical and identical size particles, in a streamline flow conditions. The only factors considered in this equation were fluid flow rate, particle diameter, fluid viscosity and density, and fractional void volume (i.e. porosity) [207, 208].

At a steady state, the pressure drop in a column is usually kept balanced by the hydrostatic pressure above the packing:

$$\Delta P = \rho g h \qquad (17)$$

Where h is the water level above the packed bed. By combining equations 16 and 17, the flow velocity of the water (U) can be determined. The equation can be further simplified to follow Darcy's law that describes the flow of a fluid through a porous medium:

$$\Delta P = \frac{\mu L U}{k} \qquad (18)$$

Where k is permeability of the packed bed which can be described as [207]:

$$k = \frac{D^2{}_p \varepsilon^3}{150\ (1\ -\varepsilon)^2} \tag{19}$$

Therefore, the flow velocity can be determined by the following equation:

$$U = \frac{\rho g h \dfrac{D^2{}_p\ .\ \varepsilon^3}{150\ (1\ -\varepsilon)^2}}{\mu L} \tag{20}$$

9.6.3 Comparison between the Experimental and Predicted Water Flow Rate in Porous Media

In ordered to estimate the predicted flow rate, the constant parameters in equation 20 listed in Table 9.10 are required. The variables in this equation are the porosity (ε) and the thickness of the filters.

Table 9.10: Constant parameters required for estimating flow rate of disc-shaped filters

Parameter	Unit	Values
Water density (ρ)	kg/m³	998
Acceleration of gravity (g)	m/s²	9.81
Height of water (h)	m	0.70
Particle diameter (D_p)	m	0.000196
Water viscosity (μ)	Pa.s	0.00089

Table 9.11 and Figure 9.20 show the measured and predicated flow rate values as obtained from the experimental flow rate tests and Ergun equation, respectively.

Table 9.11: Measured and predicated water flow rate of the disc-shaped filters

Sample ID	Water Flow Rate (mL/min)	
	Measured	Predicted
WF-PE15-117.5-8	234.08	222.12
WF-PE15-117.5-12	277.60	190.67
WF-PE15-120-8	256.15	237.47
WF-PE20-117.5-8	160.88	181.64
WF-PE20-117.5-12	176.88	197.38
WF-PE20-120-8	171.83	122.16
WF-PE30-117.5-8	107.12	117.02
WF-PE30-117.5-12	143.39	117.52
WF-PE30-120-8	184.51	116.63

The results show that the predicated flow rate data obtained from Ergun equation did not fit very well the experimental data in one to one comparison. However, in both methods a similar linear trend of the flow rate was observed with the change in weight fraction ratio of the activated carbon and UHMWPE composite. Figure 9.20 show that the flow rate decreased with the increasing of the UHMWPE binder content.

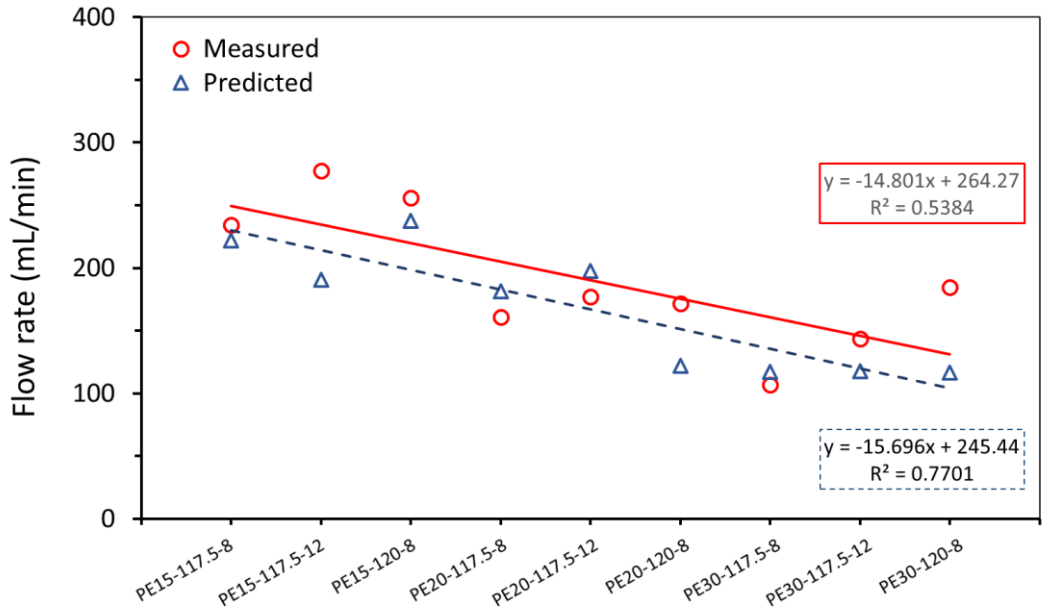

Figure 9.20 : The measured and predicted water flow rate of disc-shaped filters

9.7 Summary

Activated carbon disc-shaped and cylinder-shaped filters have been manufactured successfully using different UHMWPE binder contents and processing parameters.

9.7.1 Disc-shaped filters

The results of the disc-shaped filters indicate that the flow rate is substantially influenced by the weight fraction of UHMWPE in the AC-UHMWPE composite powder. A linear trend in the variation of the flow rate was observed with the change in weight fraction ratio of the activated carbon and UHMWPE composite powders used in manufacturing the water filters. The flow rate increased with the decreasing of the UHMWPE binder content.

The results also show that the flow rate increased with the high energy input generated by the laser power and the bed temperature. However, the relationship between the flow rate and the processing parameters at a fixed

UHMWPE content of 20% remains unclear. The flow rate fluctuates with the changes in laser power and bed temperature, with an overall average of approximately 161 ±14 mL/min.

9.7.2 Cylinder-shaped filters

The results data of the experiments carried out by Unilever are reported in Appendix A.

Chapter 10 Conclusions and Recommendations for Future Work

10.1 Conclusions

This research is concerned with the development of 3D printing for a new range of materials that will lead to new product opportunities for Unilever plc. 3D printing techniques largely rely on taking advantage of the material's properties in order to create the structures. The key scientific challenge here is to:

- match the properties of materials with the selected printing technique
- to incorporate multiple materials and hold the structures together
- to characterise the structure and hence performance

The feasibility of processing the materials used in manufacturing activated carbon filters using Laser Sintering has been investigated aiming to:

- produce porous structures
- control pores structure and properties
- improve mechanical properties and performance
- reproducibility

The contributions of this thesis have significantly provided the understanding to substantiate that there are many areas where Additive Manufacturing technologies can be applied with improved performance, good control of the internal structure and a possible low cost (by using less binder material), in comparison with the conventional method of manufacturing AC filters.

10.1.1 Feasibility of Processing UHMWPE by Laser Sintering

UHMWPE particles are non-spherical in shape with highly agglomerated structure of smaller particles with fibrils also exist in the microstructure of the UHMWPE powders. The particles of laser sintering powders should be at

approximately spherical in order to induce a free flowing behaviour. The Hausner ratio of UHMWPE powder was found to be just below 1.4 indicating that the powder has decreased flow and is close to being cohesive which is not favourable for laser sintering.

The thermal analysis indicated that the processing window of UHMWPE is small (less than 5°C) and this could cause a substantial problem during laser sintering process if small fluctuations in bed temperature or laser power occurs. However, the TGA result clearly shows a high temperature for thermal degradation (478°C) and hence the temperature window is wide enough and favourable for laser sintering.

The effect of cooling rate on the temperature and degree of crystallinity was investigated. The result shows that with the increase in the cooling rate, the crystallisation temperature is decreased. For the cooling rates of 1, 5, 10 and 100°C/min, the crystallisation temperatures were 122, 119, 117 and 97°C, respectively. However, different cooling rates did not alter the degree of crystallinity of UHMWPE significantly. This behaviour is very much affected by the extremely long molecular chains in UHMWPE.

10.1.2 Laser Sintering of UHMWPE

Trials to laser-sinter the commercial UHMWPE GUR 2122 powder (Celanese, Germany) have been made. Although, processing UHMWPE using laser sintering was challenging, good parts were fabricated successfully at various laser powers using a commercial laser sintering machine (EOS P100, Germany). The effects of laser power on the flexural, tensile and morphological properties of the sintered parts have been evaluated. This is significant because limited attempts, with limited success, were made to process UHMWPE by laser sintering. Additionally, there are still difficulties of processing UHMWPE and further work was needed to investigate the effect of process parameters on the mechanical properties of UHMWPE parts produced by laser sintering.

The mechanical properties of the UHMWPE sintered parts were evaluated by performing three point bend and tensile tests and were compared in terms of maximum strength, modulus and elongation.

The average flexural strength of the sintered parts increased with increase in laser energy density up to 0.027 J/mm^2 (LP = 10 watts) with a maximum value of the flexural strength of 2.12 ± 0.05 MPa. However, a slightly lower strength (1.61 ± 0.03 MPa) was observed at energy density of 0.032 J/mm^2 (LP = 12 watts), due to a decrease in bulk density. The results show that flexural strength is influenced by laser energy density and a good flexural strength (1.37 ± 0.30 MPa) is still achievable with energy density of 0.016 J/mm^2 (LP = 6 watts). A minimum ultimate tensile strength of 1.63 ±0.13 MPa was achieved at laser energy density of 0.016 J/mm^2 (LP = 6 watts) while a maximum of 2.42 ±0.20 MPa was achieved at 0.027 J/mm^2 (LP = 10 watts). The same trend was reflected in the tensile Young's modulus with average values in range between 46.5 ±5.1 and 72.6 ±14.9 MPa at laser energy density of 0.016 J/mm^2 (LP = 6 watts) and 0.027 J/mm^2 (LP = 10 watts), respectively. A maximum elongation of 51.4 % ±6.6 was achieved at laser energy density of 0.027 J/mm^2 (LP = 10 watts).

The results show substantial improvements in properties and process window compared with the most advanced previous work on UHMWPE using laser sintering [61]. There appears to be an optimum where strength and relative density reach a maximum, and ductility increases with laser energy density. However, with increasing energy density from the optimum, degradation of the polymer is expected to occur, which results in a reduction in strength [35].

The effects of laser power on the morphological properties of UHMWPE part with three-dimensional interconnectivity were investigated. The results show a high level of porosity in the laser sintered UHMWPE parts with a range of 60-62% and 61-65% measured by micro-CT and helium gas pycnometry, respectively. A slight decrease in porosity was observed when the laser power increased from 6 to 10 watts. Further increase in laser power to 12 watts

showed a slight increase in porosity. The porosity results, obtained by helium gas pycnometry, combined with the flexural measurements, showed that the flexural strength decreases as the porosity increases.

10.1.3 Laser Sintering of AC-UHMWPE Composite

This work demonstrated that AC-UHMWPE composite can be processed using Laser Sintering with a range of processing parameters at different binder content. The results and subsequent analysis have generated an understanding of the influence of processing parameters, such as laser power and bed temperature, on the internal structure, morphology and mechanical properties of the parts produced.

The AC has a high powder flow and the addition of AC has improved the flow of UHMWPE. This improvement was observed during spreading and distribution of the powder in the laser sintering machine.

The intrinsic thermal properties of UHMWPE powder are not significantly affected by the introduction of activated carbon, indicating that there was no interaction occurred between the UHMWPE and AC materials at the targeted temperature.

The thermal stability of the AC-UHMWPE has increased with the increase in the content of the activated carbon. Activated carbons can preferentially adsorb the volatile degraded UHMWPE components during the degradation process. This could delay the mass loss and retard the thermal degradation, resulting in a higher degradation temperature of the composites compared to that of the neat UHMWPE. The result clearly shows that the temperature window is wide enough and favourable for laser sintering.

The degree of crystallinity of the neat UHMWPE powder was decreased from 57.45% to 48.28% (using DSC) and from 67.80% to 61.35% (using XRD) for AC-UHMWPE composite powder with 70% AC and 30% UHMWPE. However, the crystallinity of AC-UHMWPE composite powders with 30, 20 and 15% UHMWPE

showed statistically insignificant changes in the trend, confirming that the change in the composition ratio of untreated composite does not have a significant effect on the degree of crystallinity.

An average relative density of 20.95 ±0.08%, 17.74 ±0.18% and 16.49 ±0.40% was achieved for laser sintered AC-UHMWPE parts with compositions of 70:30, 80:20 and 85:15 AC-UHMWPE, respectively. These parts were produced at a fixed laser power of 8 watts and bed temperatures of 117.5°C and 120°C. By comparison, the UHMWPE and AC virgin powders had relative densities of 24.33 ±0.23% and 16.27 ±0.09%, respectively. Based on the rule of mixtures, the relative densities of the PE30, PE20 and PE15 un-sintered composite powders found to be 17.55 ±0.06%, 17.07 ±0.07% and 16.85 ±0.07%, respectively.

The porosity of laser sintered AC-UHMWPE parts did not change significantly when bed temperature and laser power were changed. However, the UHMWPE content had the most obvious impact on flexural stress and an increase in the UHMWPE content yielded to improvement of the mechanical properties of the laser sintered AC-UHMWPE parts.

10.1.4 Manufacture of 3D Printed Activated Carbon Filters

This project has demonstrated that, for the first time, 3D printed activated carbon filters can be produced using laser sintering process. In comparison with the filters produced by the conventional process, the following outcomes can be drawn (the evaluation and the results data of Unilever are reported in Appendix A):

- Higher water flow rate
- Possibility to reduce cost by using less binder
- Filtration that matches current benchmarks
- Lower process temperature, which should allow for high melt flow index materials to be used as binders. This in turn allows cheaper and degradable polymers
- High repeatability

10.2 Recommendations for Future Work

The UHMWPE powder used in this study was a commercial powder and was not optimised for laser sintering, in terms of density and morphology. The microstructure of UHMWPE particle is highly complex. The irregular morphology causes difficulty when spreading the powder to achieve a uniform part bed. Therefore, these powders can be modified in order to achieve spherical particles with a higher bulk density that is suited for laser sintering. Additionally, particle size could influence powder flow, physical properties and performance of the final product. Therefore, it is recommended to test smaller particle size for both AC and binding material UHMWPE and investigate its effect.

The microstructure, physical, mechanical properties and quality of the laser sintered parts are fundamentally affected by the process parameters of laser sintering. The main parameters involved in the process include laser power, laser speed (scan speed), hatch spacing (scan spacing) and scan count, which are directly related to the amount of energy applied on the powder surface in the part bed [12, 81]. There are other important parameters influence the properties of laser sintered parts which include part bed temperature and layer thickness that make up the part. Therefore, using process parameters other than laser power and bed temperature is recommended, such as laser speed and hatch spacing. Additionally, since the particle size of UHMWPE and AC is larger than 100 μm, a layer thickness larger than 100 μm (e.g. 150, 200, 250, 300, 350 and 400 μm) can be explored, in order to examine the effect of layer thickness on the physical properties and performance of the manufactured parts.

There are other conventional polymeric binders used in manufacturing of carbon filters by traditional process, such as Low Density Polyethylene (LDPE), Ethylene Vinyl Acetate copolymer (EVA) and High Density Polyethylene (HDPE) [201]. The feasibility of processing these materials by Additive Manufacturing

techniques would be highly recommended as well as using cheaper and degradable polymers such as Polylactic acid (PLA).

Activated carbons have been used in water purification primarily in the removal of pollutant organic compounds that produce bad tastes and odours, and also may constitute a source of infection [136]. Recently, graphene and graphene oxide have been generating a rising interest in the material science and technology. These material are widely considered for many applications, including water purification, due to their atomically thin structure, large surface area and mechanical strength [209-212]. Therefore, research into the laser sintering of graphene-polymeric material composite would provide an opportunity to improve the mechanical properties and performance of the 3D printed parts and enable their use in wider AM applications, specifically in water purification.

In laser sintering, the preparation of the starting material (composite powder) is a key factor to produce parts with improved properties [95]. The AC-UHMWPE composite powder used in this project, was prepared by simple mechanical mixing of the AC with the neat UHMWPE polymer, using a tumbler mixer. It is very difficult to prepare two powders of different materials and different particle size that are uniformly mixed using this method. Therefore, mixing techniques other than mechanical mixing can be explored, such as melt-mixing [95] and solution processing [98].

Finally, AM techniques other than laser sintering can be explored for manufacturing activated carbon filters, such as Selective Mask Sintering and Selective Inhibition Sintering (these methods were explained in chapter 2 of this thesis). These technologies are noticeably faster and more cost efficient. They are based on infrared heating lamps instead of expensive lasers. The lasers can only process one point of material at any instant in time, compared to the SMS and SIS techniques where lines or layers of polymer material are fused at a time [39]. These technologies would eventually mature and directly

compete with the established mass production processes, in terms of quality and accuracy of products.

References

[1] R. M. Pink, *Water Rights in Southeast Asia and India*: Palgrave Macmillan US, 2016.

[2] J. B. Mandumpal, *A Journey Through Water: A Scientific Exploration of The Most Anomalous Liquid on Earth*: Bentham Science Publishers, 2017.

[3] WaterAid. (accessed on 12/05/2017). *India's Water Crisis* [Online]. Available: http://www.wateraid.org/where-we-work/page/india

[4] Unilever. (accessed on 12/05/2017). *Providing safe drinking water* [Online]. Available: www.unilever.com/sustainable-living/improving-health-and-well-being/health-and-hygiene/providing-safe-drinking-water

[5] Unilever. (accessed on 06/11/2017). *Pureit Classic system* [Online]. Available: www.unilever.com.lk/brands/our-brands/pureit.html

[6] AchaWater. (accessed on 06/11/2017). *Pureit Water Purifier* [Online]. Available: www.achawater.com/pureit-marvella-RO-filter

[7] J. Chatterjee, S. K. Gupta, and R. K. Ramachandran, "A process for making a filter block cum sediment filter," in *EP2635362B1*, ed: Google Patents, 2012.

[8] SeparationTechnology&Materials. (accessed on 23/07/2017). *Ultrafiltration Membrane Modules* [Online]. Available: www.stm.net.nz/products-and-services/water-and-wastewater-purification/ultrafiltration-membrane-modules

[9] G. Pyka, M. Speirs, E. Van de Casteele, B. Alpert, and M. Wevers, "Micro-CT based local strain analysis of porous materials: potential for industrial applications," presented at the Bruker microCT User Meeting 2015, Bruges, Belgium, 2015.

[10] M. Schmid, A. Amado, and K. Wegener, "Polymer powders for selective laser sintering (SLS)," presented at the 30th International Conference of the Polymer Processing Society, 2015.

[11] S. Berretta, O. Ghita, and K. E. Evans, "Morphology of polymeric powders in Laser Sintering (LS): From Polyamide to new PEEK powders," *European Polymer Journal,* vol. 59, pp. 218-229, 2014.

[12] J. D. Williams and C. R. Deckard, "Advances in modeling the effects of selected parameters on the SLS processnull," *Rapid Prototyping Journal,* vol. 4, pp. 90-100, 1998.

[13] L. Hao, M. M. Savalani, Y. Zhang, K. E. Tanner, and R. A. Harris, "Selective laser sintering of hydroxyapatite reinforced polyethylene composites for bioactive implants and tissue scaffold development," *Proceedings of the Institution of Mechanical Engineers, Part H: Journal of Engineering in Medicine,* vol. 220, pp. 521-531, 2006.

[14] L. Hao, M. M. Savalani, Y. Zhang, K. E. Tanner, and R. A. Harris, "Effects of material morphology and processing conditions on the characteristics of hydroxyapatite and

high-density polyethylene biocomposites by selective laser sintering," *Proceedings of the Institution of Mechanical Engineers, Part L: Journal of Materials Design and Applications,* vol. 220, pp. 125-137, 2006.

[15] A. Siegmann, I. Raiter, M. Narkis, and P. Eyerer, "Effect of powder particle morphology on the sintering behaviour of polymers," *Journal of materials science,* vol. 21, pp. 1180-1186, 1986.

[16] S. Andjelić and R. E. Richard, "Crystallization behavior of Ultrahigh Molecular Weight Polyethylene as a function of in vacuo γ -irradiation," *Macromolecules,* vol. 34, pp. 896-906, 2001.

[17] G. V. Salmoria, J. L. Leite, C. H. Ahrens, A. Lago, and A. T. N. Pires, "Rapid manufacturing of PA/HDPE blend specimens by selective laser sintering: Microstructural characterization," *Polymer Testing,* vol. 26, pp. 361-368, 2007.

[18] A. Amado, M. Schmid, G. Levy, and K. Wegener, "Advances in SLS Powder Characterization," *Group,* vol. 7, p. 12, 2011.

[19] S. Berretta, O. Ghita, K. E. Evans, A. Anderson, and C. Newman, "Size, shape and flow of powders for use in Selective Laser Sintering (SLS)," presented at the High Value Manufacturing: Advanced Research in Virtual and Rapid Prototyping: Proceedings of the 6th International Conference on Advanced Research in Virtual and Rapid Prototyping, Leiria, Portugal, 2013.

[20] H. H. Hausner, "Friction conditions in a mass of metal powder," *Int. J. Powder Met.,* vol. 3, pp. 7-13, 1967.

[21] E. C. Abdullah and D. Geldart, "The use of bulk density measurements as flowability indicators," *Powder Technology,* vol. 102, pp. 151-165, 1999.

[22] L. Verbelen, S. Dadbakhsh, M. Van den Eynde, J.-P. Kruth, B. Goderis, and P. Van Puyvelde, "Characterization of polyamide powders for determination of laser sintering processability," *European Polymer Journal,* vol. 75, pp. 163-174, 2016.

[23] S. Hambir and J. P. Jog, "Sintering of ultra high molecular weight polyethylene," *Bulletin of Materials Science,* vol. 23, pp. 221-226, 2000.

[24] G. M. Vasquez, C. E. Majewski, B. Haworth, and N. Hopkinson, "A targeted material selection process for polymers in laser sintering," *Additive Manufacturing,* vol. 1–4, pp. 127-138, 2014.

[25] E. D. Dickens, B. L. Lee, G. A. Taylor, A. J. Magistro, H. Ng, K. McAlea*, et al.*, "Sinterable semi-crystalline powder and near-fully dense article formed therewith," ed: Google Patents, 1996.

[26] M. Vasquez, B. Haworth, and N. Hopkinson, "Optimum sintering region for laser sintered nylon-12," *Proceedings of the Institution of Mechanical Engineers, Part B: Journal of Engineering Manufacture,* vol. 225, pp. 2240-2248, 2011.

[27] D. L. Bourell, T. J. Watt, D. K. Leigh, and B. Fulcher, "Performance Limitations in Polymer Laser Sintering," *Physics Procedia,* vol. 56, pp. 147-156, 2014.

[28] C. Yan, L. Hao, L. Xu, and Y. Shi, "Preparation, characterisation and processing of carbon fibre/polyamide-12 composites for selective laser sintering," *Composites Science and Technology,* vol. 71, pp. 1834-1841, 2011.

[29] N. Hopkinson, C. E. Majewski, and H. Zarringhalam, "Quantifying the degree of particle melt in Selective Laser Sintering®," *CIRP Annals - Manufacturing Technology,* vol. 58, pp. 197-200, 2009.

[30] W. Zhu, C. Yan, Y. Shi, S. Wen, J. Liu, and Y. Shi, "Investigation into mechanical and microstructural properties of polypropylene manufactured by selective laser sintering in comparison with injection molding counterparts," *Materials & Design,* vol. 82, pp. 37-45, 2015.

[31] A. Peacock, *Handbook of Polyethylene: Structures: Properties, and Applications*: Taylor & Francis, 2000.

[32] S. Dupin, O. Lame, C. Barrès, and J.-Y. Charmeau, "Microstructural origin of physical and mechanical properties of polyamide 12 processed by laser sintering," *European Polymer Journal,* vol. 48, pp. 1611-1621, 2012.

[33] K. Liu, Y. Shi, W. He, C. Li, Q. Wei, and J. Liu, "Densification of alumina components via indirect selective laser sintering combined with isostatic pressing," *The International Journal of Advanced Manufacturing Technology,* vol. 67, pp. 2511-2519, 2013.

[34] B. Caulfield, P. E. McHugh, and S. Lohfeld, "Dependence of mechanical properties of polyamide components on build parameters in the SLS process," *Journal of Materials Processing Technology,* vol. 182, pp. 477-488, 2007.

[35] T. J. Gill and K. K. B. Hon, "Experimental investigation into the selective laser sintering of silicon carbide polyamide composites," *Proceedings of the Institution of Mechanical Engineers, Part B: Journal of Engineering Manufacture,* vol. 218, pp. 1249-1256, 2004.

[36] ISO/ASTM Standard 52900, "Additive manufacturing - General principles - Terminology," ed. Switzerland: ISO/ASTM International, 2015.

[37] A. Gebhardt and J. S. Hötter, *Additive Manufacturing: 3D Printing for Prototyping and Manufacturing*: Carl Hanser Verlag GmbH & Company KG, 2016.

[38] N. Hopkinson, R. Hague, and P. Dickens, *Rapid Manufacturing: An Industrial Revolution for the Digital Age*: Wiley, 2006.

[39] I. Gibson, D. Rosen, and B. Stucker, *Additive Manufacturing Technologies: 3D Printing, Rapid Prototyping, and Direct Digital Manufacturing*: Springer New York, 2014.

[40] EnvisionTEC. (accessed on 23/07/2017). *Selective Lamination Composite Object Manufacturing (SLCOM)* [Online]. Available: www.envisiontec.com/3d-printers/slcom-1

[41] N. Guo and M. Leu, "Additive manufacturing: technology, applications and research needs," *Frontiers of Mechanical Engineering,* vol. 8, pp. 215-243, 2013.

[42] T. Wohlers and T. Caffrey, "Additive Manufacturing: Going Mainstream," *Manufacturing Engineering,* pp. 67-73, 2013.

[43] C. W. Hull, "Apparatus for production of three-dimensional objects by stereolithography," US004575330, 1986.

[44] C. R. Deckard, "Method and apparatus for producing parts by selective sintering," US004863538, 1989.

[45] 3D Systems, "3D Systems completes acquisition of DTM," ed: 3D Systems Press Release, 2001.

[46] E. M. Sachs, J. S. Haggerty, M. J. Cima, and P. A. Williams, "Three-dimensional printing techniques," US005204055, 1993.

[47] 3D Systems, "3D Systems completes the acquisition of Z Corp and Vidar," ed: 3D Systems Press Release, 2012.

[48] N. Hopkinson and P. Erasenthiran, "Method and apparatus for combining particulate material," US007879282 B2, 2011.

[49] N. Hopkinson and P. Erasenthiran, "High Speed Sintering-Early Research into a New Rapid Manufacturing Process," presented at the Solid Freeform Fabrication Symposium, University of Texas, Austin, 2004.

[50] H. R. Thomas, N. Hopkinson, and P. Erasenthiran, "High Speed Sintering-Continuing research into a new Rapid Manufacturing process," presented at the Solid Freeform Fabrication Symposium, University of Texas, Austin, 2006.

[51] C. E. Majewski, B. S. Hobbs, and N. Hopkinson, "Effect of bed temperature and infra-red lamp power on the mechanical properties of parts produced using high-speed sintering," *Virtual and physical prototyping,* vol. 2, pp. 103-110, 2007.

[52] B. Wendel, D. Rietzel, F. Kühnlein, R. Feulner, G. Hülder, and E. Schmachtenberg, "Additive Processing of Polymers," *Macromolecular Materials and Engineering,* vol. 293, pp. 799-809, 2008.

[53] D.-I. F. Kühnlein, D.-I. D. Rietzel, and I. D. Drummer, "Investigations of the directional mechanical properties and reasons of fracture of mask sintered PA12-components," *Journal of Plastics Technology,* vol. 8, p. 107, 2012.

[54] B. Khoshnevis, B. Asiabanpour, M. Mojdeh, and K. Palmer, "SIS – a new SFF method based on powder sintering," *Rapid Prototyping Journal,* vol. 9, pp. 30-36, 2003.

[55] B. Khoshnevis, "Selective inhibition of bonding of power particles for layered fabrication of 3-D objects," US006589471 B1, 2003.

[56] B. Asiabanpour, K. Palmer, and B. Khoshnevis, "An experimental study of surface quality and dimensional accuracy for selective inhibition of sintering," *Rapid Prototyping Journal,* vol. 10, pp. 181-192, 2004.

[57] B. Asiabanpour and K. Palmer, "Systematic approach for Rapid Prototyping processes development," in *IIE Annual Conference. Proceedings*, 2004.

[58] B. Asiabanpour, B. Khoshnevis, K. Palmer, and M. Mojdeh, "Advancements in the SIS process," presented at the Proceedings from the 14th SFF Symposium, Austin, Texas, 2003.

[59] B. Asiabanpour, R. Cano, C. Subbareddy, F. Wasik, L. VanWagner, and T. McCormick, "A new heater design by radiation modeling and a new polymer waste-saving mechanism design for the SIS process," *Rapid Prototyping Journal,* vol. 13, pp. 136-147, 2007.

[60] M. M. Savalani, L. Hao, Y. Zhang, K. E. Tanner, and R. A. Harris, "Fabrication of porous bioactive structures using the selective laser sintering technique," *Proceedings of the Institution of Mechanical Engineers, Part H: Journal of Engineering in Medicine.,* vol. 221, pp. 873-86, 2007.

[61] R. D. Goodridge, R. J. M. Hague, and C. J. Tuck, "An empirical study into laser sintering of ultra-high molecular weight polyethylene (UHMWPE)," *Journal of Materials Processing Technology,* vol. 210, pp. 72-80, 2010.

[62] A. Gebhardt, *Understanding Additive Manufacturing: Rapid Prototyping, Rapid Tooling, Rapid Manufacturing*: Hanser, 2012.

[63] G. N. Levy, R. Schindel, and J. P. Kruth, "Rapid Manufacturing and Rapid Tooling With Layer Manufacturing (LM) Technologies, State of the Art and Future Perspectives," *CIRP Annals - Manufacturing Technology,* vol. 52, pp. 589-609, 2003.

[64] L. Carrabine. (accessed on 25/05/2017). *3D Printers Deliver Competitive Alternative to Traditional Prosthetic Limbs* [Online]. Available: www.makepartsfast.com/3d-printers-deliver-competitive-alternative-to-traditional-prosthetic-limbs

[65] R. Beckett and S. Babu. (accessed on 25/05/2017). *Additive Layer Manufactured Fur Tiles* [Online]. Available: www.richard-beckett.com/cilia.html

[66] S. J. L. Kang, *Sintering: Densification, Grain Growth and Microstructure*: Elsevier Science, 2004.

[67] R. M. German, *Sintering Theory and Practice*: Wiley, 1996.

[68] R. German, *Sintering: From Empirical Observations to Scientific Principles*: Elsevier Science, 2014.

[69] J. P. Kruth, G. Levy, F. Klocke, and T. H. C. Childs, "Consolidation phenomena in laser and powder-bed based layered manufacturing," *CIRP Annals - Manufacturing Technology,* vol. 56, pp. 730-759, 2007.

[70] J.-P. Kruth, P. Mercelis, J. Van Vaerenbergh, L. Froyen, and M. Rombouts, "Binding mechanisms in selective laser sintering and selective laser melting," *Rapid prototyping journal,* vol. 11, pp. 26-36, 2005.

[71] H. Zarringhalam, N. Hopkinson, N. F. Kamperman, and J. J. De Vlieger, "Effects of processing on microstructure and properties of SLS Nylon 12," *Materials Science and Engineering: A,* vol. 435, pp. 172-180, 2006.

[72] E. Scribben, D. Baird, and P. Wapperom, "The role of transient rheology in polymeric sintering," *Rheologica acta,* vol. 45, pp. 825-839, 2006.

[73] J. Frenkel, "Viscous Flow of Crystalline Bodies under the Action of Surface Tension," *J. Phys.(USS R),* vol. 9, p. 385, 1945.

[74] C. T. Bellehumeur, M. Kontopoulou, and J. Vlachopoulos, "The role of viscoelasticity in polymer sintering," *Rheologica Acta,* vol. 37, pp. 270-278, 1998.

[75] C. T. Bellehumeur, M. K. Bisaria, and J. Vlachopoulos, "An experimental study and model assessment of polymer sintering," *Polymer Engineering and Science,* vol. 36, pp. 2198-2207, 1996.

[76] M. Rezaei, N. G. Ebrahimi, and M. Kontopoulou, "Thermal properties, rheology and sintering of ultra high molecular weight polyethylene and its composites with polyethylene terephthalate," *Polymer Engineering & Science,* vol. 45, pp. 678-686, 2005.

[77] U. Ajoku, N. Saleh, N. Hopkinson, R. Hague, and P. Erasenthiran, "Investigating mechanical anisotropy and end-of-vector effect in laser-sintered nylon parts," *Proceedings of the Institution of Mechanical Engineers, Part B: Journal of Engineering Manufacture,* vol. 220, pp. 1077-1086, 2006.

[78] M. Vasquez, N. Hopkinson, and B. Haworth, "Laser sintering processes: Practical verification of particle coalescence for polyamides and thermoplastic elastomers," presented at the Annual Technical Conference - ANTEC, Boston, Massachusetts, USA, 2011.

[79] H. Barry, H. Neil, H. David, and Z. Xiaotao, "Shear viscosity measurements on Polyamide-12 polymers for laser sintering," *Rapid Prototyping Journal,* vol. 19, pp. 28-36, 2013.

[80] J. Bai, R. D. Goodridge, R. J. M. Hague, and M. Song, "Improving the mechanical properties of laser-sintered polyamide 12 through incorporation of carbon nanotubes," *Polymer Engineering & Science,* vol. 53, pp. 1937-1946, 2013.

[81] R. D. Goodridge, C. J. Tuck, and R. J. M. Hague, "Laser sintering of polyamides and other polymers," *Progress in Materials Science,* vol. 57, pp. 229-267, 2012.

[82] J. P. Kruth, G. Levy, R. Schindel, T. Craeghs, and E. Yasa, "Consolidation of polymer powders by selective laser sintering," presented at the PMI International Conference, Ghent, Belgium, 2008.

[83] D. Drummer, D. Rietzel, and F. Kühnlein, "Development of a characterization approach for the sintering behavior of new thermoplastics for selective laser sintering," *Physics Procedia,* vol. 5, Part B, pp. 533-542, 2010.

[84] S. Ziegelmeier, P. Christou, F. Wöllecke, C. Tuck, R. Goodridge, R. Hague*, et al.*, "An experimental study into the effects of bulk and flow behaviour of laser sintering polymer powders on resulting part properties," *Journal of Materials Processing Technology,* vol. 215, pp. 239-250, 2014.

[85] G. V. Salmoria, C. H. Ahrens, P. Klauss, R. A. Paggi, R. G. Oliveira, and A. Lago, "Rapid manufacturing of polyethylene parts with controlled pore size gradients using selective laser sintering," *Materials Research,* vol. 10, pp. 211-214, 2007.

[86] A. Mazzoli, "Selective laser sintering in biomedical engineering," *Medical & Biological Engineering & Computing,* vol. 51, pp. 245-256, 2013.

[87] H. C. H. Ho, W. L. Cheung, and I. Gibson, "Morphology and Properties of Selective Laser Sintered Bisphenol A Polycarbonate," *Industrial & Engineering Chemistry Research,* vol. 42, pp. 1850-1862, 2003.

[88] S. R. Athreya, K. Kalaitzidou, and S. Das, "Mechanical and microstructural properties of Nylon-12/carbon black composites: Selective laser sintering versus melt compounding and injection molding," *Composites Science and Technology,* vol. 71, pp. 506-510, 2011.

[89] D. Rouholamin and N. Hopkinson, "An investigation on the suitability of micro-computed tomography as a non-destructive technique to assess the morphology of laser sintered nylon 12 parts," *Proceedings of the Institution of Mechanical Engineers, Part B: Journal of Engineering Manufacture,* vol. 228, pp. 1529-1542, 2014.

[90] M. O. de la Cuesta and F. W. Billmeyer, "The molecular structure of polyethylene. XII. Intrinsic viscosities of polyethylene solutions," *Journal of Polymer Science Part A: General Papers,* vol. 1, pp. 1721-1734, 1963.

[91] G. C. Berry and T. G. Fox, *The Viscosity of Polymers and Their Concentrated Solutions*: Springer, 1968.

[92] L. Hao, M. M. Savalani, Y. Zhang, K. E. Tanner, R. J. Heath, and R. A. Harris, "Characterization of selective laser-sintered hydroxyapatite-based biocomposite structures for bone replacement," *Proceedings of the Royal Society A: Mathematical, Physical and Engineering Science,* vol. 463, pp. 1857-1869, 2007.

[93] G. V. Salmoria, J. L. Leite, R. A. Paggi, A. Lago, and A. T. N. Pires, "Selective laser sintering of PA12/HDPE blends: Effect of components on elastic/plastic behavior," *Polymer Testing,* vol. 27, pp. 654-659, 2008.

[94] X. Yi, Z.-J. Tan, W.-J. Yu, J. Li, B.-J. Li, B.-Y. Huang*, et al.*, "Three dimensional printing of carbon/carbon composites by selective laser sintering," *Carbon,* vol. 96, pp. 603-607, 2016.

[95] R. D. Goodridge, M. L. Shofner, R. J. M. Hague, M. McClelland, M. R. Schlea, R. B. Johnson*, et al.*, "Processing of a Polyamide-12/carbon nanofibre composite by laser sintering," *Polymer Testing,* vol. 30, pp. 94-100, 2011.

[96] G. V. Salmoria, R. A. Paggi, A. Lago, and V. E. Beal, "Microstructural and mechanical characterization of PA12/MWCNTs nanocomposite manufactured by selective laser sintering," *Polymer Testing,* vol. 30, pp. 611-615, 2011.

[97] M. Wu, M. C. Leu, and N. Guo, "Simulation and testing of Polymer Electrolyte Membrane Fuel cell bipolar plates fabricated by selective laser sintering," *ASME/ISCIE 2012 International Symposium on Flexible Automation,* pp. 493-500, 2012.

[98] S. R. Athreya, K. Kalaitzidou, and S. Das, "Processing and characterization of a carbon black-filled electrically conductive Nylon-12 nanocomposite produced by selective laser sintering," *Materials Science and Engineering: A,* vol. 527, pp. 2637-2642, 2010.

[99] G. Kerckhofs, G. Pyka, D. Loeckx, S. Van Bael, J. Schrooten, and M. Wevers, "The combined use of micro-CT imaging, in-situ loading and non-rigid image registration for 3D experimental local strain mapping on porous bone tissue engineering scaffolds under compressive loading," in *Proceedings of European Conference for non-Destructive Testing (ECNDT)*, 2010.

[100] A. Armillotta and R. Pelzer, "Modeling of porous structures for rapid prototyping of tissue engineering scaffolds," *The International Journal of Advanced Manufacturing Technology,* vol. 39, pp. 501-511, 2008.

[101] A. Franco and L. Romoli, "Characterization of laser energy consumption in sintering of polymer based powders," *Journal of Materials Processing Technology,* vol. 212, pp. 917-926, 2012.

[102] G. Höhne, W. Hemminger, and H. J. Flammersheim, *Differential Scanning Calorimetry*: Springer, 2003.

[103] U. Ajoku, N. Hopkinson, and M. Caine, "Experimental measurement and finite element modelling of the compressive properties of laser sintered Nylon-12," *Materials Science and Engineering: A,* vol. 428, pp. 211-216, 2006.

[104] S. K. Pradhan, E. S. Dwarakadasa, and P. J. Reucroft, "Processing and characterization of coconut shell powder filled UHMWPE," *Materials Science and Engineering: A,* vol. 367, pp. 57-62, 2004.

[105] Q. Zhang, M. Jia, and P. Xue, "Study on molding process of UHMWPE microporous filter materials," *Journal of Applied Polymer Science,* vol. 126, pp. 1406-1415, 2012.

[106] S. V. Panin, L. A. Kornienko, N. X. Thuc, L. R. Ivanova, and S. V. Shilko, "Role of micro- and nanofillers in abrasive wear of composites based on ultra-high molecular weight polyethylene," in *Advanced Materials Research*, 2014, pp. 148-154.

[107] S. Piriyayon, S. V. Panin, and L. R. Ivanova, "Influence of adding graft UHMWPE and nanofillers onto wear resistance of Ultra-High Molecular Weight Polyethylene

(UHMWPE) mixture," presented at the 7th International Forum on Strategic Technology (IFOST), Tomsk, Russia, 2012.

[108] G. H. Michler, V. Seydewitz, M. Buschnakowski, L. P. Myasnikowa, E. M. Ivan'kova, V. A. Marikhin*, et al.*, "Correlation among powder morphology, compactability, and mechanical properties of consolidated nascent UHMWPE," *Journal of Applied Polymer Science,* vol. 118, pp. 866-875, 2010.

[109] S. M. Kurtz, *UHMWPE biomaterials handbook: ultra high molecular weight polyethylene in total joint replacement and medical devices*: Academic Press, 2009.

[110] V. Tulatorn, S. Ouajai, R. Yeetsorn, and N. Chanunpanich, "Mechanical Behavior Investigation of UHMWPE Composites for Pile Cushion Applications," *KMUTNB: International Journal of Applied Science and Technology,* vol. 8, pp. 271-282, 2015.

[111] T. Deplancke, O. Lame, F. Rousset, I. Aguili, R. Seguela, and G. Vigier, "Diffusion versus Cocrystallization of Very Long Polymer Chains at Interfaces: Experimental Study of Sintering of UHMWPE Nascent Powder," *Macromolecules,* vol. 47, pp. 197-207, 2014.

[112] S. M. Kurtz, *The UHMWPE Handbook: Ultra-High Molecular Weight Polyethylene in Total Joint Replacement*: Elsevier Science, 2004.

[113] G. Reiter, "Some unique features of polymer crystallisation," *Chemical Society Reviews,* vol. 43, pp. 2055-2065, 2014.

[114] D. I. Bower, *An Introduction to Polymer Physics*: Cambridge University Press, 2002.

[115] SPring-8. (accessed on 21/08/2017). *Folded structures of existing polymer crystals and spherulite* [Online]. Available: http://www.spring8.or.jp/en/news_publications/publications/scientific_results/soft_matter/topic7

[116] P. Fairclough. (accessed on 21/08/2017). *Correlation Function - Lamella Structure* [Online]. Available: www.slideshare.net/AbhiramKannan1/just-an-example-of-a-presentation

[117] K. s. McGuire, D. R. Lloyd, and G. B. A. Lim, "Microporous membrane formation via thermally-induced phase separation. VII. Effect of dilution, cooling rate, and nucleating agent addition on morphology," *Journal of Membrane Science,* vol. 79, pp. 27-34, 1993.

[118] K. S. Kanaga Karuppiah, A. L. Bruck, S. Sundararajan, J. Wang, Z. Lin, Z.-H. Xu*, et al.*, "Friction and wear behavior of ultra-high molecular weight polyethylene as a function of polymer crystallinity," *Acta Biomaterialia,* vol. 4, pp. 1401-1410, 2008.

[119] S. M. Kurtz, O. K. Muratoglu, M. Evans, and A. A. Edidin, "Advances in the processing, sterilization, and crosslinking of ultra-high molecular weight polyethylene for total joint arthroplasty," *Biomaterials,* vol. 20, pp. 1659-1688, 1999.

[120] D. Jauffrès, O. Lame, G. Vigier, and F. Doré, "Microstructural origin of physical and mechanical properties of ultra high molecular weight polyethylene processed by high velocity compaction," *Polymer,* vol. 48, pp. 6374-6383, 2007.

[121] S. K. Sinha and B. J. Briscoe, *Polymer Tribology*: World Scientific, 2009.

[122] P. E. Lawrence W. Fisher, *Selection of Engineering Materials and Adhesives*: CRC Press, 2005.

[123] A. Bhattacharyya, S. Chen, and M. Zhu, "Graphene reinforced ultra high molecular weight polyethylene with improved tensile strength and creep resistance properties," *Express Polymer Letters,* vol. 8, pp. 74-84, 2014.

[124] J. C. Baena, J. Wu, and Z. Peng, "Wear Performance of UHMWPE and Reinforced UHMWPE Composites in Arthroplasty Applications: A Review," *Lubricants,* vol. 3, pp. 413-436, 2015.

[125] C. N. Della and D. W. Shu, "Mechanical properties of carbon nanotubes reinforced ultra high molecular weight polyethylene," *Solid State Phenomena,* vol. 136, pp. 45-50, 2008.

[126] S. Spiegelberg, "Analytical techniques for assessing the effects of radiation on UHMWPE," Cambridge Polymer Group, Application Note 8.2001.

[127] R. C. Bansal and M. Goyal, *Activated carbon adsorption*. Boca Raton: Taylor & Francis, 2005.

[128] B. Crittenden and W. J. Thomas, *Adsorption Technology & Design*: Elsevier Science, 1998.

[129] H. Marsh and F. Rodríguez-Reinoso, "Chapter 1 - Introduction to the Scope of the Text," in *Activated Carbon*, H. M. Rodríguez-Reinoso, Ed., ed Oxford: Elsevier Science Ltd, 2006, pp. 1-12.

[130] A. E. Eltom, M. P. Fournier Lessa, M. J. da Silva, and J. C. da Rocha, "Production & Characterization of Activated Carbon Membranes," *Journal of Materials Research and Technology,* vol. 1, pp. 80-83, 2012.

[131] G. McKay, *Use of Adsorbents for the Removal of Pollutants from Wastewater*: Taylor & Francis, 1995.

[132] P. Ariyadejwanich, W. Tanthapanichakoon, K. Nakagawa, S. R. Mukai, and H. Tamon, "Preparation and characterization of mesoporous activated carbon from waste tires," *Carbon,* vol. 41, pp. 157-164, 2003.

[133] M. A. Yahya, Z. Al-Qodah, and C. W. Z. Ngah, "Agricultural bio-waste materials as potential sustainable precursors used for activated carbon production: A review," *Renewable and Sustainable Energy Reviews,* vol. 46, pp. 218-235, 2015.

[134] F. Rodríguez-Reinoso and A. Sepúlveda-Escribano, "Chapter 9 - Porous Carbons in Adsorption and Catalysis," in *Handbook of Surfaces and Interfaces of Materials*, H. S. Nalwa, Ed., ed Burlington: Academic Press, 2001, pp. 309-355.

[135] H. Marsh and F. Rodríguez-Reinoso, "Chapter 8 - Applicability of Activated Carbon," in *Activated Carbon*, H. M. Rodríguez-Reinoso, Ed., ed Oxford: Elsevier Science Ltd, 2006, pp. 383-453.

[136] H. Marsh and F. Rodríguez-Reinoso, "Chapter 9 - Production and Reference Material," in *Activated Carbon*, H. M. Rodríguez-Reinoso, Ed., ed Oxford: Elsevier Science Ltd, 2006, pp. 454-508.

[137] Zeman, *Microfiltration and Ultrafiltration: Principles and Applications*: Taylor & Francis, 1996.

[138] T. J. Bandosz, *Activated Carbon Surfaces in Environmental Remediation*: Elsevier Science, 2006.

[139] J. Przepiórski, "Chapter 9 Activated carbon filters and their industrial applications," in *Interface Science and Technology*. vol. Volume 7, J. B. Teresa, Ed., ed: Elsevier, 2006, pp. 421-474.

[140] S. M. Manocha, "Porous carbons, in Frontiers in materials science and technology," in *Sadhana*. vol. 28, ed: Springer, 2003, pp. 335-348.

[141] G. L. Culp and R. L. Culp, *New concepts in water purification*: Van Nostrand Reinhold Co., 1974.

[142] Z. K. Chowdhury, *Activated Carbon: Solutions for Improving Water Quality*: American Water Works Association, 2013.

[143] A. Aworn, P. Thiravetyan, and W. Nakbanpote, "Preparation of CO2 activated carbon from corncob for monoethylene glycol adsorption," *Colloids and Surfaces A: Physicochemical and Engineering Aspects,* vol. 333, pp. 19-25, 2009.

[144] P. Nowicki and et al., "The effect of chemical activation method on properties of activated carbons obtained from pine cones," *Central European Journal of Chemistry,* vol. 11, pp. 78-85, 2013.

[145] P. Steven, *Hydrogen - Unabridged Guide*: Emereo Pty Limited, 2012.

[146] N. P. Cheremisinoff, *Handbook of Water and Wastewater Treatment Technologies*: Elsevier Science, 2001.

[147] J. M. D. Tascón, *Novel Carbon Adsorbents*: Elsevier Science, 2012.

[148] E. Worch, *Adsorption Technology in Water Treatment: Fundamentals, Processes, and Modeling*: De Gruyter, 2012.

[149] F. Cecen and Ö. Aktas, *Activated Carbon for Water and Wastewater Treatment: Integration of Adsorption and Biological Treatment*: Wiley, 2011.

[150] P. Klauss, G. V. Salmoria, L. A. Kanis, and K. M. Zepon, "Manufacturing of Drug Delivery Device by Selective Laser Sintering Using of Polycaprolactone and Polyethylene," 2009.

[151] J. T. Rimell and P. M. Marquis, "Selective laser sintering of ultra high molecular weight polyethylene for clinical applications," *Journal of Biomedical Materials Research,* vol. 53, pp. 414-420, 2000.

[152] J. E. Mark, *Physical Properties of Polymers Handbook*: Springer New York, 2007.

[153] S. Rüsenberg, L. Schmidt, and H. Schmid, "Mechanical and physical properties–a way to assess quality of laser sintered parts," presented at the Proceedings of the 22nd International Solid Freeform Fabrication Symposium, 2011.

[154] M. Yuan, D. Bourell, and T. Diller, "Thermal conductivity measurements of polyamide 12," in *Proceedings of the Solid Freeform Fabrication Symposium*, Austin, Texas, USA, 2011.

[155] S. T. Ho and D. W. Hutmacher, "A comparison of micro CT with other techniques used in the characterization of scaffolds," *Biomaterials,* vol. 27, pp. 1362-1376, 2006.

[156] M. Schmid, F. Amado, G. Levy, and K. Wegener, "Flowability of Powders for Selective Laser Sintering (SLS) investigated by Round Robin Test," presented at the High Value Manufacturing: Advanced Research in Virtual and Rapid Prototyping: Proceedings of the 6th International Conference on Advanced Research in Virtual and Rapid Prototyping, Leiria, Portugal, 2013.

[157] M. Van den Eynde, L. Verbelen, and P. Van Puyvelde, "Assessing polymer powder flow for the application of laser sintering," *Powder Technology,* vol. 286, pp. 151-155, 2015.

[158] J. P. Sibilia, *A Guide to Materials Characterization and Chemical Analysis*: Wiley, 1996.

[159] C. Sonntag. (accessed on 04/06/2017). *XRD Principle* [Online]. Available: www.slideshare.net/christophsontag/spectroscopy-xrd

[160] B. H. Stuart, *Polymer Analysis*: Wiley, 2008.

[161] M. B. Turell and A. Bellare, "A study of the nanostructure and tensile properties of ultra-high molecular weight polyethylene," *Biomaterials,* vol. 25, pp. 3389-3398, 2004.

[162] T. H. Lee, F. Y. C. Boey, and K. A. Khor, "X-ray diffraction analysis technique for determining the polymer crystallinity in a polyphenylene sulfide composite," *Polymer Composites,* vol. 16, pp. 481-488, 1995.

[163] E. Enqvist and N. Emami, "Nanodiamond reinforced ultra high molecular weight polyethylene for orthopaedic applications: dry versus wet ball milling manufacturing methods," *Tribology-Materials, Surfaces & Interfaces,* vol. 8, pp. 7-13, 2014.

[164] K. Shahzad, J. Deckers, S. Boury, B. Neirinck, J.-P. Kruth, and J. Vleugels, "Preparation and indirect selective laser sintering of alumina/PA microspheres," *Ceramics International,* vol. 38, pp. 1241-1247, 2012.

[165] A. V. Maksimkin, S. D. Kaloshkin, V. V. Tcherdyntsev, D. I. Chukov, and I. V. Shchetinin, "Effect of high-energy ball milling on the structure and mechanical properties of ultra-high molecular weight polyethylene," *Journal of Applied Polymer Science,* vol. 130, pp. 2971-2977, 2013.

[166] S. Berretta, Y. Wang, R. Davies, and O. R. Ghita, "Polymer viscosity, particle coalescence and mechanical performance in high-temperature laser sintering," *Journal of Materials Science,* vol. 51, pp. 4778-4794, 2016.

[167] J. Gu, N. Li, L. Tian, Z. Lv, and Q. Zhang, "High thermal conductivity graphite nanoplatelet/UHMWPE nanocomposites," *RSC Advances,* vol. 5, pp. 36334-36339, 2015.

[168] W. Dewulf, M. Pavan, T. Craeghs, and J.-P. Kruth, "Using X-ray computed tomography to improve the porosity level of polyamide-12 laser sintered parts," *CIRP Annals - Manufacturing Technology,* vol. 65, pp. 205-208, 2016.

[169] M. Tanniru, Q. Yuan, and R. D. K. Misra, "On significant retention of impact strength in clay–reinforced high-density polyethylene (HDPE) nanocomposites," *Polymer,* vol. 47, pp. 2133-2146, 2006.

[170] S. P. Soe, D. R. Eyers, and R. Setchi, "Assessment of non-uniform shrinkage in the laser sintering of polymer materials," *The International Journal of Advanced Manufacturing Technology,* vol. 68, pp. 111-125, 2013.

[171] K. Manetsberger, J. Shen, and J. Muellers, "Compensation of non-linear shrinkage of polymer materials in selective laser sintering," presented at the Solid Freeform Fabrication Symposium, Auston, Texas, USA, 2001.

[172] K. Senthilkumaran, P. M. Pandey, and P. V. M. Rao, "Influence of building strategies on the accuracy of parts in selective laser sintering," *Materials & Design,* vol. 30, pp. 2946-2954, 2009.

[173] S. Danjou and P. Köhler, "Determination of optimal build direction for different rapid prototyping applications," in *Proceedings of the 14th European forum on rapid prototyping*, Ecole Centrale Paris, 2009.

[174] N. Hopkinson and T. B. Sercombe, "Process repeatability and sources of error in indirect SLS of aluminium," *Rapid Prototyping Journal,* vol. 14, pp. 108-113, 2008.

[175] M. Berzins, T. H. C. Childs, and G. R. Ryder, "The Selective Laser Sintering of Polycarbonate," *CIRP Annals,* vol. 45, pp. 187-190, 1996.

[176] L. De Chiffre, S. Carmignato, J. P. Kruth, R. Schmitt, and A. Weckenmann, "Industrial applications of computed tomography," *CIRP Annals - Manufacturing Technology,* vol. 63, pp. 655-677, 2014.

[177] J. Matějíček, B. Kolman, J. Dubský, K. Neufuss, N. Hopkins, and J. Zwick, "Alternative methods for determination of composition and porosity in abradable materials," *Materials Characterization,* vol. 57, pp. 17-29, 2006.

[178] M. Navvab Kashani, V. Zivkovic, H. Elekaei, and M. J. Biggs, "A new method for reconstruction of the structure of micro-packed beds of spherical particles from desktop X-ray microtomography images. Part A. Initial structure generation and porosity determination," *Chemical Engineering Science,* vol. 146, pp. 337-345, 2016.

[179] T. B. Kim, S. Yue, Z. Zhang, E. Jones, J. R. Jones, and P. D. Lee, "Additive manufactured porous titanium structures: Through-process quantification of pore and strut networks," *Journal of Materials Processing Technology,* vol. 214, pp. 2706-2715, 2014.

[180] P. P. Magampa, N. Manyala, and W. W. Focke, "Properties of graphite composites based on natural and synthetic graphite powders and a phenolic novolac binder," *Journal of Nuclear Materials,* vol. 436, pp. 76-83, 2013.

[181] H. C. H. Ho, I. Gibson, and W. L. Cheung, "Effects of energy density on morphology and properties of selective laser sintered polycarbonate," *Journal of Materials Processing Technology,* vol. 89–90, pp. 204-210, 1999.

[182] G. Sui, W. H. Zhong, X. Ren, X. Q. Wang, and X. P. Yang, "Structure, mechanical properties and friction behavior of UHMWPE/HDPE/carbon nanofibers," *Materials Chemistry and Physics,* vol. 115, pp. 404-412, 2009.

[183] D. I. Chukov, A. A. Stepashkin, A. V. Maksimkin, V. V. Tcherdyntsev, S. D. Kaloshkin, K. V. Kuskov*, et al.*, "Investigation of structure, mechanical and tribological properties of short carbon fiber reinforced UHMWPE-matrix composites," *Composites Part B: Engineering,* vol. 76, pp. 79-88, 2015.

[184] J. Guo and A. Chong Lua, "Characterization of chars pyrolyzed from oil palm stones for the preparation of activated carbons," *Journal of Analytical and Applied Pyrolysis,* vol. 46, pp. 113-125, 1998.

[185] S. S. Gupta, T. S. Sreeprasad, S. M. Maliyekkal, S. K. Das, and T. Pradeep, "Graphene from Sugar and its Application in Water Purification," *ACS Applied Materials & Interfaces,* vol. 4, pp. 4156-4163, 2012.

[186] M. F. Ashby, H. Shercliff, and D. Cebon, *Materials: Engineering, Science, Processing and Design*: Elsevier Science, 2007.

[187] R. Chávez-Medellín, L. A. S. d. A. Prado, and K. Schulte, "Polyamide-12/Functionalized Carbon Nanofiber Composites: Evaluation of Thermal and Mechanical Properties," *Macromolecular Materials and Engineering,* vol. 295, pp. 397-405, 2010.

[188] S. Chen, D. L. Bourell, and K. L. Wood, "Fabrication of PEM Fuel Cell Bipolar Plates by Indirect SLS," presented at the Proceedings of the International Solid Freeform Fabrication Symposium, Austin, Texas, 2004.

[189] K. Alayavalli and D. L. Bourell, "Fabrication of electrically conductive, fluid impermeable direct methanol fuel cell (DMFC) graphite bipolar plates by indirect selective laser sintering (SLS)," presented at the International Solid Freeform Fabrication Symposium, Austin, Texas, USA, 2008.

[190] X.-Y. Liu, M. Huang, H.-L. Ma, Z.-Q. Zhang, J.-M. Gao, Y.-L. Zhu*, et al.*, "Preparation of a Carbon-Based Solid Acid Catalyst by Sulfonating Activated Carbon in a Chemical Reduction Process," *Molecules,* vol. 15, pp. 7188-7196, 2010.

[191] J. P. Kruth, X. Wang, T. Laoui, and L. Froyen, "Lasers and materials in selective laser sintering," *Assembly Automation,* vol. 23, pp. 357-371, 2003.

[192] J. Bai, R. D. Goodridge, R. Hague, M. Song, and M. Okamoto, "Influence of carbon nanotubes on the rheology and dynamic mechanical properties of polyamide-12 for laser sintering," *Polymer Testing,* vol. 36, pp. 95-100, 2014.

[193] N. Guo and M. C. Leu, "Effect of different graphite materials on the electrical conductivity and flexural strength of bipolar plates fabricated using selective laser sintering," *International Journal of Hydrogen Energy,* vol. 37, pp. 3558-3566, 2012.

[194] D. L. Bourell, M. C. Leu, K. Chakravarthy, N. Guo, and K. Alayavalli, "Graphite-based indirect laser sintered fuel cell bipolar plates containing carbon fiber additions," *CIRP Annals - Manufacturing Technology,* vol. 60, pp. 275-278, 2011.

[195] G. Lu, G. Q. Lu, and Z. M. Xiao, "Mechanical Properties of Porous Materials," *Journal of Porous Materials,* vol. 6, pp. 359-368, 1999.

[196] H. Giesche, "Mercury Porosimetry: A General (Practical) Overview," *Particle & Particle Systems Characterization,* vol. 23, pp. 9-19, 2006.

[197] A. Zohrevand, A. Ajji, and F. Mighri, "Microstructure and properties of porous nanocomposite films: effects of composition and process parameters," *Polymer International,* vol. 63, pp. 2052-2060, 2014.

[198] H. Yan, W. R. Cannon, and D. J. Shanefield, "Thermal decomposition behaviour of poly(propylene carbonate)," *Ceramics International,* vol. 24, pp. 433-439, 1998.

[199] Y. L. Hsieh and X. P. Hu, "Structural transformation of ultra-high modulus and molecular weight polyethylene fibers by high-temperature wide-angle X-ray diffraction," *Journal of Polymer Science Part B: Polymer Physics,* vol. 35, pp. 623-630, 1997.

[200] J. Han, S. Ding, W. Zheng, W. Li, and H. Li, "Microstructure and anti- wear and corrosion performances of novel UHMWPE/graphene-nanosheet composite coatings deposited by flame spraying," *Polymers for Advanced Technologies,* vol. 24, pp. 888-894, 2013.

[201] G. Bommi and K. M. Bommi, "Filter cartridge for gravity-fed water treatment device," US7396461 B2, 2008.

[202] S. Haftka, J. Ehlers, C. Barth, and L. Wang, "Activated carbon filter - Polyethylene binder," ed: Google Patents, 2004.

[203] A. Domme, "Process for the manufacture of a filter unit," ed: Google Patents, 1996.

[204] M. Pavan, T. Craeghs, R. Verhelst, O. Ducatteeuw, J.-P. Kruth, and W. Dewulf, "CT-based quality control of Laser Sintering of Polymers," *Case Studies in Nondestructive Testing and Evaluation,* 2016.

[205] K. F. Leong, C. K. Chua, W. S. Gui, and Verani, "Building Porous Biopolymeric Microstructures for Controlled Drug Delivery Devices Using Selective Laser Sintering," *The International Journal of Advanced Manufacturing Technology,* vol. 31, pp. 483-489, 2006.

[206] S. Ergun, "Fluid Flow Through Packed Columns," *Chemical Engineering Progress,* vol. 48, pp. 89-94, 1952.

[207] Y. Bruni, L. Garrido, and E. Aglietti, "Application of the Ergun's Equation in Porous Ceramic Based on CaO-Stabilized ZrO2," *Procedia Materials Science,* vol. 1, pp. 418-424, 2012/01/01/ 2012.

[208] J. Trahan, A. Graziani, D. Y. Goswami, E. Stefanakos, C. Jotshi, and N. Goel, "Evaluation of Pressure Drop and Particle Sphericity for an Air-rock Bed Thermal Energy Storage System," *Energy Procedia,* vol. 57, pp. 633-642, 2014/01/01/ 2014.

[209] S. Dervin, D. D. Dionysiou, and S. C. Pillai, "2D nanostructures for water purification: graphene and beyond," *Nanoscale,* vol. 8, pp. 15115-15131, 2016.

[210] J. Chen, B. Yao, C. Li, and G. Shi, "An improved Hummers method for eco-friendly synthesis of graphene oxide," *Carbon,* vol. 64, pp. 225-229, 2013.

[211] K. Zhang, V. Dwivedi, C. Chi, and J. Wu, "Graphene oxide/ferric hydroxide composites for efficient arsenate removal from drinking water," *Journal of Hazardous Materials,* vol. 182, pp. 162-168, 2010.

[212] G. Gollavelli, C.-C. Chang, and Y.-C. Ling, "Facile Synthesis of Smart Magnetic Graphene for Safe Drinking Water: Heavy Metal Removal and Disinfection Control," *ACS Sustainable Chemistry & Engineering,* vol. 1, pp. 462-472, 2013.

[213] L. Francis, N. Ghaffour, A. S. Alsaadi, S. P. Nunes, and G. L. Amy, "Performance evaluation of the DCMD desalination process under bench scale and large scale module operating conditions," *Journal of Membrane Science,* vol. 455, pp. 103-112, 2014.

[214] F. Abiriga and S. O. Kinyera, "Water Purification by Double Filtration Using Ceramic Filters," *Environment and Natural Resources Research,* vol. 4, p. p92, 2014.

[215] WHO, "Water quality and health-review of turbidity: information for regulators and water suppliers," ed: World Health Organization, 2017.

[216] Z. Zhu, P. Pradel, R. J. Bibb, and J. Moultrie, "A framework for designing end use products for direct manufacturing using additive manufacturing technologies," in *Proceedings of the 21st International Conference on Engineering Design (ICED17)*, Vancouver, Canada, 2017, pp. 327-336.

Appendix A

A.1 Experimental Procedures of 3D printed Filters

The evaluation and measurement of the 3D printed prototype cylinder-shaped filters were conducted by Unilever R&D in Bangalore.

A.1.1 Bulk Density

The bulk density of the 3D printed cylinder-shaped filters was determined using a volumetric method, which is defined by the mass of the filter per unit volume. The mass of the filters was determined by weighing the filters using a digital balance and the volume of the filters was determined using a Vernier calliper measurement of dimensions.

A.1.2 Porosity

The porosity measurement of the 3D printed cylinder-shaped filters was conducted by Unilever R&D in Bangalore. The geometrical volume (V_t) and the dry weight (w_1) of the 3D printed filters were measured initially. The filters then were immersed in water and kept overnight so that all empty voids are filled with water. The wet weight (w_2) of the samples was measured and the pore volume (V_p) was calculated by the ratio of the difference in the sample's weight ($w_2 - w_1$) to the density of the water (ρ_w). The porosity was then calculated by the ratio of the pore volume to the total geometrical volume of the filter as described in the following equations [213]:

$$Pore\ volume\ (V_p) = \frac{(w_2 - w_1)}{\rho_w} \tag{A.1}$$

$$Porosity = \frac{V_p}{V_t} \times 100 \tag{A.2}$$

A.1.3 Water Flow

Figure A.1 shows a detailed schematic of the experimental rig used for the water flow rate test at Unilever R&D in Bangalore. The volume of the collected water was measured using a measuring beaker and the time during which it was collected was measured using a stopwatch and the water flow rate then was calculated. The flow rate was measured at water column head of 17 cm after allowing 1 Litre of water to pass through the filter.

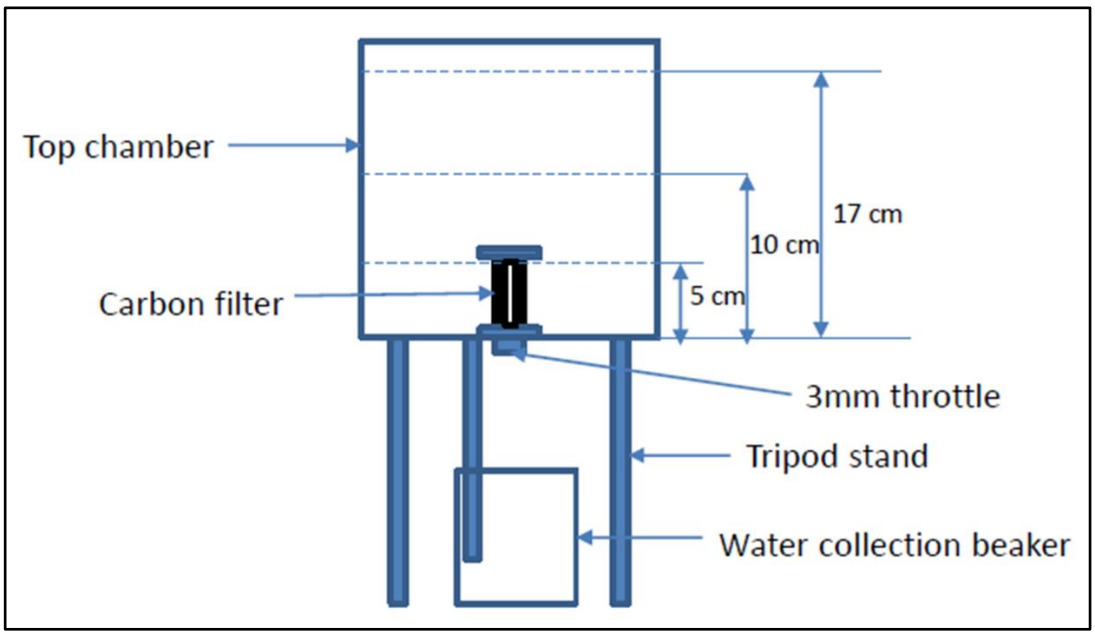

Figure A.1 : A schematic diagram of filtration assembly (Unilever R&D - Bangalore)

A.1.4 Turbidity Removal

Turbidity is a measure of the relative clarity of a liquid and is an expression of the amount of light that is scattered by materials in water when light passes through the water sample [214]. Turbidity is typically quantified by the Nephelometric Turbidity Unit (NTU). The World Health Organization (WHO), recommends that the turbidity of drinking water should ideally be below 1 NTU and in some cases, it is allowed to be kept below 5 NTU [215].

Test water was prepared by adding specific salts in Reverse Osmosis (RO) water to get a Total Dissolve Solids (TDS) concentration of 1000- 1200 ppm.

The concentration of inorganic particles (i.e. test dust) and humic acids were 15 ppm and 2.5 ppm, respectively. The filter was inserted into a 10 Litre chamber that was placed over a stand. 20 Litres of RO water was passed through the filter for conditioning. After conditioning, the test water was filled in the chamber till top head of 17 cm and allowed 1 Litre of water to pass through the filter. Output water sample was then collected and analysed for turbidity. Turbidity of both input and output water samples were analysed using Turbiquant 1500 turbidity meter (Merck KGaA, Germany).

A.2 Results and Discussion of 3D Printed Filters

The effects of manufacturing process parameters on water flow rate of the cylinder-shaped filters were examined. Experimental study was conducted to evaluate the physical properties and performance of the 3D printed filters and the results were benchmarked with the performance of the filters made by conventional process.

A.2.1 Preliminary Trials

To examine the feasibility of manufacturing 3D printed filter prototypes (Hollow cylinder-shaped), a 70:30 AC-UHMWPE composite powder was selected for the preliminary trials (Sample ID: ACF-PE30-117.5-8-V). Cylinder-shaped AC filters with a height of 50mm and outer and inner diameters of 40mm and 10mm respectively, were manufactured successfully. Figure A.2 shows the first of its kind 3D printed AC water filters that have been manufactured successfully using laser sintering.

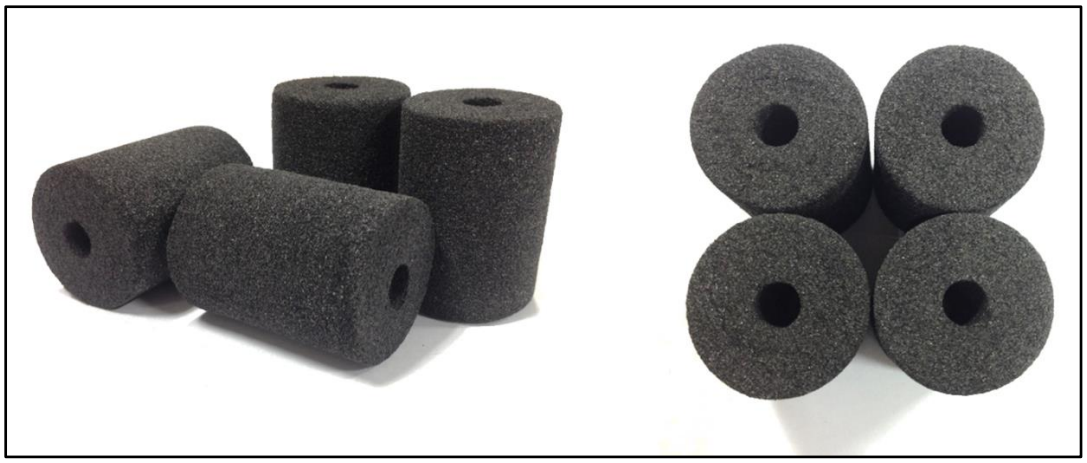

Figure A.2 : 3D printed AC filters manufactured using laser sintering

The physical properties and performance of 3D printed filters were measured and compared with the filters made by conventional process. The effect of activated carbon particle size (IAC and PAC) on the properties and performance of the filters made by conventional process were also evaluated and benchmarked with 3D printed filters.

Figure A.3 shows that the bulk density of the 70:30 AC-UHMWPE filter is similar to that of AC filters manufactured by the conventional process with an average density of 0.47 g/cm^3, approximately. Unlike the bulk density, the porosity measurement shows that the laser sintered 70:30 AC-UHMWPE filters have lower values of porosity with an average of 41% compared to that of the AC filters, 47%, as shown in Figure A.4. The higher content of the UHMWPE binder has contributed to the low porosity values of the 3D printed filters.

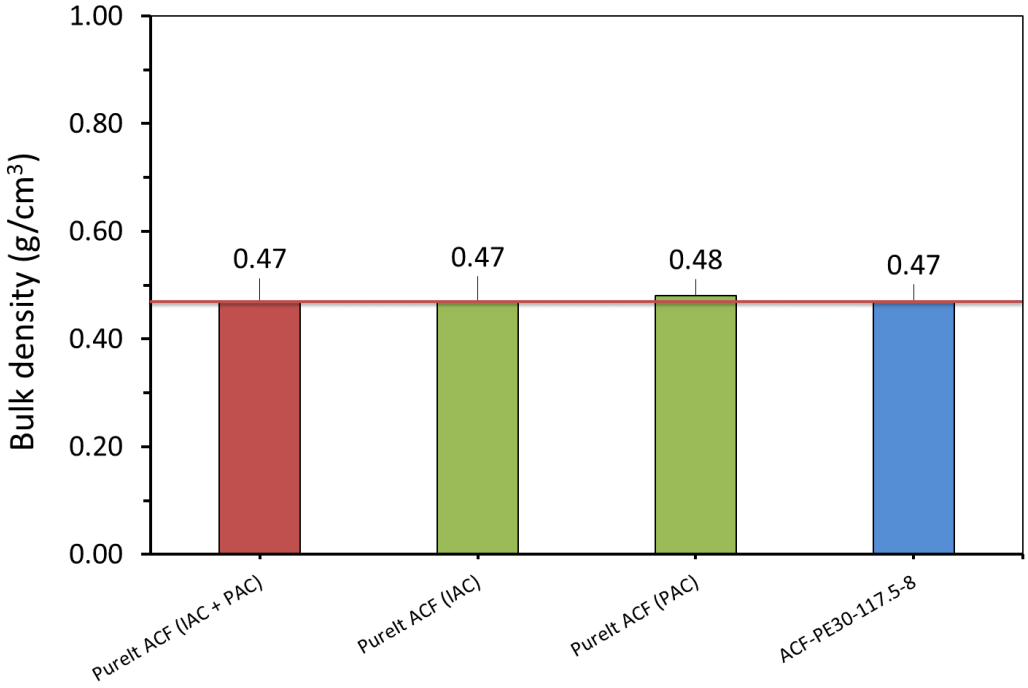

Figure A.3 : Bulk density of 3D printed filter compared to filters made by conventional process

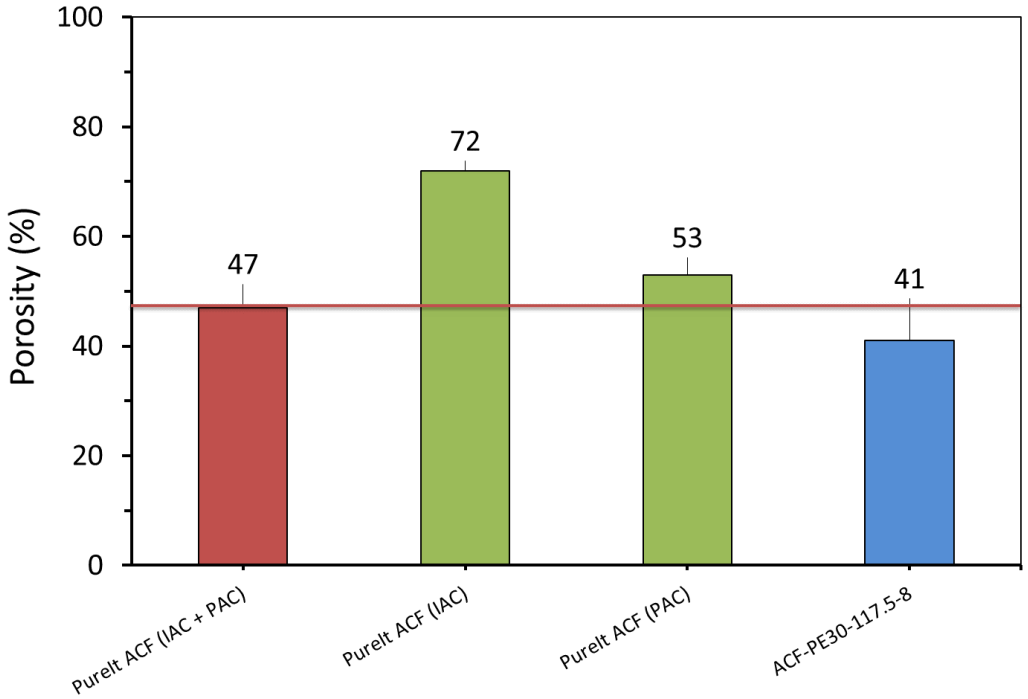

Figure A.4 : Porosity of 3D printed filter compared to filters made by conventional process

Figure A.5 shows that the average water flow rate of the 3D printed filters is lower than that of the AC filters made by the conventional process.

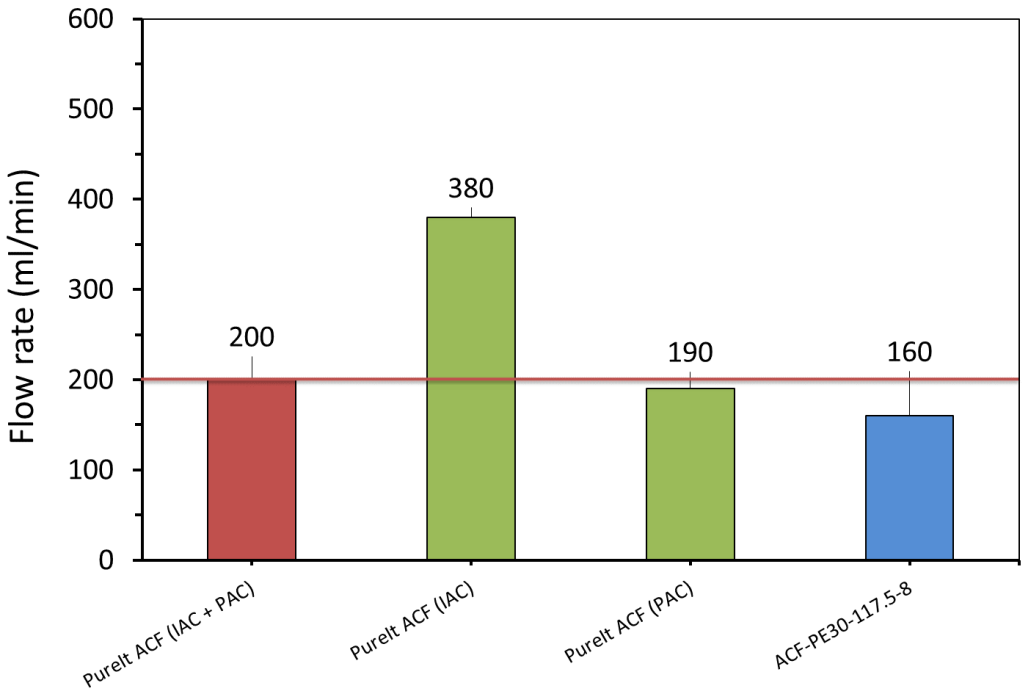

Figure A.5 : Water flow rate of 3D printed filter compared to filters made by conventional process

The results reveal that the flow of the 3D printed filters with 30% UHMWPE is approximately 16% lower than that of the filters with 80:20 PAC-UHMWPE, and the standard filters with 80:20 (IAC + PAC)-UHMWPE (mixture of 50% IAC and 50% PAC). The results also show that the filters with 80:20 IAC-UHMWPE have higher flow rate which was attributed to the larger particle size and higher porosity.

It is possible that the higher content of the UHMWPE binder has contributed to the low flow rate of the 3D printed 70:30 AC-UHMWPE filters. This result was expected since UHMWPE is a hydrophobic material. However, the main aim of this trial was to build a mechanically strong filters and determine whether the water flows successfully through the new 3D printed filters manufactured by laser sintering process. These objectives were achieved and

subsequent sections will show the performance of the filters with a smaller level of UHMWPE.

Figure A.6 shows that the 3D printed filters and the activated carbon filters made by conventional process have a similar turbidity removal efficacy. It was also observed that the turbidity removal of the PAC filters was slightly higher (by approximately 3.9-5.4%) compared to the turbidity removal of the other three filters. The smaller particles of activated carbon powder tend to have significantly higher surface area compared to the larger particles, thus offering larger surface area for adsorption and improving the turbidity of the filtrate.

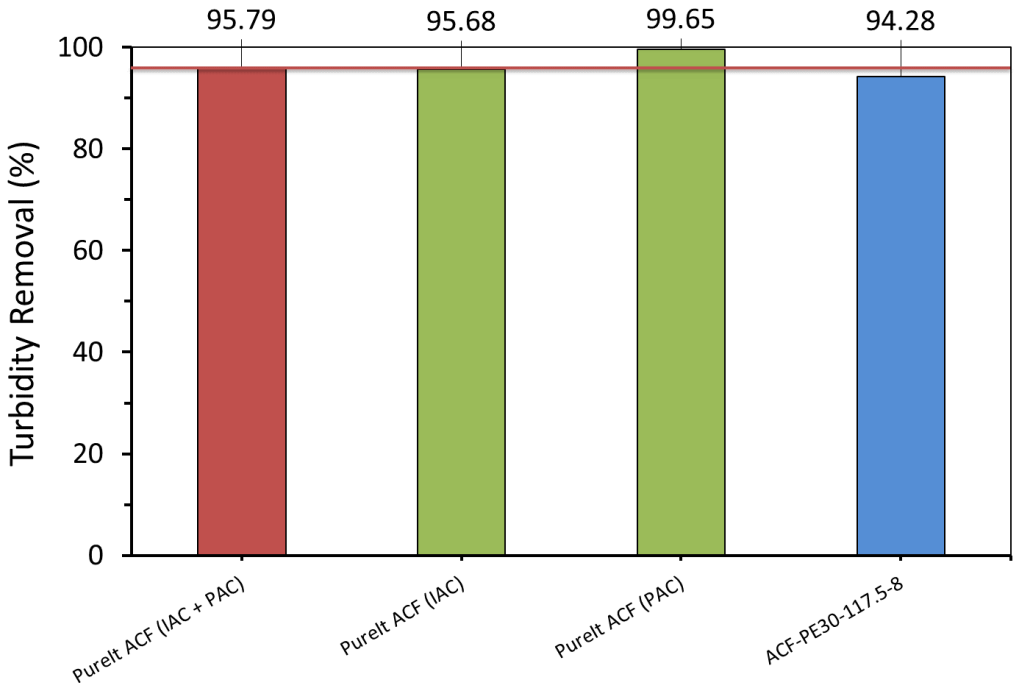

Figure A.6 : Turbidity removal of 3D printed filter compared to filters made by conventional process

A.2.3 Effect of Laser Power on Physical Properties and Performance of 3D Printed Filters

After successfully manufacturing 3D printed filters with a 70:30 AC-UHMWPE composite powder, new filters from 80:20 AC-UHMWPE powder were also

manufactured at laser powers of 8 and 12 watts and a bed temperature of 120°C (Samples ID: ACF-PE20-120-8-V and ACF-PE20-120-12-V)

The effect of the laser power on the physical properties and performance of the laser sintered filters is shown in Table A.1, Figure A.7, Figure A.8, Figure A.9 and Figure A.10.

Table A.1 : Properties and performance of 3D printed filters compared to the filters manufactured by conventional process

Properties and Performance	Unit	Conventional Process		3D Printing Process	
		IAC + PAC	PAC	ACF – 01*	ACF – 02*
Binder (UHMWPE)	w/w %	20	20	20	20
Bulk Density	g/cm^3	0.47	0.48	0.49	0.48
Porosity	%	47	53	76	68
Flow Rate	mL/min	200	190	320	360
Flow Rate	L/h	12	11.4	19.2	21.9
Turbidity Removal	%	95.79	99.65	98.49	90.98

** Samples denoted as ACF-01 and ACF-02 represent samples ACF-PE20-120-8-V and ACF-PE20-120-12-V, respectively.*

The results in Figure A.7 show that both 3D printed filters have similar bulk density compared to that of the filters made by the conventional process with an average of approximately 0.48 g/cm^3. The change in laser power from 8 watts to 12 watts does not show a significant change in bulk density.

However, the porosity of the laser sintered filters is higher than that of the filters manufactured by conventional process as shown in Figure A.8. The porosity of the sintered filters produced at laser powers of 8 and 12 watts was 76% and 68%, respectively while the porosity of the standard (IAC + PAC) and PAC filters was 47% and 53%, respectively. The laser sintered filter produced

at laser power of 8 watts exhibits an increase in porosity by 38% and 30% compared to the standard (IAC + PAC) and PAC filters, respectively.

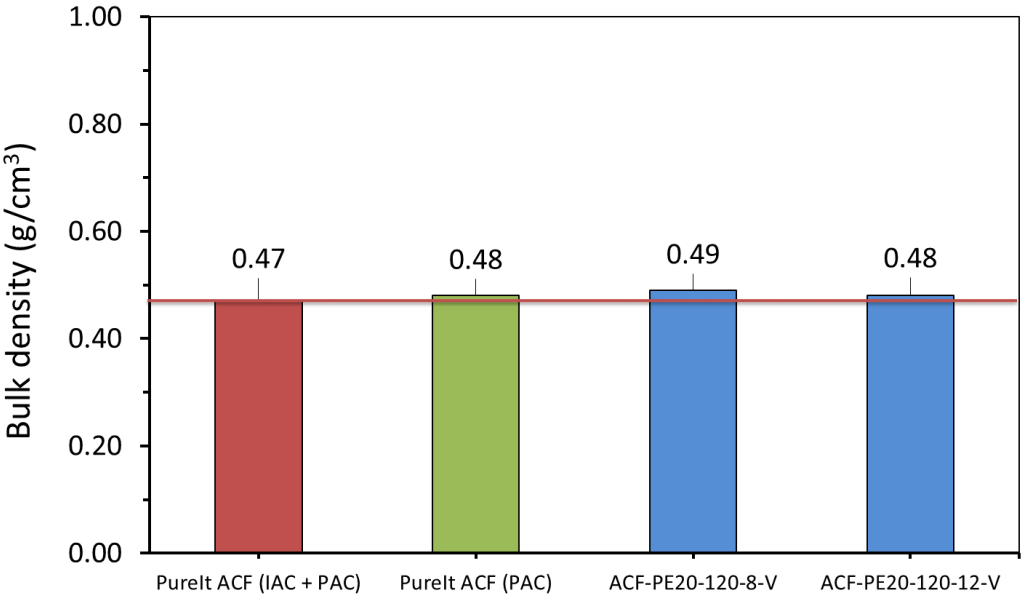

Figure A.7 : Effect of laser power on bulk density of 3D printed filters

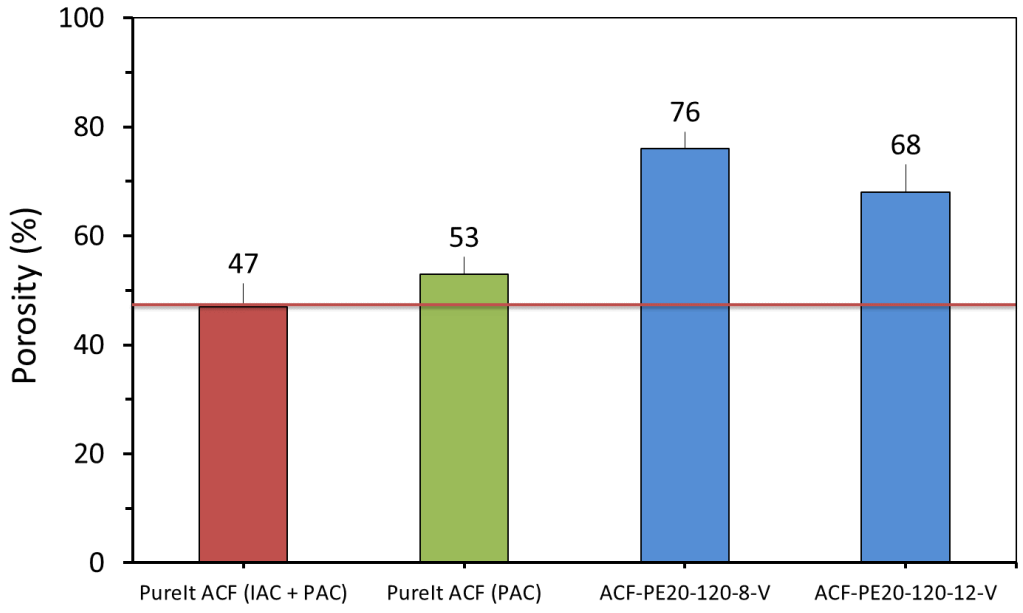

Figure A.8 : Effect of laser power on porosity of 3D printed filters

The porosity of the sintered filters produced at a laser power of 8 watts was higher than that of the sintered filters produced at a laser power of 12 watts by approximately 10.5%. This result indicates that the porosity decreases with increasing of the laser powder. Higher energy density combined with the thermal energy stored during the long build time for these filters, providing sufficient heat to completely melt and fuse the binding powder, thus reducing the porosity.

Figure A.9 shows that the water flow rate of the 3D printed filters is considerably higher than that of AC filters made by the conventional process.

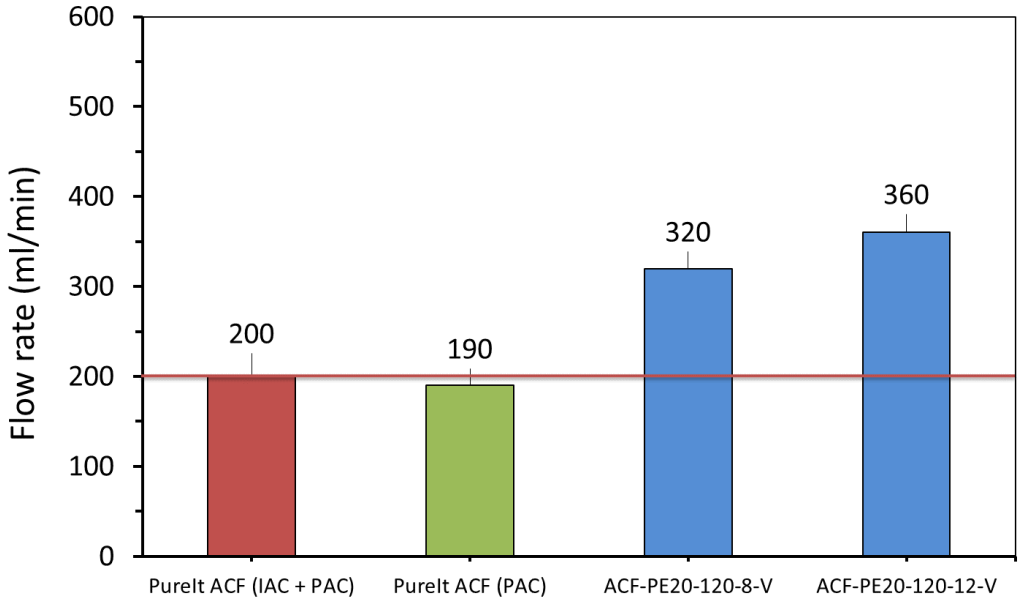

Figure A.9 : Effect of laser power on water flow rate of 3D printed filters

The flow rate of the sintered filters produced at laser powers of 8 and 12 watts was 320 and 360 mL/min, respectively while the flow rate of the standard (IAC + PAC) and PAC filters was 200 and 190 mL/min, respectively. The laser sintered filter produced at laser power of 12 watts exhibits an increase in flow rate by approximately 44% and 47% compared to the standard (IAC + PAC) and PAC filters, respectively.

The flow rate of the sintered filters produced at a laser power of 12 watts was higher than that of the sintered filters produced at a laser power of 8 watts by approximately 11%. This result indicates that the laser power has an influence on the flow rate of water and the flow increases with increasing of the laser powder.

Figure A.10 shows that the 3D printed filters and the AC filters made by conventional process have a similar turbidity removal efficacy. However, it was observed that the turbidity removal of the sintered filter produced at a laser power of 12 watts has a lower turbidity removal, by approximately 8%, compared to that of the sintered filter produced at a laser power of 8 watts. This result indicates that the turbidity removal decreases with increasing the laser power.

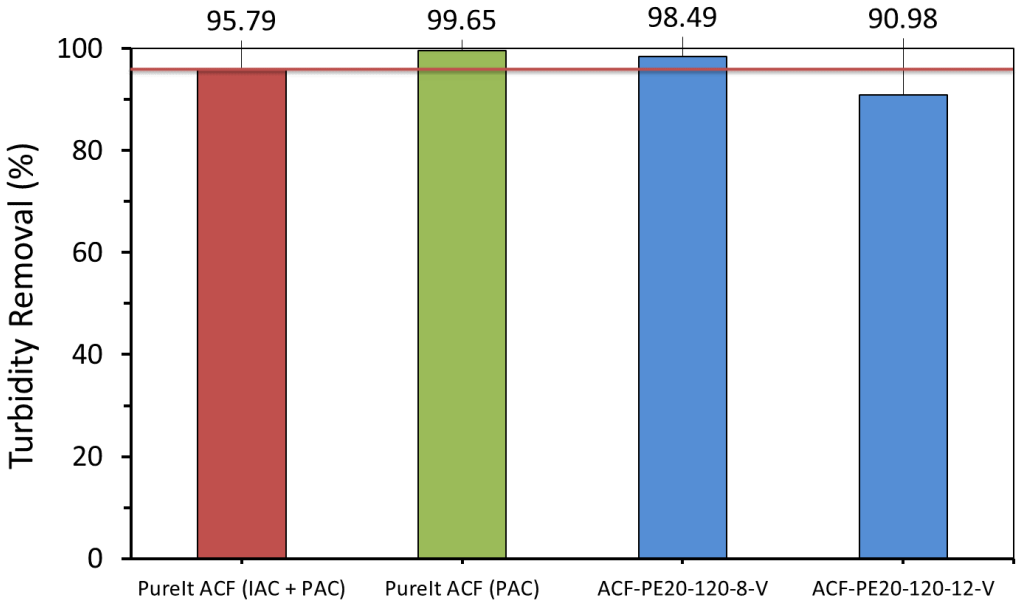

Figure A.10 : Effect of laser power on turbidity removal of 3D printed filters

A.2.4 Effect of Bed Temperature and Orientation on Physical Properties and Performance of 3D Printed Filters

The effect of the bed temperature and orientation of filters in the part bed on the physical properties and performance of the laser sintered filters are shown in Figure A.11, Figure A.12, A.13 and A.14. To make it easier to compare to previous section, the Pureit ACF and ACF-PE20-120-12-V were reproduced in these figures.

The 3D printed filters manufactured with different bed temperatures and in different building orientations show no significant differences in the density values (Figure A.11). The results show that the 3D printed filters have similar bulk density to that of the filters made by the conventional process with an average of approximately 0.47 g/cm^3.

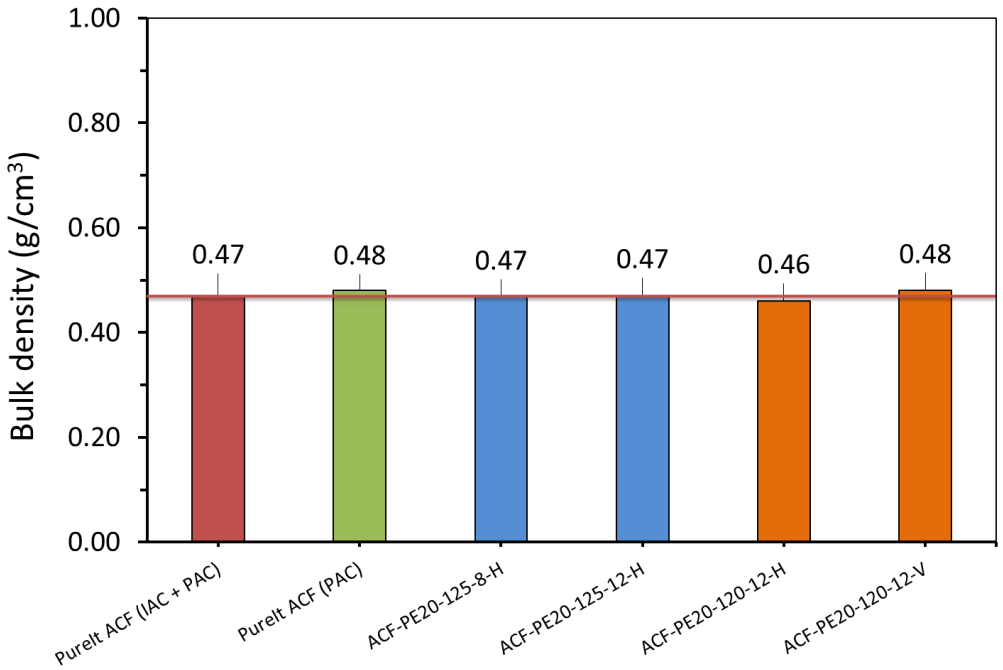

Figure A.11 : Effect of laser power, bed temperature and part orientation on bulk density of 3D printed filters

Unlike the density, the porosity of the 3D printed filters appeared to be higher than that of the filters manufactured by conventional process (Figure A.12).

The average porosity of the sintered filters was 68.5 ±1.29%, while the porosity of the standard (IAC + PAC) and PAC filters was 47% and 53%, respectively. The result of the porosity measurements of the 3D printed filters, produced at different bed temperatures, does not show a significant increase or decrease in porosity. The porosity increased by 1.4% when the bed temperature increased from 120°C to 125°C. Filters produced with a bed temperature of 125°C and a laser power of 12 watts induce higher porosity of 70% and increased by 4.3% compared to that of the filters produced at the same bed temperature but with a laser power of 8 watts (67%). This result indicates that a higher energy input may lead to a polymer degradation and hence the slight increase in porosity.

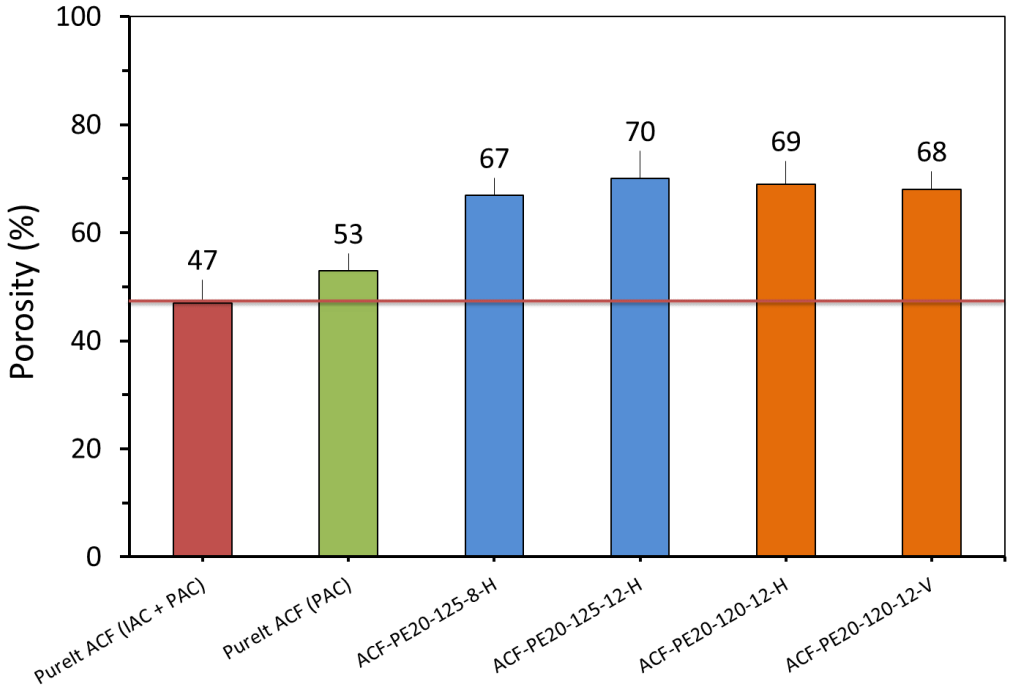

Figure A.12 : Effect of laser power, bed temperature and part orientation on porosity of 3D printed filters

The result of the flow test (Figure A.13) shows that filters produced with a bed temperature of 125°C and a laser power of 12 watts induce higher flow rate compared to the filters produced at the same laser power but with a bed temperature of 120°C. This increase was approximately 3%.

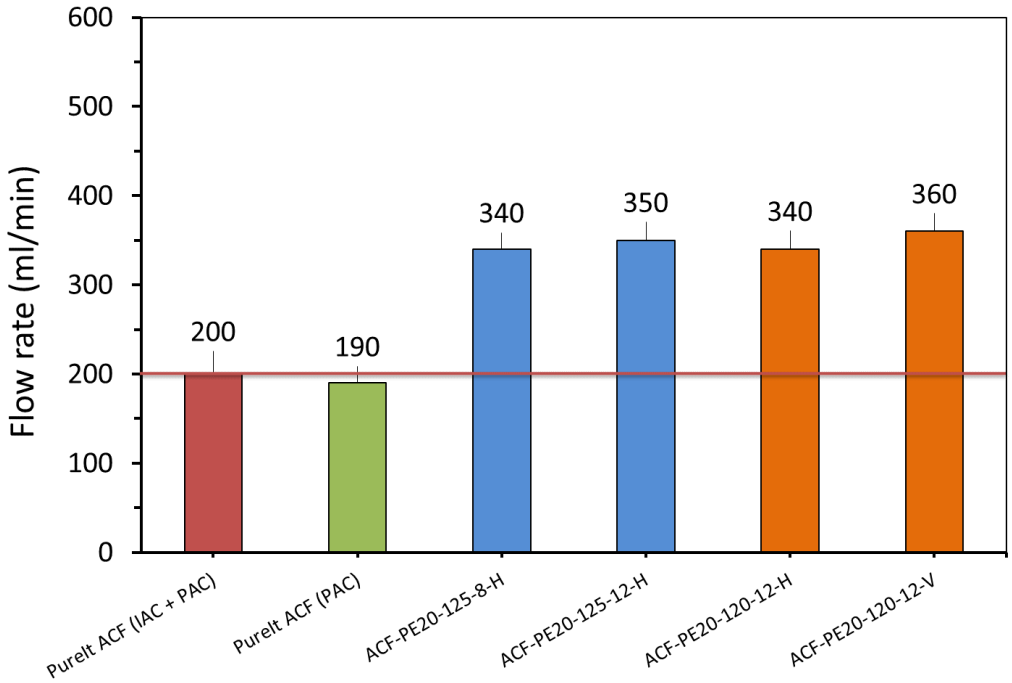

Figure A.13 : Effect of laser power, bed temperature and part orientation on flow rate of 3D printed filters

The result also shows that the flow rate of the sintered filters oriented vertically in the part bed was higher than that of the sintered filters produced horizontally by approximately 5.56%. This is possibility due to the increased number of layers for vertically produced filters. Insufficient bonding between these layers as well as the reduction in the degree of necking between particles at the borders between these layers may increase porosity and leads to a higher flow rate.

Figure A.14 shows that the sintered filters produced horizontally (Sample ID: ACF-PE20-120-12-H) resulted better turbidity removal over vertical orientation (Sample ID: ACF-PE20-120-12-V) for fixed laser power and bed temperature. The turbidity removal of the horizontally oriented filters was higher by approximately 7%, compared to that of the vertically oriented filters.

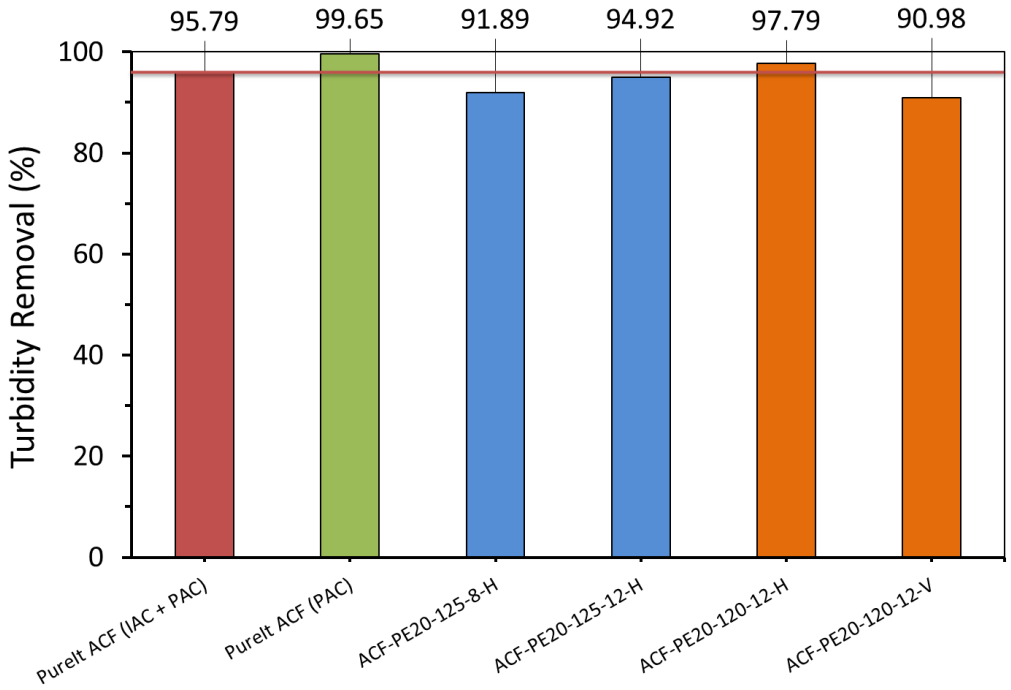

Figure A.14 : Effect of laser power, bed temperature and part orientation on turbidity removal of 3D printed filters

In the right circular cylinder filters (tube-shaped), the flow of the water is directed in a radial direction through the wall of the filter (either outwardly or inwardly). Therefore, the water can flow faster between the layers, with a highly porous area, in the vertically oriented filters, whereas in the horizontally oriented filters, the water flows throw the layers where the surface area of filtration is increased (Figure A.15). This is possibly why the turbidity removal was improved in the case of the horizontally oriented filters.

The result also shows that sintering at a lower bed temperature resulted a marginal better turbidity removal for a fixed laser power and orientation (Sample ACF-PE20-120-12-H vs Sample ACF-PE20-125-12-H). As indicated earlier that a higher energy input (in this case, high bed temperature), may lead to a polymer degradation that contributes to a higher porosity and larger pore size. Subsequently, a low turbidity removal could be achieved.

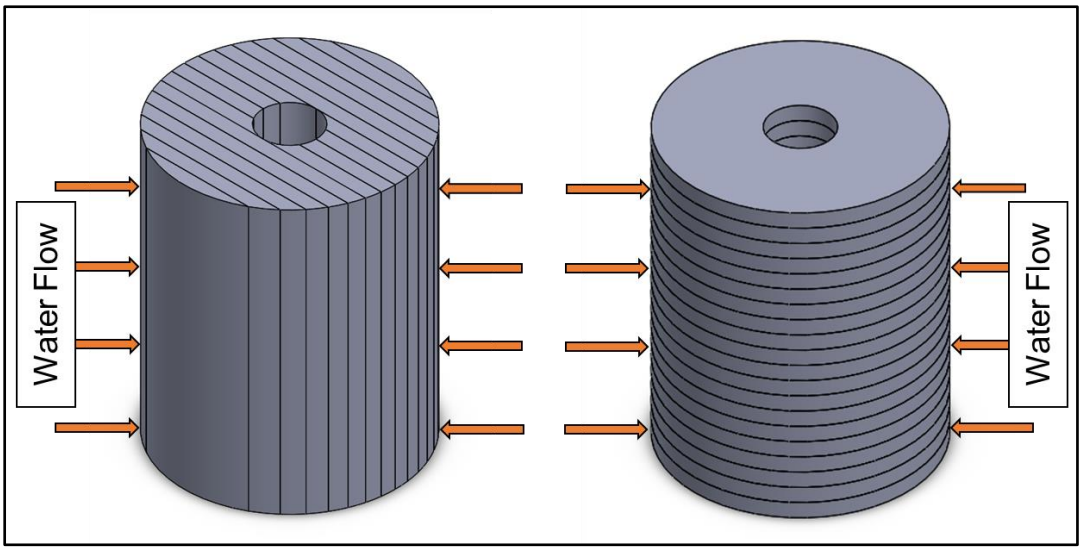

Figure A.15 : Schematic representation of the radial water flow through the 3D printed filters, which were produced horizontally (left) and vertically (right)

A.2.5 Effect of Laser Gradient and Orientation on Physical Properties and Performance of 3D Printed Filters

The results presented in Figure A.16 show that the 3D printed filters have a similar bulk density to that of the filters made by the conventional process with an average density of approximately 0.48 g/cm^3.

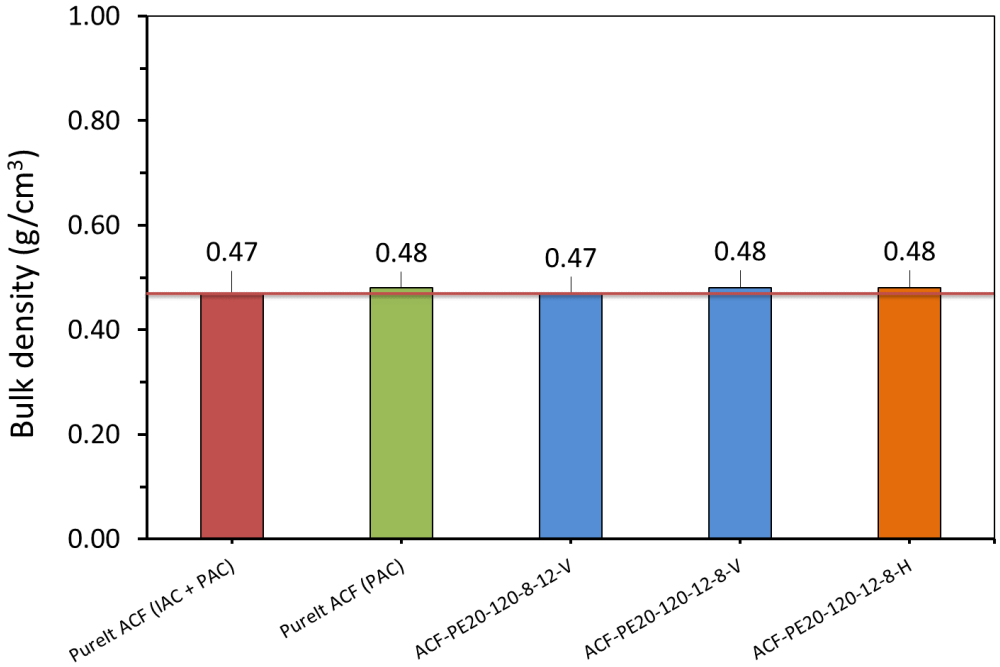

Figure A.16 : Effect of laser gradient and orientation on bulk density of 3D printed filters compared to filters made by conventional process

The 3D printed filters manufactured with different laser gradients and in different building orientations show no significant differences in the density values.

Figure A.17 shows that the porosity of the 3D printed filters is higher than that of the filters manufactured by conventional process. The average porosity of the sintered filters was 74 ±1% and the results indicated that no significant changes in porosity occurred for the three filters. Filters produced with the same orientation but with different laser gradients show a marginal porosity difference of 2.6% (Sample ACF-PE20-120-8-12-V vs Sample ACF-PE20-120-12-8-V). While filters produced with different orientation but with the same laser gradients show a marginal porosity difference of 1.35% (Sample ACF-PE20-120-12-8-V vs Sample ACF-PE20-120-12-8-H).

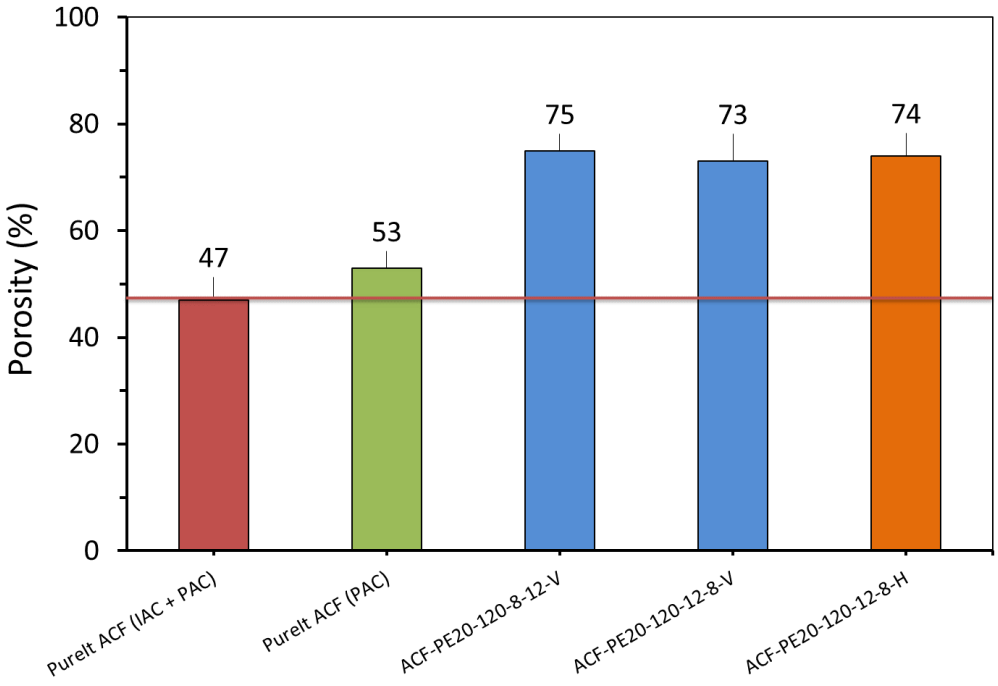

Figure A.17 : Effect of laser gradient and orientation on porosity of 3D printed filters compared to filters made by conventional process

Figure A.18 shows that the water flow rate of the 3D printed filters is higher than that of AC filters made by the conventional process. The flow rates of the

sintered filters produced at fixed laser powers with vertical and horizontal orientation were 320 and 280 mL/min, respectively (Samples ACF-PE20-120-12-8-V and ACF-PE20-120-12-8-H). Filters produced with the same orientation but with different laser gradients show a significant flow rate difference of 12% (Sample ACF-PE20-120-8-12-V vs Sample ACF-PE20-120-12-8-V). The sample filter "ACF-PE20-120-8-12-V" exhibits an increase in flow rate by approximately 45% and 48% compared to the standard (IAC + PAC) and PAC filters, respectively.

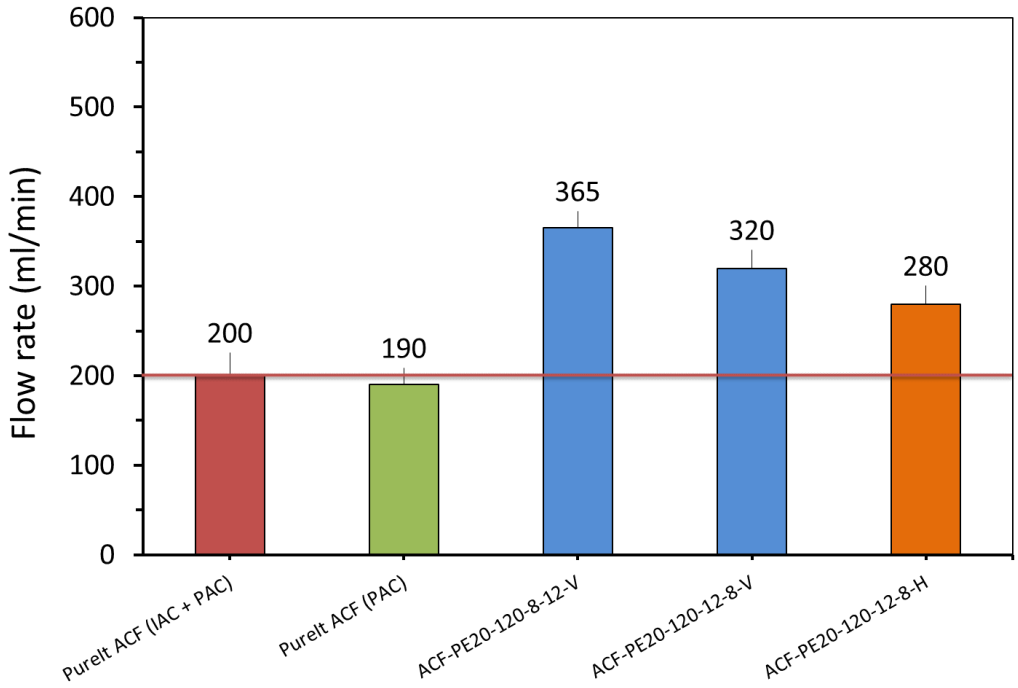

Figure A.18 : Effect of laser gradient and orientation on water flow rate of 3D printed filters compared to filters made by conventional process

The results indicate that the flow rate of the filters produced with an inner shell sintered at laser power of 8 watts and an outer shell sintered at 12 watts is higher than that of the filters produced with an inner shell sintered at laser power of 12 watts and an outer shell sintered at 8 watts. This is possibly due to the larger pore size created at laser power of 12 watts which allows more water to flow through the filter wall.

Figure A.19 shows that the turbidity removal of the 3D printed filters and the AC filters made by conventional process are in a similar range. Filters produced with the same orientation but with different laser gradients show a marginal turbidity removal difference of 1.34% (Sample ACF-PE20-120-8-12-V vs Sample ACF-PE20-120-12-8-V). Filters produced at fixed laser powers with vertical and horizontal orientation show the similar turbidity removal (Samples ACF-PE20-120-12-8-V and ACF-PE20-120-12-8-H).

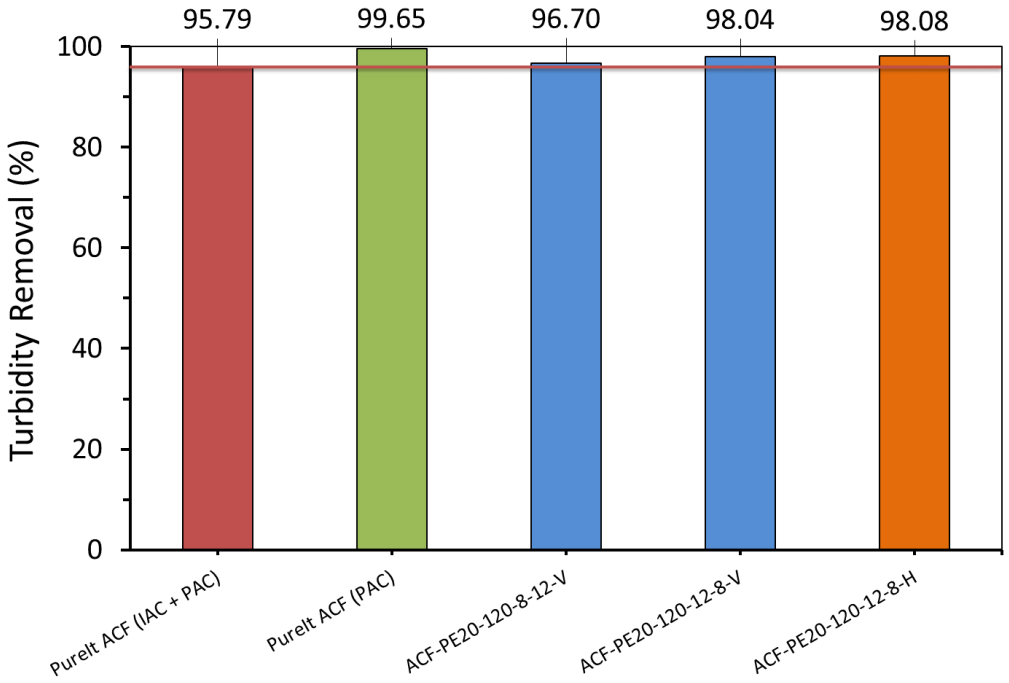

Figure A.19 : Effect of laser gradient and orientation on turbidity removal of 3D printed filters compared to filters made by conventional process

A.2.6 Feasibility of Manufacturing 3D Printed Filters from Used Powder

When a build is completed, the filters and surrounding supporting material in the part bed (known as the "part cake"), are removed from the laser sintering machine. The filters are then removed from the part cake and the loose powder is brushed off. Un-consolidated powder by the laser can be sieved and reused for subsequent builds. In this study, 3D printed filters were manufactured successfully from 100% used powder of 80:20 AC-UHMWPE composite. The physical properties and performance of these filters were

measured and compared with 3D printed filters made from 100% virgin powder and with the filters made by conventional process.

Figure A.20 shows that the bulk density of the filters made from 100% used powder is slightly higher than that of 3D printed filters made from 100% virgin powder and the AC filters manufactured by the conventional process. The average density of these 3D printed filters was 0.51 ±0.02 g/cm^3. Compared to that of the standard (IAC + PAC) and PAC filters manufactured by the conventional process, the average densities were 0.485 g/cm^3 and 0.475 g/cm^3, respectively. This result indicates that the thermal history has slightly impacted the bulk density of the filters made from 100% used powder.

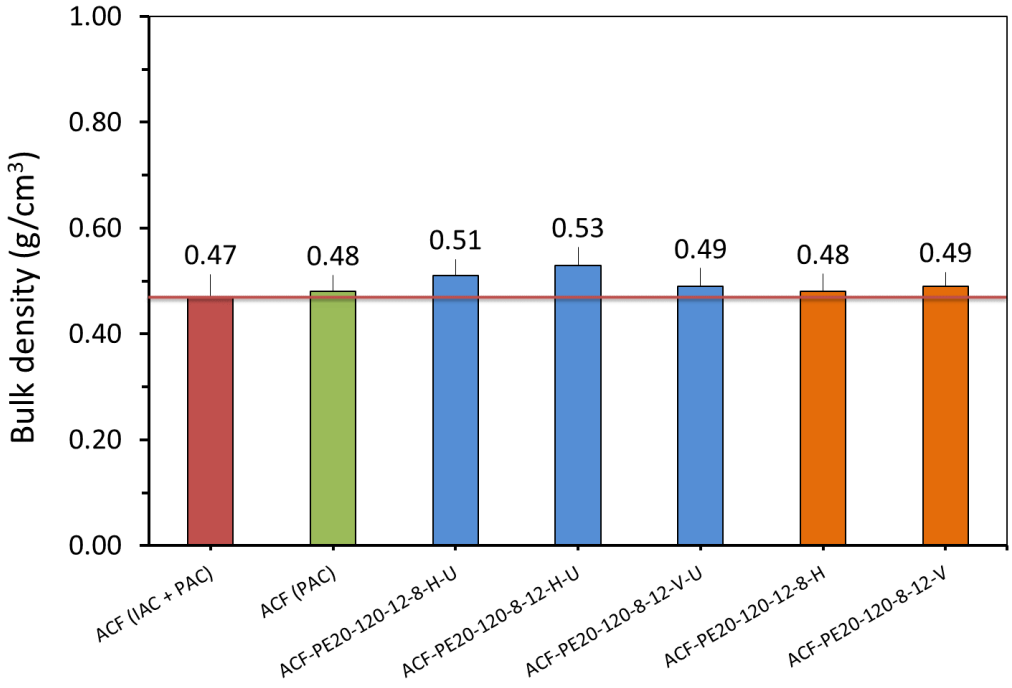

Figure A.20 : Bulk density of 3D printed filters made from 100% virgin powder and 100% used powder compared to filters made by conventional process

Figure A.21 shows that the porosity of the 3D printed filters made from used powder is similar to that of the filters made from virgin powder with an average porosity of 75 ±1.7% and 74.5 ±0.7%, respectively.

The results indicated that no significant changes in porosity occurred after re-using the powder for subsequent build. Filters produced horizontally with the same laser power and bed temperature show a marginal porosity difference of 2.6% (Sample ACF-PE20-120-12-8-H-U vs Sample ACF-PE20-120-12-8-H) and filters produced vertically show a difference of 1.3% (Sample ACF-PE20-120-8-12-V-U vs Sample ACF-PE20-120-8-12-V). Filters produced from used powder with a different orientation and the same laser power and bed temperature show a marginal porosity difference of approximately 4% (Sample ACF-PE20-120-8-12-H-U vs Sample ACF-PE20-120-8-12-V-U).

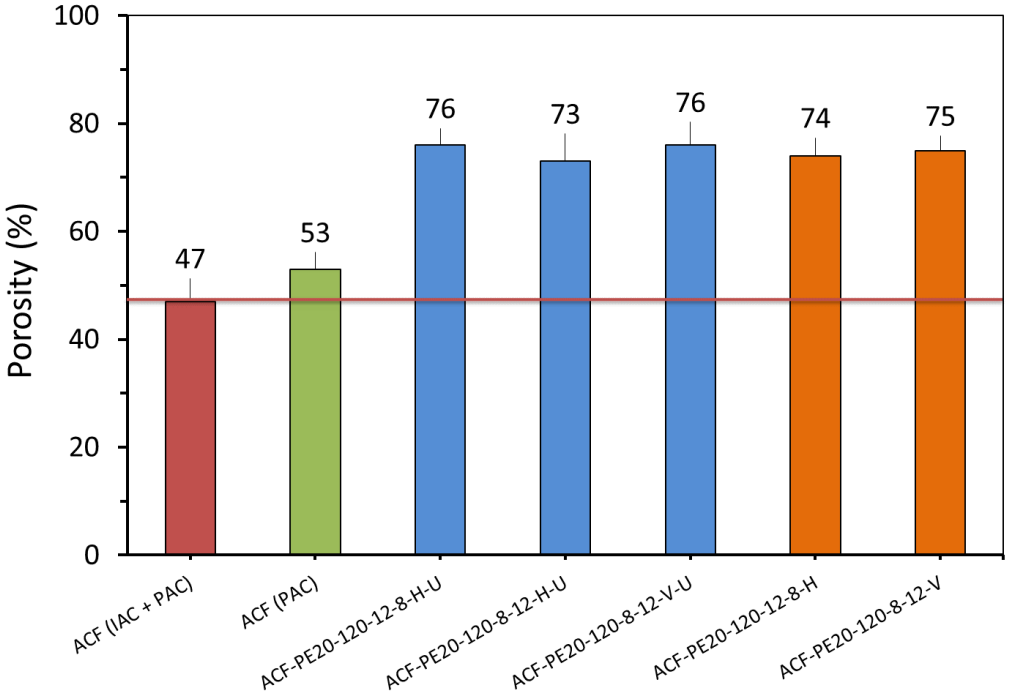

Figure A.21 : Porosity of 3D printed filters made from 100% virgin powder and 100% used powder compared to filters made by conventional process

A.22 shows the water flow rate test results of the 3D printed filters made from virgin and used powders and also the AC filters made by the conventional process.

Filters made from used powder show low flow characteristics, compared to that of the filters made from virgin powder. This decrease is probably due to a high bulk density.

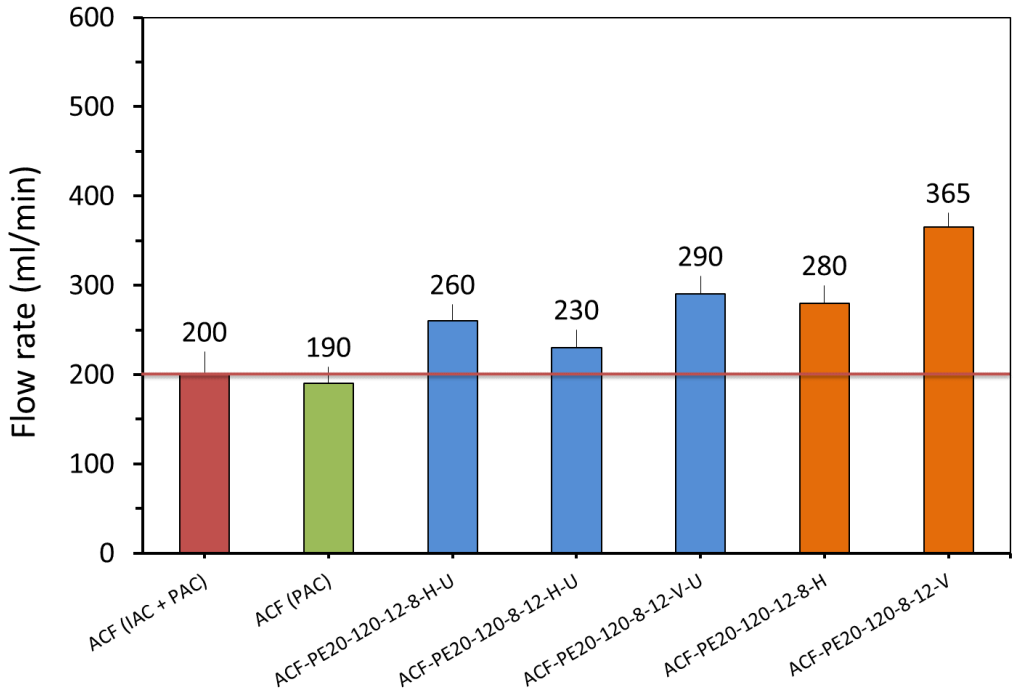

Figure A.22 : Water flow rate of 3D printed filters made from 100% virgin powder and 100% used powder compared to filters made by conventional process

Filters produced horizontally with the same laser power and bed temperature show a marginal water flow difference of approximately 7% (Sample ACF-PE20-120-12-8-H-U vs Sample ACF-PE20-120-12-8-H). Filters produced vertically show a water flow difference of approximately 20.5% (Sample ACF-PE20-120-8-12-V-U vs Sample ACF-PE20-120-8-12-V). Filters produced from used powder with different orientations and the same laser power and bed temperature show a marginal water flow difference of approximately 20.7% (Sample ACF-PE20-120-8-12-H-U vs Sample ACF-PE20-120-8-12-V-U).

Figure A.23 shows that the turbidity removal of the 3D printed filters made from used powder and compared to the filters made of virgin powder and the AC filters made by conventional process.

The highest turbidity removal efficiency of the 3D printed filters made from used powder was 99.54% (Sample ACF-PE20-120-8-12-H-U), while the lowest was 99.25% (Sample ACF-PE20-120-12-8-H-U).

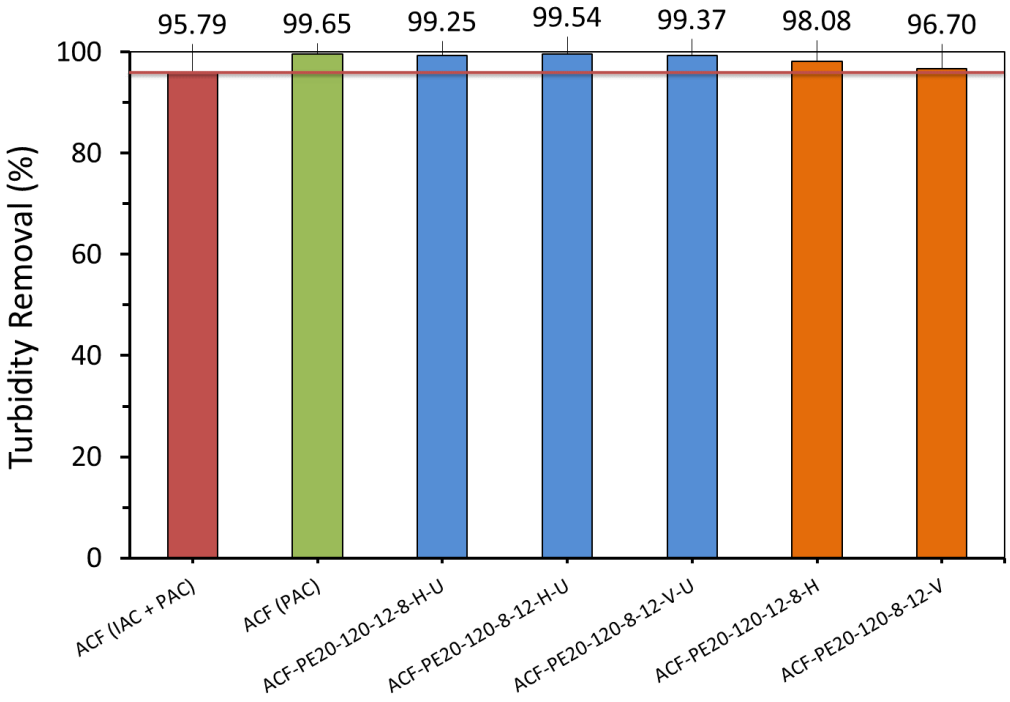

Figure A.23 : Turbidity removal of 3D printed filters made from 100% virgin powder and 100% used powder compared to filters made by conventional process

The result shows that filters produced horizontally from used powder resulted a marginal better turbidity reduction of approximately 1.2% compared to that of the 3D printed filters made from virgin powder (Sample ACF-PE20-120-12-8-H-U vs Sample ACF-PE20-120-12-8-H).

Filters produced vertically show a better turbidity removal of approximately 2.7% (Sample ACF-PE20-120-8-12-V-U vs Sample ACF-PE20-120-8-12-V). This can be due to the higher bulk density resulting from re-using the powder. The results clearly indicate that the turbidity removal efficiency of the filters made from used powder has not been affected by the powder condition. However, this result may change negatively if the used powder is used again in subsequent build.

A.2.7 Repeatability

Repeatability and consistency of the manufactured parts are critical and one of the key needs in any manufacturing process. Repeatability and consistency

of the produced parts are one of challenges which remain major concerns in AM processes [41, 89, 216]. Therefore, it is very important requirement that the 3D printed filters are produced with minimal variations in physical properties and performances, with a high level in repeatability of the results.

In this work, the repeatability was examined by producing more than one filter in separate builds, but with the same set of processing parameters and conditions (ACF-PE20-120-12). The physical properties and performance were then compared and benchmarked with the filters made by conventional process.

The results of the physical properties and performance of the laser sintered filters produced with the same processing parameters are presented in Figure A.24, Figure A.25, Figure A.26 and Figure A.27 and compared with the filters produced by the conventional process. As a further comparison, the equivalent vertical build is included.

As shown in Figure A.24, the 3D printed filters manufactured in separate builds show no significant differences in the density values. The results show that the 3D printed filters have similar bulk densities to that of the filters made by the conventional process with an average of approximately 0.48 g/cm^3.

The results presented in Figure A.25 show that the highest porosity achieved was 72% and 69% for the filters manufactured in a horizontal orientation. The lowest porosity was 68% for the filters manufactured in a vertical orientation. While the porosities of the standard (IAC + PAC) and PAC filters were 47% and 53%, respectively.

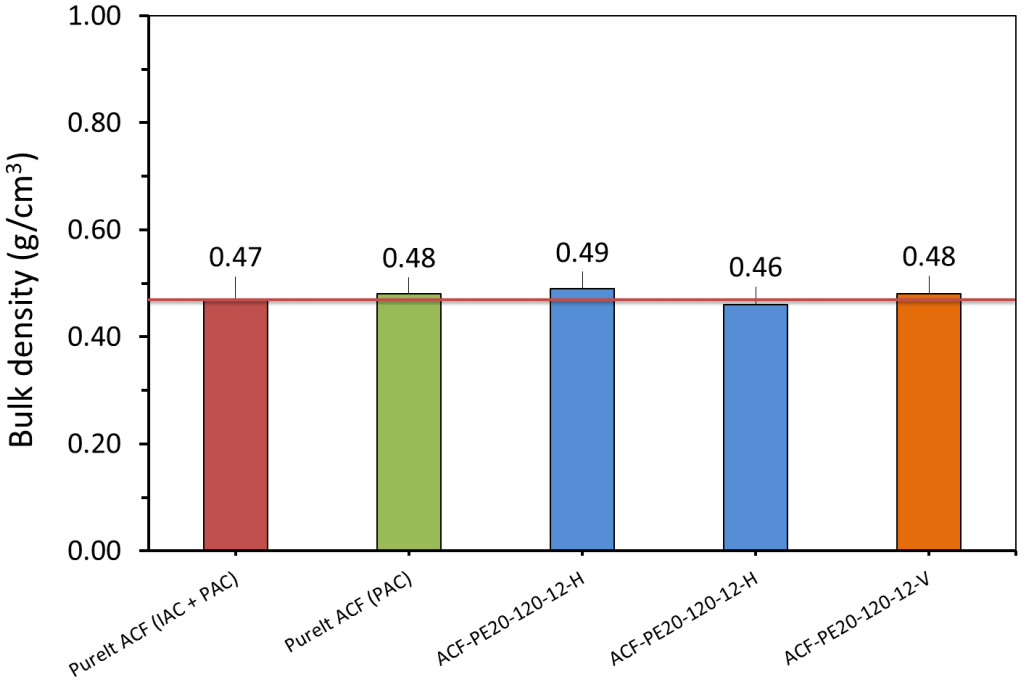

Figure A.24 : Repeatability - Bulk density of 3D printed filters compared to filters made by conventional process

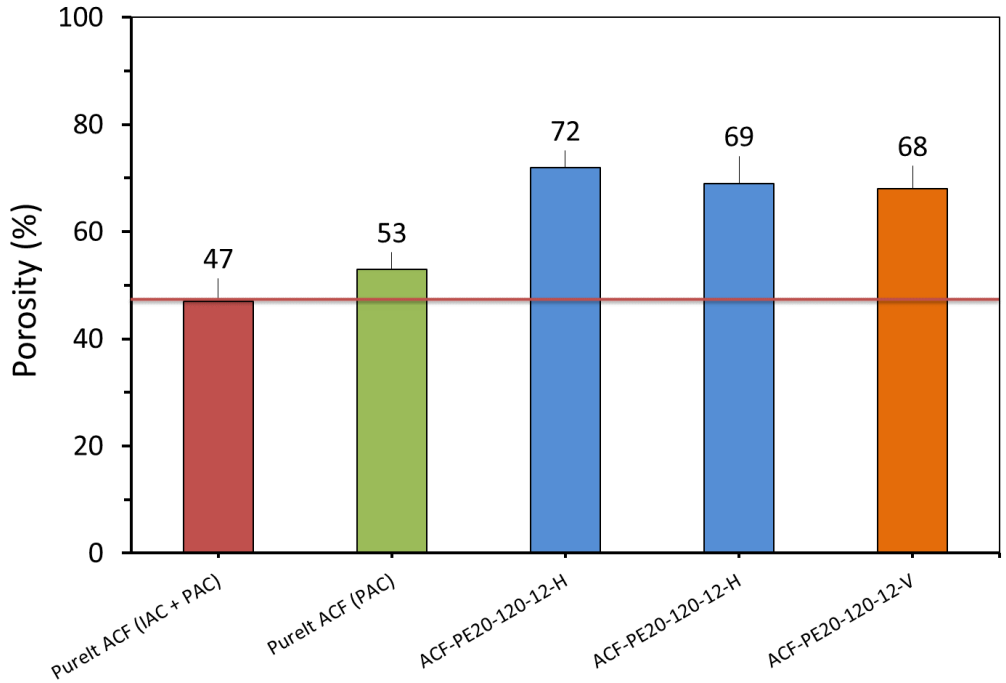

Figure A.25 : Repeatability – Porosity of 3D printed filters compared to filters made by conventional process

The results indicated that the porosity of the laser sintered filters is higher than that of the filters manufactured by conventional process. Additionally, the porosity of the 3D printed filters shows no significant differences between them with an average of 69.67±2.08%.

Figure A.26 shows that different filters exhibit minimal variations in flow rate when produced from the same set of processing parameters and conditions. The laser sintering of 3D printed filters shows highly consistent and reproducible results that can be achieved. As observed before, the flow rate of the vertically produced filters is slightly higher than that of the horizontally produced filters by approximately 5.56%. The vertically produced filters have more layers compared to the horizontally produced filters which can lead to a higher flow rate.

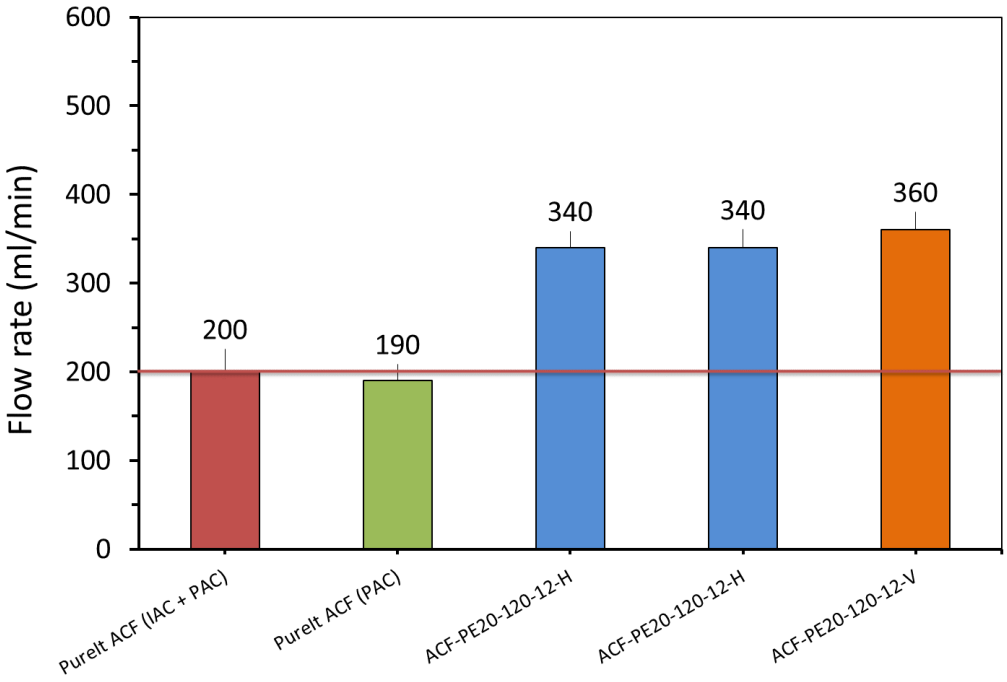

Figure A.26 : Repeatability – Water flow rate of 3D printed filters compared to filters made by conventional process

Figure A.27 shows that a similar turbidity removal efficacy can be achieved when filters are produced at the same processing parameters and conditions. Nevertheless, the sintered filters produced horizontally resulted better

turbidity removal over the vertical filters for the same laser power and bed temperature (Sample ID: ACF-PE20-120-12-H vs Sample ID: ACF-PE20-120-12-V).

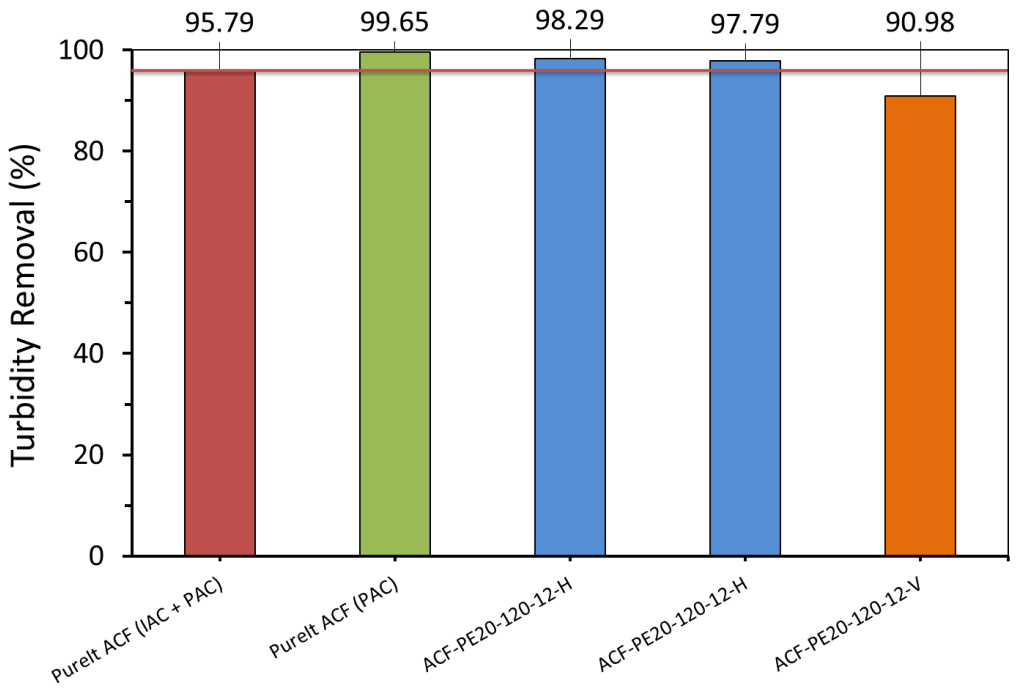

Figure A.27 : Repeatability – Turbidity removal of 3D printed filters compared to filters made by conventional process

A.2.8 Feasibility of Manufacturing 3D Printed Filters with Reduced Binder Content

New filters from 82.5:17.5 AC-UHMWPE powder were manufactured successfully, at laser powers of 8, 12 and 16 watts with a fixed bed temperature of 120°C (Samples ID: ACF-PE17.5-120-8-H, ACF-PE17.5-120-12-H and ACF-PE17.5-120-16-H). All these filters were produced horizontally (shorter manufacturing time).

The effect of laser power on the physical properties and performance of the 3D printed filters are shown in Figure A.28, Figure A.29, Figure A.30 and Figure A.31.

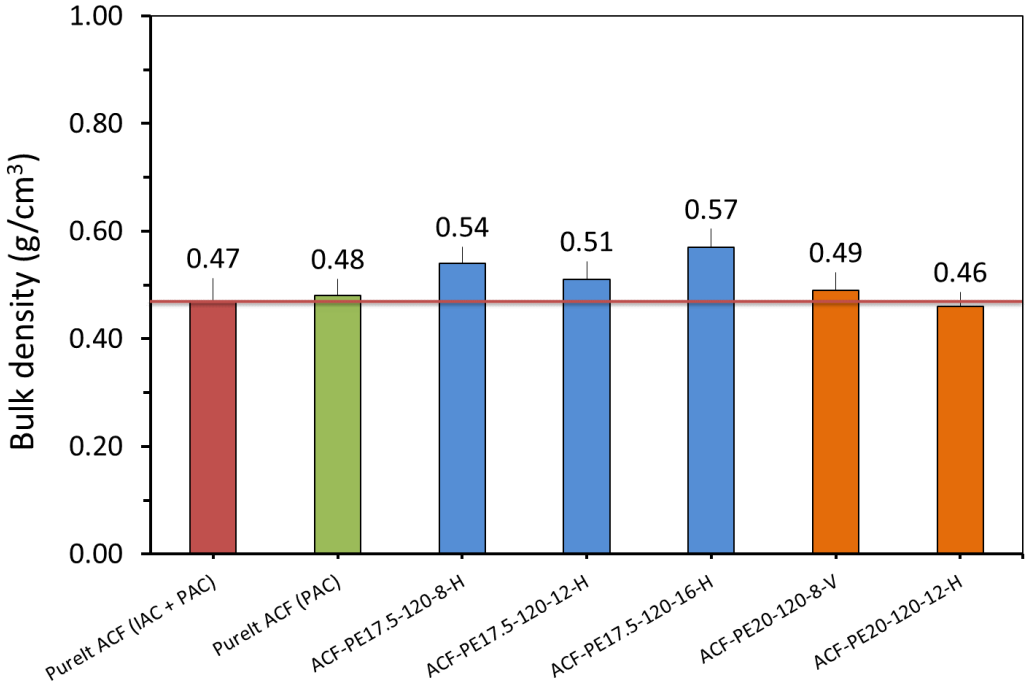

Figure A.28 : Bulk density of 3D printed filters made from 82.5:17.5 and 80:20 AC-UHMWPE compared to filters made by conventional process

The results in Figure A.28 show that all three 3D printed filters with 17.5% UHMWPE have a higher bulk density compared to that of the filters made by the conventional process and the 3D printed filters with 20% UHMWPE. The filters with reduced binder have an average bulk density of approximately 0.54 $\pm$0.03 g/cm^3. This is an increase of approximately 11% compared to that of the filters produced with 20% UHMWPE.

The results of the porosity measurement are shown in Figure A.29. The 3D printed 82.5:17.5 AC-UHMWPE filters produced at different laser powers have higher values of porosity compared to that of the AC filters produced by conventional process. The results also show that the average porosity of the filters with reduced binder is lower by approximately 6% compared to that of the 3D printed filters with 20% UHMWPE. This is possibly due to the higher density of the filters with reduced binder.

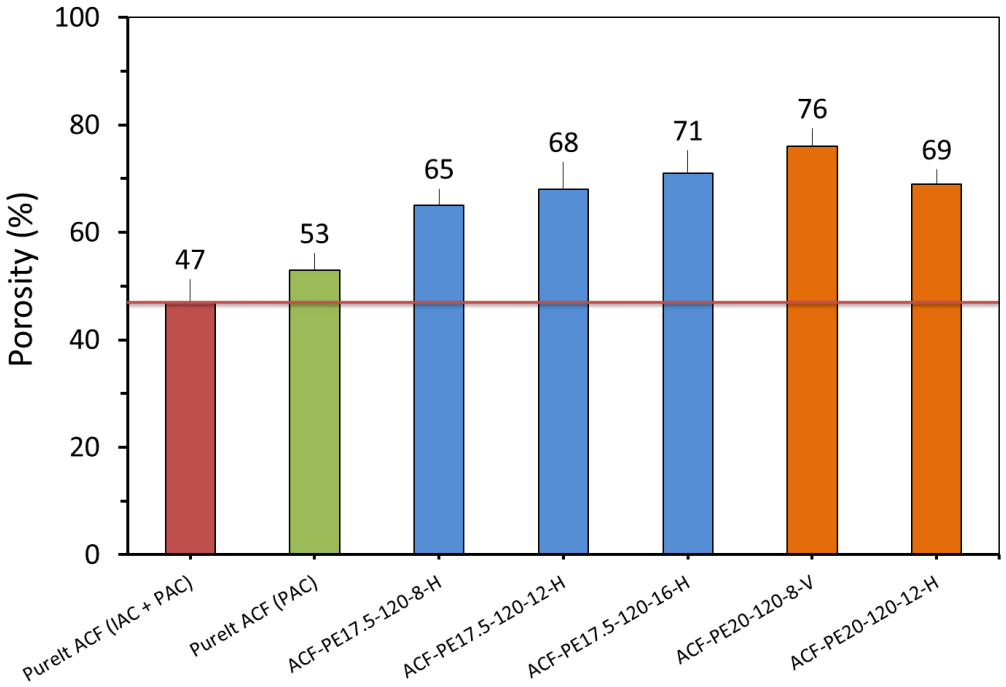

Figure A.29 : Porosity of 3D printed filters made from 82.5:17.5 and 80:20 AC-UHMWPE compared to filters made by conventional process

Figure A.30 shows the average water flow rate of the 3D printed filters with reduced binder (i.e. 17.5% UHMWPE) compared to that of the AC filters made by the conventional process and the 3D printed filters with 20% UHMWPE.

The results reveal that the overall average flow rate of the 3D printed filters with 17.5% UHMWPE is approximately 183±32 mL/min. This value is lower by 3.68% and 8.5% compared to that of the filters produced by conventional process with 80:20 PAC-UHMWPE and the standard 80:20 (IAC + PAC)-UHMWPE, respectively.

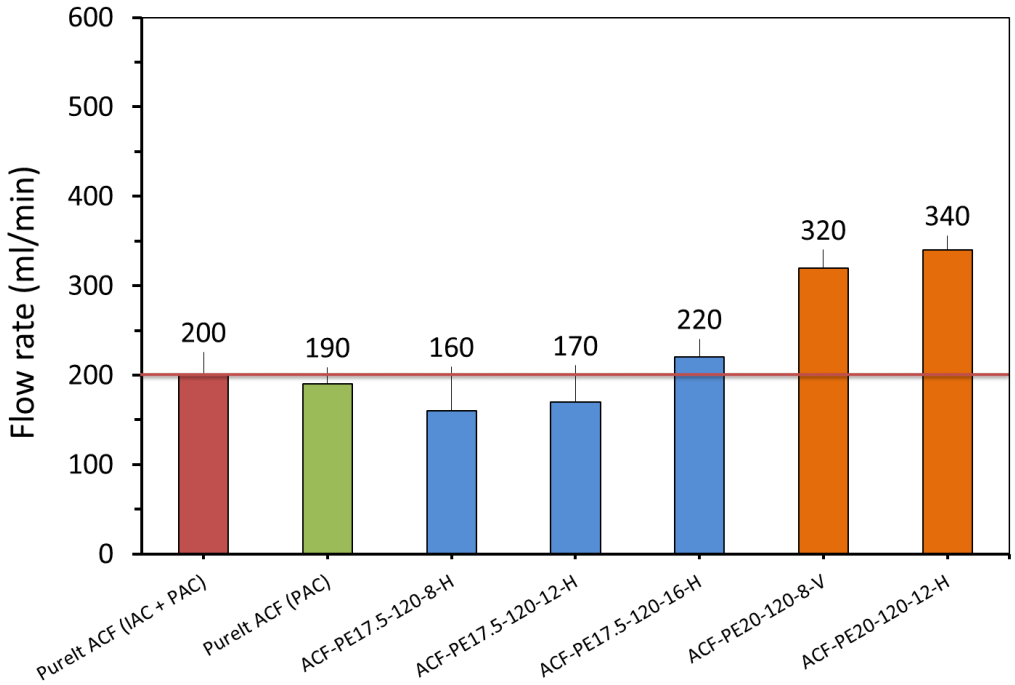

Figure A.30 : Water flow rate of 3D printed filters made from 82.5:17.5 and 80:20 AC-UHMWPE compared to filters made by conventional process

The results also show that the 3D printed filters with 20% UHMWPE have a higher flow rate compared to that of the filters with reduced binder. This result was un-expected since the reduction in the UHMWPE binder would reduce the hydrophobicity of the filters and hence would lead to a higher flow rate. However, these filters were manufactured from a new batch of activated carbon powder, the supplier information claimed same specification. Examination of the sample by this candidate revealed that this batch was not the same quality as the previous one. Scales/flakes with large particles were found when the AC powder was examined using a sieve. Therefore, it is very highly likely that the quality of this material has contributed to the low performance of these filters. Additionally, the low flow rate was attributed to the higher bulk density of the filters with 17.5% UHMWPE.

Figure A.31 shows that the 3D printed filters with reduced binder, the PAC filters made by conventional process and 3D printed filters produced with 20% UHMWPE have a similar turbidity removal efficacy.

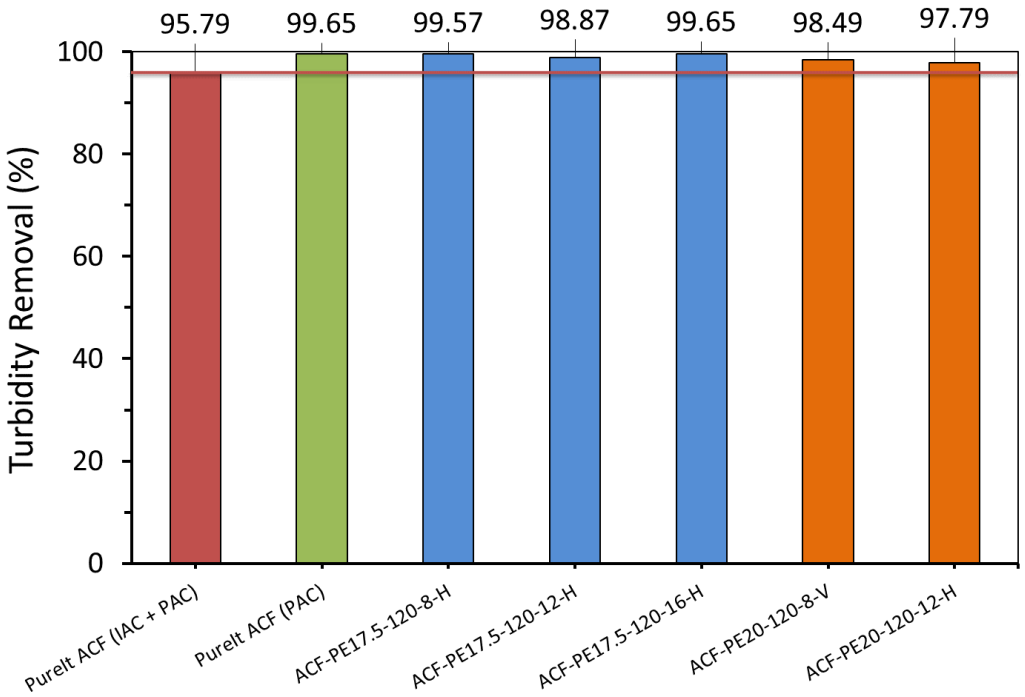

Figure A.31 : Turbidity removal of 3D printed filters made from 82.5:17.5 and 80:20 AC-UHMWPE compared to filters made by conventional process

It was also observed that the turbidity removal of the filters produced from 80:20 (IAC + PAC)-UHMWPE was slightly lower than that of the other three filters.

A.2.9 Comparison of Physical Properties and Flow Rate Between Disc-shaped and Cylinder-shaped 3D Printed Filters

This section is intended to provide a comparison between the disc-shaped and cylinder-shaped filters in terms of their physical properties and performance. This comparison can serve as a resource for baseline information regarding the production of the 3D printed water filters and the benchmarking with the disc-shaped filters, which are considered to be a simple shape, take less time and cost to produce. Consequently, if we could rely on the disc then many more process conditions and formulations could be examined, thereby accelerating the research and reducing cost of operations.

A.2.9.1 Bulk Density

The results in Figure A.32 show that the bulk density of the disc-shaped filters is lower than that of the cylinder-shaped filters. The average bulk densities of the discs and cylinders were approximately 0.40 ±0.02 g/cm^3 and 0.47 ±0.01 g/cm^3, respectively.

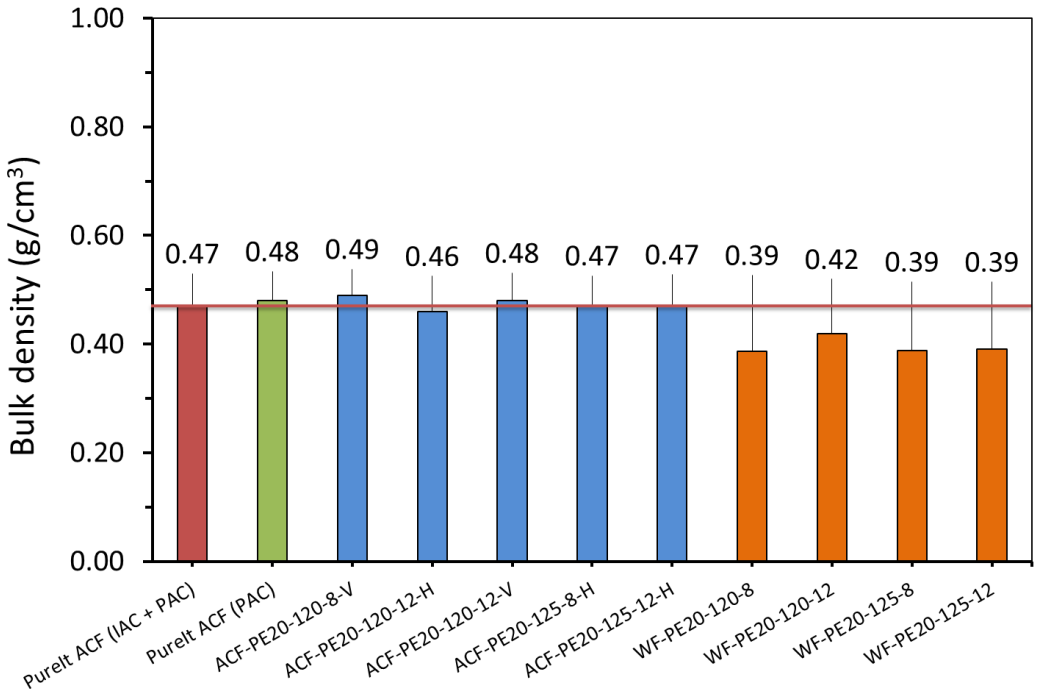

Figure A.32 : Bulk density of 3D printed cylinder-shaped filters compared to disc-shaped filters

The bulk density of the discs was directly measured without any post processing other than brushing in order to remove the un-sintered powder. Measurements of the discs' diameter and thickness were taken at different locations. Three measurements of each dimension were taken and an average value was then generated for each disc. Since the surface of the 3D printed disc was uneven, this may therefore lead to overestimated volume and subsequently resulting in an underestimated bulk density. Another reason that could possibly impact the bulk density is the time the build takes to be completed. The longer the parts remain in the bed during the processing, the longer they are exposed to heat which can lead to denser parts [87, 205].

A.2.9.2 Porosity

The results in Figure A.33 show that the average porosities of the discs and cylinders were approximately 79.5 ±1% and 70.3 ±4%, respectively.

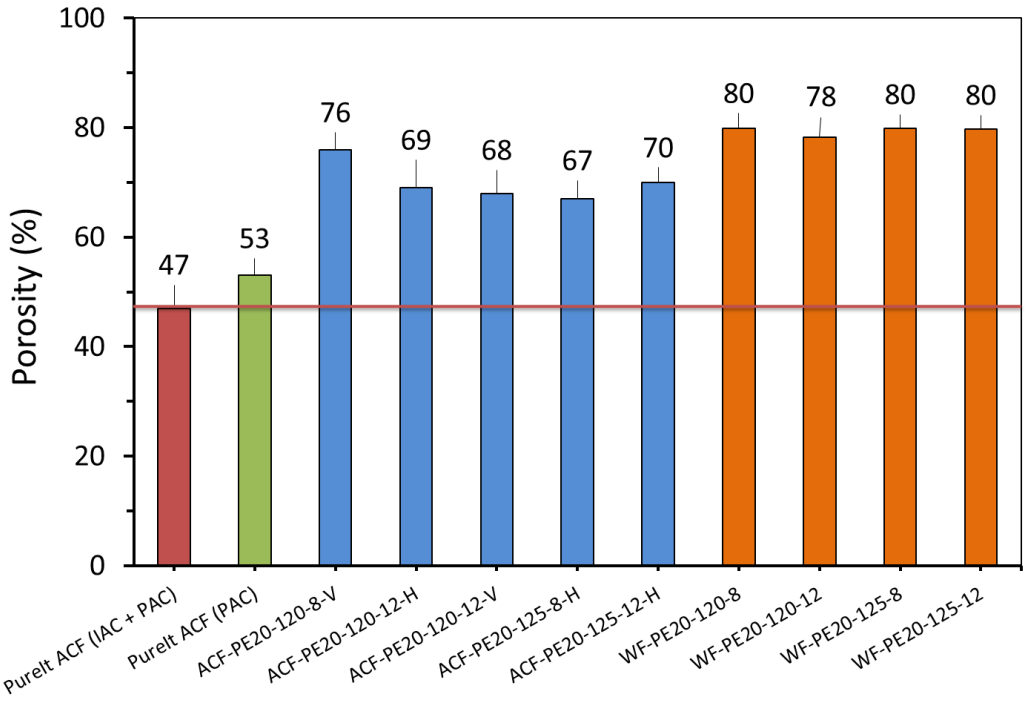

Figure A.33 : Porosity of 3D printed cylinder-shaped filters compared to disc-shaped filters

Two different techniques were used to estimate the total porosity of the 3D printed disc-shaped and cylinder-shaped filters. The porosity of the discs was measured by the ratio of the bulk density of the filters to the true density of the composite powder (i.e. reference density) which was determined using Helium Gas Pycnometry (HGP) method. While, water saturation and immersion (WIP) technique was used for the cylinder-shaped filters.

The comparison of the measured porosity shows that HGP porosity is consistently higher relative to the WIP porosity for all comparable samples. The difference in overall average porosity values was approximately 11.6%. There could be many reasons for these differences. Among these reasons, probably is the sub-microstructure of the AC-UHMWPE composite particles,

which have fine pores inside that could be detected by the helium pycnometry, but cannot be penetrated by water. Additionally, the low bulk density for the disc-shaped filters may have contributed to the high porosity observed compared to the cylinder-shaped filters.

A.2.9.3 Water Flow Rate

Figure A.34 shows a comparison of water flow between the disc-shaped and cylinder-shaped filters manufactured at the same processing parameters and with 20% UHMWPE.

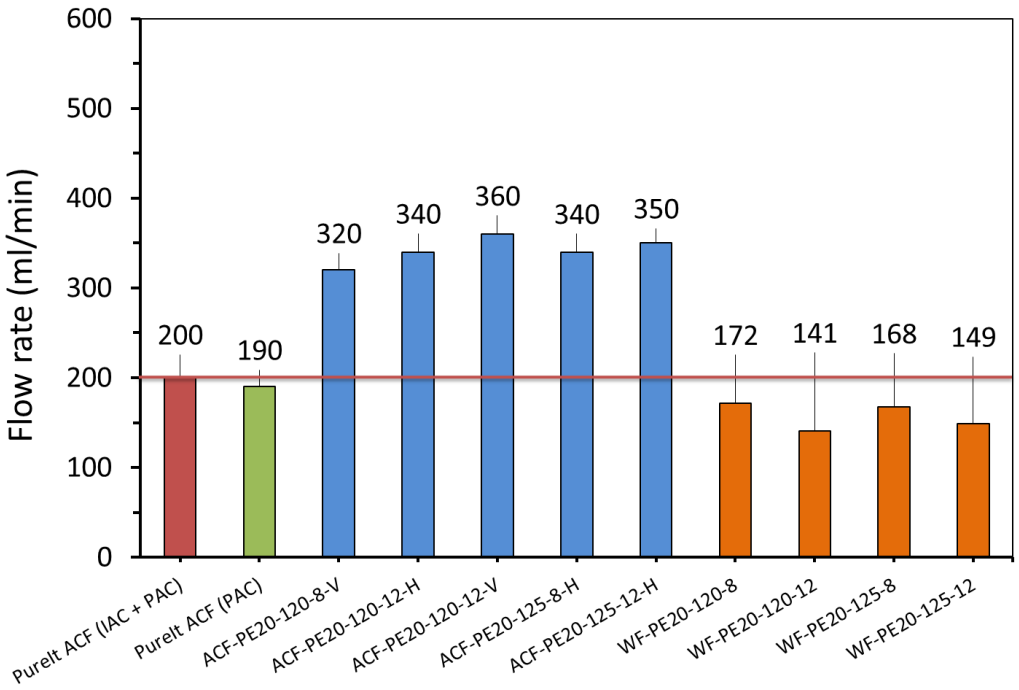

Figure A.34 : Water flow rate of 3D printed cylinder-shaped filters compared to disc-shaped filters

The overall average flow rates of the discs and cylinders were approximately 157.50 ±14.89 and 337.50 ±12.58 mL/min, respectively. The result reveals that the flow rate of the disc-shaped filters is consistently lower than that of all comparable cylinder-shaped filters. This is due to the geometrical differences between these filters as well as the conditions of the flow tests which were carried out on two different test rigs.

As shown in Figure A35, the relationship between the flow rates of the disc-shaped and cylinder-shaped filters, produced at different processing parameters, remains unclear for all comparable samples.

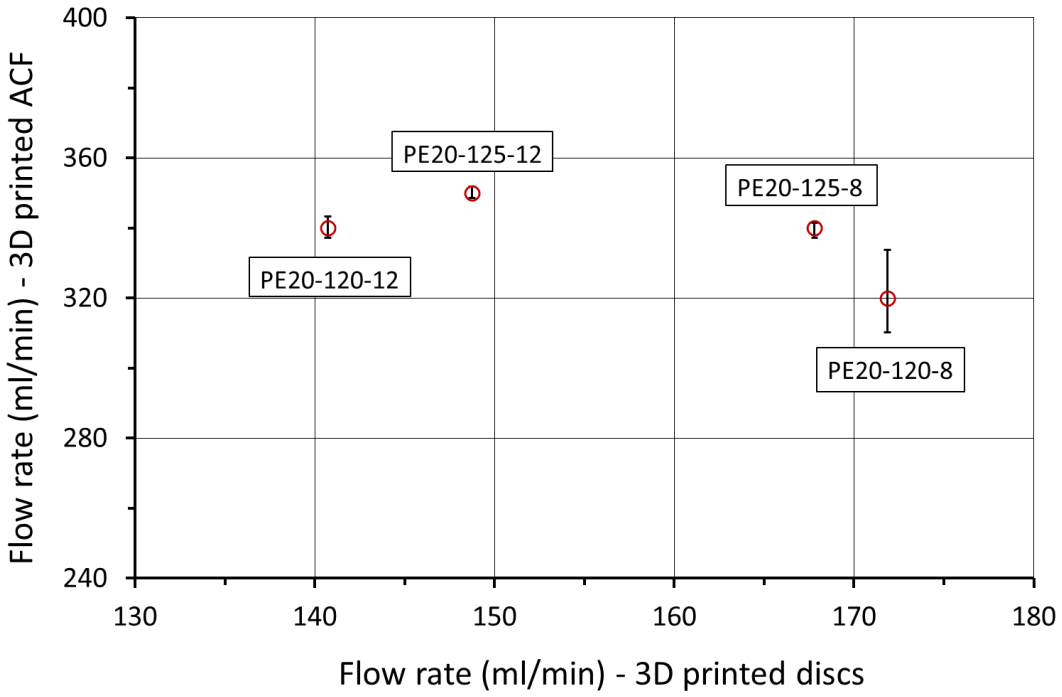

Figure A.35 : Relationship between water flow rates of 3D printed cylinder-shaped and disc-shaped filters

Nevertheless, this comparison can be useful for the prediction of the flow rate of the cylinder-shapes water filters. Based on the overall average values, a low standard deviation can be observed which indicates that the data points are close to the mean value (i.e. expected value) of the samples tested. Therefore, a factor of 2.14 (i.e. the ratio of the flow rate of the cylinder-shaped filters to that of the disc-shaped filters) can be used to predict the estimated flow rate of the cylinder-shaped filters.

A.3 Summary

Activated carbon cylinder-shaped filters have been manufactured successfully using different UHMWPE binder contents and processing parameters.

A.3.1 Preliminary Trials

The preliminary trials revealed that the flow of the 3D printed filters with 30% UHMWPE is lower than that of the filters produced with 80:20 PAC-UHMWPE and the standard 80:20 (IAC + PAC)-UHMWPE by approximately 16% and 20%, respectively. Higher content of UHMWPE binder has contributed to the reduction in the flow rate of the 3D printed 70:30 AC-UHMWPE filters.

A.3.2 Effect of Laser Power

The porosity and flow rate of the 3D printed filters, produced with 20% UHMWPE, were higher than that of the filters manufactured by conventional process. The laser sintered filters produced at laser power of 12 watts exhibits an increase in flow rate by approximately 44% and 47% compared to that of the standard (IAC + PAC) and PAC filters, respectively.

The results also revealed that the flow rate is influenced by the laser power. The flow rate increased with increasing of the laser powder from 8 watts to 12 watts by 11%. Additionally, the 3D printed filters have similar density and turbidity removal efficacy compared to that of the AC filters made by conventional process.

A.3.3 Effects of Bed Temperature and Part Orientation

The 3D printed filters manufactured with different bed temperatures show no significant differences in the density and porosity values. However, the result shows that the flow rate of the sintered filters oriented vertically in the part bed was higher than that of the sintered filters produced horizontally by approximately 5.56%.

Additionally, the result of the flow test also shows that filters produced with a bed temperature of 125°C and a laser power of 12 watts induce a marginal better flow rate compared to that of the filters produced at the same laser power but with a bed temperature of 120°C. Laser sintered filters produced

horizontally resulted a better turbidity removal over vertical orientation for a fixed laser power and bed temperature.

A.3.4 Effect of Laser Gradients

The 3D printed filters manufactured with different laser gradients and different building orientations show no significant differences in the density and porosity values.

Filters produced with the same orientation but with different laser gradients show a flow rate difference of 12%. The results indicated that the filters produced with an inner shell sintered at lower laser power and an outer shell sintered at higher laser power induce better flow rate than that of the filters produced with an inner shell sintered at a higher laser power and an outer shell sintered at a lower laser power.

Filters produced with the same orientation but with different laser gradients, and filters produced at fixed laser gradients with both vertical and horizontal orientation, show similar turbidity removal.

A.3.5 3D Printed Filters Manufactured from 100% Used Powder

The bulk density of the filters made from 100% used powder was slightly higher than that of 3D printed filters made from 100% virgin powder and also higher than that of the AC filters manufactured by the conventional process. Unlike bulk density, the porosity of the 3D printed filters made from used powder was similar to that of the filters made from virgin powder. However, filters made from used powder show low flow characteristics, compared to that of the filters made from virgin powder. The filters produced from 100% used powder resulted a marginal better turbidity removal compared to the 3D printed filters made from 100% virgin powder.

A.3.6 Repeatability

The 3D filters manufactured in different builds but with the same processing parameters, show no significant differences in the density, porosity, flow rate and turbidity removal efficacy. The laser sintering of 3D printed filters shows a highly consistent and reproducible results that can be achieved.

A.3.7 3D Printed Filters Manufactured from Reduced UHMWPE Binder

The 3D printed filters with 17.5% UHMWPE have a higher bulk density compared to that of the filters made by the conventional process and the 3D printed filters with 20% UHMWPE. The density of the filters with reduced binder, has affected the porosity values and the result shows that the porosity was lower by approximately 6% compared to that of the 3D printed filters with 20% UHMWPE. This has also impacted the flow rate resulting in lower flow rate compared to that of the 3D printed filters with 20% UHMWPE. This result was not expected since the reduction in the UHMWPE binder would lead to a higher flow rate. A new batch of activated carbon powder was used to manufacture the filters with 17.5% UHMWPE. This batch appeared to be not having the same quality as the previous batch. However, the 3D printed filters with reduced binder induced a similar turbidity removal efficacy, compared with the PAC filters made by conventional process and 3D printed filters produced with 20% UHMWPE.

A.3.8 Relationship between the flow rates of the 3D Printed Disc-shaped and Cylinder-shaped Filters

The bulk density of the disc-shaped filters was lower than that of the cylinder-shaped filters. However, the porosity of the disc-shaped filters was consistently higher than that of the cylinder-shaped filters. The low bulk density of the disc-shaped filters may have contributed to the high porosity observed compared to the cylinder-shaped filters. Additionally, since the porosity was calculated using two different methods (i.e. HGP and WIP), the sub-microstructure of the AC-UHMWPE composite particles, which have fine

pores inside that could be detected by the helium pycnometry, but cannot be penetrated by water. This resulted in underestimated values of porosity when using water immersion technique.

The flow rate of the disc-shaped filters is consistently lower than that of all comparable cylinder-shaped filters. This is due to the geometrical differences between these filters as well as that the flow tests were carried out on two different test rigs. Nevertheless, the relationship between the flow rates of the disc-shaped and cylinder-shaped filters, produced at different processing parameters, remains unclear for all comparable samples.

Appendix B

ANOVA Full Report

General Linear Model: Density (g/cm3) versus UHMWPE (%); Laser Power (watt); Bed Temperature (°C)

Method
Factor coding: (-1; 0; +1)

Factor Information

Factor	Type	Levels	Values
UHMWPE (%)	Fixed	3	15; 20; 30
Laser Power (watts)	Fixed	2	8; 12
Bed Temperature (°C)	Fixed	2	117.5; 120

Analysis of Variance

Source	DF	Adj SS	Adj MS	F-Value	P-Value
UHMWPE (%)	2	0.008226	0.004113	14.93	0.000
Laser Power (watts)	1	0.000029	0.000029	0.10	0.750
Bed Temperature (°C)	1	0.001250	0.001250	4.54	0.045
Error	22	0.006062	0.000276		
Lack-of-Fit	4	0.005358	0.001339	34.21	0.000
Pure Error	18	0.000705	0.000039		
Total	26	0.016247			

Model Summary

S	R-sq	R-sq(adj)	R-sq(pred)
0.0166001	62.69%	55.90%	43.80%

Coefficients

Term	Coef	SE Coef	T-Value	P-Value	VIF
Constant	0.35626	0.00391	91.05	0.000	
UHMWPE (%)					
15	-0.02232	0.00452	-4.94	0.000	1.33
20	0.00202	0.00452	0.45	0.660	1.33
Laser Power (watts)					
8	0.00126	0.00391	0.32	0.750	1.33
Bed Temperature (°C)					
117.5	-0.00833	0.00391	-2.13	0.045	1.33

Regression Equation

Density (g/cm3) = 0.35626 - 0.02232 UHMWPE (%)_15 + 0.00202 UHMWPE (%)_20
+ 0.02030 UHMWPE (%)_30 + 0.00126 Laser Power (watts)_8
- 0.00126 Laser Power (watts)_12 - 0.00833 Bed Temperature (°C)_117.5
+ 0.00833 Bed Temperature (°C)_120

Fits and Diagnostics for Unusual Observations

Obs	Density (g/cm3)	Fit	Resid	Std Resid	
2	0.40721	0.36787	0.03934	2.63	R

R Large residual

General Linear Model: Porosity (%) versus UHMWPE (%); Laser Power (watt; Bed Temperature (°C)

Method

Factor coding: (-1; 0; +1)

Factor Information

Factor	Type	Levels	Values
UHMWPE (%)	Fixed	3	15; 20; 30
Laser Power (watts)	Fixed	2	8; 12
Bed Temperature (°C)	Fixed	2	117.5; 120

Analysis of Variance

Source	DF	Adj SS	Adj MS	F-Value	P-Value
UHMWPE (%)	2	74.6023	37.3011	49.95	0.000
Laser Power (watts)	1	0.1126	0.1126	0.15	0.701
Bed Temperature (°C)	1	3.1762	3.1762	4.25	0.051
Error	22	16.4285	0.7468		
Lack-of-Fit	4	14.5534	3.6384	34.93	0.000
Pure Error	18	1.8751	0.1042		
Total	26	96.2135			

Model Summary

S	R-sq	R-sq(adj)	R-sq(pred)
0.864148	82.92%	79.82%	74.28%

Coefficients

Term	Coef	SE Coef	T-Value	P-Value	VIF
Constant	81.266	0.204	398.99	0.000	
UHMWPE (%)					
15	1.950	0.235	8.29	0.000	1.33
20	0.162	0.235	0.69	0.499	1.33
Laser Power (watts)					
8	-0.079	0.204	-0.39	0.701	1.33
Bed Temperature (°C)					
117.5	0.420	0.204	2.06	0.051	1.33

Regression Equation

Porosity (%) = 81.266 + 1.950 UHMWPE (%)_15 + 0.162 UHMWPE (%)_20
- 2.112 UHMWPE (%)_30
- 0.079 Laser Power (watts)_8 + 0.079 Laser Power (watts)_12
+ 0.420 Bed Temperature (°C)_117.5 - 0.420 Bed Temperature (°C)_120

Fits and Diagnostics for Unusual Observations

Obs	Porosity (%)	Fit	Resid	Std Resid	
2	78.882	80.929	-2.047	-2.62	R

R Large residual

General Linear Model: Flexural Stress versus UHMWPE (%); Laser Power (watt); Bed Temperature (°C)

Method

Factor coding: (-1; 0; +1)

Factor Information

Factor	Type	Levels	Values
UHMWPE (%)	Fixed	3	15; 20; 30
Laser Power (watts)	Fixed	2	8; 12
Bed Temperature (°C)	Fixed	2	117.5; 120

Analysis of Variance

Source	DF	Adj SS	Adj MS	F-Value	P-Value
UHMWPE (%)	2	1.50409	0.752047	154.13	0.000
Laser Power (watts)	1	0.00021	0.000206	0.04	0.839
Bed Temperature (°C)	1	0.00419	0.004188	0.86	0.364
Error	22	0.10734	0.004879		
Lack-of-Fit	4	0.06928	0.017320	8.19	0.001
Pure Error	18	0.03806	0.002115		
Total	26	1.61853			

Model Summary

S	R-sq	R-sq(adj)	R-sq(pred)
0.0698519	93.37%	92.16%	90.01%

Coefficients

Term	Coef	SE Coef	T-Value	P-Value	VIF
Constant	0.3859	0.0165	23.44	0.000	
UHMWPE (%)					
15	-0.2480	0.0190	-13.05	0.000	1.33
20	-0.0695	0.0190	-3.65	0.001	1.33
Laser Power (watts)					
8	-0.0034	0.0165	-0.21	0.839	1.33
Bed Temperature (°C)					
117.5	0.0153	0.0165	0.93	0.364	1.33

Regression Equation

Flexural Stress (MPa) = 0.3859 - 0.2480 UHMWPE (%)_15
- 0.0695 UHMWPE (%)_20
+ 0.3175 UHMWPE (%)_30 - 0.0034 Laser Power (watts)_8
+ 0.0034 Laser Power (watts)_12 + 0.0153 Bed Temperature (°C)_117.5
- 0.0153 Bed Temperature (°C)_120

Fits and Diagnostics for Unusual Observations

Obs	Flexural Stress (MPa)	Fit	Resid	Std Resid	
25	0.5157	0.6848	-0.1690	-2.68	R

R Large residual